University College London

HYDROGEN ADSORPTION AND DYNAMICS IN CLAY MINERALS

Submission for Philosophiae Doctor

Candidate:
Jacqueline Edge

Supervisor:
Prof. Neal Skipper

June 2014

Abstract

A new class of hydrogen storage material (HSM), the swelling clay minerals, is introduced by the investigation of laponite, a representative smectite. Simple ion exchange allows for a diverse range of charged species to be studied as possible adsorption sites for H_2 within the laponite interlayer, while a sub-monolayer of water pillars the interlayers apart by 2.85 Å, close to the kinetic diameter of H_2. Neutron diffraction shows that the 001 peak, representing the clay *d*-spacing, is directly affected by the introduction of H_2 or D_2, confirming intercalation into the interlayers. Volumetric adsorption isotherms and neutron scattering show that laponites with 3 wt% H_2O rapidly physisorb 0.5-1 wt% H_2 at 77 K and 80 bar, with low binding enthalpies (3.40-8.74 kJ mol^{-1}) and consequently low room temperature uptake (0.1 wt% at 100 bar). The higher structural density of clays results in lower H_2 densities than MOFs and activated carbons, however some cation-exchanged forms, such as Mg and Cs, show promise for improvement having capacities of 22.8 g H_2 per litre at 77K, 80 bar, intermediate between AX-21 and IRMOF-20. At low coverage, INS spectra reveal up to five adsorption sites with low rotational energy barriers (0.7-4.8 kJ mol^{-1}), persisting up to at least 50 K. Analysis of quasielastic neutron scattering (QENS) spectra for Ca-laponite expanded with 3 wt% H_2O reveals two populations of interlayer H_2: one immobile up to 100 K and localised to the Ca^{2+} cations, while the other diffuses by jump diffusion at a rate of 1.93±0.23 Å^2 ps^{-1} at 80 K, 60% slower than in the bulk (D_{bulk} = 4.90±0.84 Å^2 ps^{-1}). Arrhenius analysis gives activation energies of 188±28 K for the calcium and 120±32 K for the sodium form, comparable to the range for activated carbons. The adsorbate phase density of H_2 in laponite interlayers at 40 K is 67.08 kg m^{-3}, close to the bulk liquid density of 70.6 kg m^{-3}. Jump lengths of 3.2±0.4 Å for Ca-laponite measured by QENS at 40 K are similar to the H_2-H_2 nearest neighbour distance in condensed H_2 (3.79 Å). Thus data from a variety of techniques provides a coherent model for the structure and behaviour of H_2 in laponite. The experimental achievement of a two-dimensional film of liquid-like H_2 confined within the interlayers up to 40 K is of great interest for the field of superfluidics, since it may be possible to supercool liquid hydrogen confined in laponite interlayers below the predicted Bose-Einstein condensation temperature at 1 K.

Declaration

I, Jacqueline Sophie Edge, do hereby declare that the work presented in this thesis is unique and all my own work.

Acknowledgements

I wish to thank my primary supervisor, Prof. Neal Skipper, for his insightful advice and guidance throughout. Also, my second supervisor, Prof. Stephen Bennington, for his patience and helpful explanations. Thanks to Arthur Lovell, for his art and scientific advice, as well as his friendship. I wish to thank the ILL instrument scientists, Andrea Orecchini and Stefan Rols for their invaluable assistance in running the experiments and in understanding the data afterwards. Also a special mention to Simon Baudoin, a technician at the ILL, who made the hydrogen dosing of our samples safe and simple. The instrument scientists at ISIS: Daniel Bowron, Tristan Youngs and Felix Fernandez-Alonso were all extremely helpful and showed strong commitment to their work. Without scientific guidance from Felix Fernandez-Alonso, Spencer Howells, Alan Soper, Victoria Garcia-Sakai and Mark Telling, much of the data herein could not have been analysed. The friendly, warm advice and support offered by Chris Howard, Patrick Cullen, David Buckley, Atahl Nathanson, Zeynep Kurban and Radhika Patel have been invaluable throughout.

I would like to extend a special thank you to my friends Nicholas Constantino and Matthew Shiers, who have helped me through the inevitable difficult moments.

I would also like to thank the Engineering and Physical Sciences Research Council (EPSRC) for the funding of this work, through grant EP/P505224/1.

I dedicate this work to the Earth's biosphere and all the wonderful creatures therein (including my Mom and Dad).

Contents

1 **The Hydrogen Economy** **7**

1.1 Climate change, economics and politics 7

1.2 A solar hydrogen economy 8

1.3 Stationary storage 10

1.4 Hydrogen as a fuel 11

1.5 Fuel cells 13

1.6 Transportation 15

  1.6.1 Land-based transport 16

  1.6.2 Shipping 17

1.7 Current HSMs 18

2 **Storing H_2** **20**

2.1 Dihydrogen properties 20

  2.1.1 Ortho and para states 20

  2.1.2 Rotational states 22

  2.1.3 Binding to cations 24

  2.1.4 Equation of state 28

2.2 Requirements and approaches 30

2.3 Chemisorption vs physisorption 31

2.4 Physisorption thermodynamics 34

3 **Solid-state hydrogen storage materials** **36**

3.1 Chemisorption materials 37

  3.1.1 Metal hydrides 37

  3.1.2 Complex hydrides 38

  3.1.3 Novel chemisorption materials 38

3.2 Physisorption materials 39

  3.2.1 Carbon-based materials 39

- 3.2.2 Activated carbon 39
- 3.2.3 Carbon nanostructures 40
- 3.2.4 Graphite Intercalation Compounds (GICs) 40
- 3.2.5 Zeolites 41
- 3.2.6 Metal-organic frameworks (MOFs) 43
- 3.2.7 Novel physisorption materials 45

4 Clays 47

- 4.1 Structure 48
- 4.2 Clay classification 50
  - 4.2.1 Smectites 51
  - 4.2.2 Laponite 52
  - 4.2.3 Vermiculites 53
  - 4.2.4 Micas and Brittle Micas 53
- 4.3 Suitability for hydrogen storage 54

5 Characterisation through scattering 58

- 5.1 Neutron scattering 61
  - 5.1.1 Scattering by a single fixed nucleus 62
  - 5.1.2 Scattering by two identical fixed nuclei 64
  - 5.1.3 Elastic scattering by a general system of nuclei 65
  - 5.1.4 Inelastic scattering by a general system of nuclei 65
  - 5.1.5 Correlation functions 66
  - 5.1.6 Four classes of neutron scattering 67
  - 5.1.7 The principle of detailed balance 68
- 5.2 Diffraction 68
  - 5.2.1 The pair distribution function (PDF) 70
  - 5.2.2 X-ray diffraction 74
  - 5.2.3 Powder diffraction 74
- 5.3 Spectroscopy 75
  - 5.3.1 Incoherent quasielastic neutron scattering 78
  - 5.3.2 Inelastic neutron scattering 85
  - 5.3.3 Small angle scattering 87

6 Experimental methods 88

- 6.1 Clay preparation 88
  - 6.1.1 Ion exchange 88
  - 6.1.2 Pillaring 89

6.1.3 Deuteration 90
6.1.4 Drying and transferral to instruments 90
6.2 Isotherms 91
6.2.1 Measuring isotherms 91
6.2.2 Analysing excess adsorption isotherms 95
6.2.3 Limiting coverage and density 101
6.2.4 Extracting isosteric heat of adsorption 101
6.2.5 Determining surface area 103
6.2.6 Porosity 105
6.2.7 Hysteresis 105
6.3 Neutron instruments 105
6.3.1 NIMROD 105
6.3.2 IRIS 109
6.3.3 IN4 116

7 Pillaring temperature 123
7.1 Controlling water content 123
7.2 The effect of temperature on *d*-spacing 126
7.2.1 Background removal from XRD data 126
7.2.2 Treatment temperature selection 129
7.3 The effect of preheating on H_2 uptake 133
7.4 Chapter Summary 136

8 H_2 binding site structure from neutron diffraction 137
8.1 The effect of pressure on *d*-spacing 137
8.2 Q-space structure 141
8.3 Structure of H_2 and D_2 in laponite interlayers 144
8.4 Chapter Summary 154

9 Adsorption isotherms 156
9.1 High pressure uptake 156
9.2 Low pressure uptake 161
9.3 Hysteresis 167
9.4 Volumetric and gravimetric energy density 167
9.5 Surface area and pore size distributions 168
9.6 Chapter Summary 171

10 Diffusion of H_2 in laponite 173

10.1 Samples and loadings 173
10.2 Neutron scattering intensity 174
10.3 Jump diffusion models 176
10.4 Temperature trends in diffusion 181
10.5 Structure from QENS 187
10.6 Restricted motion 187
10.7 Effect of cation and surface charge on diffusion mechanism 188
10.8 Insights from QENS 189

11 Confirmation of H_2 binding from INS 192
11.1 Binding sites for Na-laponite (RD) 192
11.2 Binding sites for Ca-laponite (RD) 195
11.3 Binding sites for Ca-laponite (EL) 198
11.4 Sample comparison 206
11.5 Insights from INS 209

12 Conclusions 211

References 218

List of Figures 243

List of Tables 265

1. THE HYDROGEN ECONOMY

1.1 Climate change, economics and politics

Human activity during the industrial revolution of the 18th and 19th centuries has directly led to an increase in greenhouse gas emissions. As a consequence, the Earth's global average temperature has risen by about 0.8 K since pre-industrial levels, particularly in the most recent 50 years. A wealth of scientific evidence [1] [2] confirms not only that the global climate is changing, but also that its cause is anthropogenic. Predictions based on this evidence indicate that a rise in the global average temperature of more than 2 K above what it was before 1900 greatly increases the likelihood of the Earth's climate being severely and negatively altered, threatening the survival of much of the Earth's biosphere.

In response to this, the United Nations - comprised of 195 members, including the UK - negotiated the United Nations Framework Convention on Climate Change (UNFCCC) treaty in 1992. In 2008, the Climate Change Act was drawn up [3], establishing the world's first legally binding climate change target. To address this, the UK's Department of Energy and Climate Change (DECC) produced a policy paper entitled "Reducing the UK's greenhouse gas emissions by 80% by 2050", on the 4th September 2013. This is based on estimates suggesting that a 50% chance of mitigating climate change may be possible if global greenhouse gas emissions reach a peak before 2020 and decline steeply afterwards. Approaches for reaching these ambitious targets include replacing fossil fuels with low-carbon energy sources, such as wind and solar power, as well as decreasing the overall demand by improving the efficiency of energy transmission and use.

Continued use of current energy sources, such as nuclear and fossil fuels, will also lead to pollution through the emission of other chemicals and waste products and both require finite, non-renewable resources which are rapidly being depleted by the increasing demand for energy from a burgeoning human population. Oil has other uses, as it is an essential ingredient in the manufacture of many everyday products which modern human society has come to rely on, including most plastics, synthetic textiles and rubber, dyes, food additives and preservatives, lubricants and fertilizer. Uranium is extremely limited on our planet and may need to be conserved for unforeseen future events, such as the diversion of large asteroids on a collision course with Earth. Nuclear power stations have the potential to fail catastrophically and require careful and costly procedures during installation, maintenance and eventual shut-down, as well as rigorous security measures to ensure that no weapons-grade uranium can be removed from the site illegally. While some of these problems can be alleviated by using thorium as the nuclear fission feedstock, the initial cost to build nuclear power stations and the long-term clean-up costs are very high. Both nuclear fission and fusion produce waste products having long-term effects on the Earth's biosphere.

1.2 A solar hydrogen economy

By contrast, solar radiation is freely available for the Sun's lifetime, with a total of 166 PW being incident on the daytime side of our planet. Through absorption and reflection, the Earth's atmosphere removes 49% of this, leaving 85 PW available at surface level. This is more than 5,000 times the current global energy consumption of 15 TW (1.3 kWh per year), so even if only 10% of the 7.6 PW radiation falling on desert regions is collected, covering an area of 1.6 million km^2, at a conversion efficiency of 10%, this will provide five times the world's current energy requirement [4]. An analysis by Abbott in 2010 [4] compares a range of energy sources, including nuclear fission and fusion, shale oil and renewables such as solar, wind power and geothermal, taking into account the costs for the full cycle from fuel production to end-user delivery. He shows that a solar hydrogen economy is sustainable, economically competitive and provides a higher power output than all other sources combined. While a hydrogen economy on its own has been shown to be more costly than other energy solutions [5], a carbon-independent hydrogen economy drawing on solar thermal collection has the advantages of tapping a direct, free, unlimited resource, requiring low-maintenance installation and negligible clean-up costs.

High temperature solar thermal collectors employ sun-tracking parabolic reflectors, focussing sunlight energy to generate electricity either through heating water to drive a steam-turbine, or by heating the absorbing plate of a Stirling engine [6]. In contrast to semiconductor solar cells, solar thermal collector efficiencies can be as high as 50% [7], requiring no finite or toxic chemicals in their manufacture and form robust installations requiring low-maintenance. The harvested solar energy can be exported as portable liquid H_2 or by transmission of electricity via high-voltage DC cables.

One of the biggest challenges for a clean hydrogen economy is emissions-free production of H_2. Molecular hydrogen can be produced from any primary energy source by electrolysis of water, but renewable energy sources avoid CO_2 emissions. The most common method for producing commercial bulk H_2 gas is, at present, steam-reforming of methane or other fossil fuels. High temperature (1000-1400 K) steam interacts with the hydrocarbon, aided by metallic catalysts, emitting H_2 and CO_2, among others. Without costly sequestration to capture the CO_2, this process contributes to climate change and undermines the key benefits of a hydrogen economy.

Water, abundant and freely available on our planet, can be split into H_2 and O_2 by the following endothermic reaction:

$$2H_2O \overset{-237kJmol^{-1}}{\longrightarrow} 2H_2 + O_2. \tag{1.1}$$

This reaction is reversible and its inverse is performed in fuel cells to extract the energy stored in H_2, discussed in Section 1.5. If these reactions are used in combination to form a balanced cycle, then there is no net loss of water and the availability of this valuable commodity is unaffected. The energy needed to drive Equation 1.1 can be supplied by electricity or directly from solar power. When electric energy is used in conjunction with waste heat, this lowers the activation energy and thus the voltage required [8]. Solar power has the advantage of being emissions-free and freely available in hot regions. The HYDROSOL process [9] has been successfully demonstrated, using an iron oxide-coated ceramic cylinder and focussed sunlight energy to harness both O_2 and H_2 in two alternating steps of a thermochemical cycle, the redox reactions for which are presented in Equation 1.2. Heated steam reacts with the metal oxide coating, releasing hydrogen and leaving the oxygen trapped by the metal. This is an exothermic reaction helping to heat the cylinder further for the second step, which requires a higher temperature. The steam is shut off and O_2 is liberated in this step, cooling the metal oxide coating. This two-step process separates the O_2 and H_2 streams, avoiding the danger of forming an explosive mixture.

$$\begin{aligned} MO_{red} + H_2O &\xrightarrow{1100K} MO_{ox} + H_2 \\ 2MO_{ox} &\xrightarrow{1400K} 2MO_{red} + O_2. \end{aligned} \tag{1.2}$$

1.3 Stationary storage

The global political acceptance of climate change has led to increasing development of renewable energy technology, such as tidal, wind and solar harvesting, all of which are notorious for their intermittent availability [10] [11]. The energy fluxes delivered by all three of these primary sources follow diurnal and seasonal cycles, changing the paradigm for traditional energy grid infrastructures, which are designed for distributable, immediate-access energy carriers, such as petroleum and natural gas. This poses a difficult engineering problem which must be overcome in order to move the energy economy towards a more sustainable future.

A number of solutions have been proposed to this problem, one being the development of technologies to store energy during periods of low energy demand (off-peak), releasing it during higher demand (peak load) periods, such as at night-time, to smooth out the demand-supply curves. This has been approached in diverse ways, including pumped water systems, batteries, compressed and liquid air and hydrogen. Pumped hydro stores the potential energy of water by pumping it to an elevated reservoir, for later release as hydro-electricity. While this technology is capable of storing and delivering a large amount of energy, in the region of thousands of megawatts, it is limited to only a few geographical sites around the UK having features suitable for cost-effective development. Batteries, such as Li-ion, NiCd and NaS, store chemical energy in the redox reactions of a range of closed-cycle chemical systems, but low output (10 MW), chemical leakage and safety concerns about having large quantities of volatile substances on site have limited this technology. Batteries are only able to store energy for a short time, on the order of days or weeks and can therefore not address seasonal variations. A range of gases, such as air and hydrogen, can be condensed by liquefaction or high pressures, storing hundreds of megawatts of energy thermodynamically, but there are safety concerns and high costs associated with using large-scale, high-pressure storage tanks. However, hydrogen is unique among these solutions, being both an energy carrier and an energy store.

1.4 Hydrogen as a fuel

Decarbonisation of the atmosphere can be achieved by using pure hydrogen as our primary energy carrier [12] [13]. Hydrogen is the most abundant element in the universe - making up an estimated 75% of its mass - and the ninth-most abundant element in the Earth's biosphere, by mass [14]. It is also the lightest element, as well as nontoxic, colourless and odourless. H_2 is a portable fuel forming part of a natural, closed cycle and emitting only water vapour when burnt with pure oxygen, involving no acid rain, ozone depletion nor greenhouse gases.

Decarbonisation of the atmosphere can be achieved by using pure hydrogen as our primary energy carrier [12] [13]. Hydrogen is the most abundant element in the universe - making up an estimated 75% of its mass - and the ninth-most abundant element in the Earth's biosphere, by mass [14]. It is also the lightest element, as well as nontoxic, colourless and odourless. H_2 is a portable fuel forming part of a natural, closed cycle and emitting only water vapour when burnt with pure oxygen, involving no acid rain, ozone depletion nor greenhouse gases.

Molecular hydrogen's chemical energy, by mass (120 MJ kg^{-1}), is at least three times higher than that of hydrocarbon fuels [15] and six times higher than that of methanol, making it an attractive material for storing and releasing energy. However, in its molecular gas form, it is difficult to store at ambient conditions (volumetric density of only 9.72 kJ l^{-1}), requiring large volumes, high pressures (H_2 at 70 MPa provides 5 MJ l^{-1}) or liquefaction at temperatures below hydrogen's critical point of 33.23 K [16] at ambient pressure. Both compression and liquefaction would consume about a third of the energy to be stored. Storage in solid-state materials, either by non-dissociative surface adsorption (physisorption) or chemical incorporation (chemisorption), can potentially store hydrogen at temperatures and pressures closer to ambient, improving the overall efficiency of energy storage. Physisorptive materials can be placed inside high pressure tanks, enabling a combination of adsorptive storage and pressurised gas storage in the voids within the material. This lowers the enthalpy of adsorption, speeding up refueling times and also slows down the release of hydrogen should an accident occur, allowing any escaping H_2 more time to dissipate before reaching its lower explosive limit in air [17].

The relevant safety properties for hydrogen, methane and petroleum are summarised in Table 1.1. Hydrogen is deemed to have greater safety concerns than hydrocarbon fuels, largely because hydrogen is more likely to explode than hydrocarbons, having

Property	**Unit**	**Hydrogen**	**Methane**	**Petroleum**
Minimal ignition energy	mW s	0.02	0.29	0.24
Self ignition temperature	K	858	813	501-774
Ignition limits (NTP air)	Vol.-%	4-75	5.3-15	1-7.6
Explosion energy for gas	kg TNT/m	2.02	7.03	44.22
Lower heating value	kWh kg^{-1}	33.33	13.9	12.4
Flame temperature	K	2,318	2,148	2,473
Diffusion coefficient (NTP air)	cm^2/s	0.61	0.16	0.005

Table 1.1: Comparison of relevant safety properties for hydrogen, methane and petroleum [18].

a lower ignition energy and far wider limits of detonability in air. However, H_2 is less flammable than petroleum, having a higher minimum ignition limit in air, requiring a higher self-ignition temperature and burning at a lower temperature than petroleum, diesel, methanol or kerosene [18]. Thus the radiant heat from a hydrogen fire is much less than for petroleum fires and less likely to ignite secondary fires. In addition, it does not collect on the ground, enabling it to be easily dissipated through well-designed ventilation. Smoke inhalation is the main cause of death in petroleum fires, while hydrogen combustion produces only water vapour. However, this process consumes oxygen, posing an asphyxiation risk which can be minimised by ensuring that no leaks occur and that enclosed areas are well ventilated, preventing build-up of H_2. Decades of industrial use of hydrogen have demonstrated that it can be handled successfully through well-understood safety procedures [4]. Large-scale underground storage of up to 200 bar of hydrogen in salt caverns having an extremely low H_2 permeability of less than <0.015 % per year has been successfully implemented by ICI for several years and there are long-distance hydrogen pipelines across the US, Germany, France, South Korea and Thailand.

H_2 can be stored more efficiently and over much longer time periods than electricity can be in, for example, batteries and capacitors. H_2 combustion produces clean water, which is in itself a valuable byproduct. In combustion engines, liquid H_2 can act as a cold sink. Before combustion, the liquid H_2 must be heated to a gas - this can be done using waste heat from both the engine and the exhaust, providing the additional benefits of improving the efficiency of the engine by cooling and assisting in the recovery of clean water by cooling the exhaust [4].

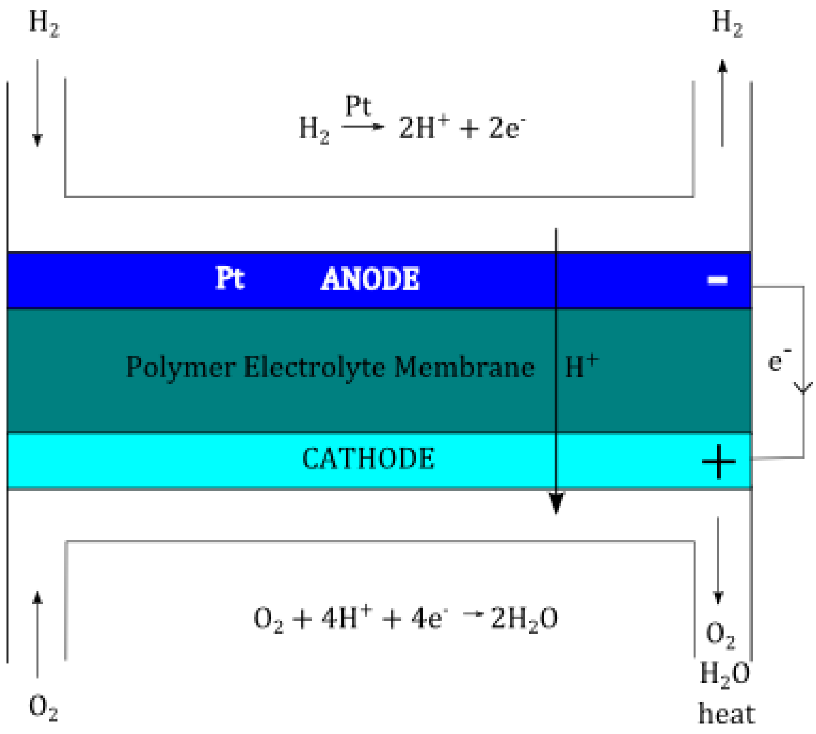

Figure 1.1: (Adapted from [8].) Schematic view of an acidic proton exchange membrane (PEM) fuel cell, showing input fuels and waste products, as well as the chemical reactions at each electrode.

1.5 Fuel cells

Fuel cells convert chemical energy into electricity and can use fuels other than H_2, however H_2 fuel cells are simple and efficient, producing neither carbonaceous nor nitrogenous emissions. A schematic representation of a simple solid polymer (PEM) fuel cell using an acidic electrolyte is illustrated in Figure 1.1. Two electrodes connected by an external circuit are separated by the electrolytic membrane and exposed to continuous gas or liquid flows of fuel (H_2) and oxidant (O_2 or air). The electrodes must be porous to allow the chemical redox reactions to occur, causing electrons to flow in the external circuit. For alkaline electrolytes, H_2 is oxidised at the cathode, catalysed by platinum, and O_2 is reduced at the anode. The membrane is also called a proton exchange membrane, because it only allows protons to pass through. The protons and the electrons are therefore unable to recombine, forcing the electrons to form a current in the external circuit. In addition, the membrane separates the fuel and oxidant gases, allowing both to be collected in a high purity form.

The efficiency of a hydrogen fuel cell is the ratio of electrical energy produced to the input energy, i.e. the enthalpy of hydrogen (using the lower heating value of H_2, 241.98 kJ mol^{-1}). The theoretical limit is reached by assuming that all of the Gibbs' free energy (ΔG = 228.74 kJ mol^{-1}), that available from chemical reactions, can be converted into electrical power. Thus the theoretical electric efficiency of a fuel cell is:

$$\eta_{eff} = \frac{\Delta G}{\Delta H}, \tag{1.3}$$

where ΔG is the Gibbs' free energy and ΔH is the total chemical energy of H_2. The real efficiency is reduced through losses to heat, voltage losses arising from different kinds of overpotentials and resistance and current losses arising from the non-ideal fuel consumption. Fuel cells which utilise the heat produced have improved efficiencies.

Hydrogen fuel cells are up to twice as efficient as hydrogen-powered internal combustion engines (ICE), with a theoretical maximum of up to 94.5% versus the ICE upper limit of 50% below 1100 K [19]. While H_2 fuel cells are lighter than batteries, the storage tank for the fuel requires a larger volume. Fuel cells can run continuously over long periods, limited only by the volume of fuel available. The electrochemical reactions involved are highly selective, thus even if the oxidant used is air instead of pure O_2, no nitrates or nitrites will form. Water must be removed from the cell, but can be collected for a source of clean, potable water. Fuel cells have no moving parts to create noise and are largely silent, with low noise levels generating only from flow mechanisms. This aspect makes them very attractive for vessels requiring stealth, such as submarines and police vehicles.

There are essentially five types of hydrogen-based fuel cell, differing mainly in the electrolyte used: alkaline fuel cells achieve efficiencies of 40-50% and are used in vehicles and aerospace; solid polymer fuel cells (e.g. PEM) are 35-50% efficient, can be small and portable and are therefore suited to transport; phosphoric acid fuel cells have efficiencies of 35-45% and are of medium size, suitable for small-scale stationary storage; molten carbonate fuel cells have the highest efficiency (50-60%) and are ideal for large-scale stationary storage; and solid oxide/ceramic fuel cells have high efficiencies of 45-55% and can be used for either large-scale or residential stationary storage. The latter two have high operating temperatures in excess of 873 K [19]. Issues such as electrical resistance, reaction kinetics, heat and hydrogen leakage reduce the operating efficiencies below their theoretical maxima.

Fuel cells are a relatively young technology and are still expensive to manufacture, but as the technology matures and distributed energy networks develop, economies of scale can be employed to reduce the costs and the market is expected to grow significantly [12]. The US Department of Energy (DoE) 2017 H_2 storage subprogram is in the process of setting technical and cost targets for fuel cells to meet, focussing on safety, capacity and durability. The key limiting technology for fuel cells is the expensive membrane required to separate the protons and the electrons. If this were to fail, the results would be catastrophic, allowing the oxygen/air and hydrogen to form an explosive mixture. The complex chemicals used in polymer membranes may form irreversible products and the catalytic activity of platinum is extremely sensitive to impurities in the fuel, reducing the membrane's effectiveness. This catalyst poisoning effect reduces the lifetime of the fuel cell, which is typically only about six months. The need for platinum, a very rare metal occurring at only 5 parts per billion by weight in the Earth's crust, greatly increases the manufacturing costs for fuel cells. Research into ways to reduce the amount of platinum needed through the use of nanoparticles [20], as well as alternative catalysts, such as cobalt-doped graphene [21], is currently underway.

1.6 Transportation

With a quarter of all domestic CO_2 emanating from land- and water-based vehicles [19], targetting the transport sector is a priority. The DoE has focussed its research and funding support on reducing emissions from this sector, specifically aiming to introduce low-emission cars. Innovations in this area have focussed on producing, or retro-fitting, ultra-low emission engines running on electricity, hydrogen, or a combination of the two.

The DoE has defined a set of technical targets for achieving viable onboard H_2 storage and these are updated on a regular basis. A few of the main DoE technical targets are summarised in Table 1.2. The main focus of their research and development activities are to increase gravimetric and volumetric densities and to reduce costs for transportation and small portable storage units. The demands for portability are far more stringent than for stationary storage, because of the limited space and weight requirements. There is a strong emphasis on materials being compact and lightweight.

Feature	2010	2015	Units
Gravimetric density	6%	9%	wt% H_2
Volumetric density	0.045	0.081	kgH_2 l^{-1}
Cycle life	1000	1500	Cycles
Storage system cost	4	2	\$/kWh
Min. operating temp	223	233	K
Max. operating temp	323	333	K
Fill-time for 5 kgH_2	3	2.5	minutes
Loss of usable H_2	0.1	0.05	gh kg^{-1}

Table 1.2: DoE technical targets for onboard hydrogen storage [22].

1.6.1 Land-based transport

There are two ways to transform the chemical energy in hydrogen into mechanical energy to power vehicles. The first uses technology similar to a traditional ICE, injecting hydrogen fuel into an electronically-controlled rotary engine for combustion. Examples are Mazda's RX-8 Hydrogen RE and BMW's Hydrogen 7, the latter having demonstrated good performance on a composite aluminum-glass fiber double-walled liquid hydrogen tank. The second uses a hydrogen-fuelled PEM fuel cell stack as its primary power source and has an onboard tank of H_2 fuel. This technique is used in a hydrogen fuel cell vehicle (FCV), such as Hyundai's ix35 and Toyota's FCV-R Concept. Hydrogen is pumped from the tank to the fuel cell stack, made up of several hundred fuel cells.

Electric motors are 3-4 times more efficient at converting their stored energy than most petroleum-based internal combustion engine (ICE) cars, which have a typical tank-to-wheel efficiency of around 20% [19]. Electric cars are propelled by an electric motor deriving power from an onboard energy storage system: either a fuel cell or a rechargeable battery (usually lithium-ion). A controller regulates the power supply and determines how much energy to draw from the storage system whenever the accelerator is operated by the driver. Hybrid vehicles, such as the Honda Accord and Subaru Viziv-2, use both battery and fuel cell energy to power the electric motor.

The Vauxhall Ampera and Nissan LEAF are examples of electric cars running on battery energy alone. Recharging of a battery takes up to 12 hours and the range of most electric cars is limited to less than 120 km on a full battery. However, the current car manufacturing industry and transport infrastructure are better able to adapt for battery-powered electric motors than for hydrogen-fuelled vehicles and the US government has backed battery electric car technology since cancelling the Bush administration's Hydrogen Highway project in 2012. However, the US's booming shale gas industry has improved the economic prospects for hydrogen production and resulted in the Obama administration launching a new H_2USA programme in 2013 to boost the development of hydrogen-fuelled vehicles [23]. Since 2008, fuel cell costs have dropped significantly, largely due to an 80% reduction in the amount of platinum needed in their manufacture [24]. However, the difficulties with membrane technology discussed in Section 1.5 above, combined with the ease of converting traditional ICE vehicles and vehicle manufacturing processes make H_2 ICEs a more attractive and economic option. For Europe, however, the dependence of hydrogen production on steam-reforming of natural gas may well lead to an increase in carbon emissions [25], especially if used in hydrogen ICE vehicles. The recent discovery of low-temperature catalysis of water-splitting by the mineral olivine in the presence of aluminium may resolve this issue [26].

Hydrogen buses are already in operation in a number of large cities around the world. The reason for their relative success over private cars is their larger size, enabling them to carry large tanks employing simple H_2 gas compression storage. The same logic applies to trains and a number of countries, such as Denmark and Japan, are developing hydrail trains, using onboard hydrogen to power the traction motors [27].

1.6.2 Shipping

The emissions from the growing shipping industry are largely unregulated and thought to be much greater and harmful than those from aviation. The International Maritime Organisation (IMO) estimates that shipping is responsible for 4-5% of global carbon emissions. Large vessels such as supertankers, cruise liners, oil tankers and container ships also emit considerable quantities of sulphur and nitrogen oxides from diesel-powered engines. A hydrogen-powered energy system for boats could greatly reduce pollution from this sector and has different requirements from those for land-based vehicles. While space may still be limited on smaller boats, the emphasis on gravimetric density is reduced, since boats require ballast. A heavy fuel store may be an advantage.

The UK's first commercial boat powered by a 12 kW fuel cell, Hydrogenesis, was launched in 2013 by Bristol Hydrogen Boats. It is an 11 m, 12-seat ferryboat which completed a successful six-month trial operation in September 2013. Fuel cell passenger boats are also in operation in Amsterdam (Fuel Cell Boat BV), the US (the Duffy Ferryboat) and Germany (Zemships, Hydra 1). In Canada, a hybrid H_2-diesel fleet is envisioned for the coast guard, since silent running vehicles would be an advantage.

1.7 Current HSMs

No material has as yet achieved sufficient gravimetric storage and release within the pressure and temperature ranges suitable for mobile storage (1-10 bar, 273-373 K, representing an enthalpy change of 15-24 kJ mol^{-1} [18]. In general, chemisorption materials have higher storage capacities, such as 7.6 wt% H_2 for MgH_2 [28] and 19.6 wt% for AB [29], but they tend to have slow kinetics and require high temperature release, in excess of 473 K. The best performing chemisorption materials contain expensive metals, as well as displaying a significant amount of irreversible H_2 adsorption, prohibiting their long-term use [28]. On the other hand, the best experimental result for a physisorption material, which generally demonstrate rapid uptake and release kinetics, is 8 wt% H_2 for MOF-210 [30], but this requires cryogenic temperatures (77 K) and high pressures (70 bar) to maintain. Under room conditions, MOF-200, like many current physisorption materials, has much lower storage capacities: only 0.54 wt% excess at 298 K and 100 bar [30], due to a low binding energy of <5 kJ mol^{-1} [31].

This study aims to examine the interactions between dihydrogen and a versatile class of materials: clay minerals. To date, little is known about H_2 dynamics in clay minerals and only one research paper investigating clays as HSMs has been published [32]. Several features of the interlayer region of certain phyllosilicates, such as the charge characteristics and pore dimensions, can be tuned for H_2 adsorption suitability. Preliminary results indicate that the clay mineral interlayer provides a tuneable environment for studying the adsorption and dynamics of H_2, as well as showing promising characteristics for rapid, reversible physisorption of molecular hydrogen with favourable thermodynamics. In addition, the nuclear and waste industries employ clay minerals as a key component of the barrier mechanism in containing toxic wastes, the smectite bentonite in particular having the desirable properties of low hydraulic conductivity and low effective porosity [33] [34]. Since a number of toxic waste products, such as bitumen [35] and radioactive incinerator ash [36], release significant quantities of H_2 during their decay lifetime, as do the metallic containers themselves by corrosion [34], information about the mobility of H_2 in clay minerals is of great value.

2. STORING H_2

2.1 Dihydrogen properties

Hydrogen is a simple, homonuclear diatomic molecule consisting of two protons bound together at a distance of 0.74 Å [37], sharing their electrons equally. The valence electrons are both involved in the H-H σ-bond and there are no additional electrons which may interact with substrate atoms. Therefore in the absence of charged sites, molecular hydrogen can only bind to surfaces through weak van der Waals' forces. The H_2 diatom has two axes of symmetry: one joining the two protons (the major axis) and one perpendicular to this, lying directly between the two protons (the minor axis). The ratio of the extent of the electron density along the major axis to that along the minor axis is approximately 94% in the ground state, making the H_2 molecule prolate, with a van der Waals' radius of 1.375 Å [38]. The diatomic symmetry results in molecular hydrogen having no permanent dipole moment, however it does have a weak electric quadrupole moment of 0.13 eÅ^2 [39], where e is the electron charge, which can be visualised as a charge of $+x$ on the protons and $-2x$ midway between them. Dihydrogen is also polarisable in the presence of an external potential, with an isotropically averaged polarisability volume of 0.76 Å^3 [40], leading to stronger binding through the induced dipole and enhanced quadrupole moments, illustrated in Figure 2.6 c). Both the ion-quadrupole and ion-induced dipole interaction energies are distance-dependent, decaying with distance r as $\frac{1}{r^3}$ and $\frac{1}{r^4}$ respectively [41].

2.1.1 Ortho and para states

The symmetry of an H_2 molecule places certain restrictions on the wave function, in accordance with Pauli's exclusion principle. The overall wavefunction, Ψ, is the product of the vibrational, rotational and nuclear wavefunctions ($\Psi_{vib} \times \Psi_{rot} \times \Psi_{nuclear}$) and must be antisymmetric with respect to exchange of particles, since the particles involved (electrons and protons) are indistinguishable fermions. For temperatures below room temperature, Ψ_{vib} is symmetric, therefore one of Ψ_{rot} and $\Psi_{nuclear}$ must be antisymmetric, while the other must be symmetric. Each of the protons of H_2 has a spin of $\frac{1}{2}$. If the spins are antiparallel, then the total nuclear spin (I_N) is 0 (antisymmetric $\Psi_{nuclear}$). Conversely, parallel protonic spins give rise to I_N of 1 (symmetric $\Psi_{nuclear}$).

If a diatomic molecule is treated as a rigid entity, then the rotational wave functions are the spherical harmonics, $Y_J^{(m_J)}(\bar{r})$ with degree J and order m_J being the angular momentum quantum numbers and $\bar{r}$ being the unit vector along the internuclear axis. Interchange of the protons reverses the direction of $\bar{r}$, having the following effect on Ψ_{rot}:

$$Y_J^{(m_J)}(\bar{r}) \rightarrow Y_J^{(m_J)}(-\bar{r}) = -1^J Y_J^{(m_J)}(\bar{r}). \tag{2.1}$$

This function is symmetric if J is even (= 0, 2, 4, etc.) and antisymmetric if J is odd.

Two spin isomers of H_2 exist - orthohydrogen (o-H_2) and parahydrogen (p-H_2):

- p-H_2 has an antisymmetric $\Psi_{nuclear}$ ($I_N = 0$), making p-H_2 the nuclear spin singlet state with antiparallel proton spins. Ψ_{rot} must be symmetric and thus J is even. The ground state of H_2 is parahydrogen, with J and $m_J = 0$ and the rotational wave function $Y_0^0(\bar{r})$, similar to the atomic s-orbital. The electronic charge distribution of a p-H_2 molecule is therefore always isotropic.
- o-H_2 is the excited nuclear triplet state of H_2, having parallel proton spins, i.e. symmetric $\Psi_{nuclear}$ ($I_N = 1$) and antisymmetric Ψ_{rot}. Only the spherical harmonics which have odd J satisfy the latter condition, such as the dumbbell-shaped $Y_J^{(m_J)}(\bar{r})$. The electronic charge distribution of an o-H_2 molecule is anisotropic.

Thermally equilibrated H_2 gas at standard temperature and pressure is a mixture of these two species, consisting of 25% p-H_2 and 75% o-H_2, proportions consistent with the expected 1:3 ratio of singlet to triplet states. Conversion between the two species is restricted by the Pauli Exclusion Principle and will only occur if conditions exist which permit a spin-flip of the nuclear state, such as the presence of either a paramagnetic absorber which catalyses the transition from o-H_2 to p-H_2, or a diamagnetic catalyst for the reverse transition. Therefore the energy differences between rotational levels is large, giving o-H_2 and p-H_2 very different physical properties. The two lowest energy states are separated in energy by 170.5 K [37], therefore at temperatures below this, the $J = 0$ state will rapidly dominate. At temperatures below 20 K, nearly all the molecules will convert to the p-H_2 state, a process that can take many hours.

Deuterium (^{2}H) is a stable isotope of hydrogen, occurring at a natural frequency of one atom in 6420. The nucleus has a proton and a neutron, making the atom heavier than a normal H atom. Deuterium occurs naturally as a diatomic gas, either hybridised with ^{1}H as ^{1}H^{2}H (HD), or as $^2H_2$ (D_2). D_2's van der Waals' radius of 1.38 Å [37] is slightly larger than that of $^1H_2$ (1.375 Å [38]), but both have the same internuclear distance of 0.74 Å in the ground state [42]. In most instances, it interacts in a similar fashion to ^{1}H, but with larger mass and inverted parity of para- and ortho- states: p-D_2 has odd J and consequent electronic charge anisotropy [37].

2.1.2 Rotational states

Unhindered homonuclear diatomic molecules can rotate around two axes, with the associated rotational energy being quantised. Even in the condensed phases, H_2 molecules are free to rotate [43], approximating a three-dimensional linear rigid rotor and providing a way to experimentally measure the rotational constant [37]. The energy levels, E_J, obtained from the Schrödinger equation, where the Hamiltonian is expressed in terms of the angular momentum or rotational quantum number, J, are:

$$E_J = B_v J(J+1), \tag{2.2}$$

where $B_v = \frac{\hbar^2}{2I}$ is the rotational constant, $I = \mu R_v^2$ is the moment of inertia of the diatomic molecule, $\mu = \frac{(m_1 m_2)}{(m_1+m_2)}$ is the reduced mass, R_v is the distance between the hydrogen nuclei and v is the vibrational quantum number.

In free H_2, R_v is 0.74 Å, giving a B_v of 7.37 meV [44]. Rotational states are $(2J+1)$-fold degenerate, each sub-state labelled by the angular momentum projection quantum number, $m_J = 0, \pm 1, \pm 2, \ldots, \pm J$. The rotational transition from $J = 0$ to $J = 1$ is split by an energy of 14.74 meV. This is represented in the rotational spectrum of solid H_2 as a peak at this energy transfer level. Most of

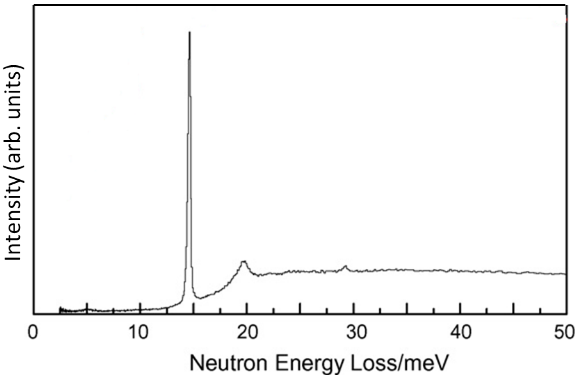

Figure 2.1: The INS rotational spectrum of solid p-H_2, showing the strong, free rotor transition peak at 14.74 meV (from [45]).

the other transitions experience recoil, with simultaneous excitation of rotation and translation modes, and are therefore visible as a broad band in the spectrum, rather than an intense peak. Figure 2.1 shows these features.

In the adsorbed state, where the H_2 molecule is in the presence of an anisotropic external potential, some of the allowed transitions for the excited state may be restricted or subject to a potential barrier. The energy levels associated with the quantum number m_J split into higher (hindered) and lower (unhindered) energy states [46], with a pair of these states ($m_J = \pm 1$) being degenerate. The single free rotor transition at 14.74 meV, representing the transition from the $J = 0, m_J = 0$ ground state to the degenerate state $J = 1, m_J = 0, \pm 1$, splits into two transition lines, one representing the transition $(J = 0, m_J = 0) \to (J = 1, m_J = 0)$ and the other representing the transition $(J = 0, m_J = 0) \to (J = 1, m_J = \pm 1)$. The potential for such a system can be expressed, in purely orientational terms, as [47]:

$$V(\theta, \phi) = \phi \cos^2 \theta. \tag{2.3}$$

This potential has axial symmetry and is expressed in spherical coordinates, with θ and ϕ being the angles shown in Figure 2.2. White and Lassettre [46] showed that there are two limiting cases for this potential: $\phi \to +\infty$, in which the molecule's internuclear axis lies parallel to the plane of the adsorption surface, and $\phi \to -\infty$, with the axis perpendicular to the adsorption plane. In the former case, referred to as the 2D case, rotation in only one dimension is hindered and the other two states, having $m_{\mathrm{J}} = \pm 1$, are superposed and lower in energy [45]. The opposite is true in the latter case, which is referred to as the 1D case [48]. Adsorption of H_2 on Grafoil is an example of a 2D rotor; a terminal methyl group is a typical 1D rotor [49]. Previous work using this potential and variations thereof has examined

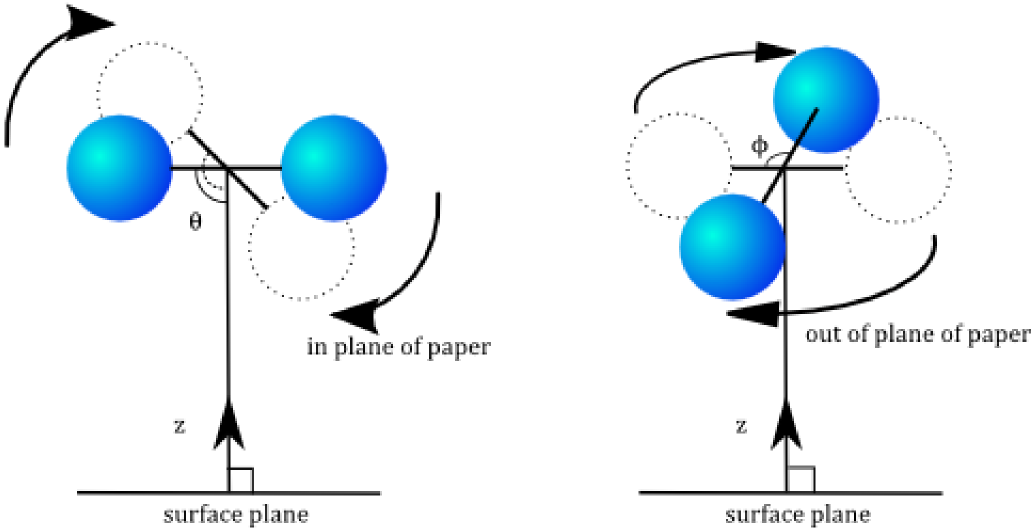

Figure 2.2: Schematic representation of H_2 physisorption, showing the angles represented in the potential equation: $V(\theta, \phi) = \phi \cos^2 \theta$ (Equation 2.3).

H_2 adsorption on caesium graphite [49], on Rb-intercalated graphite [50] and on potassium graphite [51].

The 2D case mentioned above has cylindrical symmetry. A cylindrically symmetrical potential can be described as having no dependence on ϕ, but some preferred orientation, θ, for the H_2 axis, as in the following sinusoidal equation, where $2V_0$ is the barrier constant:

$$V(\theta) = V_0(1 - \cos 2\theta). \tag{2.4}$$

Figure 2.3 illustrates the 2D hindered rotor case for H_2 in the presence of a cylindrically symmetric potential represented by Equation 2.4. When the 1D or 2D potentials are used to solve Schrödinger's wave equation, the relationship between the energy level splittings and the potential field strength can be determined. Figure 2.4 illustrates this for an axially symmetric $\cos 2\theta$ potential.

2.1.3 Binding to cations

H_2 displays a very wide range of non-dissociative binding affinities to other molecules, ranging from very weak dispersive van der Waals' interactions (~-4 to -5 kJ mol^{-1} [41]), in which the potential decays as $\frac{1}{r^6}$ with separation (r), to strong bonds (~-40 to -50 kJ mol^{-1} [41]) involving electrostatic attractions, some electron sharing and an associated lengthening of the H-H bond up to 1.6 Å [41]. Bonds stronger

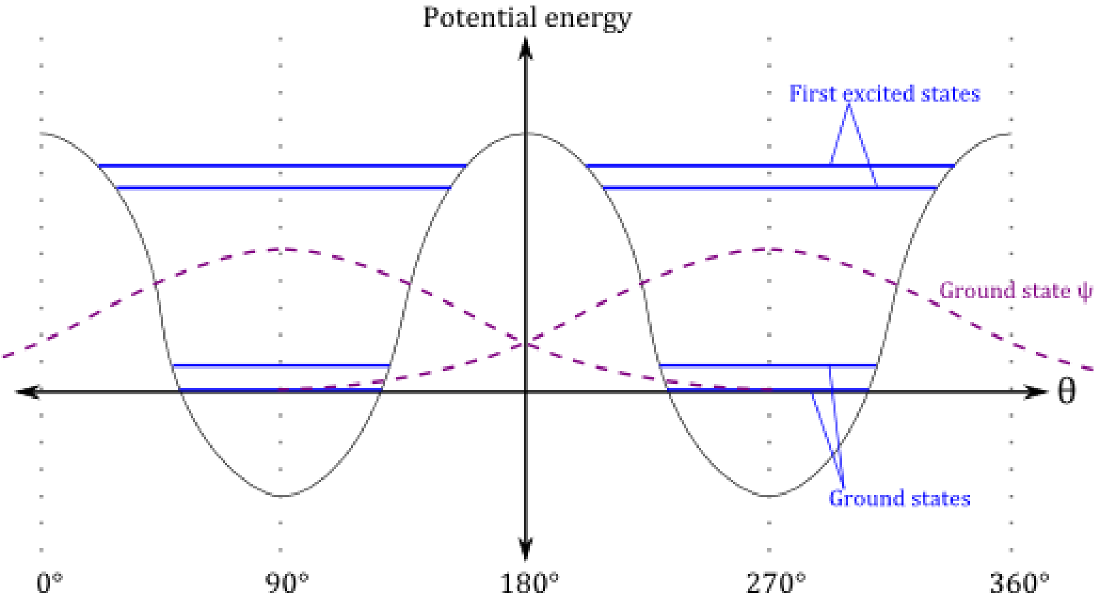

Figure 2.3: (Adapted from [52].) 2D hindered rotor for H_2 in the cylindrically symmetric potential, $V(\theta) = V_0(1 - \cos 2\theta)$.

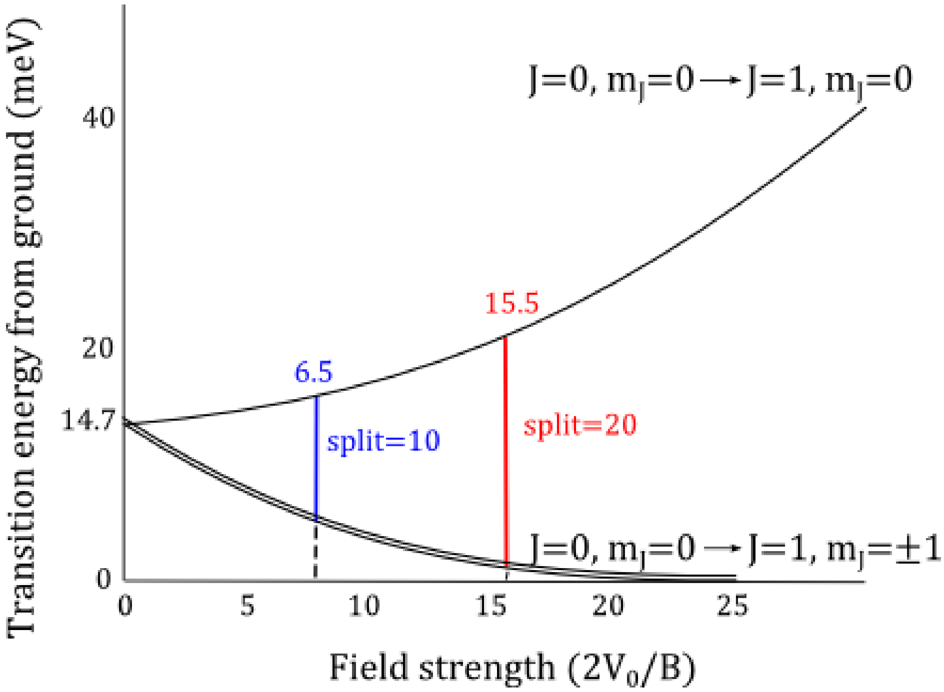

Figure 2.4: (Adapted from [49].) Splitting pattern for the 2D hindered rotor rotational energy levels of H_2, showing how the height of the rotational barrier can be determined from the degree of splitting between ground and first excited state energies.

than this are considered to be hydrides [53]. For efficient energy storage, storage and extraction of H_2 in the pressure region of 1-30 bar and temperatures between 273-373 K is desired. The ideal binding range for this near-ambient uptake and release of H_2 without molecular dissociation, the so-called strong physisorption regime, is estimated to be ~-15 to -20 kJ mol^{-1} [54] [41] [53]. Weaker interactions require lower temperatures for storage while stronger interactions require high temperature and/or pressure to extract the stored H_2.

The binding between any two molecules is strengthened if attractive electrostatic interactions are involved. The significance of H_2's polarisability in strengthening the bond between H_2 and alkali metal cations has been demonstrated both theoretically [55] and experimentally [56]. Incorporating such cations in an adsorbent surface in such a way that they are directly accessible to adsorbate hydrogen molecules as bare or open metal binding sites, may provide a route to the desirable strong physisorption regime for hydrogen storage [53]. This is the principle behind much research on intercalates, zeolites and metal-organic frameworks [57], seeking to improve the thermodynamic properties for H_2 adsorption.

However, the strength of this interaction also needs to be weak enough to release H_2 in its molecular form at near-ambient conditions. For instance, in a Kubas complex, H_2 binds very strongly to transition metals such as Scandium and Zinc, owing to molecular orbital overlap and a resulting cross-donation of electrons to form a stable sigma bond [53]. The H-H electron density is "forward donated" to vacant metal d-orbitals and metal electron density is "back donated" to the antibonding H_2 σ orbital. The strength of these bonds typically varies between 20 and 160 kJ mol^{-1}, stronger than that required for strong physisorption [41]. Thus cations suitable for physisorptive storage of H_2 in clays for this study were sought from the main-group elements, looking for those which can provide sufficient non-dissociative binding to H_2 and preferentially a large enough surface area to accommodate multiple hydrogen molecules. In addition, environmentally friendly and readily available elements are desirable, suggesting the alkali and alkaline earth metal cations, such as Li^+, Na^+, Ca^{2+}, Mg^{2+} and Al^{3+}.

In the absence of direct experimental data for H_2 binding to naked cations, measurements or *ab initio* calculations done on the enthalpy change associated with the loss of water molecules from hydrated cations can lead to a first approximation, multiplied by an appropriate factor. Desorption measurements of water and H_2 adsorbed to clay taken during the course of this study show that water starts to desorb at around 400 K, whereas hydrogen starts at around 40 K, so a reasonable estimate for this factor is about one-tenth. The cations in the clay interlayers are not fully hydrated and, for this study, have been pretreated to remove all but one of the surrounding waters. If the second to last of the six closest water molecules surrounding a fully hydrated Ca^{2+} ion is removed, the enthalpy changes by -60 kJ mol^{-1} [58], by *ab initio* calculations, compared with an enthalpy change of -40 kJ mol^{-1} when the same water is removed from the hydration shell (also six molecules) around a Na^+ ion [59] and an *ab initio* estimate of -70 kJ mol^{-1} for removing the second to last water from the six-water Mg^{2+} hydration shell [58]. Thus calcium and magnesium seem to be the better candidates for reaching the strong physisorption regime.

Bare alkali metal ions can interact with more than one H_2 [60], but each subsequent physisorbed molecule will experience a slightly reduced binding energy as each bound H_2 reduces the ionic charge available for subsequent hydrogen molecules to interact with. In addition, H_2-H_2 interactions tend to be repulsive, further lowering the binding energy. Larger cations can accommodate more hydrogen molecules, but their charge density, and therefore their ability to induce polarisation in H_2, is lower. From a purely geometrical point of view, the three-dimensional H_2 close-packing coordination numbers for Mg^{2+} and Ca^{2+} are expected to be similar to those for the slightly larger H_2O, thus a minimum of 6 and 8 respectively [61]. However, when cations are embedded within complex adsorbent surfaces, the maximum coordination number cannot be realised. Water is a strongly polar molecule and forms much stronger bonds with naked cations than H_2 does, thus competing for the available binding sites.

Stable cation-H_2 complexes with these elements have already been studied theoretically [41]. The polarising ability of a cation depends on its charge density, which is governed by its valency and inversely proportional to the square of its radius. Thus small, divalent cations have a greater capacity than large or monovalent cations to induce the H_2 dipole moment. Therefore the divalent cations Ca^{2+} and Mg^{2+}, having radii of 100 pm and 72 pm respectively [62], are suitable candidates for improving adsorption strength, with Mg^{2+} being the smaller and more polarising of the two. Studies of hydrogen doping of graphites intercalated with either Li or Ca have shown that these cations readily form hydrides [63] [53] [64], indicating that the bonding mechanism in these materials is too strong in these materials. Hydride formation requires backdonation of electrons and is specific to materials which, like graphite intercalation compounds (GICs), have excess electron density. The average binding strengths between H_2 and the cations Na^+ and Mg^{2+} in complexes containing $n =$

Cation	No. of bonded H_2's $M-(H_2)_n$	Average $M-(H_2)$ distance (Å)	Average binding strength (kJ mol-1)
Na^+	$n=1$	2.471	-12.55
Na^+	$n=2$	2.471	-12.18
Na^+	$n=3$	2.475	-11.30
Mg^{2+}	$n=1$	2.034	-90.37
Mg^{2+}	$n=2$	2.037	-83.81
Mg^{2+}	$n=3$	2.051	-71.59

Table 2.1: Calculated binding strengths between hydrogen molecules and bare Na^+ and Mg^{2+} cations, showing the variation of energies and bond distances expected for the first three H_2's in a hypothetical solvation shell (from [41]).

1, 2 or 3 hydrogen molecules, have been calculated by Lochan *et al.* [41] and are presented in Table 2.1.

Table 2.1 shows that the theoretical binding energy between Na^+ and H_2 is slightly below the strong physisorption range, even at optimum conditions of the bare cation being bound to a single hydrogen molecule and nothing else. However, confinement effects may strengthen this interaction by exposing the adsorbed molecule to more potential surfaces. The binding strength for Mg^{2+} is much higher than the ideal range, but this is only expected for an isolated Mg^{2+}-H_2 system. In reality, such a system is extremely difficult to manufacture and the Mg^{2+} will generally be bound to a number of surface atoms or other molecules, for example in a partial solvation shell. This will reduce the effective charge on the cation and temper the binding strength for H_2, bringing it closer to the desired range. A microporous material containing unsaturated Mg^{2+} centres synthesised by Dincă and Long in 2005 [65] showed an improved, relatively strong interaction with H_2 (-7 to -10 kJ mol^{-1}), confirming this approach, although the binding energy achieved is still much weaker than the ideal range. The H_2 binding strength for Ca^{2+} lies between that for Na^+ and Mg^{2+}, so this cation is also a suitable candidate for investigation. Simulations of the Ca^{2+}-H_2 complex show a maximum binding strength of -40.2 kJ mol^{-1} at a separation of 2.5 Å [64]. Unfortunately, no theoretical calculations for complexes of partially hydrated cations with H_2 exist in the literature.

2.1.4 Equation of state

The ideal gas law, with compressibility (Z) of 1, prescribes a linear relationship between volumetric density and temperature. At room temperature and pressures

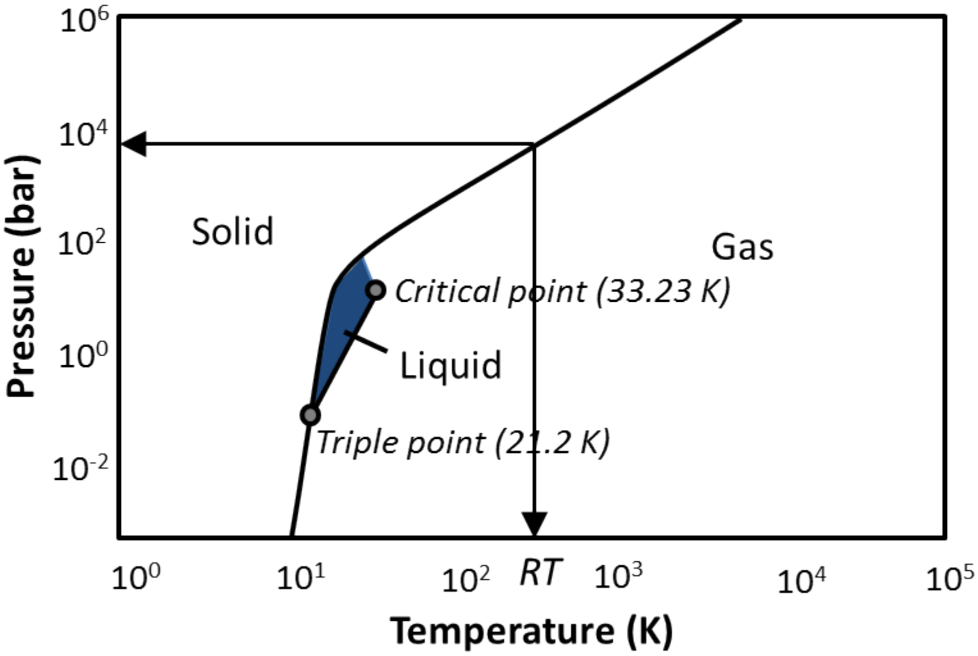

Figure 2.5: The phase diagram of H_2, showing transition points (simplified from [67]).

below 10 MPa, H_2 approximates an ideal gas, but the density-pressure relationship deviates from linearity at higher pressures, due to interactions between H_2 molecules as they are forced closer together. An equation of state (EOS) of a gas is a thermodynamic equation relating pressure, volume and temperature. The Redlich-Kwong EOS [66] is generally accepted as being appropriate for calculating the compressibility factor of H_2 at various temperatures and pressures, since it correlates well with experimental data. This EOS has the form:

$$p = \frac{RT}{(V-b)} - \frac{a}{(\sqrt{T}V(V+b))}, \tag{2.5}$$

where a and b are empirical constants ($\frac{(0.42748R^2T_c^{2.5})}{p_c}$ and $\frac{(0.08664RT_c)}{p_c}$, respectively), R is the ideal gas constant (8.314472 J mol^{-1} K^{-1}), p_c is the critical pressure of H_2 (1.316 x 10^6 Pa) [16], T_c is the critical temperature of H_2 (33.23 K) [16], p is pressure, T is absolute temperature and V is the molar volume, in m^3 mol^{-1}. A simplified phase diagram for H_2 is shown in Figure 2.5.

2.2 Requirements and approaches

Molecular hydrogen has a very low volumetric density: at ambient temperatures and pressures, 1 kg fills a volume of 11 m^3. Therefore the key requirement for hydrogen storage is to reduce this volume by compression, liquefaction or by finding ways to alter the strong intermolecular repulsion through interaction with another material. Both compression and liquefaction require work to be done, costing some of the stored energy and reducing the store's efficiency. A second requirement is for H_2 to be rapidly stored and released in its usable molecular form, implying that the processes involved be reversible.

H_2 compression requires strong, leakproof containers. H_2 gas is commonly stored up to about 20 MPa in cylinders of stainless steel, copper or aluminium, all of which are resistant to H_2 embrittlement under ambient conditions. Higher pressures need thicker walls, reducing the available storage volume and increasing the overall weight of the system (gas + cannister). Lightweight composite materials are being researched which can withstand 80 MPa, however the system's diminishing gravimetric density with increasing pressure is a limitation. At 80 MPa, the volumetric density of the compressed H_2 is 36 kg m^{-3}, slightly more than half that of its liquid form at boiling point. Hydrogen's high diffusivity requires special leak control mechanisms to avoid losses. Compressed gas is an established technology, requiring simple and well-understood equipment and procedures, however the achievable densities are limited and the compression is energetically expensive.

H_2 liquefaction requires cooling to very low temperatures (~20 K) and the liquid must be stored in cryogenic tanks with good thermal insulation. The liquefaction process is energy intensive, using up about 30-40% of the stored energy [68], because of the unique properties of the two rotational states of hydrogen. On cooling, o-H_2 converts exothermally to p-H_2. The heat of conversion increases as the temperature decreases, levelling off at around 77 K, but exceeding the latent heat of vaporisation at base pressure. Any unconverted o-H_2 still in the vessel will absorb this energy and evaporate. The conversion of ortho- to para-H_2 is usually very slow, but catalysts can speed this process up.

Hydrogen has a low critical temperature (33.23 K [67]) with no liquid phase above this, therefore storage vessels must always remain open. Any failure in the cooling mechanism would result in a rapid pressure increase exceeding current pressure tank tolerances. Open systems are prone to losses from boil-off through evaporation from the exposed surfaces, exacerbated by heat leakage. The shape of the tank affects the boil-off rate, but the ideal spherical tank is difficult and expensive to manufacture. The tank's size affects the surface area: volume ratio and therefore also the boil-off rate. Small double-walled dewars of around 100 m^3 lose around 0.2% of their H_2 per day, whereas very large tanks of 20,000 m^3 lose only 0.06% [67]. Improvements in thermal insulation are being researched, but liquid H_2 tends to be limited to short-term consumption uses, such as aerospace.

The third possibility is solid state storage, where H_2 interacts with a storage material through either physisorption or chemisorption.

2.3 Chemisorption vs physisorption

Chemisorption is the dissociative absorption of H_2 into a solid or liquid state material, disrupting the H-H bond; whereas physisorption is a weak, non-dissociative attraction between surface atoms and H_2. Storage of H_2 in near-ambient conditions requires a process involving energies between these two extremes, often called the strong physisorption regime. It can be difficult to distinguish between chemisorption and strong physisorption, but this is possible through advanced spectroscopic techniques, such as inelastic neutron spectroscopy.

Homolytic chemisorption, illustrated in Figure 2.6 b), in which H_2 is split into two identical H atoms, begins at the surface of an absorbent material, usually involving some form of physisorption initially. The gas particles approach the surface atoms and form strong chemical bonds with high enthalpies typical of covalent bonds (~100 kJ mol^{-1}). This is an activated process, requiring energy to disrupt the H-H bond (436 kJ mol^{-1} [62]). Release of molecular hydrogen from the chemisorbed system also requires energy to break the covalent bonds between the dissociated H-atoms and the chemisorption material, requiring high temperatures. The kinetics of chemisorption tend to be slow and may be partly irreversible, as in the light hydrides $NaBH_4$ and $LiAlH_4$, however these materials achieve high ambient gravimetric densities. Heterolytic chemisorption is commonly found in the chemical reactions within living cells and results in two non-identical hydrogen species: a proton, H^+, and a negative hydrogen ion, H^-. This reaction is often catalysed by first row transition metals [69].

Physisorption is the process whereby an atom or molecule from a gaseous adsorptive species approaches the atoms on the surface of an adsorbent substrate, attracted by weak van der Waals' forces, but not involved in any chemical bonds. The attractive van der Waals' forces arise from induced charge fluctuations in adjacent molecular orbitals, giving the molecules an instantaneous electric polarization. Further from the surface (8-10 Å), van der Waals' forces draw the adsorptive gas molecules closer to the surface. At short distances, typically < 2 Å, the orbitals of the two molecules start to overlap, resulting in strong repulsive forces. Equilibrium between these two opposing forces is reached at the energy minimum, typically 3 Å from the surface. The depth of the potential well at this equilibrium distance is the adsorption energy, E_{ads}. Particles of the adsorptive material stuck to the surface in this way form a new phase: the physisorbed phase, or adsorbate.

Physisorptive binding, illustrated in Figure 2.6 a), involves only a small enthalpy change of around 10 kJ mol^{-1}, which is insufficient to break the H-H bond, keeping hydrogen in its molecular form. Physisorption occurs at low (typically liquid N_2 temperature), but supercritical temperatures and this precludes multilayer adsorption from occurring, hence the physisorbed phase tends to form a monolayer following the Langmuir or IUPAC type I isotherm, discussed further in Section 6.2.2. The adsorbate density is limited to that of liquid H_2 (70.8 kg m^{-3}), with the minimum distance between the hydrogen molecules being that of the liquid phase, 3.79 Å [37]. If higher densities are present, then this implies that there is a chemisorptive process involved, with associated H-H bond-length alteration.

Physisorption capacities are greatly enhanced in materials having high surface areas, so physisorption materials tend to be porous. The main advantages of physisorption are its reversibility and fast kinetics, since the binding mechanism does not require activation. However, the best gravimetric and volumetric densities occur at cryogenic temperatures, requiring energy-intensive technologies.

An exhaustive list of all the possible HSMs is beyond the scope of this PhD, but the most well-researched classes of materials using chemisorption are metal hydrides and aminoboranes; while those within the physisorption regime are carbons and carbon nanostructures, zeolites and metal-organic frameworks (MOFs). These are discussed briefly in the next Chapter, including a brief mention of some novel high capacity materials of note.

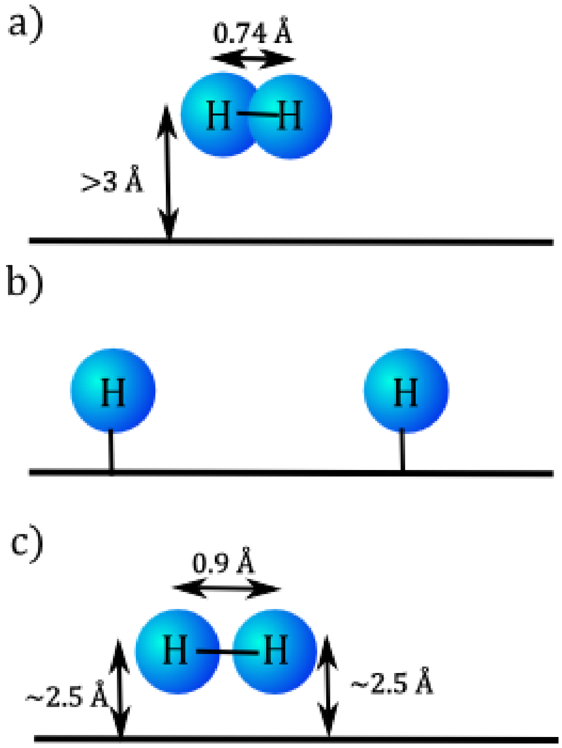

Figure 2.6: (Adapted from [70].) Schematic illustration of the three regions of H_2 binding to the surface of a solid state material (represented simply by the horizontal lines). a) Shows the typical configuration and distances involved in physisorption, while b) shows that for chemisorption. The region inbetween these two extemes is illustrated in c), where the H-H bond elongates and approaches the surface more closely.

2.4 Physisorption thermodynamics

The adsorbed amount at a given equilibrium temperature and pressure depends on the surface area available to the adsorbate molecules, as well as the binding strength between adsorbate and adsorbent (E_{ads}). According to the Gibbs' view, adsorption involves a phase equilibrium between the gaseous and physisorbed molecules, thus, assuming ideal gas behaviour, the equilibrium condition is [71]:

$$\mu_{ads} = \mu_{gas} = \mu_{gas}^0 + RT \ln\left(\frac{p}{p_0}\right), \tag{2.6}$$

where μ_{ads} is the chemical potential (partial molar Gibbs free energy) of the adsorbed phase, p is the pressure of the gaseous phase and p_0 is the standard pressure, μ_{gas} is the chemical potential of the gaseous phase, μ_{gas}^0 is the standard chemical potential of the gaseous phase at p_0, R is the ideal gas constant and T is the temperature of the system. If we let q be the adsorbed phase concentration - i.e. fractional coverage - hold this as constant (isosteric conditions) and differentiate with respect to temperature, we get the Gibbs-Helmholtz relation [71]:

$$\left(\frac{\partial\left(\frac{\mu}{T}\right)}{\partial T}\right)_q = -\frac{\bar{H}}{T^2}, \tag{2.7}$$

where $\bar{H}$ is the partial molar enthalpy. Applying this to Equation 2.6, we get [71]:

$$-\frac{\bar{H}_{ads}}{T^2} = -\frac{\bar{H}_{gas}}{T^2} + R\left(\frac{\partial \ln p}{\partial T}\right)_q, \tag{2.8}$$

where H_{gas} is the partial molar enthalpy of the gaseous phase and H_{ads} is the partial molar enthalpy of the adsorbed phase. Rearranging Equation 2.8 [71]:

$$\left(\frac{\partial \ln p}{\partial T}\right)_q = \frac{\bar{H}_{gas} - \bar{H}_{ads}}{RT^2} = -\frac{\Delta H_{ads}}{RT^2}, \tag{2.9}$$

where $-\Delta H_{ads}$ is the isosteric heat of adsorption. In practical terms, this means collecting adsorption data at a range of temperatures and investigating how pressure varies with respect to temperature, holding adsorbate coverage constant. These data can be plotted as $\ln p$ against $\frac{1}{T}$ (essentially an Arrhenius plot) to yield a line of slope $-\Delta H_{ads}$.

Two common techniques for measuring the adsorption energy are gravimetric and volumetric or manometric analysis, both of which examine the isothermal relationship between surface coverage by adsorbate molecules and pressure. The details of acquiring such isotherms through both techniques are described in more detail in Section 6.2.2, Chapter 6, along with their analysis and thermodynamic interpretation.

3. SOLID-STATE HYDROGEN STORAGE MATERIALS

The technological challenge of finding a solid-state storage medium which can rapidly absorb and release 5.5 wt% of H_2 at near-ambient conditions, as defined by the DoE 2015 targets [72] for a hydrogen storage system, has spurred a large amount of research into a variety of microporous materials, such as graphitic nanocarbons [73] [74], metal organic frameworks [75] [30] and ammonia borane [29]. Other DoE requirements include: a capacity of 40g H_2 per litre, refuelling time of 10 min or less, a lifetime of 1000 refuelling cycles, operation within the temperature range 243 to 323 K and costing no more than $2/kWh [76]. The DoE targets are specified for automotive applications and have a focus on gravimetric density. However, the requirements for static storage are less concerned with weight, instead having a greater focus on finding HSMs with favourable thermodynamics and, most importantly, low cost [4].

HSMs are classified according to the binding mechanism: physisorption or chemisorption. A number of physisorption-based solid state materials have been designed and their hydrogen storage capacity and thermodynamic properties characterised, including zeolites, a variety of carbon structures and metal-organic frameworks. Chemisorption materials are dominated by metal hydrides.

The key features for improving the physisorptive (non-dissociative) H_2 storage capacity in ambient conditions are a high internal surface area and a high density of strong physisorption binding sites, with energies lying within the ideal range of 15-20 kJ mol^{-1}. Microporous or nanoporous materials have large surface areas and the added advantage of confining hydrogen adsorbate molecules within pores of molecular dimensions, thus exposing H_2 to the overlapping potential fields of multiple binding sites and thereby increasing the binding strength [77]. This would require a pore diameter or interlayer space of only a few H_2 diameters, so ~6-9 Å [78]. Adsorption surfaces can be enhanced with accessible ions to attract and bind the H_2 molecule to the surface at energies high enough (15-20 kJ mol^{-1} [54] [41] [53]) to keep it in storage at near-ambient conditions. Rapid uptake and release of hydrogen requires all adsorptive surfaces to be accessible through interlinked channels sufficiently wide for hydrogen molecules to pass through without condensing or blocking the passage. This is a key limitation of zeolites, where the suitably-sized pores are only accessible via much narrower channels [71], slowing down the diffusion of guest molecules. Layered materials provide many of these features and carbon compounds were promising candidates, initially, but graphitic carbon's adsorption enthalpy for H_2 is too low, ~4-7 kJ mol^{-1} [54]. However, recent research at the National Renewable Energy Laboratory (NREL) has revealed near-ambient hydrogen sorption in boron-substituted silica-templated carbon materials, having an 11.4 kJ mol^{-1} H_2 binding energy [79].

3.1 Chemisorption materials

3.1.1 Metal hydrides

A variety of metals form stable hydrides, according to a simple chemical reaction:

$$M + H_2 \rightleftharpoons MH_2 + Q, \tag{3.1}$$

where Q is the heat of hydride formation and M represents a metal, in this case divalent. The hydrides formed from alkali and alkaline earth metals tend to have stable ionic or covalent bonds. Both of these groups bind hydrogen too strongly to provide reversible, ambient storage. For instance, MgH_2 has a high H_2 content of 7.6 wt% but its binding enthalpy is -79 kJ mol^{-1} and thus Mg will not desorb hydrogen within the target temperature range [80]. Since Mg is an inexpensive, abundant and non-toxic material, it is an attractive option for H_2 storage and research has focussed on finding ways to weaken the bond. One way to do this is to form alloys with other metals [81], but at the cost of capacity.

Transition metals, such as lanthanum, absorb hydrogen into the interstitial sites of the crystal lattice, with weaker bonds [80]. They take up and release hydrogen rapidly and reversibly at room conditions, but they are heavy materials. The best reversible gravimetric capacity, 3 wt% at room temperature and pressures below 15 MPa [80], has been observed in Ti-based BCC alloys. Metal hydrides offer the greatest storage capacity of all materials discussed, even for ambient conditions. However, their adsorption/desorption kinetics and reversibility are less favourable than for physisorption materials [82].

3.1.2 Complex hydrides

The complex chemical hydrides are a diverse class of hydrogen-rich chemical compounds, which can be dehydrogenated through a variety of multi-step chemical reactions. They are broadly divided into chemical hydrides, such as CaH_2, $C_{10}H_{18}$ and ammonia borane (AB) [NH_3BH_3] and light metal hydrides, including compounds such as LiH_2, alanates, amides and borohydrides. Initially, this class of materials showed poor kinetics and thermodynamics, requiring high temperatures for dehydrogenation reactions to disrupt the prevalent covalent and ionic bonds, however research into catalysts and defects have greatly lowered desorption temperatures. For example, the first dehydrogenation step for $NaAlH_4$ requires 538 K, but occurs at 423 K in the presence of titanium [70]. The reactions often lead to irreversible end products, but through chemical engineering and further catalytic research, cyclical reaction processes recombining these end products for reuse have been determined for many compounds.

AB has a very high hydrogen content of 19.6 wt% [29], accessible through acidic or catalytic hydrolysis or thermal decomposition. The dehydrogenation of up to three H_2 molecules per AB occur at mild temperatures, below 433 K [83]. AB occurs as a solid, is soluble in polar solvents and can be used directly in fuel cells as an input fuel. However, dehydrogenation and rehydrogenation can involve undesirable compounds, such as ammonia and diborane, both of which are toxic. The irreversibility of the process is its biggest drawback and research is underway to find efficient and cost effective regeneration processes for the spent fuel.

3.1.3 Novel chemisorption materials

Heterocyclic aromatic compounds based on carbon, such as N-ethylcarbazole, cyclohexane and dibenzyltoluene, and on silicon (polysilanes) can undergo cyclic, catalytic hydrogenation/dehydrogenation reactions to store and release H_2. They show extremely high capacities (8-10 wt%) and can be stored as portable liquid carriers under mild conditions of room temperature and low pressure (5-20 bar) [84]. The release of H_2 from these materials can be carefully controlled and reloading is a fast process, occurring within 15 minutes. Their component chemicals are already commercially available in large quantities and have been used safely in an industrial context for decades, however many of them show environmental toxicity. Like hydrides, they require high temperatures to release the H_2 (523-573 K), but research has shown that this temperature can be reduced to 473 K by using microwave irradiation in conjunction with catalysts [85]. The main catalysts required for dehydrogenation are precious metals such as Pt and Pd, driving up the costs and limiting the scale-up of this technology.

3.2 Physisorption materials

3.2.1 Carbon-based materials

A number of carbonaceous materials have been investigated for hydrogen storage capacity, including activated carbons, carbon nanostructures and GICs. Their capacity for storing hydrogen tends to correlate with their specific surface area (SSA) and comparative studies have found a consistent adsorption enthalpy of 5 ± 0.5 kJ mol^{-1} [86].

3.2.2 Activated carbon

Activated carbon is a non-crystalline material which has been considered for H_2 adsorption since 1967 [87]. The key feature which makes this material suitable is its microporosity, providing an extremely high SSA between 700 and 3000 m^2 g^{-1} [88]. This high porosity is achieved by activation through chemical and thermal treatments of either inorganic or organic carbon materials. However, the pore sizes of activated carbon tend to be widely distributed and only a small fraction are of the molecular dimensions suitable for confining H_2. One technique for ensuring a high proportion of suitably-sized pores is templating, in which another porous, highly crystalline material, such as zeolite, is used to deposit the carbon precursor. Carbonisation burns off the template material, leaving a carbon replica of the template structure [89]. The best cryogenic hydrogen uptake for an activated carbon material is approximately 5 wt% at 77 K and 20 atm, for AX-21, which has an extremely high SSA of 3000 m^2 g^{-1} [90]. At room temperature and 60 bar, the capacity is reduced to only 0.5 wt%. Activated carbon materials are easy to synthesise from inexpensive, abundant materials.

3.2.3 Carbon nanostructures

Highly structured, nanoporous carbons have been synthesized using thermal decomposition [91]. Bird feathers, for example, have a highly ordered network of intricate pores and retain some of this complexity when carbonized at high temperatures [92]. The structures left behind are called graphite nanofibres (GNFs), approximately 3-100 nm in diameter and up to 1 mm long. A variety of configurations of stacked graphene layers can be achieved, using a range of hydrocarbon materials. Tubular graphene, or carbon nanotubes (CNTs), forms very high SSA (1000 m^2 g^{-1}) materials and comes in two forms: single-walled (SWCNTs) and multi-walled CNTs (MWCNTs). SWCNTs are single graphene layers rolled into tubes with an inner diameter of approximately 1 nm and closed at both ends by fullerene-like hemispheres. MWCNTs are concentric graphene tubes up to an outer diameter of 30 nm. Concentric conical forms of graphene, carbon nanohorns, are also known [93].

After initial reports of extremely high room temperature H_2 capacity in these materials [94] [95], later found to be subject to large experimental errors, extensive investigations have found little more than 2 wt% capacity at 77 K and near-ambient pressures and only 0.5 wt% at room conditions [73], with storage capacity being strongly linked to the SSA. In SWCNTs, the storage capacity is further limited by repulsive interactions between H_2 and the walls of the nanotubes, as well as between H_2 molecules [96]. Binding sites for H_2 with an activation energy of about 15 kJ mol^{-1} are theorized to exist inside the tubes of smaller CNTs and between bundles of SWCNTs, however these sites are difficult to access and comprise only a small fraction of the total available surface area [97].

3.2.4 Graphite Intercalation Compounds (GICs)

Carbon materials can be doped with a variety of elements, a process called intercalation, involving whole layers of atoms or molecules being inserted between the graphitic layers. GICs provide an opportunity to investigate the planar properties of a variety of chemical species [98]. The periodicity of layer insertion is an important phenomenon, known as staging. For instance, at low dosage, potassium intercalates between every second layer of graphite, but between all layers at high dosage [99]. The structure of the intercalant layers may also differ from adjacent layers, resulting in long-range ordering sequences.

The depth of an intercalant layer depends on the dimensions of the intercalant species. For H_2 storage, the spacing between pure graphite layers is not large enough for a hydrogen molecule to fit between. In order for H_2 to intercalate graphite, the attraction to the surface would need to be strong enough to overcome the energy barrier associated with prying the layers apart. For pure graphite, this attraction is not strong enough at low temperatures and pressures. However, if the layers can be pillared apart using larger molecules, before hydrogenation, then the energy barrier to H_2 diffusion can be overcome. Intercalation with charged molecules also increases the attraction to H_2, providing enough energy to draw the molecules in. Potassium-intercalated graphite is of particular interest, because it has demonstrated the strongest binding energy of all GICs, 8.5 kJ mol^{-1} [100]. However, even intercalated carbon materials have not achieved sufficient H_2 storage capacity, with KC_{24} absorbing only 1 wt% excess H_2 into its interlayers [101].

3.2.5 Zeolites

Zeolites are microporous highly crystalline aluminosilicate materials having regular, open cavities and channels of varying geometries and dimensions. Tetrahedra of SiO_4^{4-} or AlO_4^{5-} link up, sharing corners to form a basic unit of all zeolites, a truncated octahedron having hexagonal and square faces, known as a sodalite block. These sodalite units link together in different ways to form a rigid network of cage-like pores of molecular dimensions, connected by channels. Zeolite frameworks are chemically stable, low-cost materials having SSAs of around 900 m^2 g^{-1}.

Zeolites act as molecular sieves [102], hindering the diffusion of some molecules more than others and are used as catalysts, adsorbents and for storage or purification of a variety of gases (Ar, Kr, N2, Xe). Their general formula is $M_{x/m}[(AlO_2)_x(SiO_2)_y].nH_2O$ and they are categorised into four types: X,Y, A and Rho, according to their crystalline structure and Si:Al ratio. Figure 3.1 shows the framework geometries of these four categories.

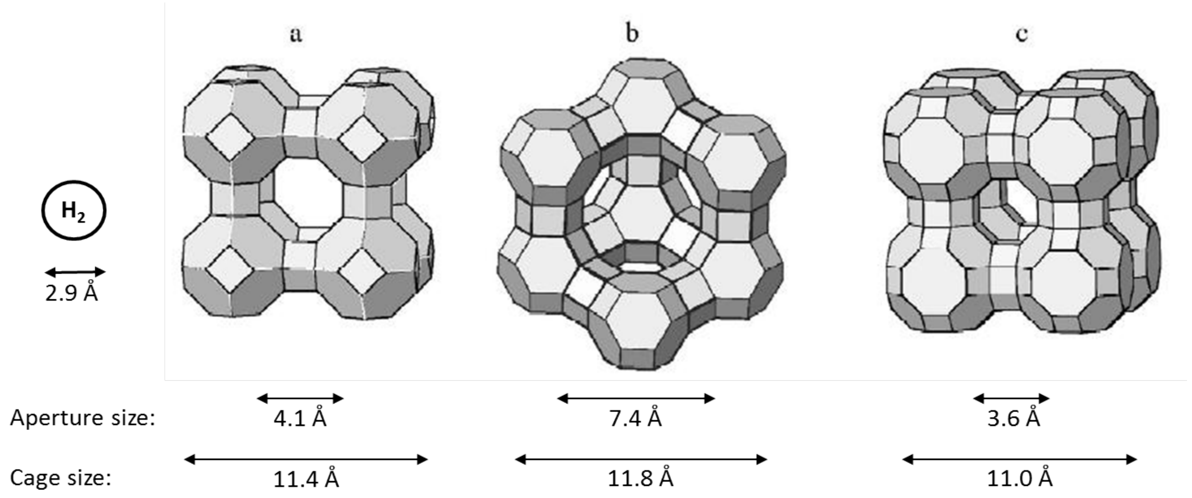

Figure 3.1: Zeolite framework structures: (a) A, (b) X and Y, (c) Rho (from [103]). The H_2 molecule is shown to scale for comparison.

The X and Y zeolites both have the Faujasite (FAU) structure, which is defined as cubic, with a crystallographic space group of Fd3m. Sodalite blocks are linked by their hexagonal faces to form cages of ~13 Å diameter, with large side windows [89]. The X and Y groups are differentiated by their Si:Al ratios, with X having half the ratio of Y. Zeolites of the A category have sodalite blocks linked by their square faces, forming cubic cages with small side apertures. This is known as the Linde Type A structure and the Si:Al ratio for A-zeolites is close to 1. Rho zeolites have a different basic block from the sodalite blocks in the other three categories. In Rho zeolites, the aluminosilicate tetrahedra link together to form a truncated tetradecahedron, consisting of 14 hexagonal faces, interspersed with 12 squares. If these are connected by their hexagonal faces, cubic cage networks form with much reduced apertures. Rho-zeolites have the highest proportion of silicon, with a 3:1 ratio of Si:Al.

The framework is anionic and thus attracts cations into the internal structure, some of which bind within the cage while others may obstruct the apertures. These cations can be exchanged by simple ion-exchange, providing the opportunity to easily tailor both the cavity size and the charge of both cages and channels [103]. Zeolites can thus be designed to trap specific molecules and provide binding sites of a particular chemical nature.

Of all four categories, X-zeolites tend to exhibit the highest H_2 storage and Rho-zeolites the least. The zeolite with the highest observed H_2 cryogenic storage capacity is CaX zeolite [104], at 2.19 wt% at 77 K and 15 bar. A and Rho-zeolites tend to be limited by the fact that the exchangeable cations settle in the window apertures, blocking the pore spaces for H_2 uptake, whereas X and Y zeolites have a more open structure, with cations settling inside the pores [104]. Zeolite X has a greater proportion of cations than the equivalent Y zeolites and also exhibits larger H_2 storage capacities, suggesting that the presence of cations is critical. The importance of the polarising power of cations in increasing the adsorption enthalpy has been confirmed in Mg-exchanged Y zeolites [105]. Cryosorption of H_2 in zeolites is perfectly reversible, with the adsorption isotherms showing no hysteresis [105]. In addition, zeolites can be synthesised and activated with low temperature techniques, involving no CO_2 emission. However, the cage volumes are too big ($>$400 Å^3) to increase the binding strength through molecular confinement of H_2.

3.2.6 Metal-organic frameworks (MOFs)

Like zeolites, MOFs have a cage-like structure, but the framework has flexibility. Organic molecules containing aromatic rings form bridges between shared metallic clusters. Two well-known MOFs are illustrated in Figure 3.2. A wide variety of MOFs have been synthesised to date [106], varying the pore dimensions, organic linkers and functional metallic groups. It is therefore possible to design an MOF for a specific function and much research has been done to achieve the ideal MOF for H_2 storage. MOFs tend to have extremely high SSAs, the current highest being for MIL-101, at 5900 m^2/g [107]. However, the pore sizes of many MOFs are too large to confine hydrogen molecules.

MOF-210 exhibits the highest H_2 storage capacity in this category of 8 wt% excess adsorption, at 77 K and 50 bar [30], with similar uptakes found for MOFs containing Mg [75]. However, for room temperatures, the best capacity is for a subgroup of MOFs known as microporous metal co-ordination materials (MMCMs), showing less than 1 wt% at 50 bar [109]. MOFs have been found to increase the H_2 uptake in high pressure tanks, above that of an empty tank, which suggests that, in addition to the adsorbed molecules, they are also able to store H_2 within their pores in a condensed phase similar to liquid [110]. The highest binding energy (10.5 kJ mol^{-1}) in a MOF was achieved by exchanging the Mn^{2+} coordination cations for Co^{2+} [111].

Metallacarboranes (MCBs) are carboranes (CBH clusters) linked together by metal atoms. The carbons in these compounds are free to link up into three-dimensional

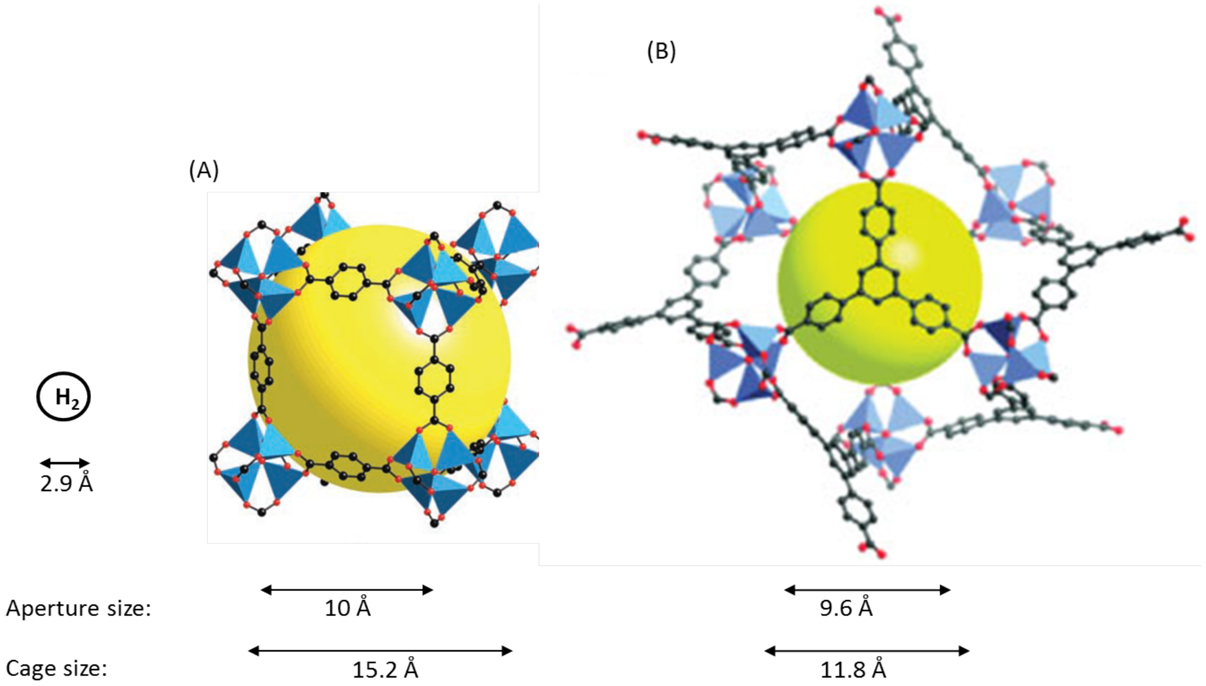

Figure 3.2: Examples of basic crystalline units for MOF frameworks: (A) MOF-5, (B) MOF-177 (from [108]). Black spheres represent carbon, red spheres oxygen. Hydrogen atoms have been omitted. Yellow spheres represent the largest sphere fitting into the cages without touching the van der Waals' volumes of the framework atoms. Blue polyhedra represent coordinating metal ions. The H_2 molecule is shown to scale for comparison.

frameworks, forming MOFs with boron incorporated into their framework. Boron has been proposed to act as anchoring sites for metals in doped carbon nanostructures, preventing the clustering of these metals and ensuring a more uniform spacing of metallic binding sites for H_2, however successful doping of carbon materials with boron has not yet been achieved. MCBs such as $C_2B_4H_6Sc$ (MCB1) are predicted by first principles calculations to have high cryogenic physisorption of H_2 up to 8.8 wt% and also a high room temperature capacity, since metals such as Sc and Ti can form Kubas complexes with multiple hydrogen molecules [112].

Thus MOFs are the most promising class of physisorption materials to date, showing great scope for tailoring the local environment of adsorbed H_2 while having extremely large, accessible surface areas and low densities. However, room temperature adsorption in these materials falls far short of the DoE targets and the materials are complex and costly to produce.

3.2.7 Novel physisorption materials

Boron nitride compounds are capable of forming nanostructures similar to those of carbon. The process of ball-milling opens up strong binding sites through crystal defects which chemisorb H_2, only releasing it at elevated temperatures (~543 K) [113]. This is 30 K below that for ball-milled carbon nanostructures and further improvements are expected. The capacity of these materials is currently 2.6 wt% H_2 [113].

Glass microstructures can be formed by softening microfine glass powder in a controlled, hot flame. The glass forms spherical particles and contains a latent substance that destabilises in the heat, forming a gas bubble in the centre. This expands in the heat, forming a hollow glass microsphere, approximately 1-200 μm in diameter, having porous walls around 100-3,000 Å thick [114]. The balloons can be filled with H_2 adsorbents and the channels in these walls allow H_2 to pass into the sphere for combined containment and physisorptive storage. The main difficulty with this material is the non-uniformity of size and thickness of the spheres, resulting in a proportion of the weaker ones collapsing during every refill. Ceramic nanospheres may allow a similar form of hydrogen storage. Glass capillaries provide an alternate structure which can be stacked and fused into strong arrays of round or hexagonal cylinders and produced with uniform wall thicknesses. The capillaries can be sealed at both ends, trapping H_2 inside. Since each individual capillary holds only a tiny amount of H_2, the likelihood of explosions occuring during handling is considerably reduced compared with high pressurised pure gas cylinders. These materials can withstand up to three times the pressure contained in metal composite cylinders and show promise for allowing safe, controlled storage of H_2. H_2 release is effected by heating the glass microstructures to outgas the H_2 into a low-pressure vessel, however release rates are very slow due to the low thermal conductivity of inorganic glasses. Infra-red radiation has been shown to increase H_2 diffusion rates through the porous walls, an effect known as photo-induced outgassing [115].

Clathrate hydrates are ice cage structures trapping H_2 inside which form under extreme pressures, at 2,000 bar and 240 K. The surrounding cage is a network of hydrogen-bonding water molecules and clathrates typically form two different alternating cage structures. If empty, these cages would collapse rapidly, but can be stabilised by the inclusion of guest molecules. They show reversible hydrogen storage at cryogenic temperatures, for example the binary-clathrate hydrate $H_2(H_2O)_2$ holds 5.3 wt% at 77 K, ambient pressure, releasing the hydrogen at 140 K [116].

4. Clays

Clays are the major component of soils and have been extensively studied for their unique set of properties, including their large surface area to mass ratio, reactive inner surfaces and high viscosity in colloidal form. Clays have applications in diverse fields, such as drug delivery for medicine [117], paper manufacturing, waste containment [118], oil-free lubrication, water purification and catalysis [119]. Several non-human animal species, such as elephants and monkeys, benefit from the absorption properties of clays, using them to soak up toxins in their digestive systems, a behaviour known as geophagy [120]. The smectite clays, examples being bentonite and attapulgite, have interlayers with high retention capacities for charged molecules. In soils, clays retain and release minerals and biochemicals, providing a reservoir for the nutrients vital to microorganisms and plants.

Clays form a subgroup of the general class of layered solids, a suite of materials including graphite intercalation compounds, layered double hydroxides and perovskites. All of these materials are capable of retaining guest species within their layers to form intercalation compounds, however clays are unusual because their layers have high rigidity, containing seven or more interconnected sheets of atoms. This layer rigidity influences many of their physical properties. During intercalation, the clay host layer remains undistorted, allowing their interlayer gallery dimensions to be precisely controlled through pillaring [121]. The empty gallery space between the pillar molecules forms an arena for a variety of catalytic chemistries and molecular sieve activities, the choice of pillaring species being highly versatile. This feature of clays is also of fundamental interest for studies of low dimensional physics, since two-dimensional layers of molecules can be isolated within the clay interlayer for characterisation.

Neutrons have been used to study clays since the 1970s, when quasielastic neutron scattering (QENS) was used to examine the diffusion of water in smectite clays [122]

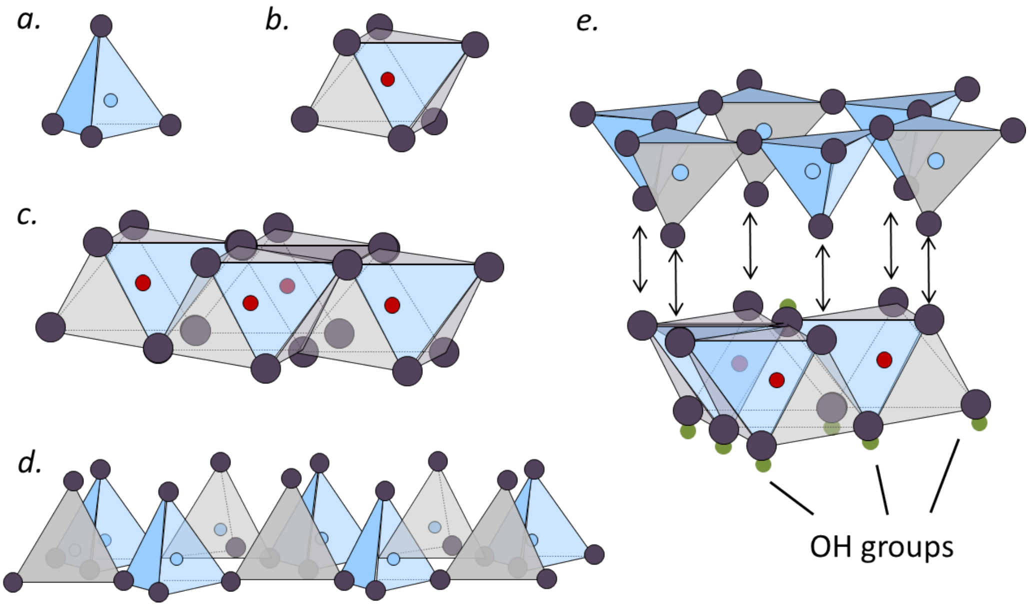

Figure 4.1: The layered structure of clay minerals. (a) A single SiO_4^{4-} tetrahedron, (b) A single AlO_8^{5-} octahedron, (c) Octahedral sheet of linked AlO_8, (d) Tetrahedral sheet of linked SiO_4, (e) A tetrahedral sheet links to an octahedral sheet to form a 1:1 layer. Colours: blue circles are Si atoms; red circles are Al atoms; dark purple circles are O atoms; green circles are H atoms.

and neutron diffraction was used to study the structure of low hydration states of montmorillonites [123]. Earlier studies of the structure of water adsorbed in clay interlayers were done using Nuclear Magnetic Resonance (NMR) spectroscopy [124] and this element-sensitive technique is still widely used, because of its ability to monitor proton dynamics [125].

4.1 Structure

Clay minerals are layered, silicate materials ("phyllosilicates") consisting of alternating planar sheets having two distinct geometries: tetrahedrally- and octahedrally-coordinated cations, most commonly Si^{4+}, Fe^{3+}, Al^{3+} in the tetrahedral sheets and Al^{3+}, Mg^{2+}, Ca^{2+}, Fe^{2+} in the octahedral. The tetrahedra (Figure 4.1a) typically consist of silicon atoms surrounded by four apical O_2^- ions, the basal three of which are planar and shared by adjacent tetrahedra, linking up to form a sheet, as shown in Figure 4.1c. The octahedral sheet (Figure 4.1d) consists of similarly linked octahedra (Figure 4.1b), each having a central cation and a framework of O_2^- ions. The apical oxygens which are not shared between octahedra are bound to a hydrogen atom, forming an hydroxyl group (OH^-) [126].

Octahedral sheets bond with adjacent tetrahedral or octahedral sheets by condensation reactions to form sandwiched sheets, referred to as layers, illustrated in Figure 4.1e. These layers form a rigid structural framework with a neutral charge, however cations of either sheet type may be substituted with other cations, without significantly altering the structural dimensions - i.e. isomorphically. If the supplanting cation has a different valency from the incumbent, for example a tetrahedral Si^{4+} exchanged for Al^{3+}, then this changes the overall charge of the sheet. Since most isomorphous substitutions are from high to low valency cations, the sheets accumulate negative charge.

If the layer accumulates enough charge, then balancing charge structures form between layers, in the aptly-named interlayer. These may be in the form of a layer of isolated cations, as in the smectites, or whole charged octahedral sheets, as in the chlorites. The unit structure or cell of a clay is the total assembly of layer and interlayer material and the formula unit specifies the proportions of elements within a half unit cell, usually written in a way to distinguish between elements in the octahedral, tetrahedral and interlayer regions. The net negative structural charge per formula unit is called the layer charge of the clay.

The cation exchange capacity (CEC) of a particular clay gives the quantity of charges that can be replaced by a high concentration of an alternative cation, expressed in milli-equivalent of charge per unit weight (meq/g), more accurately expressed as the positive molar charge per kilogram (mol_c kg^{-1}), assuming a constant charge density per unit area over the clay surface. For example, smectites have a CEC in the range of 0.8-1.5 meq/g [127]. The selectivity for cations is determined by the charge on the cation, the electrical surface charge on the clay layer and the relative strength of the bonds between cation and adjacent surface versus cation with water. Divalent cations tend to form stronger bonds with the surface than monovalent, thereby replacing them. The strength of the cation-clay surface bond relative to the cation-water bond determines the hydration of the cation: cations which bond more strongly to water, for instance the strongly polarising Mg^{2+}, will be separated from the surface by the surrounding water molecules within the interlayer, forming full hydration shells [128] [129].

4.2 Clay classification

Clay minerals are categorised according to the proportion of tetrahedral to octahedral sheets, as well as the charges on the layers and the type of charge-balancing material in the interlayer. For instance, the phyllosilicate investigated in this study is in the smectite group, which has a 2:1 layer structure, where one octahedral layer is always sandwiched between two tetrahedral layers. The principal layered clay mineral groups are kaolinites, talcs, illites, smectites, vermiculites and micas, having characteristic basal spacings of 7 Å, 10 Å, 10 Å, 10 Å, 10-15 Å and 10 Å respectively, in dry conditions [130]. The layer spacing for smectites and vermiculites vary with water content: 12.4 Å, 15 Å and 15.5 Å for 1- and 2- and 3-layer hydrate montmorillonite [128] [131] and 12 Å, 15 Å and 18 Å for 1-, 2- and 3-layer hydrate vermiculites [132] [133].

Clays are further classified according to the character of their octahedral layers. Using M to represent varying cation species and c to represent the valency of the interlayer cation, fully dehydrated dioctahedral 2:1 clays have a generic formula unit of:

$$\begin{array}{lccccc} \textbf{CATIONS:} & \text{octahedral} & \text{tetrahedral} & & & \text{interlayer} \\ & [\mathrm{M}^{3+}{}_{4\text{-}x}\ \mathrm{M}^{2+}{}_{x}] & [\mathrm{Si}_{8\text{-}y}\ \mathrm{Al}_{y}] & \mathrm{O}_{20}\ (\mathrm{OH})_4 & . & \mathrm{M}^{c+}{}_{(x+y)/c}. \end{array} \tag{4.1}$$

The subscripts x and y show the ionic proportions according to charge, where $Q = x+y$ is the total layer charge. Fully dehydrated trioctahedral 2:1 clays have a generic formula unit of:

$$\begin{array}{lccccc} \textbf{CATIONS:} & \text{octahedral} & \text{tetrahedral} & & & \text{interlayer} \\ & [\mathrm{M}^{2+}{}_{6\text{-}x}\ \mathrm{M}^{3+}{}_{x}] & [\mathrm{Si}_{8\text{-}y}\ \mathrm{Al}_{y}] & \mathrm{O}_{20}\ (\mathrm{OH})_4 & . & \mathrm{M}^{c+}{}_{(x+y)/c} \end{array} \tag{4.2}$$

In dioctahedral sheets, the octahedrons are occupied by trivalent cations and charge-balanced by filling only two out of every three octahedron. In trioctahedral sheets, all three of the octahedrons are occupied by divalent or monovalent cations. The diand tri- prefixes refer to the proportion of octahedral sites filled, not to the valency of the cations involved.

The smectites belong to a clay series, ordered by layer charge, Q, in electrons per formula unit: talc ($Q \sim 0$), smectite ($Q \sim$ 0.2-0.6), vermiculite ($Q \sim$ 0.6-0.9) and true mica ($Q \sim 1$) [134]. The smectite and vermiculite (discussed in Sections 4.2.1 and 4.2.3 below) groups of clay minerals are also known as the “swelling” clays, because of their capacity to absorb multiple layers of polar solvents into the interlayer, increasing the interlayer distance in a stepwise fashion as the water vapour pressure increases [134]. Water molecules are attracted into the interlayer by the cations, this solvation attraction being stronger than the interaction between the cation and the clay surface, causing swelling in a direction normal to the plane of the layers [132]. The chemical formulae in Equations 4.1 and 4.2 have an additional $(\mathrm{H_2O})_\mathrm{n}$ in the interlayer, the n being dependent on the humidity of the surrounding air.

4.2.1 Smectites

The layer charge of smectites ranges from 0.2 to 0.6 electrons per formula unit [134], which is enough to create a binding potential between layers, but not strong enough to prevent the hydration of interlayer cations, hence their capacity to swell. The amount of water held in the interlayer varies according to the nature of the exchangeable cations and the relative humidity. In ambient air, calcium smectites usually take up two or three layers of water in every interlayer, some of which form hydration shells around the cation, the rest interacting weakly with the clay surface and each other [128]. Most of the interlayer water can be reversibly removed with thermal treatment to temperatures between 373 and 523 K, with the most strongly bound water molecules sometimes only desorbing at temperatures up to 573 K [127]. Beyond this, structural water in the form of OH groups, is lost.

Principal clays in the smectite family are the dioctahedral montmorillonite and beidellite and the trioctahedral hectorite. Smectites all have a monoclinic unit cell and form thin platelets a few micrometres across which aggregate into a variety of microscopic structures, including leaf-like flakes and vermiform stacks [127]. Hectorite has a C2/m space group and a typical layer composition based on the general formula unit for trioctahedral clays given in Equation 4.2, with x=0.3, y=0 and having no trivalent cations, but an octahedral composition of $[\mathrm{Mg^{2+}}_{6\text{-x}}\mathrm{Li^{+}}_{\mathrm{x}}]$ instead, as well as having the hydroxyl groups occasionally replaced by fluorine. There are almost no trivalent cations, in particular Al^{3+} or Fe^{3+}, and the tetrahedral sites are almost exclusively occupied by Si atoms. The negative layer charge, which is smaller than in other smectites, comes from octahedral site substitutions of monovalent Li for divalent Mg. The CEC of hectorite is among the smallest of the smectites, at 0.5 meq/g. Hectorite has an internal SSA accessible to N_2 of 63 m^2/g [134]. Smectites can be easily and consistently synthesized in a laboratory using simple equipment and widely available solutions, such as NaOH and $AlCl_3$.

4.2.2 Laponite

Hectorite-like clays have been synthesised on an industrial scale, laponite being one of the most widely researched. Laponite$^{\mathrm{TM}}$ is a patented synthetic clay produced by Rockwood Additives (Laporte Industries in the UK), having a slightly higher CEC (0.8 meq/g) than its natural counterpart [135]. Laponite has a high physical SSA, estimated to be around 900 m^2/g [135], although only a third of that is accessible to N_2 [134]. In dilute colloidal suspensions, laponite swells fully to form elliptical platelets with a diameter of approximately 25 nm by 20 nm and a thickness of ~1.2 nm [136], incorporating a single layer of unit cells. The platelet surfaces (top, bottom and edges) are all slightly negatively charged due to the overall sheet charge of 0.017 e $Å^{-2}$ [137] [134], accumulated from structural cation substitutions. The top and bottom surfaces attract charge-balancing sodium ions, while the edges remain slightly negative, due to exposed OH groups. In the dry state, the platelets stack up, sharing hydrated interlayer cations, retaining a single layer of water molecules (1-2 per cation or 0.7-1.4 H_2O per formula unit) up to 573 K. The *d*-spacing of laponite in ambient conditions is 14-15 Å [138].

The interlayer Na cations can be readily exchanged for divalent cations, giving an interlayer structure per formula unit of: $(\mathrm{M^{2+}})_{0.35}(\mathrm{H_2O})_{\mathrm{n}}$. It is important to note that the interlayer cation density for monovalent forms of laponite will be greater than that for divalent forms, since fewer divalent cations are required to neutralise the sheet charge. Three grades of laponite were kindly supplied by Laporte Industries, UK. All three of these grades were cation-exchanged to produce a range of laponite forms, varying by both their interlayer cation and formula unit. The grades are as follows:

1. General purpose/research grade (RD): This grade has an empirical formula based on that of Equation 4.2, with x=0.3-0.4, y=0, c=1 and interlayer Na^+.

2. High surface charge grade (EL): This grade is presented by Laporte as having the same composition as that for RD, but having 0.95 sodium cations per unit cell. Precise differences in the composition are withheld as proprietary information. However, this implies that there is a higher cation density within the interlayers, with the average distance between randomly distributed cations being smaller than that for an RD grade with the same interlayer cation.

3. Fluorosilicate grade (B): This grade has a high CEC of 1 meq/g, replacing the $(OH)_4$ group in Equation 4.2 with $[(OH)_{2.5}\ F_{1.5}]$.

4.2.3 Vermiculites

Vermiculites form a class of 2:1 phyllosilicates having a higher charge density than smectites, ~0.6-0.9 electrons per formula unit [134], providing greater resistance to layer separation but not great enough to prevent swelling through interlayer hydration. As for the smectites, the vermiculite layer consists of an octahedral aluminium sheet sandwiched by two tetrahedral silicon sheets and there are dioctahedral and trioctahedral forms. The charge is located at the surface of the clay sheets, since charge substitution occurs predominantly in the tetrahedral cations [133], resulting in greater ordering in the interlayer cations of these clays [139]. A typical compositional formula for a trioctahedral vermiculite layer follows Equation 4.2 with y=3, x=1.4 [140].

4.2.4 Micas and Brittle Micas

Micas are 2:1 phyllosilicates having more strongly charged (~1 electron per formula unit [140]) layers than vermiculites, resulting in non-expandable layers. There are dioctahedral and trioctahedral forms. The compositional formula for a typical dioctahedral mica, muscovite, follows Equation 4.1 with x=2 and y=2: $[Al^{3+}{}_2\ K^+{}_2][Si_6\ Al_2]\ O_{20}\ (OH)_4$ [126]. The enhanced negative layer charge is a result of a quarter of the Si atoms being substituted by Al atoms in the tetrahedral sheet, giving a Si:Al ratio of 3:1. This gives the mica (001) surface a relatively high charge density of

-2.1×10^{14} e/cm^2, or about 1 electron per formula unit. The layer charge is balanced by interlayer potassium ions. The brittle micas, another class of charged 2:1 clays, have even more strongly charged layers, in the region of 2 electrons per formula unit [140], a typical dioctahedral form being that of margarite with compositional formula (Equation 4.1 with x=0 and y=4): $[Al^{3+}{}_4]$ $[Si_4\ Al_4]$ $O_{20}(OH)_4.Ca^{2+}$ [140].

4.3 Suitability for hydrogen storage

Of the layered clay mineral groups, kaolinites and talcs have no layer charge, thus do not attract interlayer cations and cannot provide cation binding sites for H_2. Illites predominantly have potassium as their interlayer cation and show low CEC of 0.1-0.4 meq/g [127]. In addition, the dry interlayer space is too small for a hydrogen molecule and the interlayer does not hydrate, thus limiting the opportunities for pillaring. This is also true of micas.

Smectites and vermiculites, discussed above, hold promise as candidate HSMs, being high surface area materials with readily tunable interlayer regions in terms of both dimension and charge. The size of the interlayer space can be controlled by cation exchange for larger species or by adjusting the water vapour pressure, to make it large enough to admit H_2 while still being small enough for the potentials of both layer surfaces to enhance the binding strength. The binding potential of the interlayer can be further tailored by exchanging the incumbent ions for more strongly charged ions, such as Ca^{2+} and Mg^{2+}, providing H_2 adsorption sites with suitable binding energies for accessing the thermodynamically favourable strong physisorption region for room-temperature hydrogen storage. More highly charged clay layers seem an attractive option for improving the binding strength for hydrogen, however they may also prevent expansion of the layers by a weakly binding molecule such as hydrogen. This study (see Chapter 8) shows that such interlayer expansion is possible in clays having smaller layer charge densities, such as smectites. The interlayer galleries for more strongly charged clays, such as vermiculites and micas, may become accessible to H_2 with adequate pillaring through larger cations. In the two-dimensional smectite interlayer environment, the water molecules adopt a square planar solvation geometry around the cation [139], leaving a maximum of three sites for H_2 binding. The number of water and other solvent molecules needs to be minimised, leaving sufficient binding sites for H_2 while pillaring the clay interlayers apart.

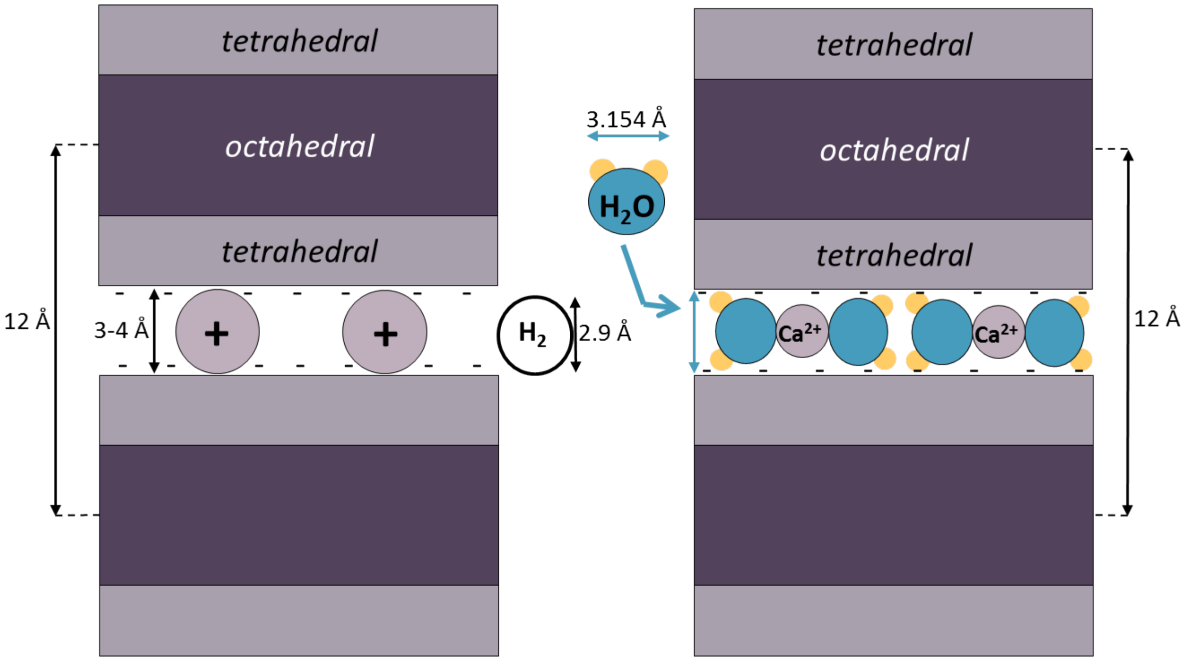

Figure 4.2: Schematic view of the interlayer structure, showing the suitability of the dimensions for (a) an ideal clay, showing the exposed cations (atomic or polyatomic) and minimum interlayer spacing required for H_2 adsorption and (b) a one-layer hydrate Ca-smectite.

Figure 4.2a shows the structure of an ideal 2:1 clay mineral interlayer, with sufficient space for H_2 molecules to penetrate between the layers and gain access to the interspersed cation binding sites. The clay layers are approximately 9 Å thick [128], so if this material were completely dry, the *d*-spacing would be approximately 12 Å. H_2 molecules within the interlayers of such a material would also be constrained within nanopores, with the influence of potential fields from both clay surfaces increasing the strength of the sorbent-H_2 interaction. However, these dimensions call for a pillaring cation of sufficient size, in order to allow H_2 to intercalate into the interlayer galleries, while still considering the need for confinement of the molecules and accessibility to the cation adsorption sites. Since bare cations in the interlayer tend to embed into the surface, collapsing the interlayers to a spacing smaller than the diameter of the cation, a larger cation is needed. Possible candidates are K^+, Cs^+, Rb^+ and polyatomic cations. Al^{3+}, which has already been attempted [32], is of interest for its higher valency and therefore stronger polarising strength.

Alternately, water has a similar van der Waals' radius to H_2 of 1.577 Å [141] and can act as a pillar. Dry Ca-laponite has an interlayer spacing slightly smaller than the diameter of the Ca^{2+} cation (~2 Å [62]) and no longer admits H_2 at reasonable temperatures and pressures. Retaining one or two molecules of water adsorbed to the cation is critical to pillaring the interlayers apart, but does have the cost of reducing the available binding sites around the cation and also weakening the H_2-cation interaction. However, this may be beneficial in cases where the cation-H_2 interaction is too strong. Calculations show that the maximum gravimetric density of H_2 bound by physisorption in a 2:1 clay, assuming monolayer coverage, is around 1 wt%. Significant improvements to this can only be obtained if multilayer adsorption can be achieved, or if a lighter clay structure is used.

Clay minerals have a number of other properties which make them suitable candidates for storing hydrogen, such as low cost (see Table 4.1), worldwide abundance, simplicity and scalability of synthesis and environmental safety. In addition, because of the structural integrity of the clay, the H_2 is unlikely to be contaminated if used under low temperature conditions. The physisorption mechanism has the advantage of fast charge/discharge kinetics and long-term reversible cycling. Although clays are heavy materials and therefore unsuitable for automotive applications, the emphasis on cost is of particular importance for the early introduction of a hydrogen energy infrastructure and is believed by some [105] to be more important than gravimetric capacity or binding strength. In Table 4.1, the Price per g H_2 column takes into account the uptake capacity of the material.

Material	**Qty***	**Price**	**Price/g material**	**Best wt%**	**Price/g H_2 stored**
Laponite	1kg	£30.80	£0.03	0.8	£3.85
Synthetic montmorillonite	1kg	£28.50	£0.03	0.8	£3.56
Alumina-pillared clay	100g	£65.60	£0.66	0.8	£82.00
Bentonite	2.5kg	£79.00	£0.03	0.8	£3.95
Zeolite A	10g	£94.50	£9.45	2.2	£429.55
MOF†	1g	£208.41	£208.41	7.5	£2,778.81
MgH_2	10g	£34.80	£3.48	7.6	£45.79
Ammonia borane (H_3N-BH_3)	500g	£5,520.00	£11.04	12	£92.00
Activated charcoal	1kg	£92.20	£0.09	5	£1.84

Table 4.1: Comparison of prices of HSMs available from Sigma-Aldrich, ignoring all considerations of storage temperature. Prices were obtained from the Sigma-Aldrich online catalogue on 22/04/2014. Unfortunately, no price could be found for AX-21, which achieves 5 wt% H_2 - a typical activated carbon is presented instead.

* - based on the maximum quantity available, for the fairest comparison, since prices are usually less for bulk buy

†- based on an average of all listed MOFs

Clays can be synthesized using simple, inexpensive equipment, providing the additional benefits of high purity, structural consistency and allowing fine control of particle size and properties. Clays are easy to prepare, stable in air and safe to work with, providing an ideal environment for studying the structure and dynamics of physisorbed H_2. The present study investigates the energetic, structural and dynamic effects associated with the adsorption of H_2 on the surface of silicate clay, using laponite as a representative example of smectite clay.

5. CHARACTERISATION THROUGH SCATTERING

In a typical scattering experiment, a beam of particles is scattered by physical interactions with the atoms in materials. The direction, coherence and energy of the scattered signal yields information about the structure and excitations within the sample. Momentum is always transferred in collisions, but particles can be scattered elastically, with no transferral of energy. If energy is transferred in a scattering event, this is termed inelastic scattering.

The scattering process is described by the following two equations for momentum transfer, $\bar{\mathbf{Q}}$, and energy transfer, ΔE, relating the incident and scattered states [142]:

$$\bar{\mathbf{Q}} = \bar{\mathbf{k_i}} - \bar{\mathbf{k_s}} \tag{5.1}$$

and

$$\Delta E = \hbar\omega = E_i - E_s, \tag{5.2}$$

where $\bar{\mathbf{k_i}}$ and $\bar{\mathbf{k_s}}$ are wave vectors for the incident and scattered particles, respectively. The particle's wavelength, λ, is related to its wavevector by $|\bar{\mathbf{k}}| = \frac{2\pi}{\lambda}$. E_s represents the energy of the scattered particle, while E_i gives the incident energy. Figure 5.1 illustrates the momentum relation for an inelastic scattering event.

A typical scattering experiment is illustrated in Figure 5.2, showing the coordinate system defining the scattering direction [142]. A detector may be placed along the scattered path, counting scattered particles over a cross-sectional area (shown in magenta in Figure 5.2). This, along with an analysis of the energies of the incoming and scattered particles, defines the measured quantity in a scattering experiment and is collected from an array of detectors placed over a wide spherical surface surrounding the sample. The scattered signal is measured as three cross-sections:

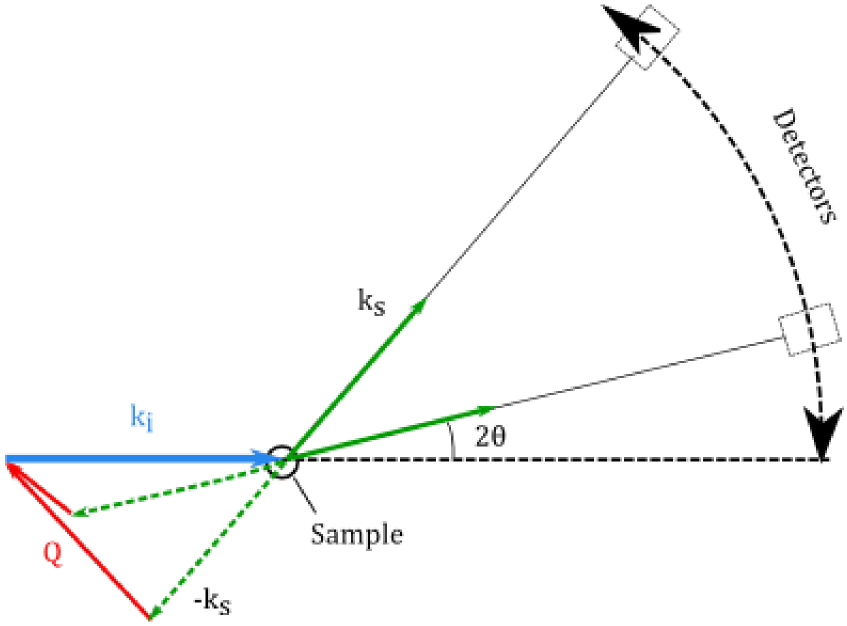

Figure 5.1: The momentum relation for a scattering experiment, in which the incident beam having wavevector $\bar{\mathbf{k_i}}$ interacts with atoms in the sample and is reradiated with wavevector $\bar{\mathbf{k_s}}$. In this case, the scattering is inelastic, having $|k_s| < |k_i|$. The momentum transfer, Q, can be inferred from the scattering angle, 2θ by: $|Q| = \frac{4\pi \sin\theta}{\lambda}$. The detectors scan through all 2θ, so as to capture the scattered signal for a range of Q's.

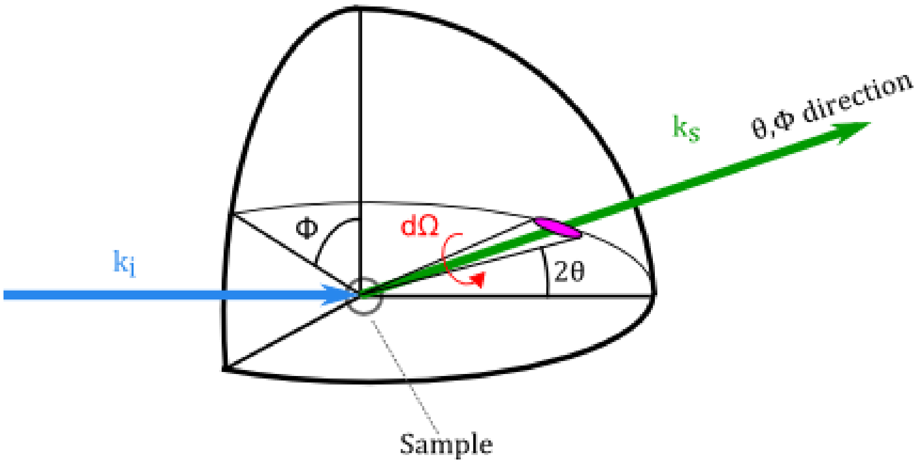

Figure 5.2: The geometry of a scattering experiment in polar coordinates, showing a monochromatic incident beam (in blue), characterised by its wavevector $\bar{\mathbf{k_i}}$ being scattered by the sample into a solid angle, $d\Omega$ (shown in red), in the direction defined by the angles θ and ϕ. In this example, the scattering particle has gained energy ($|\bar{\mathbf{k_s}}| > |\bar{\mathbf{k_i}}|$).

total cross-section, σ_{tot}, differential cross-section (DCS), $\frac{\mathrm{d}\sigma}{\mathrm{d}\Omega}$ and double-differential cross-section (DDCS), $\frac{\mathrm{d}^2\sigma}{\mathrm{d}\Omega\mathrm{d}\omega}$. The information which can be extracted from each when the scattering particle is a neutron will be discussed in Section 5.1.

The total cross-section, σ_{tot}, is the number scattered per second in all directions, divided by the incident flux [143].

If the incident flux is Φ, a count of all particles scattered per second into a solid angle element $\mathrm{d}\Omega$ gives the angular dependence of the scattered particles, leading to the DCS [143]:

$$\frac{\mathrm{d}\sigma}{\mathrm{d}\Omega} = \frac{\#\text{ particles scattered per s into }\mathrm{d}\Omega}{\Phi\mathrm{d}\Omega}. \tag{5.3}$$

If the numbers are recorded as a function of their energy transfer $\mathrm{d}\omega$, this gives the DDCS, showing both angular and energy dependence of the scattered particles [143]:

$$\frac{\mathrm{d}^2\sigma}{\mathrm{d}\Omega\mathrm{d}\omega} = \frac{\#\text{ particles scattered per s into }\mathrm{d}\Omega\text{ having gained/lost }\mathrm{d}\omega}{\Phi\mathrm{d}\Omega\mathrm{d}\omega}. \tag{5.4}$$

Spectrometers measure the DDCS over all measurable Ω and ω, to obtain the combined elastic and inelastic scattering function, $S(\bar{\mathbf{Q}},\omega)$. Diffraction instruments measure the integral of the DDCS over all ω and at a given 2θ to obtain the DCS, which is proportional to the elastic scattering function, $S(\bar{\mathbf{Q}})$. Similarly, the integral of the DCS over all Ω gives the total cross-section, proportional to N: the total number of scatterers present.

There is some inconsistency in the literature with regard to the symbols used to represent various functions relating to scattering. To avoid confusion, the following definitions are adopted throughout this work:

- $S(\bar{\mathbf{Q}})$ = the total elastic scattering function or structure factor;
- $S(\bar{\mathbf{Q}},\omega)$ = the scattering law or dynamical structure factor;
- $g(\bar{\mathbf{r}})$ = the atomic pair **distribution** function (PDF). This gives the normalised distribution of interatomic distances;
- $G(\bar{\mathbf{r}})$ = the reduced PDF, aka the differential PDF, $D(r)$. $G(\bar{\mathbf{r}})$ is in reference to a specific origin, whereas $S(\bar{\mathbf{Q}})$ is not;
- $G(\bar{\mathbf{r}},t)$ = the van Hove [144] space-time pair correlation function;

- $n(\bar{\mathbf{r}})$ = the local number density function at position $\bar{\mathbf{r}}$ in the material, with positions of j surrounding atoms given by $\bar{\mathbf{r}}_j$;
- $\rho(\bar{\mathbf{r}})$ = the atomic pair **density** function, which results from an autocorrelation of the number density function and gives the distribution of interatomic distances;
- $R(\bar{\mathbf{r}})$ = the radial distribution function (RDF), which is the PDF averaged over all directions of $\bar{\mathbf{r}}$, giving the density fluctuations with distance from a reference atom.

5.1 Neutron scattering

Thermal neutrons are an excellent probe for studying condensed matter. Neutrons are uncharged subatomic particles capable of penetrating deeply into matter and interacting directly with atomic nuclei through the strong nuclear force. The mass of the neutron leads to a de Broglie wavelength comparable to the typical distances between atoms in condensed matter [142]. The resulting interference effects provide information about the structure of the material, giving high spatial resolution at the atomic level. The neutron's mass gives it momentum for transferral in scattering events, revealing information about the dynamics. In addition, the energy of thermal neutrons closely matches the range of excitations occuring in condensed matter.

Thus neutrons uniquely satisfy both length and energy scale requirements for probing materials, whereas optical probes, such as X-rays, can only satisfy one of these conditions. The neutron's wavelength is much greater than the size of the nucleus, therefore the scattering is isotropic and can be simply described by a single parameter, the scattering length b. The neutron-nuclear interaction means that neutrons interact differently with different isotopes of the same element and thus isotopic contrast can be utilised to pinpoint the behaviour and structure of a specific population of molecules. For example, the neutron scattering lengths for ^{1}H and ^{2}H have opposite sign, allowing them to be clearly distinguishable. At a particular isotope ratio, their contributions combine so as to cancel eachother out, a condition called null-scattering. Once this condition is reached, it is possible to determine the ratio of hydrogen isotopes in a material.

Neutrons are particularly appropriate for studying hydrogen, having the strongest interaction with this element above all others. This is in contrast to X-rays, where

Property	**X-rays**	**Thermal neutrons**
Scattering strength	atomic form factor: $f_a(k)$	scattering length: b_α
Energy	$E = \hbar\omega$	$E = \frac{\hbar^2 \bar{\mathbf{k}}^2}{2m}$
	high energy (~keV)	low energy (~meV)
Mass	no mass	$m_n = 1.675x10^{-27}kg$

Table 5.1: Comparison between X-rays and thermal neutrons.

hydrogen is the weakest scatterer: photons interact with the electron cloud and hydrogen has only one electron. A brief comparison of the relevant properties of X-ray photons and thermal neutrons is given in Table 5.1. Neutrons are fermions with a spin of $\frac{1}{2}$ and are thus able to induce the para-ortho transition which is central to the H_2 rotation spectrum (see Section 2.1.2). Since this study deals with largely non-magnetic materials, the following Sections assume that the sample elements are non-magnetic, ignoring the interactions of the neutron with unpaired electrons.

5.1.1 Scattering by a single fixed nucleus

To determine what the measured cross-sections mean, consider the simple case of scattering of a thermal neutron by a single nucleus which is not free to move. This is an elastic collision, because the nucleus is unable to rebound and the nucleus is considered to be point-like, since the neutron wavelength is much larger than the nucleus. This situation is illustrated in Figure 5.3, showing a nucleus located at position $\bar{\mathbf{r}}_j$ from some chosen origin absorbing a complex incident plane wave and reradiating it as a spherical s-wave.

From a wave perspective, the scattered wave is superimposed on the incident when it arrives at a detector at some position $\bar{\mathbf{r}}$ in the far field. Using quantum mechanical formalism, the scattering interaction can be defined as an operator, $\hat{V}$, with initial state $|\psi_i\rangle = \exp\left(i\bar{\mathbf{k}}_i|\bar{\mathbf{r}} - \bar{\mathbf{r}}_j|\right)$ and scattered state $|\psi_s\rangle = \exp\left(i\bar{\mathbf{k}}_s|\bar{\mathbf{r}} - \bar{\mathbf{r}}_j|\right)$. The time-dependence of the wavefunctions only plays a role in inelastic scattering and is ignored here. The incident flux will be $\Phi_i = v|\psi_i|^2$, with v being the velocity of the incident neutron (unchanged by elastic scattering). Since only one neutron impinges on the nucleus, the magnitude of the incident wavefunction is simply 1 and the flux reduces to the velocity. Fermi's Golden rule gives the rate of change from the initial to final states, which is considered only for those neutrons scattered into $d\Omega$ [145]:

$$W_{i\to s,\mathrm{d}\Omega} = \frac{2\pi}{\hbar}\frac{k_s m_n}{4\pi^2\hbar^3}\mathrm{d}\Omega|\langle\psi_i|\hat{V}|\psi_s\rangle|^2. \tag{5.5}$$

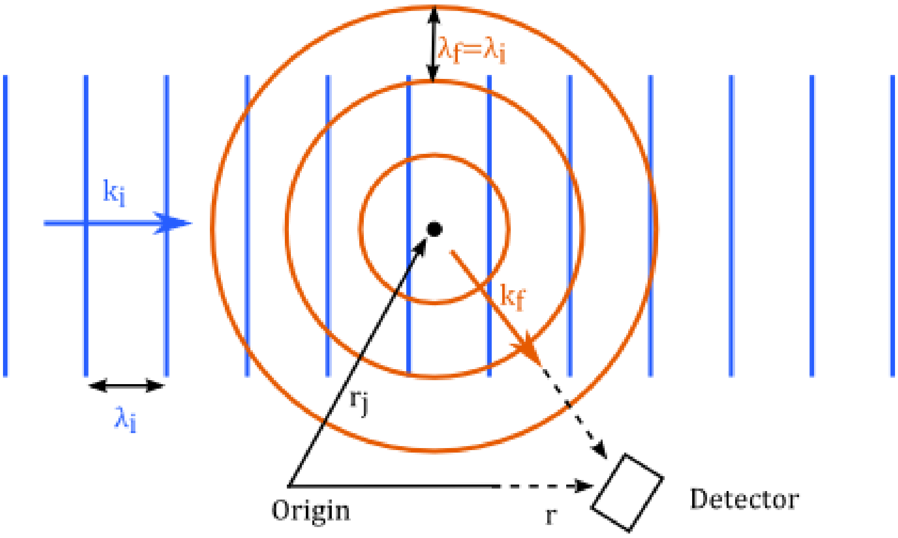

Figure 5.3: An incident plane wave is scattered elastically by a single fixed nucleus, with identical incident and scattered wavelengths. The wave is scattered isotropically from the point-like nucleus as an s-wave and reaches a detector placed far from the nucleus ($|\bar{\mathbf{r}} - \bar{\mathbf{r}}_j| >> b_j$). Positions of the nucleus and detector are defined by vectors from some chosen origin.

The DCS (Equation 5.3) is now [145]:

$$\frac{\mathrm{d}\sigma}{\mathrm{d}\Omega} = \frac{W_{i\to s,\mathrm{d}\Omega}}{\Phi_i \mathrm{d}\Omega} = \frac{k_s}{k_i}\left(\frac{m_n}{2\pi\hbar^2}\right)^2 |\langle\psi_i|\hat{V}|\psi_s\rangle|^2. \tag{5.6}$$

For elastic scattering, $|k_s| = |k_i|$, so this ratio tends to unity. The operator defining the interaction between a single neutron and nucleus is summarised by the Fermi pseudopotential, modelling the interaction potential as a delta function [142]:

$$\hat{V}_j(\bar{\mathbf{r}}) = \frac{2\pi\hbar^2}{m_n} b\delta(\bar{\mathbf{r}} - \bar{\mathbf{r}}_j). \tag{5.7}$$

The nuclear scattering length, b, is a constant independent of $\bar{\mathbf{Q}}$, indicating the magnitude of the neutron's interaction with this particular nucleus and is different for different nuclear isotopes. For a given incident energy, this quantity depends on both the isotopic mass of the nucleus and the relative spin states of the neutron and nucleus. Solving the matrix element in Equation 5.6 yields [145]:

$$\begin{aligned} \langle\psi_i|\hat{V}_j(\bar{\mathbf{r}})|\psi_s\rangle &= \frac{2\pi\hbar^2}{m_n} b \int \exp(-i\bar{\mathbf{k}}_s \cdot \bar{\mathbf{r}})\delta(\bar{\mathbf{r}} - \bar{\mathbf{r}}_j)\exp(i\bar{\mathbf{k}}_i \cdot \bar{\mathbf{r}})\mathrm{d}^3\bar{\mathbf{r}} \\ &= \frac{2\pi\hbar^2}{m_n} b \int \exp\left(i(\bar{\mathbf{k}}_i - \bar{\mathbf{k}}_s)\cdot \bar{\mathbf{r}}\right)\delta(\bar{\mathbf{r}} - \bar{\mathbf{r}}_j)\mathrm{d}^3\bar{\mathbf{r}}. \end{aligned} \tag{5.8}$$

Rearrangement of the exponential terms shows how the scattering vector, $\bar{\mathbf{Q}} =$

$\bar{\mathbf{k}}_i - \bar{\mathbf{k}}_s$, plays a role and the DCS for this simple case becomes [145]:

$$\frac{\mathrm{d}\sigma}{\mathrm{d}\Omega} = \frac{W_{i\to s,\mathrm{d}\Omega}}{\Phi_i \mathrm{d}\Omega} = \Big(\frac{m_n}{2\pi\hbar^2}\Big)^2 |\frac{2\pi\hbar^2}{m_n} b \int \exp(i\bar{\mathbf{Q}}\cdot\bar{\mathbf{r}})\delta(\bar{\mathbf{r}}-\bar{\mathbf{r}}_j)\mathrm{d}^3\bar{\mathbf{r}}|^2 = |b\exp(i\bar{\mathbf{Q}}\cdot\bar{\mathbf{r}})|^2 = b^2. \tag{5.9}$$

Integrating over all directions for a single nucleus, the scattering length is related to the total cross-section by $\sigma_{tot} = 4\pi b^2$. The magnitude of b is of the order of 10^{-12} cm, making σ_{tot} of the order of 10^{-24} cm^2, the latter equivalent to 1 barn, the conventional unit of scattering cross-sections. Table 5.2 lists the cross-sections for a number of useful elements and isotopes.

Element/Isotope	σ_{coh} **(barns)**	σ_{inc} **(barns)**
^{1}H	1.76	80.27
^{2}H	5.59	2.05
V	0.02	5.08
O	4.23	0.0008
Si	2.16	0.004
Ca	2.78	0.05
Mg	3.63	0.08
C	5.55	0.001

Table 5.2: Neutron cross-sections for some elements and isotopes relevant to this study [146].

5.1.2 Scattering by two identical fixed nuclei

Another nucleus of the same type is added to the same coordinate system as above at position $\bar{\mathbf{r}}_{j'}$. The Fermi pseudopotential becomes $\hat{V}(\bar{\mathbf{r}}) = \hat{V}_j(\bar{\mathbf{r}}) + \hat{V}_{j'}(\bar{\mathbf{r}})$. Now the matrix element is [145]:

$$\langle\psi_i|\hat{V}_j(\bar{\mathbf{r}})|\psi_s\rangle = \frac{2\pi\hbar^2}{m_n} b\big(\exp(i\bar{\mathbf{Q}}\cdot\bar{\mathbf{r}}_j) + \exp(i\bar{\mathbf{Q}}\cdot\bar{\mathbf{r}}_{j'})\big), \tag{5.10}$$

yielding a DCS of [145]:

$$\frac{\mathrm{d}\sigma}{\mathrm{d}\Omega} = \Big(\frac{m_n}{2\pi\hbar^2}\Big)^2 \left|\frac{2\pi\hbar^2}{m_n} b\left(\exp\left(i\bar{\mathbf{Q}}\cdot\bar{\mathbf{r}}_j\right) + \exp\left(i\bar{\mathbf{Q}}\cdot\bar{\mathbf{r}}_{j'}\right)\right)\right|^2 = 2b^2\left(1 + cos(\bar{\mathbf{Q}}\cdot(\bar{\mathbf{r}}_j - \bar{\mathbf{r}}_{j'}))\right). \tag{5.11}$$

For some values of $\bar{\mathbf{Q}}$, this cross-section vanishes, while intensifying for other $\bar{\mathbf{Q}}$-values. This results in an interference pattern, becoming more distinctive as more nuclei are added to the system.

5.1.3 Elastic scattering by a general system of nuclei

For a large number of nuclei varying by element and isotope, the total scattering cross-section of all the atoms in the sample is $\sigma = 4\pi \sum_{j,j'} b_j b_{j'}$, with $b_j, b_{j'}$ being the nuclear scattering lengths of the j and j' atoms, respectively. The nuclear scattering lengths even for neighbouring isotopes are not correlated and can be averaged over the sample volume, but there are two cases to consider, referred to as incoherent and coherent [142]:

$$\begin{cases} \text{(same nucleus) } j = j' : b_j b_{j'} = \langle b^2 \rangle, \\ \text{(different nuclei) } j \neq j' : b_j b_{j'} = \langle b \rangle^2. \end{cases} \tag{5.12}$$

The angular brackets denote a thermal average. The Fermi pseudopotential now sums over all nuclei and the resulting DCS, averaging over all particles, isotopes and spin orientations, can be split into two parts [142]:

$$\frac{\mathrm{d}\sigma}{\mathrm{d}\Omega} = \sum_{j=j'} \langle b^2 \rangle \exp\left(i\bar{\mathbf{Q}} \cdot (r_j - r_{j'})\right) + \sum_{j \neq j'} \langle b \rangle^2 \exp\left(i\bar{\mathbf{Q}} \cdot (r_j - r_{j'})\right) = \Big(\frac{\mathrm{d}\sigma}{\mathrm{d}\Omega}\Big)_{inc} + \Big(\frac{\mathrm{d}\sigma}{\mathrm{d}\Omega}\Big)_{coh}. \tag{5.13}$$

Only the coherent part has a phase relationship between incident and scattered waves, leading to constructive interference of plane waves scattered by different nuclei and yielding spatial relationships between atoms. In incoherent scattering there is no phase relationship, therefore no interference effects can occur. Instead, properties of individual atoms are revealed, such as isotope variation.

5.1.4 Inelastic scattering by a general system of nuclei

The DDCS takes into account the effects of energy transfer, counting the neutrons scattered into $\mathrm{d}\Omega$ having transferred a unit of energy, $\mathrm{d}\hbar\omega$, to or from the sample [146]:

$$\frac{\mathrm{d}^2\sigma}{\mathrm{d}\Omega \mathrm{d}\omega} = \frac{1}{2\pi\hbar} \frac{k_s}{k_i} \sum_{j,j'} b_j b_{j'} S(\bar{\mathbf{Q}}, \omega), \tag{5.14}$$

where $S(\bar{\mathbf{Q}}, \omega)$ combines contributions from all atoms in the sample and is derived from Fermi's golden rule (this derivation is amply covered in the literature [142]

[146]), leading to:

$$S(\bar{\mathbf{Q}},\omega) = \frac{1}{2\pi\hbar}\int \sum_{j,j'} \langle e^{-i\bar{\mathbf{Q}}\cdot\bar{\mathbf{r}}_{j'}(0)} e^{i\bar{\mathbf{Q}}\cdot\bar{\mathbf{r}}_{j}(t)} \rangle e^{-i\omega t}\mathrm{d}t. \tag{5.15}$$

The time-dependence of the wavefunctions plays a role in inelastic scattering and is now included, giving the temporal correlations between all atoms in the sample, where $\bar{\mathbf{r}}_{j'}(0)$ is the position of atom j' at time $t = 0$ and $\bar{\mathbf{r}}_j(t)$ is the position of atom j at a later time, t. The dynamical structure factor is linked to $G(\bar{\mathbf{r}}, t)$ through a double Fourier transform in both space and time [146]:

$$S(\bar{\mathbf{Q}},\omega) = \frac{1}{2\pi\hbar}\int G(\bar{\mathbf{r}},t) e^{-i(\bar{\mathbf{Q}}\cdot\bar{\mathbf{r}}-\omega t)}\mathrm{d}\bar{\mathbf{r}}\mathrm{d}t. \tag{5.16}$$

5.1.5 Correlation functions

The pair correlation function fully describes both the static and dynamical aspects of atoms in a sample and provides a physically intuitive view of the information yielded in a neutron scattering experiment. It gives the probability that two atoms are found a certain distance apart, or that the same atom is still within a certain range after a small period of time. In other words, this function gives the spatial and temporal correlations between atoms in the sample and can be separated into self and distinct parts, to distinguish between temporal correlations of motions of the same atom ($j = j'$) and spatial correlations between different atoms ($j \neq j'$) [146]:

$$G(\bar{\mathbf{r}},t) = G_{self}(\bar{\mathbf{r}},t) + G_{distinct}(\bar{\mathbf{r}},t). \tag{5.17}$$

Relating the pair correlation functions back to the measured DDCS of Equation 5.14 and eliminating $G_{distinct}(\bar{\mathbf{r}}, t)$ yields [146]:

$$\frac{\mathrm{d}^2\sigma}{\mathrm{d}\Omega d\omega} = \frac{1}{2\pi\hbar}\frac{k_s}{k_i}\int_{-\infty}^{\infty}\left(\int (\langle b\rangle^2 G(\bar{\mathbf{r}},t) + \left[\langle b^2\rangle - \langle b\rangle^2\right] G_{self}(\bar{\mathbf{r}},t)) e^{i\bar{\mathbf{Q}}\cdot\bar{\mathbf{r}}}\mathrm{d}\bar{\mathbf{r}}\right) e^{-i\omega t} dt. \tag{5.18}$$

Now the integrals can be separated into coherent and incoherent parts [146]:

$$\begin{cases} \left(\frac{\mathrm{d}^2\sigma}{\mathrm{d}\Omega\mathrm{d}\omega}\right)_{coh} = \frac{1}{2\pi\hbar}\frac{k_s}{k_i}\langle b^2\rangle S_{coh}(\bar{\mathbf{Q}},\omega) \\ \left(\frac{\mathrm{d}^2\sigma}{\mathrm{d}\Omega\mathrm{d}\omega}\right)_{inc} = \frac{1}{2\pi\hbar}\frac{k_s}{k_i}\left[\langle b^2\rangle - \langle b\rangle^2\right] S_{inc}(\bar{\mathbf{Q}},\omega). \end{cases} \tag{5.19}$$

Each nuclear isotope has a coherent (σ_{coh}) and incoherent (σ_{inc}) scattering cross-section, giving rise to these coherent and incoherent components of the dynamic structure factor: $S_{coh}(\bar{\mathbf{Q}}, \omega)$ and $S_{inc}(\bar{\mathbf{Q}}, \omega)$, respectively. ^{1}H is such a strongly incoherent scatterer of neutrons (see Table 5.2) with σ_{inc} being approximately 40 times that of most other elements and ~80 times greater than its own coherent signal, that its scattering signal dominates over any coherent signal from the deuterated sample and therefore only the incoherent scattering function need be considered. By contrast, ^{2}H has much lower σ_{coh} and σ_{inc}, with $\sigma_{coh} > \sigma_{inc}$. Neutron scattering experiments on deuterated samples immersed in a pressurised H_2 atmosphere therefore predominantly measure the incoherent structure factor of hydrogen, probing the self-dynamics of H_2 adsorbed to the sample and, to a much lesser extent, any gaseous H_2 within the beam.

5.1.6 Four classes of neutron scattering

Considering also the elastic scattering, the total cross-section has four terms [147]:

$$\frac{\mathrm{d}^2\sigma}{\mathrm{d}\Omega\mathrm{d}\omega} = \sum_j \frac{\mathrm{d}^2\sigma_j}{\mathrm{d}\Omega\mathrm{d}\omega}\bigg|_{inc} + \frac{\mathrm{d}^2\sigma}{\mathrm{d}\Omega\mathrm{d}\omega}\bigg|_{coh} + \sum_j \frac{\mathrm{d}\sigma_j}{\mathrm{d}\Omega}\bigg|_{inc} \delta(\hbar\omega) + \frac{\mathrm{d}\sigma}{\mathrm{d}\Omega}\bigg|_{coh} \delta(\hbar\omega). \tag{5.20}$$

Neutron scattering by nuclei can therefore be divided into four categories: elastic coherent, inelastic coherent, elastic incoherent and inelastic incoherent, each providing different information about the sample. Coherence is a collective phenomenon, representing the whole sample, while incoherence relates to individual sample atoms. Neutron diffraction involves scattering which is both coherent and elastic, providing information about the sample's average structure. Inelastic neutron scattering can excite quasi-particles in the solid and inelastic coherent spectra show collective excitations over a large number of atoms in the system, e.g. phonons. In incoherent inelastic scattering, properties of individual atoms and their motions, including molecular vibrations and rotations, are revealed. This is used to study molecular spectroscopy and diffusion, while elastic incoherent scattering reveals the isotopic inhomogeneity of a sample, as well as the geometry of any confinement effects in the diffusion mechanism.

5.1.7 The principle of detailed balance

Time of flight and backscattering neutron spectrometers probe motions of atoms and molecules on the timescale of 10^{-14}s. Thermal fluctuations, such as rotational and vibrational motions, occur on this timescale. Neutrons incident on the sample can always lose energy to the sample, but will only gain energy if the sample is above 0 K. Low temperature experiments tend to have an asymmetric spectrum, because neutrons are more likely to lose energy to the sample than to gain from it. Therefore a Bose factor needs to be applied to correct for this asymmetry in a spectrum dominated by interactions with bosonic protons. The equilibrium distribution at each temperature must satisfy Boltzmann laws, requiring that:

$$S(-\bar{\mathbf{Q}}, -\Delta E) = \exp -\frac{\Delta E}{k_B T} S(\bar{\mathbf{Q}}, \Delta E), \tag{5.21}$$

where $S(-\bar{\mathbf{Q}}, -\Delta E)$ represents the state of energy gain by the neutron and $S(\bar{\mathbf{Q}}, \Delta E)$ represents energy loss to the sample. The probability of the system being initially in the lower energy state is higher than its probability of being in the higher state, by the Boltzmann factor of $\exp -\frac{\Delta E}{k_B T}$.

5.2 Diffraction

Diffractometers measure the structure of the sample revealed by elastic scattering, in which no energy is transferred. Thus only $S(Q, t = 0) = \int S(Q)dE$ is measured, requiring no energy analysis. The scattering intensity depends only on the scattering vector, $\bar{\mathbf{Q}}$. In a diffraction experiment, the measured quantity is the DCS, leading to the reciprocal-space structure function and its real-space counterpart, the time-averaged pair correlation function, or static structure of the material:

$$\frac{\mathrm{d}\sigma}{\mathrm{d}\Omega} \propto S(\bar{\mathbf{Q}}) = \frac{1}{2\pi\hbar} \int G(\bar{\mathbf{r}}) e^{-iQ\cdot\bar{\mathbf{r}}} \mathrm{d}\bar{\mathbf{r}}. \tag{5.22}$$

The atoms of crystalline solids are arranged in an infinitely repeating pattern, consisting of an identical configuration of atoms, called the basis, at each point of a regular array of lattice points. The lattices of all crystalline solids fall into one of fourteen types, called Bravais lattices. The Bravais lattice is described by the dimensions and geometry of its unit cell: the fundamental shape which is repeated in three-dimensions to reconstruct the complete lattice. The crystal structure is completely described by its Bravais lattice and basis, which are combined in a process known as convolution or folding. The axes and dimensions of the unit cell are the real-space lattice unit vectors: **a**, **b** and **c**. These are combined to yield a real-space vector, $\bar{\mathbf{R}}$, describing the transformation required to move from one lattice point to another:

$$\bar{\mathbf{R}} = u\bar{\mathbf{a}} + v\bar{\mathbf{b}} + w\bar{\mathbf{c}}, \tag{5.23}$$

where u, v and w are integer values. Fourier analysis of a Bravais lattice results in a reciprocal lattice, also having a unit cell (not necessarily the same type of unit cell as the real-space lattice) with dimensions which are related to their real-space analogues. The transformation vector between points in the reciprocal lattice is:

$$\bar{\mathbf{G}} = h\bar{\mathbf{a}}^* + k\bar{\mathbf{b}}^* + l\bar{\mathbf{c}}^*, \tag{5.24}$$

where h, k and l are integer values. The Laue condition (5.25), similar to Bragg's law (5.26) but relying only on the assumption of elastic scattering, relates the real and reciprocal vectors through the scattering vector (see Equation 5.1). Bragg peaks will occur for all values of h, k and l satisfying the following equation:

$$\bar{\mathbf{Q}}.\left(\bar{\mathbf{a}} + \bar{\mathbf{b}} + \bar{\mathbf{c}}\right) = 2\pi\left(h + k + l\right) = \bar{\mathbf{G}}.\left(\bar{\mathbf{a}} + \bar{\mathbf{b}} + \bar{\mathbf{c}}\right). \tag{5.25}$$

This equation highlights two important points: 1. Scattering events are the physical equivalent of the mathematical process of Fourier transformation and 2. The reciprocal lattice vectors, $\bar{\mathbf{G}}$, represent the scattering vectors, $\bar{\mathbf{S}}$, for all elastic coherent scattering events in the sample, revealing the nature of the transformation applied to the incident waves to produce the final signal. The values h, k and l represent the Miller indices for planes within the crystal's real-space lattice.

Bragg's law follows from the Laue condition (Equation 5.25), since:

$$|\bar{\mathbf{Q}}| = \frac{4\pi\sin\theta}{\lambda} \text{ and } |\bar{\mathbf{G}}| = \frac{2\pi}{d}, \text{ leading to } \lambda = 2d\sin\theta. \tag{5.26}$$

If we consider a particular Bragg plane with Miller indices (hkl), corresponding to a particular scattering vector, $\bar{\mathbf{G}}$, in the crystal, the contribution from all j atoms in the unit cell can be summed. This quantity is the structure factor and it is an important quantity in scattering experiments, predicting not only the presence of a particular Bragg peak through a non-zero value, but also its intensity:

$$I = |S_{hkl}|^2 = \left| \sum_j f_j(Q) \exp\left(\mathbf{G}.\mathbf{r_j}\right) \right|^2 , \tag{5.27}$$

where $\mathbf{r_j}$ represents the position of an atom in the unit cell relative to a lattice point and $f_j(Q)$ is a quantity known as the "atomic structure factor" in X-ray scattering (replaced by the constant scattering length, b, in neutron experiments). This equation highlights the phase problem: by measuring the intensity, the phase is lost, holding information about the atom's absolute position relative to a given origin. Therefore only relative positions between pairs of atoms in the sample can be inferred, i.e. pair correlations.

5.2.1 The pair distribution function (PDF)

As mentioned in Section 5.1, the coherent scattering contains structural information, because only a phase relation between scattered waves leads to interference effects, showing the spatial relationships between nuclei. In this study, the structure of condensed, liquid-like H_2 adsorbed to a crystalline surface is investigated. Liquids are amorphous and have no structural periodicity, making them difficult to analyse with conventional diffraction techniques. However, this does not mean that they have a random, gas-like structure: it is still possible to extract the relative positions of atoms from diffraction data, in order to determine nearest neighbour distances, coordination numbers, etc. The PDF approach is suitable for elucidating the structure of amorphous or mixed-phase systems.

The number density, $n(\bar{\mathbf{r}})$, with respect to any particular atom at position $\bar{\mathbf{r}}$ in the sample, where the positions of all other atoms surrounding it are represented by $\bar{\mathbf{r}}_j$, is:

$$n(\bar{\mathbf{r}}) = \sum_j \delta(\bar{\mathbf{r}} - \bar{\mathbf{r}}_j). \tag{5.28}$$

In order to examine the spatial correlations between all N atoms in a sample, this number density function can be autocorrelated - i.e. correlated with itself - to give a set of interatomic distances, $\bar{\mathbf{r}}_{ab}$, between any two atoms, a and b. The distribution of interatomic distances for a macroscopically isotropic system, such as liquids, is given by the atomic pair **density** function, $\rho(\bar{\mathbf{r}})$:

$$\rho(\bar{\mathbf{r}}) = \frac{1}{4\pi r^2 N}\sum_{ab}\delta(\bar{\mathbf{r}} - \bar{\mathbf{r}}_{ab}), \tag{5.29}$$

summing over all atoms in the sample and disregarding the correlation of atoms with themselves (thus $a \neq b$). $4\pi r^2$ corrects for the shell volume. $\rho(\bar{\mathbf{r}})$ is a one-dimensional function, giving a histogram of all the atom-atom distances. As $r \to 0$, $\rho(\bar{\mathbf{r}}) \to \mathbf{0}$, since two atoms cannot overlap due to Pauli's Exclusion Principle. Thus the centre of each atom is surrounded by a void caused by short-range repulsion. For crystalline materials, as $\bar{\mathbf{r}}$ varies, a regular density fluctuation results, caused by the repeating nature of the unit cell. In disordered materials, a random density distribution occurs, but with no atomic overlaps. As r increases, $\rho(\bar{\mathbf{r}})$ oscillates around and asymptotically approaches the average number density, ρ_0.

The atomic pair **distribution** function, $g(r)$, is the normalised atomic pair **density** function:

$$g(\bar{\mathbf{r}}) = \frac{\rho(\bar{\mathbf{r}})}{\rho_0}. \tag{5.30}$$

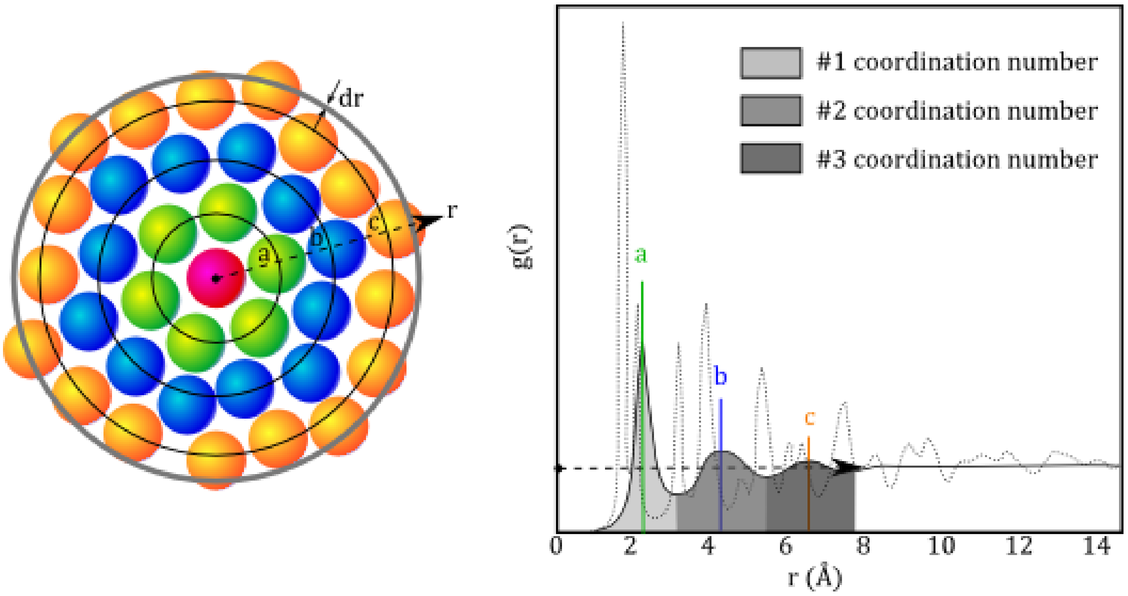

Figure 5.4: (Adapted from [148].) A typical atomic PDF for a model liquid (solid line), such as Ni. The schematic on the left shows how the two-dimensional radial distribution function progresses outwards from a reference atom (red), through the first (green), second (blue) and third (orange) coordination shells of a disordered material. In the graph on the right, the solid line shows the $g(r)$ for liquid Ni, while the dashed line shows the $g(r)$ for crystalline Ni, having much sharper peaks. The integral under the curve between successive troughs, represented by shaded areas, gives the coordination number for each shell.

Figure 5.4 shows a typical atomic PDF for supercooled liquid Ni. A large peak occurs at the average interatomic distance of ~2-3 Å: these are the nearest neighbours to a particular atom. After this, the function oscillates, with peaks indicating the locations of atoms and troughs indicating the regions forbidden by Pauli's Exclusion Principle. The peaks occur at typical bond distances between atoms.

In a monatomic system, the measured DCS is proportional to the structure factor, describing spatial correlations between pairs of atoms. The structure factor and the atomic pair distribution function are related to eachother by Fourier transformation as follows [149]:

$$S(\bar{\mathbf{Q}}) - 1 = \rho_0 \int [g(\bar{\mathbf{r}}) - 1]\, e^{i\bar{\mathbf{Q}}.\bar{\mathbf{r}}} d\bar{\mathbf{r}}. \tag{5.31}$$

$$g(\bar{\mathbf{r}}) - 1 = \frac{1}{\rho_0 (2\pi)^3} \int \left[S(\bar{\mathbf{Q}}) - 1\right] e^{i\bar{\mathbf{Q}}.\bar{\mathbf{r}}} d\bar{\mathbf{r}}. \tag{5.32}$$

In a polyatomic sample, however, the different chemical species interact through bonding mechanisms and the distribution of scattering lengths has an overall correlation with the atomic position. This means that a single structure factor cannot be defined: instead a series of partial structure factors, $S_{\alpha\beta}(\bar{\mathbf{Q}})$, for each chemical species contribute to the overall structure factor, weighted by the proportions of each atom and its scattering length. A sample of n chemical species has $\frac{n(n+1)}{2}$ independent partial structure factors. The partial PDF for a particular species is the Fourier transform of its partial structure factor and represents the probability of finding another type of atom at a given distance from the species in question. Measurements on a series of samples which vary only in their isotopic composition enables these partial structure factors to be determined.

Structural information obtained from Bragg scattering alone does not necessarily reflect the actual bond distances, giving instead an average crystal structure over the entire sample, i.e. the global structure. Local structure - i.e. correlations between neighbouring atoms - comes from diffuse scattering, caused by local disorder, which is seen in the PDF. For a single crystal, this diffuse scattering is small and shows deviations from the perfect crystal, whereas for amorphous materials, the diffuse scattering plays a greater role and must be analysed in conjunction with the Bragg peaks. Thus in order to directly measure the fully three-dimensional PDF, both the high intensity Bragg and low intensity diffuse signals must be obtained simultaneously. This is difficult to do to a high degree of accuracy and such measurements are very time-consuming, often requiring a single crystal to be grown. Powder samples have a random orientation of crystallites and information is lost through orientational averaging, reducing the PDF measured from powder samples to a one-dimensional function. However, it is possible to deduce the three-dimensional structure in reverse, by modelling the system and simulating the PDF which this system would produce.

The radial distribution function (RDF), $R(r)$, is the PDF averaged over all directions of $\bar{\mathbf{r}}$:

$$R(r) = \langle g(\bar{\mathbf{r}}) \rangle_\Omega. \tag{5.33}$$

In summary, the RDF is obtained by the following process:

- Choose some reference atom at random and set the origin of the system at its centre.
- Find every other atom in the system and measure the distance between the new origin and the other atom's centre. Each time an atom is encountered, place a unit of intensity at the position $r_m = |r_m|$ on the axis of $R(r)$. Repeat for all atoms.
- Shift the origin to another atom and repeat for all atoms, adding intensity to the same $R(r)$.
- Normalise $R(r)$ by dividing by $4\pi r^2 N \rho_0 \mathrm{d}r$ to adjust for the volume of a spherical shell of width $\mathrm{d}r$ at distance r from the origin (see Figure 5.4).

Thus $R(r)$ is the average of the partial $R(r)$'s over each atom taken as the origin. This function is zero for small r and oscillates around an asymptote of 1 as r increases. $R(r)\mathrm{d}r$ gives the number of atoms within a spherical annulus of width $\mathrm{d}r$ at a distance r from the atom at the origin, as shown in Figure 5.4, and can be used to obtain the average coordination number, N_C, of any atom in the sample:

$$N_C = \int_{r_1}^{r_2} R(r)\mathrm{d}r. \tag{5.34}$$

In a neutron diffraction experiment, all scattered neutrons are detected and incorporated into the measured intensity, regardless of energy transfer. This means that the static approximation, which assumes that the energy transferred in a scattering event is much smaller than the incident energy of the neutron, is not quite valid in neutron experiments and the intensity must therefore be corrected for inelastic effects. These are more pronounced for light atoms, such as hydrogen and deuterium, which scatter neutrons with larger momentum transfers. Inelastic effects particularly affect the low Q region.

A typical diffraction experiment will measure the combined Bragg and diffuse scattering intensity, correcting for detector efficiencies, absorption, multiple scattering, inelasticity effects and normalization, as well as background removal, to yield the total scattering structure function, $S(\bar{\mathbf{Q}})$. However, usually a limited Q range is used, particularly to remove any small angle scattering found in the low-Q region, so the real-space equivalent of what is measured is then the reduced PDF, defined as:

$$G(r) = 4\pi r[\rho(r) - \rho_0] \tag{5.35}$$

in three dimensions [148].

5.2.2 X-ray diffraction

X-rays interact with the electron clouds of atoms, causing them to move and reradiate waves of the same frequency. The wavelength of X-rays is of the order of interatomic distances, thus diffraction will occur. X-rays are widely used to study the structure of materials, because they can be produced simply and safely in portable laboratory machines.

However, X-rays are not suitable for studying hydrogen, since, of all the elements, H has the smallest number of electrons and therefore the smallest X-ray scattering cross-section. In a compound material, the signal from H is overwhelmed by the signal from other elements.

5.2.3 Powder diffraction

It is difficult to obtain pure, single-domain crystals of many materials, which are instead often available as a powder. This means that the crystalline domains are randomly oriented so that a proportion of the sample is always reflecting. This orientational averaging effectively projects the fully three-dimensional reciprocal space seen in single crystals onto a single dimension and some information is inevitably lost. However, powder diffraction is still a powerful technique in studying solid-state materials and especially useful for measuring the d-spacings within a sample. In measuring a powder diffraction pattern, both the source and the detector are scanned through a range of angles.

5.3 Spectroscopy

Spectrometers measure the full accessible $S(\bar{\mathbf{Q}}, \omega)$ range given by inelastic scattering and must be able to measure the change in energy of scattered neutrons. One way to do this is to use the time-of-flight (TOF) design, which uses short flight paths of a few metres to determine the velocity, and therefore the energy, of neutrons travelling at non-relativistic velocities. The TOF is the time taken to travel from entering the instrument's flight path to arriving at one of its detectors. The incident beam arrives in pulses, allowing the start time for each cohort of neutrons entering the instrument's flight path to be determined. If either the wavevector incident on the sample, $\bar{\mathbf{k}}_i$, or the scattered wavevector, $\bar{\mathbf{k}}_s$, is fixed by monochromatisation, the other can be determined by the TOF. There are therefore two geometries used for TOF spectrometers: direct and indirect.

Direct TOF spectrometers fix $\bar{\mathbf{k}}_i$ and measure $\bar{\mathbf{k}}_s$. A monochromatic beam hits the sample and disperses onto an array of detectors, arranged to capture neutrons scattered at angles (2θ) ranging from 0 to π radians. However, the $(\bar{\mathbf{Q}}, \omega)$-space available to the direct geometry technique is biased towards the neutron energy-gain region and therefore limited to measuring warm samples having energy to transfer to the neutron. Figure 5.5 shows the key features of this spectrometric design.

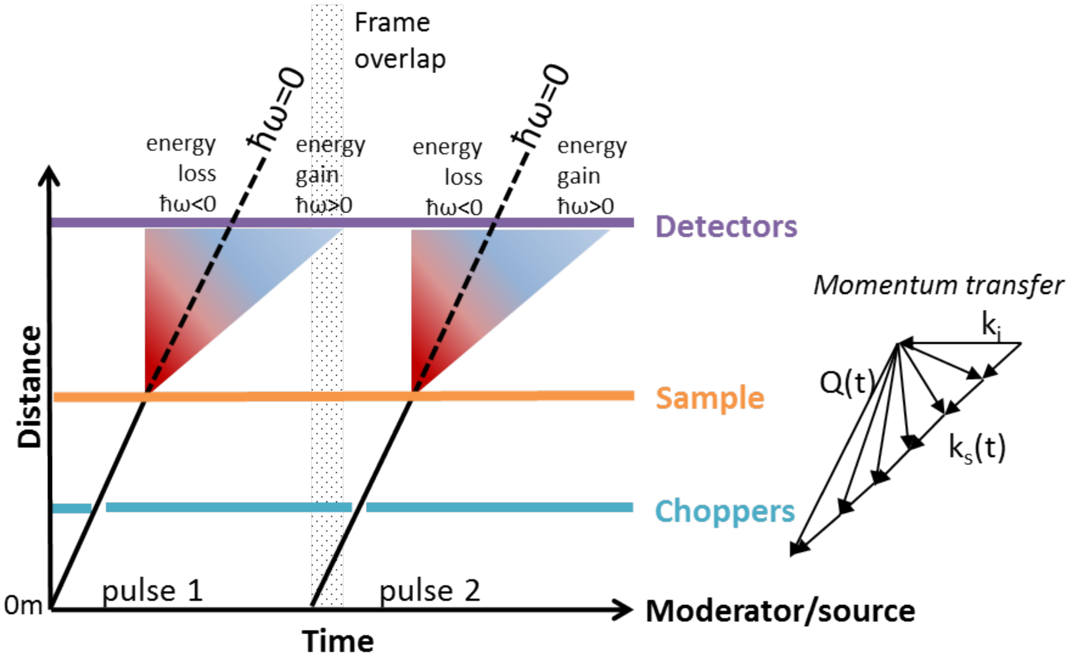

Figure 5.5: Direct geometry TOF measurements, showing the pulsed nature of the beam and how this is controlled at each stage of the instrument, from the selection of a specific wavevector from the incoming beam by choppers or filters, to the detection of scattered neutrons dispersed by the sample. The scattering triangle, relating $\bar{\mathbf{k}}_i$ (fixed), $\bar{\mathbf{k}}_s$ and $\bar{\mathbf{Q}}$, is shown on the right.

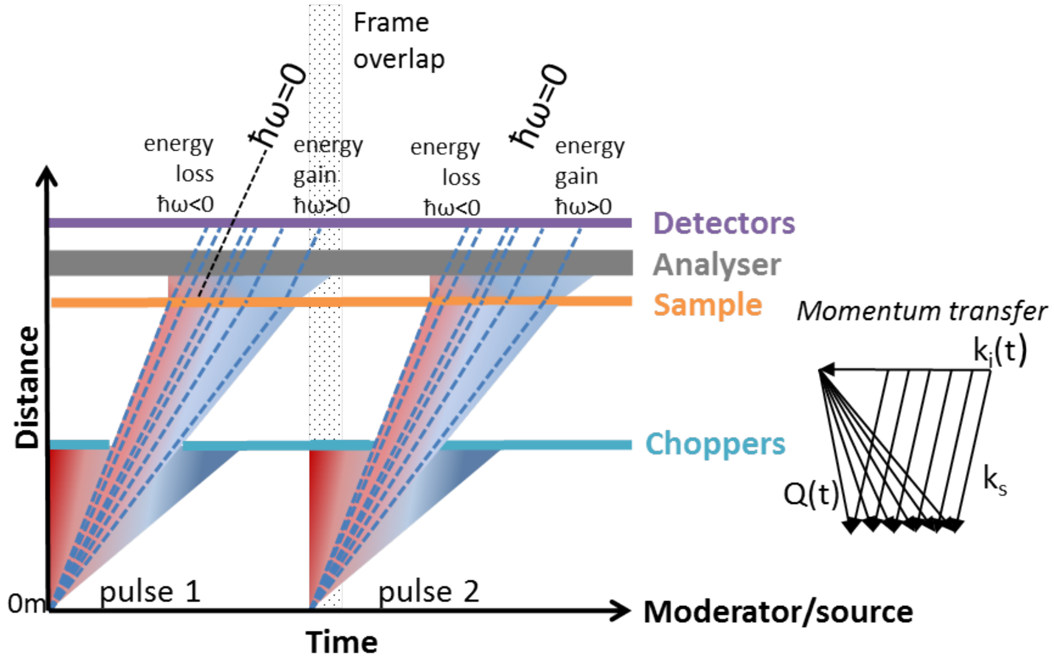

Figure 5.6: Indirect geometry TOF measurements, showing how the beam pulses are controlled at each stage of the instrument, from the initial filtering of the incoming beam by choppers, to the selection of a specific wavevector from neutrons scattered by the sample. The relation between the $\bar{\mathbf{k}}_s$ (fixed), $\bar{\mathbf{k}}_i$ and $\bar{\mathbf{Q}}$,is shown on the right.

Indirect or inverted geometry TOF spectrometers measure $\bar{\mathbf{k}}_i$ and fix $\bar{\mathbf{k}}_s$. A polychromatic beam hits the sample and is scattered onto a highly crystalline analyser which only reflects a particular $\bar{\mathbf{k}}_s$ onto the detectors. High (μeV) resolutions can be achieved by backscattering geometry, in which 2θ is close to π radians. Large areas of the analyser crystal are arranged to form a spherical surface surrounding the sample, reflecting only those neutrons which scatter at this high angle back onto the detectors arranged near the sample. Figure 5.6 shows the key selection processes which occur in a backscattering inverted geometry spectrometer. The main advantage of indirect geometry TOF spectroscopy is the ability to access the neutron energy-loss region of $S(\bar{\mathbf{Q}}, \omega)$ for cold samples, which are often in their excitational ground state.

In a spectroscopy experiment, the measured quantity is the DDCS of Equation 5.4, combining elastic and inelastic signals in the reciprocal-space dynamic scattering law and its real-space counterpart, the time-dependent pair correlation function:

$$\frac{\mathrm{d}^2\sigma}{\mathrm{d}\Omega\mathrm{d}\omega} \propto S(\bar{\mathbf{Q}}, \omega) = \frac{1}{2\pi\hbar} \int\int G(\bar{\mathbf{r}}, t) e^{-iQ\cdot\bar{\mathbf{r}}} e^{-i\omega t} \mathrm{d}\bar{\mathbf{r}} \mathrm{d}t. \tag{5.36}$$

This quantity incorporates the effects of energy transfer, as well as representing the spatial and temporal correlations between pairs of atoms in the sample. The measured signal contains the results of scattering due to molecular excitations and atomic shifts due to translational motions. The predominance of H_2's incoherent signal over its coherent means that studies of hydrogen are largely interested in the incoherent neutron scattering spectrum, which is illustrated schematically in Figure 5.7 to show the regions of interest to this study. This spectrum is obtained by removing a measured background spectrum (the deuterated sample on its own) from the spectrum of the same sample containing H_2, thus removing any coherent signal, such as Bragg peaks, leaving only the incoherent signal. Quasielastic and inelastic peaks are both energy transfer peaks, the key difference between them being that the former are centred at zero energy and have finite width, whereas the latter are centred at finite energy.

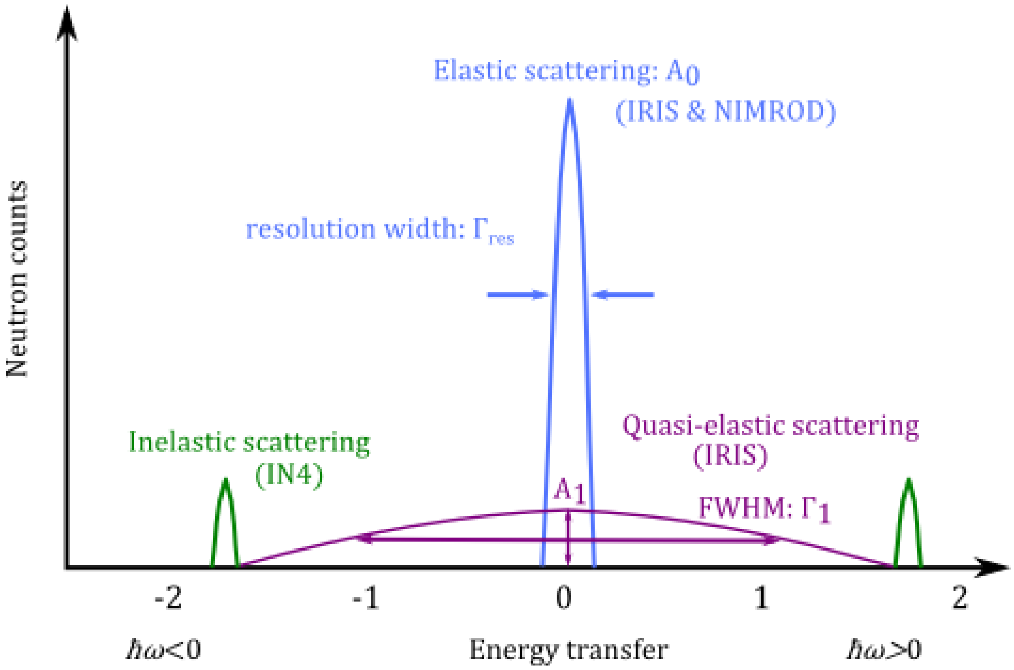

Figure 5.7: Schematic representation of an incoherent neutron scattering spectrum, displaying a single quasielastic component (magenta), centred at zero, broadening the base of the elastic line (blue), having amplitude A_1 and full width half-maximum (FWHM) Γ_1. Some peaks from the inelastic window are also shown here in green, but these may be difficult to distinguish from the quasielastic components.

5.3.1 Incoherent quasielastic neutron scattering

Molecular diffusion through translation and rotational shifts is generally considered to be a thermally-driven, stochastic, non-quantised process in which atoms in solid state materials change position, scattering neutrons largely elastically but with small Doppler energy shifts. Spectrally, these form part of the incoherent quasielastic scattering region, shown in Figure 5.7. The incoherent intermediate scattering function, $I_{inc}(\bar{\mathbf{Q}}, t)$, obtained by a temporal Fourier transform of the correlation function, correlates all the stochastic motions of a single particle, summing over all sites visited by the particle during the instrument's timeframe. Both modes of molecular motion result in an exponentially decaying $I_{inc}(\bar{\mathbf{Q}}, t)$, the rate of decay being proportional to the relaxation time of the motion, τ. The Fourier transform of this has a Lorentzian form, broadening the base of the elastic peak of the dynamical scattering law $S_{inc}(\bar{\mathbf{Q}}, \omega)$, beyond that expected by the instrumental resolution. The width of the energy broadening is related to the speed of the motions, being inversely proportional to τ. If both translational and rotational motion are present, then the narrower Lorentzian closer to the elastic line represents the slower translation.

When the temperature is raised, more scatterers become mobile and move faster, resulting in broader peaks and a concordant drop in the elastic intensity.

If no quasielastic broadening is observed, this means that there are no motions occurring within the timescale defined by the temporal resolution window of the instrument. This resolution restricts the timescale of the motions which can be observed, higher resolutions observing slower diffusive motions. Any quasielastic motions slower than the temporal resolution of the instrument will not be distinguishable from the elastic peak. The measured scattering function is a convolution with the resolution function of the instrument, thus the width of the whole elastic line is related to the width of the instrument's energy resolution. The convolution of two Lorentzians is itself a Lorentzian, therefore if the instrument's resolution function is also Lorentzian, then the spectrum can be simply fitted with a set of Lorentzians, centred at the origin of energy transfer and the broadening of sample spectra is shown in the Q-dependency of their full width half-maxima (FWHM).

Quasielastic neutron scattering (QENS) has been widely applied to studies of the dynamics of water in clays [150] [151] [152] and H_2 physisorbed in a variety of materials [93] [153] [154]. The diffusion mechanism, specifically the characteristic length- and time-scales involved, can be determined from the broadening behaviour of the quasielastic component as Q increases. Assuming monolayer adsorption, the quantity of adsorbed H_2 present can also be measured. If a large amount of H_2 has adsorbed to the material's surface, then the QENS broadening will be constrained, because the molecules are restricted from diffusing over wide ranges. At each temperature, the diffusion coefficient can be calculated from the width of the broadening and compared with the known diffusion coefficient of freely diffusing liquid hydrogen. A significant difference between these two indicates surface interactions, such as attraction to a surface potential, or confinement by one or more dimensions, in small pores. The dependence of the QENS line widths and intensities on both scattered wave vector and temperature shows the freedom of motion of hydrogen molecules within the sample, leading to a microscopic picture of how they move along the surface of the sample.

The theoretical form of the total incoherent scattering function, combining both molecular motions, is as follows:

$$S_{inc}(\bar{\mathbf{Q}},\omega) = e^{-\langle u^2\rangle Q^2}\left\{A_0(\bar{\mathbf{Q}})\delta(\omega) + \sum_{n=1}^{\infty} A_n^{rot}(\bar{\mathbf{Q}})\frac{1}{\pi}\frac{(n(n+1)D_R)}{(n(n+1)D_R)^2+\omega^2} \right.$$
$$\left. + \sum_{m=1}^{\infty} A_m^{trans}(\bar{\mathbf{Q}})\frac{1}{\pi}\frac{\Gamma_m(\bar{\mathbf{Q}})}{(\Gamma_m^2(\bar{\mathbf{Q}})+\omega^2)}\right\}, \tag{5.37}$$

where $\left[A_0(\bar{\mathbf{Q}}) + \sum_n A_n^{rot}(\bar{\mathbf{Q}}) + \sum_m A_m^{trans}(\bar{\mathbf{Q}})\right] = 1$, D_R is the rotational diffusion coefficient and Γ_m is the FWHM of the m^{th} quasielastic Lorentzian.

The exponential in front is the Debye-Waller factor, accounting for faster motion such as vibrations, in which a molecule oscillates about an equilibrium position with mean-square amplitude, $\langle u^2\rangle$. The first term inside the curly braces is the elastic component, the second term is due to rotational motion and the final term to translational diffusion.

The elastic $\delta(\omega)$-shaped component, experimentally measured as the resolution width, Γ_{res}, has a Q-dependent intensity given by the elastic incoherent structure factor ($EISF$):

$$EISF = A_0(\bar{\mathbf{Q}}) = \lim_{t\to\infty}\left[I_{inc}(\bar{\mathbf{Q}},t)\right] = \frac{I_{el}}{(I_{el}+I_{ql})}, \tag{5.38}$$

where I_{el} is the elastic intensity and I_{ql} the quasielastic intensity. The $EISF$ is the elastic proportion of the normalised spectral intensity measured in an incoherent QENS experiment, attributed to elastic collisions with scatterers confined to a small volume, defined by $\frac{2\pi}{\mathbf{Q}}$ [155]. The precise shape of the Q-dependency of the $EISF$ is indicative of the diffusion mechanism, suggesting the proportion of translational to rotational motion, as well as the geometry and degree of confinement of any rotational motions present. At $Q = 0$, the normalised EISF is 1. If no rotational motion is occurring and diffusion is purely by unrestricted translation, then the EISF is zero for all $Q > 0$. If the diffusion is only by rotational motion, then the $EISF$ would be constant with Q, indicating that all incoherent scatterers are localised or immobile. If both motions are present, then the $EISF$ falls to a minimum at a specific Q-value and is thereafter oscillatory around an asymptote, represented mathematically by spherical Bessel functions. While the quasielastic broadening is attributed to hydrogen molecules moving out of the confinement volume, the $EISF$ is essentially the probability that a particle can be found in this same volume of space at some subsequent time within the instrument's timescale.

Restricted motion

Molecular motion can be spatially restricted in a number of ways, such as between two impermeable boundaries, or within a cluster of two or more iso-energetic sites clustered within the volume defined by $\frac{2\pi}{\mathbf{Q}}$ and separated from other sites by distance or energy. The latter is rotational diffusion and the former is spatially restricted translational diffusion [151], however this last is only visible if the confining planes are oriented orthogonal to the Q direction. In an orientationally averaged powder sample, localised molecular motion is exclusively rotational and gives rise to both elastic and quasielastic terms in $S_{inc}(\bar{\mathbf{Q}}, \omega)$. If the time spent in the clustered sites is much longer than the time spent on other sites, then rotational and translational diffusion are dynamically independent. The intermediate scattering function, $I_{inc}(\bar{\mathbf{Q}}, t)$ is then the product of the rotational and translational components and its temporal Fourier transform, $S_{inc}(\bar{\mathbf{Q}}, \omega)$, is consequently the convolution of these components. However, jump diffusion, discussed further below, over energetically different sites yields a scattering function which automatically includes rotational motion [155].

The Q-dependence of the EISF gives the dimensions of the site cluster or confinement region, such as the distance, a, between the sites or boundaries. The Q-value at which the intensity halves gives the inverse of this distance. The Q-value of the first minimum is inversely related to the radius of gyration of the rotating particle, representing the confinement region. If the high-Q asymptote is non-zero, this suggests that there are also immobile scatterers within the instrument's timescale.

The simplest case of rotational motion is a back-and-forth jumping between two sites. In this case, the $\bar{\mathbf{Q}}$-dependency of the EISF in the powder-averaged model decreases with increasing $\bar{\mathbf{Q}}$ according to [155]:

$$EISF(\bar{\mathbf{Q}}) = \frac{N}{2}(1 + j_0(\bar{\mathbf{Q}}a)), \tag{5.39}$$

where j_0 is the zeroth order spherical Bessel function and N is the number of particles involved. The powder-averaged model for localised three-site rotational diffusion gives [156]:

$$EISF(\bar{\mathbf{Q}}) = N\frac{2}{3}\left[\sum_{n=1}^{3} j_0(\bar{\mathbf{Q}}d)\sin\frac{n\pi}{3}\right], \tag{5.40}$$

where the distance parameter this time is d, the diameter of the smallest circle enclosing the three sites.

The elastic proportion is also temperature-dependent. At temperatures below 20 K, for a fixed number of adsorbed H_2 molecules all the intensity lies inside the elastic window, with nothing in the quasi- and inelastic regions. As the temperature rises, molecules start diffusing and intensity shifts from the elastic to the quasielastic region. Taking an integrated count at $Q = 0$ indicates how many molecules are diffusing over large distances (the slowest motions).

Unbounded translational diffusion

The spatially unrestricted H_2 molecules undergo translational diffusion at sufficiently high temperatures. The third term in the curly braces of Equation 5.37 represents this motion: one or more Lorentzian-shaped peaks, each with FWHM $\Gamma_m(\bar{\mathbf{Q}})$ (usually measured in meV) and intensity $A_m^{trans}(\bar{\mathbf{Q}})$. The latter are the quasielastic incoherent structure factors (QISF). Generally, data is fitted using just one quasielastic peak. If there is good reason to believe that there are two or more populations of hydrogen diffusing in the sample, then more peaks should be included. This may happen if the sample was not fully deuterated, or if water vapour has entered the sample environment, or if there are distinctly different channels for diffusion.

The simplest model is Fickian diffusion [157], where particles move due to random collisions between them as in the Brownian motion of a liquid, unhindered by a crystal lattice. In this case, the widths of the Lorentzians will increase linearly with the square of momentum transfer, Q^2 [158], showing a continuous range of hopping distances in all directions. This model defines the upper, unhindered limit of diffusion and the gradient of the line gives the translational diffusion coefficient. If the trend is nonlinear, then other models need to be considered, such as those based on the jump diffusion model [159]. This model proposes discrete steps, assuming that an atom oscillates about a given equilibrium position for some time τ (residence time) and then moves rapidly to a new site at some distance, l (in units of Å), from the first site. Both the time taken to jump, t_j, and the oscillation distance, μ are considered to be negligible ($t_j << \tau$ and $\mu << l$). Q^2 is inversely related to the jump distance and Γ_m is related to the residence time. The probability of a diffusing molecule being found adsorbed to a particular site between jumps in time interval t is given by $e^{(-t/\tau)}$ and, since jumps are relatively rare, discrete events, the probability of jumping from one site to another is given by a Poisson distribution.

The FWHM-Q^2 relationship for such a trend shows a plateau, curving away from the linear maximum and towards a lower asymptote of $\frac{2}{\tau}$, illustrated in Figure 5.8. This trend is especially evident at very low temperatures, where the movements of molecules are kinetically limited. There are a number of jump diffusion models to consider, varying only in their assumed jump length distribution and therefore also their Q-dependent broadening behaviour, but all converging to Fick's law at low-Q. In all models discussed here, all sites are assumed to be equivalent and equally available and both diffusing particles and successive jumps are assumed to be uncorrelated. The fitting parameters extracted, l and τ, can be used to calculate the translational diffusion coefficient, using Einstein's relation:

$$D = \frac{l^2}{6\tau}. \tag{5.41}$$

The Chudley-Elliott model [160] is the simplest of the jump diffusion models considered here, in that it assumes that the diffusing molecule has equally-spaced jump sites in all directions, therefore the jump distance is treated as a constant. This form of jump diffusion is typical of diffusion along the surface of a simple crystal lattice, where a single hop distance is permissible. The Q-dependency of the FWHM for isotropic, three-dimensional diffusion in disordered systems, such as liquids and polycrystalline powders, has the form:

$$\Gamma(\bar{\mathbf{Q}}) = \frac{\hbar}{\tau}\left(1 - \frac{\sin{(\bar{\mathbf{Q}}l)}}{\bar{\mathbf{Q}}l}\right), \tag{5.42}$$

where h is Planck's constant, in units of eV/s.

The Singwi-Sjölander model [161] assumes that the diffusing species moves over a varied lattice of possible jump sites, involving a continuous number of jump lengths. The physical meaning behind this model is that of a molecule alternating between oscillatory motion and directed diffusion, for example a system with clustered sites where these clusters are separated by a potential barrier or distance. Their model assumes that the range of jump lengths follows an exponential distribution, giving the probability, $p(r)$, of finding the diffusing molecule at a particular jump site position, r, after jumping as:

$$p(r) = \frac{r}{r_0^2}e^{\left(-\frac{r}{r_0}\right)}, \tag{5.43}$$

where r_0 is the position of site occupied by the diffusing species before jumping. This distribution is memoryless, meaning that the jump event does not become any more or less likely the longer the residence time on a particular site. In this distribution, the mean of the squared jump length is given by:

$$< l^2 >= 6r_0^2 \tag{5.44}$$

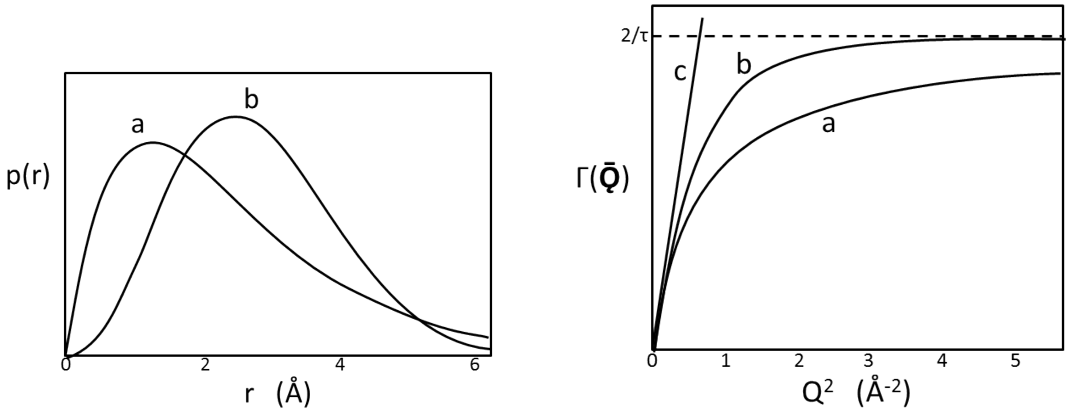

Figure 5.8: (from [158]) The left hand figure shows the jump length distributions used in the jump diffusion models proposed by (a) Singwi-Sjölander (exponential) [161] and (b) Hall-Ross (Gaussian) [158]. The right hand figure shows the broadening behaviour resulting from these distributions, with (c) showing the broadening due to Fick's law.

and the Q-dependency of the FWHM becomes:

$$\Gamma(\bar{\mathbf{Q}}) = \frac{\hbar D \bar{\mathbf{Q}}^2}{1 + D\bar{\mathbf{Q}}^2 \tau}. \tag{5.45}$$

The Hall-Ross model, also known as the Gaussian jump model [158] also assumes a continuous range of jump lengths, but this time following a Gaussian distribution. Physically, this model represents confined motion within a restricted volume. Now the probability, $p(r)$, becomes:

$$p(r) = \frac{2r^2}{r_0^3 (2\pi)^{\frac{1}{2}}} e^{(-\frac{r^2}{2r_0^2})} \tag{5.46}$$

and the mean jump length squared is now given by:

$$< l^2 >= \int_0^\infty r^2 p(r) dr = 3r_0^2. \tag{5.47}$$

This distribution leads to the following FWHM Q-dependency, converging rapidly to its asymptotic high-Q value:

$$\Gamma(\bar{\mathbf{Q}}) = \frac{\hbar}{\tau} \left[1 - \exp\left(-D\bar{\mathbf{Q}}^2 \tau\right)\right]. \tag{5.48}$$

The latter two models have been widely used to study the dynamics of water confined in clay interlayers [162] [151] [150]. Figure 5.8 shows the difference between the Singwi-Sjölander and Hall-Ross models, resulting from their choice in jump length distributions. The Singwi-Sjölander distribution is skewed towards smaller jump lengths, resulting in a slower convergence of $\Gamma(\bar{\mathbf{Q}})$ to its asymptote.

The temperature dependence of the diffusion coefficient leads to calculation of the activation energy - i.e. the energy required to move between sites - using the Arrhenius law:

$$D = D_0 \exp\left(\frac{-E_a}{RT}\right), \qquad or \qquad ln(D) = ln(D_0) - \frac{E_a}{R}\frac{1}{T}, \tag{5.49}$$

where E_a is the activation energy for diffusion, in J mol^{-1} and R is the gas constant, 8.314 J mol^{-1} K^{-1}. If the activation follows Arrhenius behaviour, then the plot of $ln(D)$ against $(1/T)$ will show a linear relation, having a slope of $-\frac{E_a}{R}$. The intercept gives the natural logarithm of the pre-exponential factor, D_0.

5.3.2 Inelastic neutron scattering

Neutron spectroscopy is an ideal technique for examining the quantum effects, discussed in Sections 2.1.1 and 2.1.2, of dihydrogen physisorbed onto a solid surface, providing insights into the strength and symmetry of the adsorption site. In their solid states, p-H_2 and o-H_2 scatter neutrons differently: the former is isotropic, contributing to the coherent signal in the quasielastic and inelastic regions, whereas the latter is anisotropic, producing an elastic incoherent signal. When H_2 is free to move isotropically, as it is even at temperatures below its freezing point of 20 K, the rotational transition line for neutron-facilitated para- to ortho-H_2 transition falls in the inelastic window, presenting a peak centred at 14.74 meV [37]. Deviations from this free rotor peak indicate interactions between the molecular hydrogen and an adsorption site, or possible interactions between adjacent H_2 molecules. Thus the rotational spectrum of hydrogen at subcritical temperatures provides a useful probe for assessing the properties of H_2 binding sites in an adsorptive solid-state material.

The transitions between the ground ($J = 0$) and first excited ($J = 1$) rotational states for the free and hindered rotors are illustrated in Figure 5.9. In the free rotor case (Figure 5.9a), all three energy levels associated with quantum number m_J of the first excited state are degenerate, since H_2 is free to move isotropically. However if H_2 is in the presence of a potential (Figure 5.9b and c), this will hinder the rotation in either one or two dimensions, lifting the degeneracy of the energy levels of the excited state. The higher energy level represents the hindered state or states.

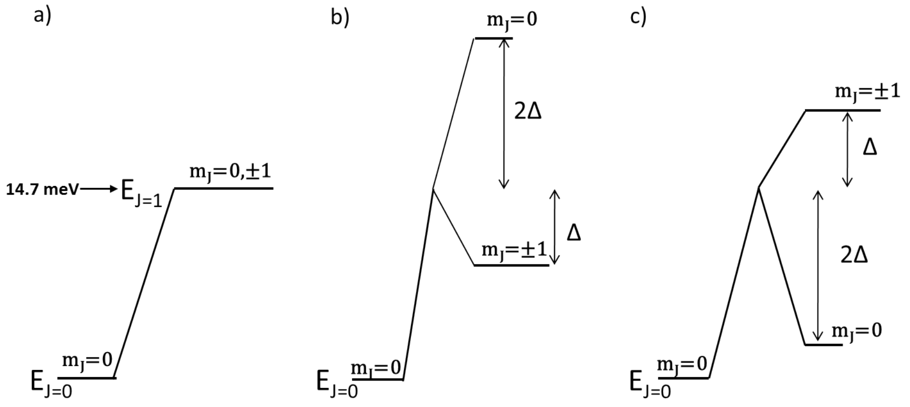

Figure 5.9: Quantum rotational transitions between the ground ($J = 0$) and first excited ($J = 1$) states for a) unhindered H_2, b) H_2 bound in such a way that one dimension is hindered and c) H_2 hindered in two dimensions. The degeneracy of the m_J states is lifted when H_2 is in the presence of a potential, so that the hindered dimension(s) have a higher energy level.

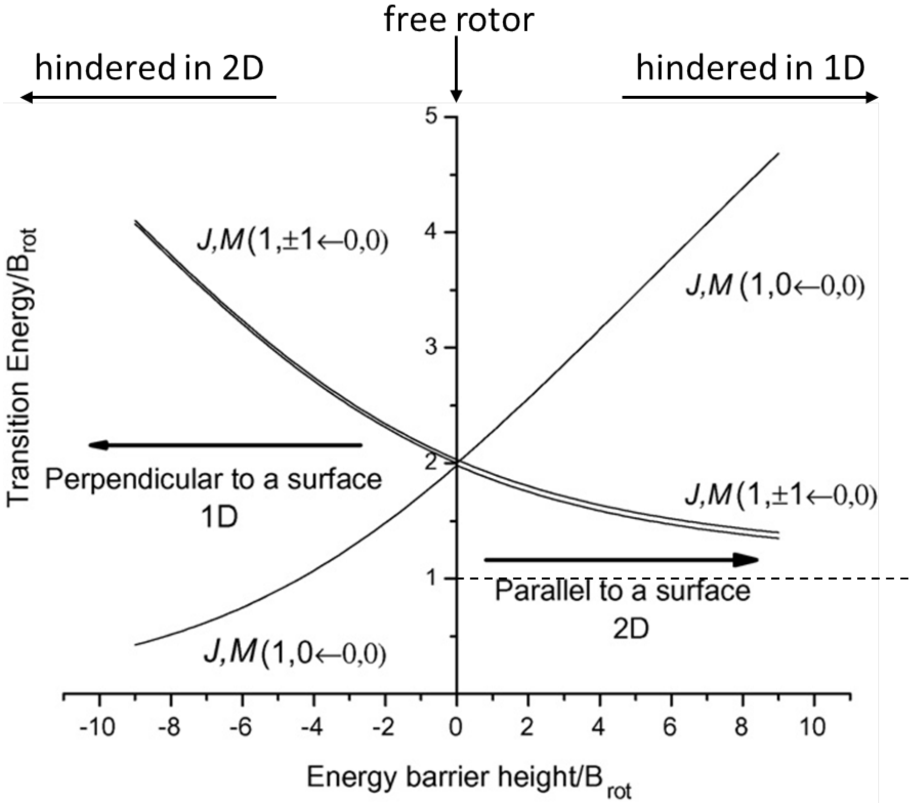

Figure 5.10: (Modified from [45].) The relationship between quantum mechanical energy levels and the rotational barrier field strength, showing how the degeneracy may be lifted when H_2 is exposed to an asymmetrical potential.

In rotational spectroscopy, this splitting is visible as two separate peaks to either side of the free rotor energy of 14.74 meV. The hindered m_J state or states shift to a higher energy level, giving a rotational transition peak at an energy above 14.74 meV, while the unhindered m_J state(s) give rise to a peak below this. The energy difference between the quantised states provides information about the bond strength. Their position relative to the free rotor line and the ratios between the intensities of the split peaks provides information about the adsorption site symmetry. The model is summarised in Figure 5.10, with the energy barrier height being 0 for free rotation. The degenerate energy peak has twice the intensity of the single state peak. The distance between the degenerate peak and the original free rotor peak will be half that between the free rotor and the single state peak. Thus the geometry of the adsorption site can be deduced, along with an estimate of the potential barrier height.

5.3.3 Small angle scattering

XRD can be used to measure the interlayer, or *d*-spacing, of a layered material. This spacing is large and falls within the low-Q region, where $Q < 1$ nm^{-1}. The *d*-spacing is large relative to interatomic distances and is usually the largest periodic spacing in the sample, represented by the first or lowest-Q peak on a diffractogram, the (001) peak. This is also the region where small angle scattering is observed and the (001) peak may be obscured by other features which scatter into this region, such as Porod scattering. These background features need to be removed in order to reveal the Gaussian function representing the (001) peak. The centre of this peak gives a Q-value inversely related to the *d*-spacing.

Porod scattering probes a region which is smaller than the scattering objects, such as a portion of the surface of a clay particle. Porod scattering manifests within the low-Q range ($< 1nm^{-1}$) and is caused by scattering from a surface made up of distinct mesoscopic particles, significantly larger than atoms, but having dimensions smaller than a micrometre. Porod's law predicts a power-law reduction in the signal intensity as Q increases, the magnitude of the power indicating the surface structure. Plotting the base-10 logarithms of intensity and Q against each other reveals a linear relation, the slope of which indicates the local interface roughness. For example, a slope of 1 is typically produced by scattering from rigid rods, while a slope of 4 indicates a smooth surface [163].

6. EXPERIMENTAL METHODS

6.1 Clay preparation

The three grades of laponite, described in Section 4.2.1, were prepared in homoionic form to ensure a pure interlayer composition with a single cation species. For neutron measurements, the clays were deuterated and for both isotherm and neutron experiments they were dried in a vacuum oven. All of these procedures are described in detail in the Sections below.

6.1.1 Ion exchange

To prepare the clay in a homoionic form, the Na^+ ions were exchanged for divalent cations by placing approximately 10 g of laponite into presoaked Visking dialysis tubing (Fischer Scientific: molecular weight cut-off of 12 000-14 000 daltons) and soaking them in 250 ml each of 1M solutions of $CaCl_2$ and $MgCl_2$ (>99% pure $MgCl_2$ and $CaCl_2$ hexahydrate salts obtained from Sigma-Aldrich) over a period of at least five days, the solution being drained off and refreshed at least three times, so as to keep the chemical potential in favour of the desired exchange. A more concentrated exchange solution would risk collapse of the interlayers. The Ca- and Mg-laponite samples hereby produced have the laponite RD formula unit with an interlayer structure of $(Ca^{2+},Mg^{2+})_{0.175}$ $(H_2O)_n$, the value of n depending largely on the relative humidity (RH) of the surrounding air.

As a control, the same treatment was performed using 1M NaCl solution (>99% pure NaCl salt also obtained from Sigma-Aldrich). This is not expected to significantly alter the cation content of the untreated laponite, which is already the sodium form, but serves to expose the sample to the same procedures.

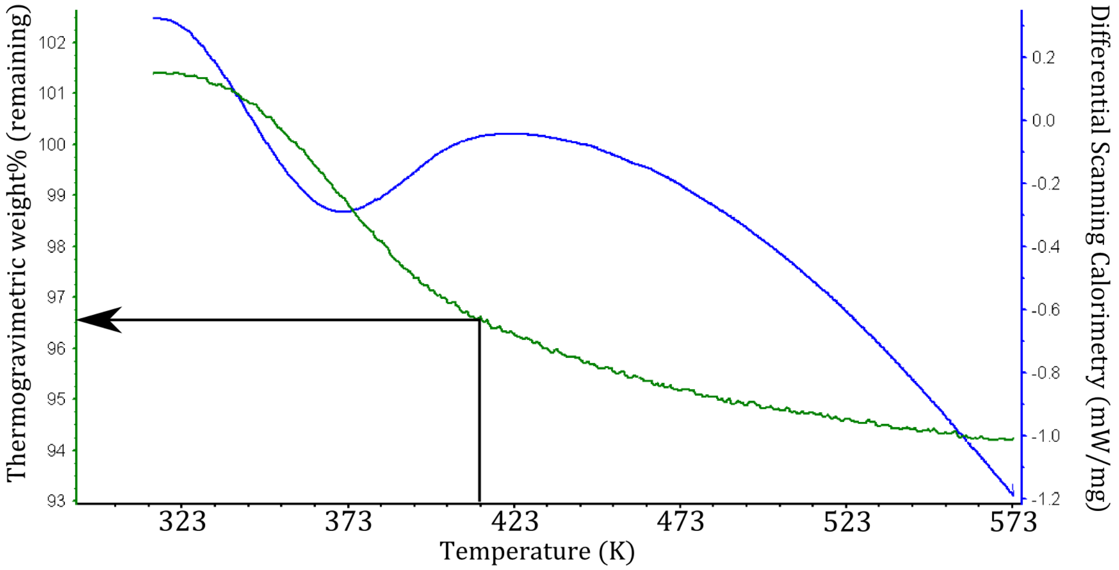

Figure 6.1: Thermogravimetric curves obtained for untreated laponite. Green shows the mass loss with temperature; blue shows the differential scanning calorimetry for this relation. The arrow indicates the mass loss attributable to interlayer water evaporation (96.7%) for 413 K.

For rinsing, the exchanged clays were kept in the same dialysis tubes and soaked in at least 5 litres of de-ionised water, with the water being exchanged at least three times to ensure that any excess salts were removed.

6.1.2 Pillaring

The water content of smectites is dependent on relative humidity (RH), temperature, pressure, pH and type of interlayer cation [134], for instance smectite clays undergo semi-stepwise loss of interlayer water when heated. Therefore the number of water molecules retained can be carefully controlled with treatment at the right temperature, while keeping all other conditions constant. A temperature of 413 K was suggested by previous thermogravimetric analysis (TGA) studies [164] [138] as being sufficient to ensure the loss of most of the interlayer water, leaving a sub-monolayer of water in the interlayers. An STA 449C ThermoGravimetric Analyser was used to confirm the suitability of this temperature and the results for untreated laponite are displayed in Figure 6.1. Further confirmation of the validity of this temperature is discussed in the results presented in Chapter 7.

The product literature on laponite [135] estimates the water content of laponite to be around 8 wt% under ambient conditions. From the curve in Figure 6.1, the weight loss of untreated laponite from its ambient state is approximately 5 wt%. All this weight loss can be attributed to water, since structural losses only occur at temperatures in excess of 473 K [165], [166]. This means that there is an estimated 3 wt% water left in the clay after heating to 413 K. This represents 1.3 H_2O molecules per unit cell, or 3.7 per cation, whereas the ideal treatment would leave only one H_2O per cation, i.e. 0.33 H_2O molecules per unit cell or 0.82 wt% H_2O, leaving the cation as unsaturated as possible, without losing the essential pillars.

To confirm that the desired *d*-spacing was achieved by this treatment, an X-ray diffractometer using Cu-$K_{\alpha 1}$ (1.5060 Å wavelength) source radiation with *in situ* heating capabilities was used to measure the *d*-spacing while heating samples under nitrogen flow, in steps of 20 K from room temperature up to 475 K. In addition, isotherms were measured after a range of pre-treatment temperatures (373-473 K), to investigate the effect of removing more interlayer water on uptake. These results are discussed in Sections 7.2 and 7.3, respectively.

6.1.3 Deuteration

Neutron scattering from hydrogen gives a strong signal. However, since hydrogen is ubiquitous and abundantly present in clays, it is difficult to isolate the sample signal from that of the adsorbed hydrogen molecules. Fortunately, hydrogen's isotopes have different scattering cross-sections for neutrons: ^{1}H is a strong incoherent scatterer ($\sigma_{\mathrm{inc}} = 79.9$ barns; $\sigma_{\mathrm{coh}} = 1.8$ barns), while ^{2}H is a coherent scatterer ($\sigma_{\mathrm{inc}} = 2.0$ barns; $\sigma_{\mathrm{coh}} = 5.6$ barns) [167]. Exchanging the hydrogen atoms in the sample for deuterium, a process known as deuteration, means that the behaviour of adsorbate H_2 molecules can be clearly distinguished from any hydrogen in the sample.

Samples were deuterated by immersion in 99.98% pure D_2O (obtained from Sigma-Aldrich), providing a steep concentration gradient to encourage the hydrogen atoms in the sample to move out into solution and be replaced with deuterium atoms. The diluted D_2O solution was evaporated off inside a vacuum oven and replaced three times to maximise the amount of hydrogen replaced.

6.1.4 Drying and transferral to instruments

Although *in situ* drying is possible, the sample environments for neutron instruments used in this study involved capillary pipework and full drying from ambient RH would take several hours. Therefore the ground, deuterated samples were baked in vacuum at 413 K in an LTE Qualivac vacuum oven for at least 8 hours before being loaded onto the beamline. The clays were ground to a fine powder in a pestle and mortar and transferred to a sample cell suitable for the relevant instrument. The grinding was performed under normal laboratory conditions, which generally involve a lower RH than ambient, but do not preclude the possibility of some water vapour being absorbed by the clay particles. While the clays were being weighed, the reading on the digital balance was noted to have gradually increased (at a rate of a few micrograms per second) confirming that some water vapour was reabsorbed during this time. Precautions were taken to ensure that the air exposure time was kept to a minimum, but some of the scattering signal may be attributed to this reabsorbed H_2O. Once loaded onto the instrument's sample environment, the sample cell was re-evacuated and dried *in situ* for about an hour, reaching a vacuum of at least 10^{-6} mbar.

6.2 Isotherms

6.2.1 Measuring isotherms

Measurements were taken on equipment in the hydrogen laboratory at the Rutherford Appleton Laboratory (RAL) as well as in the UCL Chemistry and Physics departments.

Isotherms can be measured gravimetrically or through Sievert's method, a manometric technique [168]. Thermogravimetric analysis involves continuously monitoring the sample's weight as the environmental conditions (temperature, pressure, etc.) are varied in a precisely controlled manner. Sievert's method uses the ideal gas law at low pressures, with compression factors included for higher pressures, to determine excess adsorption uptake after a precise dose of sorbate gas has been added to the sample chamber. There are essentially two calibrated volumes of known capacity: one containing a gas of known pressure, allowing the number of moles to be calculated, and the other containing the sample in vacuum, or under known equilibrium conditions. The gas in the first volume is released into the second and the system is allowed to equilibrate before pressure and temperature measurements are recorded. The hydrogen uptake can be deduced from the decrease in pressure, following ideal gas law to determine the number of moles of gas still in the gas phase. If this matches the number of moles in the gas phase before the first volume was opened to the second, then no additional uptake occurred. If the system is leak-proof and adsorption has occurred, then the number of moles in the gas phase will be reduced.

However, both methods are prone to intrinsic errors. Gravimetric analysis is hindered by the need to adjust for changes in weight due to buoyancy. As gas is added to the sample chamber, some of the nanoscale particles in a microporous adsorbent, as well as any materials supporting the sample, will be buoyed up by the gas molecules in a way that is difficult to predict. In addition, the sample density may change if the gas is adsorbed, or the buoyancy of the gas may decrease as it changes temperature ahead of the sample and crucible. The concept of buoyancy is a complex phenomenon involving these and other effects, including convection currents and thermomolecular forces. Since gravimetric analysis attributes weight loss to a reduced uptake by the sample, these buoyancy factors need to be corrected for. There is no precise model for how this should be done and many of the correction factors used are estimates, subject to large errors, especially when made by an inexpert user. These errors also increase with pressure and are larger for samples with low density or light, separate particles. Gravimetric measurements are also highly sensitive to gas impurities in the system and the strongly hygroscopic nature of dried clays renders the gravimetric technique particularly difficult to perform [169]. On the other hand, the volumetric method is very sensitive to any changes in volume, pressure or temperature and equipment must be stringently leak-tested before use. The volumetric method also has intrinsic errors, but these are limited to determining the proportion of the total volume (manifold, pipework, sample chamber and sample skeletal volume) which is at the temperature of the sample chamber, this proportion varying slightly with temperature. This also involves a certain amount of estimation from the user, however it is a single estimate per temperature (and therefore per isotherm), rather than a series of estimates for each component within the sample chamber, as in gravimetry. Both techniques suffer from the errors associated with maintaining high vacuum and stable temperatures.

During isotherm measurements, each change in environmental conditions, be it pressure or temperature-driven, needs to be given sufficient time to equilibrate before the measurement for an isotherm can be accurately incorporated. All data is recorded during equilibration, allowing a kinetic assessment of the processes involved and confirming that equilibrium was satisfactorily reached for each point. The kinetics can be used to confirm that the results were not affected by sorption of any contaminants.

In the gravimetric technique, the temperature sensor cannot be in contact with the sample, whereas in the manometric method, it is in direct contact. Hydrogen has a high thermal conductivity (0.1971 W m^{-1} K^{-1}), thus the variation in temperature can be significant. Manometric analysis is widely accepted as being the more accurate of the two techniques [170], however it must be borne in mind that the construction of an isotherm using Sievert's method is also prone to cumulative errors. Each point on the isotherm involves the addition (or subtraction) of the calculated uptake amount in a cumulative manner, i.e. with reference to the previous point, not to the starting point, for each measurement. The errors therefore build up as the isotherm is recorded and the more points there are on the isotherm, the larger the errors are at the end. Hiden Isochema advise restricting the number of points on isotherms to between 50 and 100, to minimize inaccuracies while providing sufficient resolution. Another recommendation is to allow the first measurement of every isotherm a long time for equilibration, to minimise the initial uncertainty.

Another source of error for either technique relates to the amount of sample used for measurements. A greater amount of sample will adsorb more hydrogen and the measurement will be well above any instrumental errors. Rouquerol *et al.* [89] suggest that the sample mass choice be based on the SSA and recommend a total area of 20-50 m^2 for reliable results. For laponite, assuming an SSA of 300 m^2/g [135], this suggests a sample mass of around 167 mg. However, this SSA was measured using the Brunauer, Emmett and Teller (BET) technique [171], based on adsorption of N_2, which will give a different SSA than that available to H_2, so sample sizes may need to be adjusted once the H_2 SSA has been determined. It is not recommended that the sample mass be less than 50 mg, to keep the adsorption measurement as accurate as possible [170].

An IGA-001 Gas Sorption Analyser (IGA) from Hiden Isochema was used to measure isothermal data gravimetrically. This instrument has a temperature range of 77 to 1273 K and pressures ranging from ultra-high vacuum (UHV) to 20 bar. An HTP1-V Volumetric Analyser (HTP) from Hiden Isochema and a Quantachrome Autosorb-iQ2 were used to measure excess adsorption isotherms using Sievert's method. The HTP is specifically designed for the analysis of HSMs, operating in the temperature range of 103 - 773 K and at pressures from UHV up to 200 bar. The Autosorb can analyse two samples at once, but temperature can only be controlled by immersion in a liquid at the desired temperature, so only 77 K (for liquid N_2) and 87 K (for liquid Ar) were used for low temperature isotherms.

The non-ideal behaviour of gases is taken into account by using a variety of equations of state (EOS), which can be specified by the user, such as the Soave-Redlich-Kwong (SRK) EOS [172], or the Modified-Benedict-Webb-Rubin (MBWR) EOS which is empirically determined and typically used for H_2 adsorption studies [173]. The latter is used in this study, with compressibility data taken from the NIST Reference Fluid Thermodynamics and Transport Properties (REFPROP) database [174].

All three instruments are software-controlled and enable the user to design and automate a complex sequence of measurements, including a range of pre-treatments, such as outgassing, heating or cooling, as well as the steps required for isothermal construction. The kinetics of pressure or temperature equilibration for each isothermal point can be extracted, since measurements are continuously recorded and analysed in real-time. The HTP and Autosorb can receive a range of sorbate gases, such as the inert gas Helium, used to measure the skeletal or dead volume (i.e. that taken up by the material itself, excluding the volume of any internal pores) of a microporous sample (pycnometry). Since He, with a diameter of 2.8 Å [175], is smaller than H_2, the volume measured will over-estimate the volume available to H_2 and lead to an underestimation of the measured excess adsorption isotherms [176].

To ensure that the equipment was running correctly, regular volume calibrations were performed, using an empty stainless steel sample holder as a blank. This allows the user to get a reasonable estimate for the fractional volumes for each temperature. Normal isothermal data is collected using H_2 gas in the empty sample holder for a range of temperatures. The user can plot these data and adjust the fractional volumes until the isotherms show no uptake. In addition, isotherms were run on known samples, such as zeolite NaX, to confirm that the data collected is in accordance with literature data. Since all relevant data is recorded while isotherms are taken, the user can also retrospectively examine the pressure, temperatures of both sample chamber and manifold, etc. to assess the accuracy at each point. For instance, large temperature fluctuations would render the data non-isothermal and therefore unusable.

Hydrogen adsorption isotherms were carried out using the HTP. Prepared clay samples were weighed in ambient conditions (this constitutes the “wet weight” of the sample), loaded into the sample chamber and kept in place with a quartz wool plug, of known weight. The sample was outgassed *in situ*, by pumping on the sealed sample container for about an hour, down to a vacuum of 10^{-6} mbar. In the case of clays, this will remove a large amount of loosely-bound water. The pre-treatment process involves heating to 413 K for 40 minutes and subsequent cooling for 30 minutes, while continuously outgassing the chamber to at least 10^{-6} mbar. The skeletal volume was determined by an automated pycnometric procedure, with the wet weight of the sample and the quartz wool being entered into the system at the time of loading. The volume calculated from this is inaccurate, since it is based on a wet weight for a dry sample, but can be easily corrected once the dry weight of the sample is known (measured when the sample is unloaded, in as short a time as possible, so as to minimise the amount of water re-absorbed). The isotherm data also needs to be corrected in the same way. A range of adsorption-desorption isotherms with 20 evenly-spread points, each given 10 minutes equilibration time, were run for the following temperatures: (77 K, 87 K, 98 K, 148 K and 293 K). Uptake for each dose is measured in μmol H_2.

6.2.2 Analysing excess adsorption isotherms

Experimental isotherms of porous materials measure excess adsorption: the amount present in the pores exceeding that expected in the same volume filled with the same gas at bulk equilibrium density. Absolute adsorption is the total amount of adsorbate present in the pores. At sub-atmospheric pressures, absolute and excess adsorption do not differ significantly, but these differences become relevant at pressures close to and exceeding 100 bar [177].

The hydrogen uptake (excess adsorption or Gibbs excess) measured in an adsorption-desorption isotherm is plotted as a function of the equilibrium pressure and analysed by fitting them to a number of appropriate models, the simplest and most widely-used being the Langmuir model [178], describing monolayer coverage of a homogeneous surface. This model has a number of key assumptions:

- The surface of the adsorbent is uniform (i.e. all adsorption sites are equivalent)
- There is no interaction between adsorbate molecules
- Adsorption occurs through the same mechanism throughout

- At maximum adsorption, only a monolayer forms

The Langmuir equation (Equation 6.7) is derived from a kinetic approach [89]. If we consider the adsorbent surface to be an array of N_s adsorption sites, then the fractional surface coverage θ, by N_a molecules is:

$$\theta = \frac{N_a}{N_s}. \tag{6.1}$$

Adsorption and desorption are described by the chemical equation:

$$\text{gas molecule} + \text{bare site} \xrightleftharpoons{\text{rate constants}} \text{occupied site}, \tag{6.2}$$

where the frequency of free gas molecules is represented by the pressure, that of bare sites by $(1 - \theta)$, and that of occupied sites by θ.

From the kinetic theory of gases, the rates of adsorption (r_{ads}) and desorption (r_{des}) are:

$$r_{ads} = \alpha P(1 - \theta) \text{ and } r_{des} = \beta\theta, \tag{6.3}$$

where α and β are the rate constants, specific to a particular adsorption system. From the Arrhenius relation, these constants are given by:

$$\alpha = \alpha_0 exp\left(-\frac{E_{ads}}{RT}\right) \text{ and } \beta = \beta_0 exp\left(-\frac{E_{des}}{RT}\right). \tag{6.4}$$

At equilibrium, the net rate is zero, thus:

$$\frac{dN_a}{dt} = \alpha P(1 - \theta) - \beta\theta = 0. \tag{6.5}$$

A rate constant b may be defined as:

$$b = \frac{\alpha}{\beta} = \frac{\alpha_0}{\beta_0} exp\left(\frac{(-(E_{ads} - E_{des}))}{RT}\right) = b_0 exp\left(-\frac{\Delta H_{ads})}{RT}\right), \tag{6.6}$$

where ΔH_{ads} is the adsorption enthalpy, which reflects the strength of adsorptive-substrate binding. $\frac{\Delta H_{ads}}{RT}$ represents the fraction of molecules present in a gas which have energies at least equal to ΔH_{ads}. Thus, at a given pressure, the extent of the adsorption depends on b, which in turn depends on the temperature and the enthalpy of adsorption. Equation 6.6 can now be rearranged to give:

$$b = \frac{\theta}{(1 - \theta)p} \text{ usually presented as the equivalent: } \theta = \frac{bp}{(1 + bp)}, \tag{6.7}$$

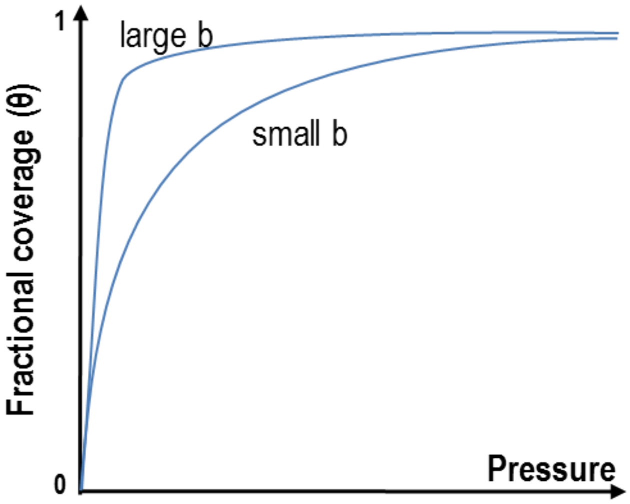

Figure 6.2: Typical Langmuir isotherms, showing how the characteristic shape of the curve is affected by the value of the Langmuir constant, b.

where b is the Langmuir constant or adsorption coefficient, affecting the isotherm curvature, and p is the equilibrium partial pressure of adsorbate at the adsorption temperature. Two Langmuir isotherms are illustrated in Figure 6.2, showing the difference between high and low adsorption coefficients. Both show an asymptotic approach to saturation coverage as pressure increases: a characteristic feature of Langmuir coverage.

Henry's law applies to extremely dilute solutions, stating that, under isothermal conditions, the amount of a given gas that dissolves in a given volume of liquid depends on the partial pressure of the gas in equilibrium with the liquid. All adsorption equations should ideally reduce to Henry's law in the low coverage limit, giving a linear isotherm. The Langmuir equation, Equation 6.7 does this.

Alternate Isotherm models

The Freundlich equation is an adsorption model which takes into account both the heterogeneity of adsorption sites in a material and the tendency for the ΔH_{ads} to decrease exponentially with coverage. It has been widely applied to adsorption in zeolites [179] and to adsorption of pesticides in clay minerals [180] and has the form:

$$n_a = n_s.k_F.p^{\frac{1}{m}}, \tag{6.8}$$

where n_a is the number of moles adsorbed at the given pressure, n_s is the number of moles adsorbed at saturation and the empirical parameters, k_F and m, are specific for a particular combination of adsorbate and adsorbent. k_F is generally taken to represent the saturation capacity of the material and m is considered to give a measure of the heterogeneity of the adsorption sites in the material, where m ~1 indicates a homogeneous adsorbent surface and $m > 1$ a heterogeneous surface. This model does not exhibit saturation at high pressures and does not reduce to Henry's law at very low coverage (below 0.2 wt%), but it generally provides a good fit at low coverages. A combination of the Freundlich and Langmuir equations was therefore proposed by Sips in 1948 [181], enabling a good fit over a wider range of pressures:

$$n_a = n_s \frac{(k_F p)^{\frac{1}{m}}}{1 + (k_F p)^{\frac{1}{m}}}, \tag{6.9}$$

where n_a, n_s, k_F and m are the Freundlich constants described above. This Freundlich-Langmuir equation does not reduce to Henry's law in the low coverage limit, but does tend to a finite limit at high pressures. It has been widely used to model adsorption in MOFs [182] [183].

The Tóth model is an alternative model satisfying both limits (p → 0 and p → ∞) of an isotherm, reducing to Henry's law at low pressures and reaching a finite saturation limit at high pressures. The equation is:

$$n_a = n_s \left(\frac{(k_F p)^m}{1 + (k_F p)^m} \right)^{\frac{1}{m}}, \tag{6.10}$$

where the parameters are the same as for the Sips equation (Equation 6.9), except that now $m < 1$ for heterogeneous adsorption surfaces. It can be applied to porous media with multilayer adsorbate coverage and generally gives a better fit to isotherms over a wide range of pressures. However, it tends to overestimate the saturation coverage.

In summary, the Sips model, Equation 6.9, combines features of both the Langmuir (Equation 6.7) and Freundlich (Equation 6.8) models, providing a better estimate of the saturation coverage in the high pressure limit, while the Tóth model, Equation 6.10, is expected to give a better overall fit to the isotherm over the full range of pressure and particularly at low coverage, yielding a more accurate ΔH_{ads}. A comparison of the models applied to adsorption of H_2 in clay minerals measured in this study and further analysed in Section 9.2, is shown in Figure 6.3. It is clear that no single model applies to all laponite samples and temperatures. In Figure 6.3a, the best fit for both 77 and 87 K is to the Tóth model, while in Figure 6.3b, no one model can fit both temperatures - at 77 K, the best fit is to the Freundlich model, but at 87 K, the best model is the Sips equation (Equation 6.9). Figure 6.3c shows a similar pattern, but this time the best model for the 77 K data is neither Sips nor Tóth, but something in-between.

The choice of model is important for understanding the underlying mechanisms and since it is unlikely that these mechanisms would change significantly between temperatures only ten degrees apart, it is clear that a new model combining the features of the Sips and Tóth models is required to describe adsorption of H_2 in clay minerals. For the purposes of calculating the isosteric heat of adsorption, the choice of model only matters as to how well it can extrapolate the data between measured points, allowing true isochoric comparison between isotherms taken at different temperatures. Initially no single model was favoured and each isotherm in Section 9.2 was fitted independently, using the model which most closely represented the data, however using disparate models for the different temperature isotherms measured on the same sample and extrapolating the calculation of ΔH_{ads} to higher coverages gave invalid results, such as an increasing ΔH_{ads}. Therefore the model was selected based on how closely it matched both temperature isotherms, while an independent choice of model was allowed for different samples. The imperfect isotherm matching resulted in some distortion of the ΔH_{ads} function, particularly at higher coverages.

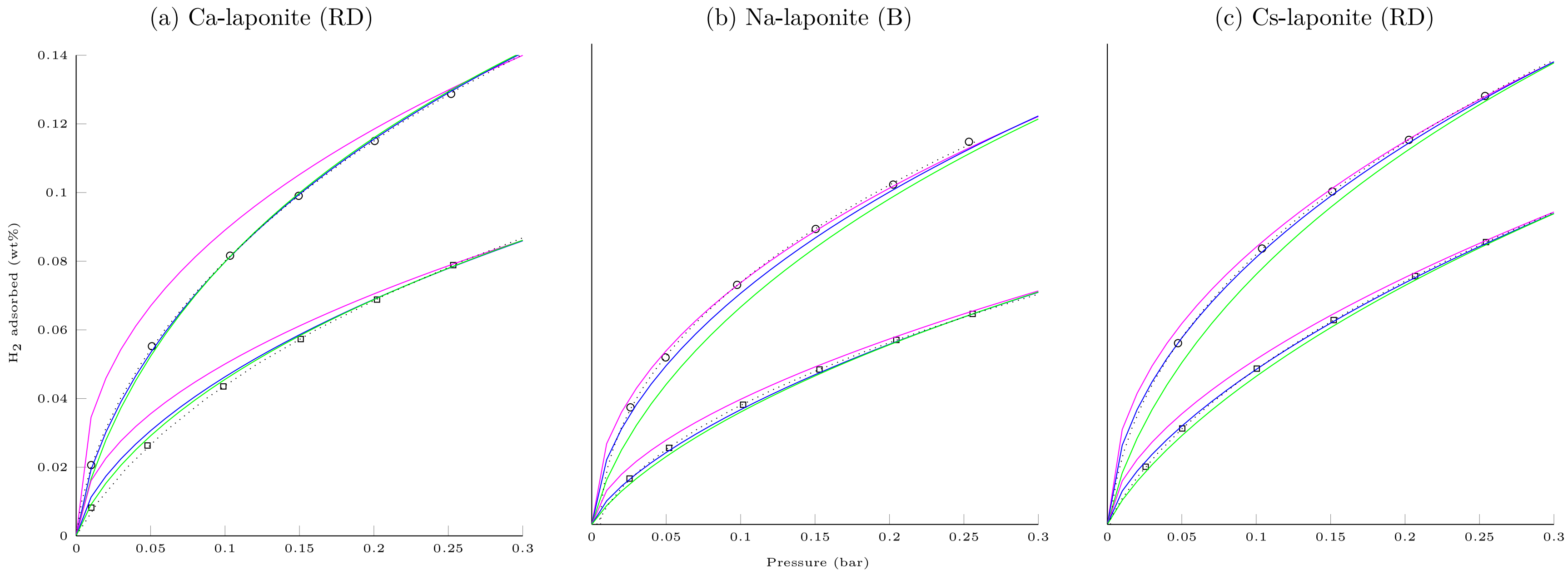

(a) Ca-laponite (RD)

(b) Na-laponite (B)

(c) Cs-laponite (RD)

Figure 6.3: Comparing a variety of fit models for the low pressure region of adsorption isotherms for three representative samples of laponite. The measured data points for 77 and 87 K are shown as open circles and open squares, respectively, while the lines represent the fits. The solid magenta line gives the Freundlich fit (Equation 6.8); the solid blue shows the Sips (Langmuir-Freundlich) (Equation 6.9); the solid green line shows the Tóth model (Equation 6.10) and the dotted black line is the virial expansion model (Equation 6.12), this last being the best fit across all samples and temperatures.

Experimental isotherms can be fitted to the chosen model using a non-linear least-squares regression procedure, usually done by minimising the vertical error between the data points and the fitted curve. However, this introduces an error bias towards the low pressure region. Instead, both vertical and horizontal errors should be accounted for by using the distance between each data point and the nearest tangent to the curve. Analysis software does not usually allow for this and, ideally, an appropriate package which allows the user to control the error minimisation technique is required.

6.2.3 Limiting coverage and density

The limiting coverage is the saturation capacity of the material at the limit of high pressures and is extracted from the fits through the parameter n_s. It is useful as a measure of the theoretical limit of H_2 capacity, but will rarely be achieved in practice.

The adsorbate phase density can be calculated by dividing the mass of adsorbed substance by the volume within which it is held, for instance, the volume of the clay interlayers, calculated from the crystallographic dimensions of 5.28 Å and 9.14 Å [184], an interlayer separation of 3 Å (estimated from XRD measurements: see Chapter 7) and the estimated number of unit cells in the sample, determined by dividing the sample mass by the unit cell mass. This is different from the volumetric H_2 storage density, which takes into account the total volume occupied by the adsorbent material.

6.2.4 Extracting isosteric heat of adsorption

Equation 6.6 is an Arrhenius relation, yielding a linear relation between $ln(b)$ and $\frac{1000}{T}$, with a slope of ΔH_{ads} and a y-intercept of $ln(b_0)$. The enthalpy of adsorption can be obtained from a linear regression analysis of a number of isotherms run to the same pressure, but at different temperatures, plotting temperature variance for a constant coverage, i.e. the isosteric dependence of the adsorption coefficient on temperature.

From the fitted curves to the data measured for two isotherms run at different temperatures, such as those shown in Figure 6.4, it is possible to extract the isosteric

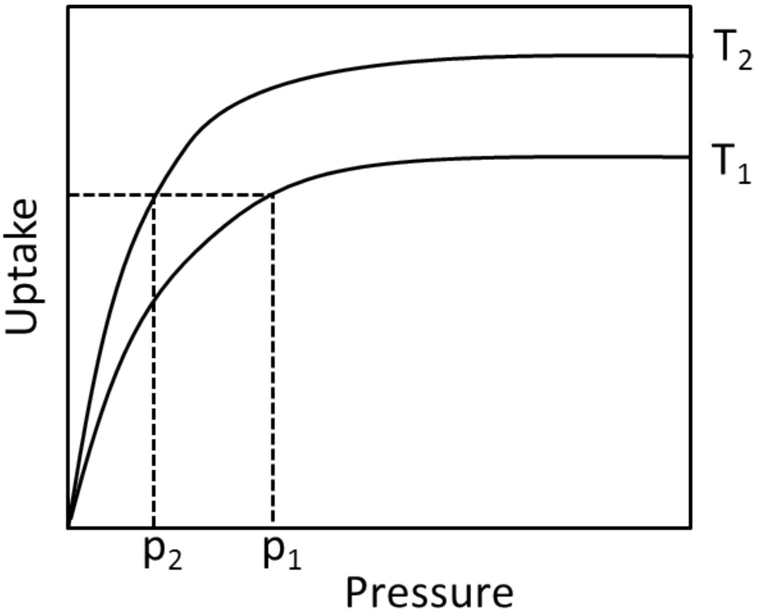

Figure 6.4: Extraction of the isosteric heat of adsorption, ΔH_{ads}, for a particular coverage requires two isotherms at different temperatures, $T_1 > T_2$. For physisorption systems, the pressure required to achieve the same coverage at a higher temperature will be lower.

heat of adsorption for a particular coverage, using the Clausius-Clapeyron relation [185]:

$$\left(\ln\left(\frac{p_1}{p_2}\right)\right)_\theta = -\frac{\Delta H_{ads}}{R}\left(\frac{1}{T_1} - \frac{1}{T_2}\right). \tag{6.11}$$

However, unless isochoric measurements have been made, this can only be performed using fits to the isotherm data and the choice of fit can greatly distort the resulting value [186]. It is therefore important to choose a fitting model which gives the best possible fit over the pressure range of interest.

Performing this calculation over a range of coverages shows how ΔH_{ads} varies with coverage: generally, ΔH_{ads} should decrease with increasing coverage. The measured isotherm data gives a macroscopic average over all activated binding sites and higher coverages will include weaker sites. Analysis of the very low coverage region elucidates only the adsorbate-adsorbent interactions, free of the complications of compressibility.

The isosteric heat of adsorption in the low coverage limit, H_0, can be determined by fitting supercritical adsorption isotherms to a modified virial equation:

$$P(n_a) = \frac{n_a}{k_H}\left[\frac{n_s}{n_s - n_a}\right]\exp(c_1 n_a + c_2 {n_a}^2 + c_3 n_a^3 + \ldots), \tag{6.12}$$

where k_H is the Henry law constant, n_s is the saturation capacity, n_a is the specific amount adsorbed (in mol H_2 kg^{-1}) and c_1, c_2, etc. are the virial coefficients, of which three is usually sufficient. The first coefficient, c_1, relates to the Henry's law constant. This equation is unconstrained by any particular adsorption mechanism and can be applied to the very low coverage region. Applying the Clausius-Clapeyron relation, Equation 6.11, as before, yields H_0.

6.2.5 Determining surface area

The surface area of a microporous material is an important factor affecting its physisorptive capacity and therefore an important aspect of the characterisation of an HSM. The accessible volume of a porous material can be estimated from a single high-pressure volumetric dose with the relevant purified gas, from which the number of moles of adsorbate can be calculated. If the dimensions of the gas molecules are known, then the area that a single molecule occupies on the surface, the adsorption cross-section (σ_{ads}), can be determined and multiplied by the number of adsorbed molecules. This is the basis of the BET technique, where N_2 having $\sigma_{ads} = 0.162$ nm^2 [89], is typically used as the sorbate gas.

The application of the BET method to microporous materials has been criticised [187] especially when used on swelling clays [188], but N_2 vapour adsorption is still widely used. The choice of sorbate greatly affects the result for microporous materials, because smaller molecules can access smaller pores. N_2, with a diameter of approximately 4.5 Å, is larger than H_2 and will consequently underestimate the surface area available to H_2. The average N_2-BET SSA of laponite is 279 m^2/g [188], but the physical surface area is estimated at 900 m^2/g in the product literature [135].

The BET technique, using H_2 as the sorbate, can be used to estimate the surface area accessible to H_2 in a microporous material. Since the interlayer pores of a clay such as laponite are small enough to cause capillary condensation, it is reasonable to assume that the packing of H_2 on micro-porous surfaces is similar to the liquid form. An estimate for dihydrogen's σ_{ads} (14.401 Å^2) can be obtained from the following formula:

$$\sigma_{ads} = 1.093 \left(\frac{M 10^{24}}{\rho_a N_A} \right)^{\frac{2}{3}}, \tag{6.13}$$

where 1.093 is the circular close packing factor, expanding the circular surface area to a square ($\frac{\pi}{(2\sqrt{3})}$ = the fraction of surface covered by circles in a hexagonal close-packed formation), M is the molar mass of H_2 (2.016 g/mol), ρ_a is the adsorbate density (0.07 g/cc) and N_A is Avogadro's number. This represents the projection of the H_2 molecule onto a flat surface.

The number of moles of H_2 (n_{H_2}) adsorbing to the surface of a porous material can be determined experimentally using Sievert's method and the surface area available to H_2 can then be determined by:

$$SSA_{H_2} = \frac{n_{H_2} N_A \sigma_{ads}}{m_a}, \tag{6.14}$$

where N_A is Avogadro's number and m_a is the mass of the adsorbent.

It is also useful to estimate the total physical surface area available to H_2, i.e. the Langmuir monolayer capacity. This can be estimated by scaling up the unit cell dimensions, taking into account the specific micro- and macroscopic structure of the material.

As a first approximation for laponite, the complexity of any interlayer volume taken up by the cations and the water molecules bound to them can be disregarded. Based on a dry laponite unit cell having composition $[{Mg^{2+}}_{5.5}\ {Li^{+}}_{0.3}]\ [Si_8]\ O_{20}\ (OH)_4{}^{-0.7}$. ${Na^{+}}_{0.7}$, the dimensions, unchanged by cation exchanges and deuteration [137], give a surface area of 48 Å^2 [137] on each of the upper and lower surfaces of the cell, thus a total of 96.52 Å^2 per unit cell, or 762 m^2/g of interlayer surface. This needs to be adjusted slightly to account for surface which is not part of the interlayer - i.e. the outer surfaces of stacked unit cells. In dry laponite, the clay platelets join together to form stacks of about 1000 platelets [135]. Therefore the ratio of outer surface to interlayer surface is approximately 1:1000, reducing the interlayer surface only very slightly, by no more than 1 m^2/g. The surface area of the edges of the platelets is unlikely to adsorb any hydrogen molecules, since there are no cations here and the charge is only very weakly positive.

From the physical surface area, the maximum wt% H_2 for a dry material can be ascertained. Assuming monolayer coverage over the entire available surface, the number of H_2's which can be accommodated in 1 g of laponite (n_{mon}) is calculated by:

$$n_{mon} = 0.999\left(\frac{\text{physical SSA}}{2\sigma_{ads}}\right) + 0.001\left(\frac{\text{physical SSA}}{\sigma_{ads}}\right), \tag{6.15}$$

where the first term represents the interlayer H_2's and the second term the H_2's adsorbed to the outer surfaces. The factor of 2 for the first term accounts for the fact that an H_2 molecule confined in an interlayer pore is in contact with two surfaces: above and below. Using Equation 6.15, 1 g of dry Ca-laponite accommodates a maximum of 0.89 wt% H_2.

6.2.6 Porosity

According to the IUPAC classification system, porous materials are divided into three categories, based on the average size of their pores: microporous ($<$ 2 nm), e.g. zeolites and MOFs, mesoporous (2 - 50 nm), e.g. some porous silicas, and macroporous ($>$ 50 nm), e.g. cavities within soils [89]. Materials exhibiting Type I adsorption isotherms are generally considered to be microporous. Both the surface area and pore size distribution of a material can be determined from a 77 K N_2 isotherm fitted to a density functional theory (DFT) model, however this will consider only those pores that are accessible to the N_2 molecule.

6.2.7 Hysteresis

Hysteresis loops in adsorption-desorption isotherms indicate that these two processes occur by different mechanisms and may suggest some irreversibility of the adsorption process. Four types of hysteresis for adsorption-desorption isotherms have been proposed [89]. As a general rule, supercritical isotherms yield no hysteresis loops, however it may be observed when the pores are large enough for the adsorbing molecules to condense to a liquid. During the process of adsorption and desorption, the pore geometry of the material may change slightly, giving rise to small differences in the thermodynamics of these two mechanisms.

6.3 Neutron instruments

6.3.1 NIMROD

NIMROD [189] is a diffractometer on the second target station of the ISIS facility, optimised for the study of disordered systems, such as liquids and condensed gases.

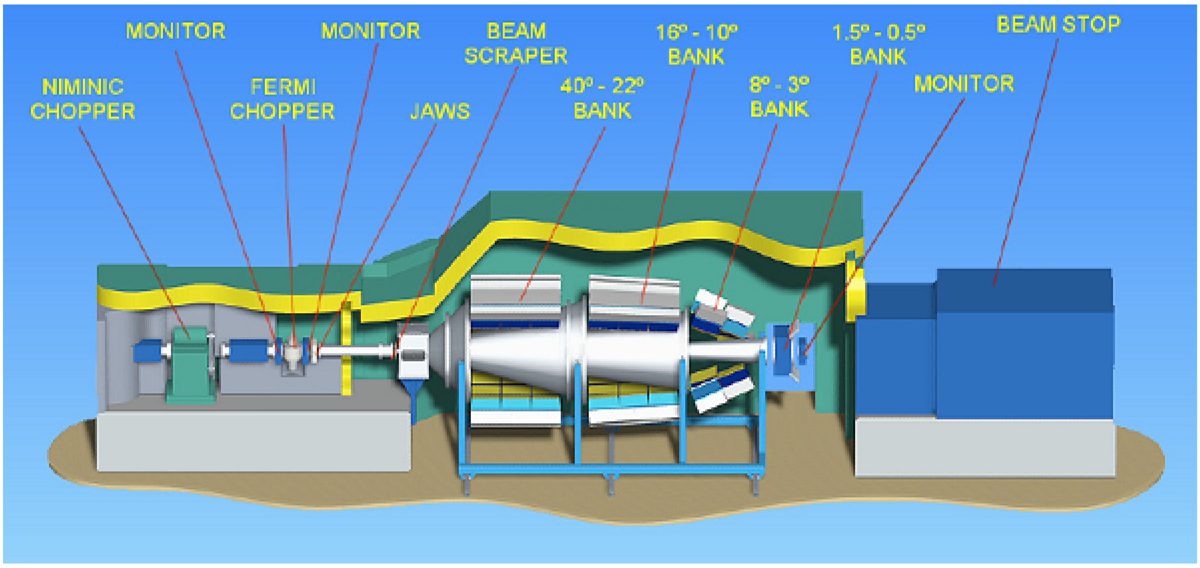

Figure 6.5: (From the ISIS website.) A schematic of the NIMROD diffractometer on target station 2 at the ISIS facility of RAL, showing the choppers and the detector array, covering a scattering angle range of 0.5-40°.

Target station two provides an incident beam with a broad spectral range, including both short and long wavelength neutrons. The latter access the low-Q region and provide structural correlations over long length scales (~300 Å). Short wavelength neutrons access high-Q, achieving a high structural resolution of the order of 0.1 Å. This makes NIMROD especially useful for performing hydrogen-deuterium isotopic substitution studies, giving contrast information vital for determining structure in hydrogenated materials. NIMROD minimises inelastic effects by using a forward scattering geometry and measures the differential scattering cross-section, giving the total structure factor $S(\bar{\mathbf{Q}})$ of a disordered material.

Beamtime on this instrument was awarded for four days in March 2013. Samples were loaded into a rectangular TiZr cell rated for up to 10 bar pressure having a 30 by 30 by 1 mm central space to hold the sample upright in the beam. Ca-laponite (EL) was dried as described in Section 6.1.4 and 1.3 g was transferred to the sample cell, loaded onto the beamline and evacuated down to 10^{-6} mbar. Background readings (sample in vacuum) were taken at 6, 25 and 40 K, and the sample was subsequently subjected to a range of dosings (3-, 5-, 7.5- and 9-D_2:Ca^{2+} followed by 3-, 5- , 6.5- and 8-H_2:Ca^{2+}) and four temperatures (6, 25, 40 and 60 K). After the final dosing with D_2, the samples were gradually heated up to 260 K to ensure complete desorption, before cooling and dosing with H_2. For some samples, runs of about three hours may be necessary, but a comparison of the statistics for the first three-hour run with that of a subsequent one-hour run showed little difference and it was thereafter possible to perform each run over just one hour.

Standard corrections as described in the Gudrun manual [148] for attenuation, multiple scattering effects, deadtime and normalisation were applied to the data, from which the background was removed before applying corrections for inelasticity and using Fourier transforms to remove any Q-dependent background from the raw data. The GudrunN program was permitted to guess the packing fraction corrections, based on the estimated sample composition of ${Ca^{2+}}_{0.35}[(Si_8\ Mg_{5.5}\ Li_{0.3})\ O_{20}\ (OD)_4]^{-0.7} nD_2O$ and powder density of 2.277 g cm^{-3}.

It was intended that the dosings for H_2 and D_2 would match for isotopic substitution analysis, but it proved extremely difficult to ensure this. The H_2 measurements were done after the D_2 measurements and desorption. The dosage was determined by pressure and the drop after each dose was less than the drop after the corresponding D_2 dose, suggesting that the H_2 required a higher pressure to intercalate the laponite layers. Further experiments are required to ascertain whether this is a real effect and whether it is due to some irreversible structural changes made by the first dose. Some interlayers may collapse if all of their water pillars are removed, in a flushing effect analogous to dry-cleaning, caused by the adsorption and desorption of D_2/H_2. This effect may be the cause of the slight hysteresis visible in some of the adsorption-desorption isotherm measurements presented in Chapter 9, however this does not seem to be a significant effect. The same gas rig was used as for the IRIS experiments, having the same features and volume calibrations. The data was analysed using the ISIS software, GudrunN v4 [148], over a Q-range of 0.05 to 15 Å^{-1}.

Figure 6.6 shows the constancy of the data for measurements at three different temperatures, showing that the d-spacing changes discussed in Chapter 8 are not due to experimental variations.

Contrast matching

There is a large difference in the coherent neutron scattering lengths between hydrogen (-3.739 fm [190]) and deuterium (+6.671 fm [190]), the negative sign for H indicating that the scattered neutron's wavefunction is out of phase with respect to the incident neutron's wavefunction. This large difference allows coherent scattering techniques, such as SANS, to highlight structures or phases in a material by the contrast between associated deuterated and non-deuterated molecules, much like microscopy uses staining to bring out particular features. This partial deuteration

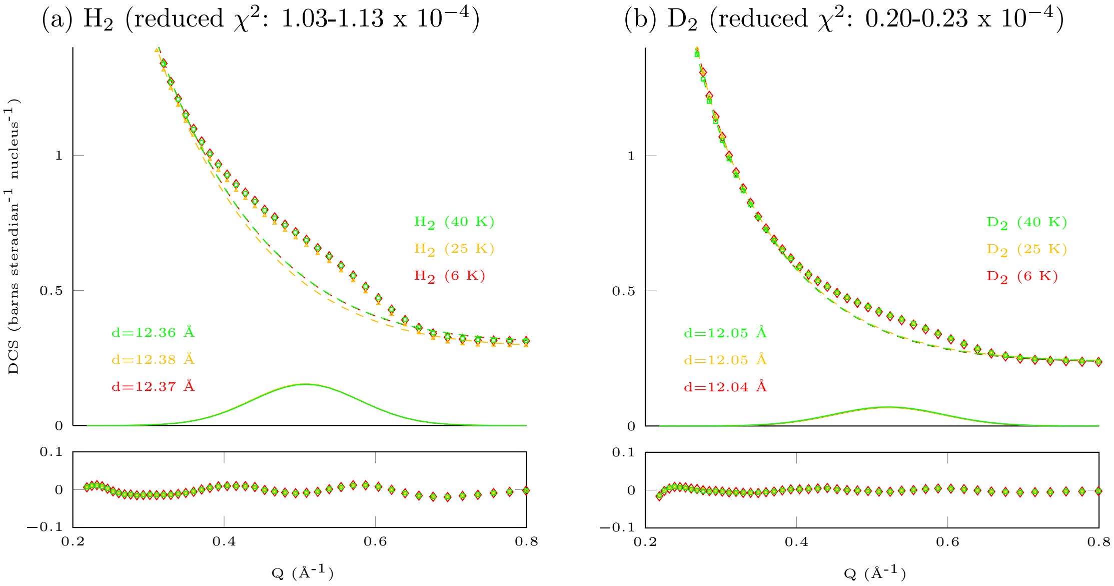

Figure 6.6: Small angle scattering data from NIMROD measurements of Ca-laponite (EL), showing that, for the same pressures of H_2/D_2, the *d*-spacing remains constant over three temperatures. The red, representing the sample at 6 K, is obscured by the 40 K data, confirming that the small angle-data is not subject to either thermal or instrumental fluctuations and therefore changes here can be fully ascribed to the H_2/D_2 adsorption amount.

technique is a unique feature of neutron scattering and has been widely used to determine the size and distribution of pores in porous media [191] [17].

The overall scattering of a hydrogenous molecule depends on the ratio of hydrogen to deuterium in the molecule and the scattering signal from water depends on the amount of D_2O present. Typically, mixtures of H_2O to D_2O are used to determine the contrast-match point with a particular phase within the material: the point at which this phase becomes effectively invisible to the neutron beam [17], because its scattering is equal to that of the surrounding H/D mixture and can be eliminated by background subtraction. Any structural peaks indicative of this phase which fall within the small angle region disappear, leaving only the peaks of the unmatched phases visible. For porous materials, any peaks due to regular spacings of voids disappear as the voids are filled with scatterers. This effect will be an important aspect of the discussion of the results from NIMROD, in Section 8.1.

The scattering intensity is proportional to the contrast factor, which is the square of the difference between the scattering length densities of two closely associated molecules, such as a solute surrounded by a solvent shell [192]. The neutron scattering length density for a molecule of formula $\mathrm{A_mB_n}$ is given by:

$$\rho_{A_mB_n} = \frac{mb_A + nb_B}{v}, \tag{6.16}$$

where b_A and b_B are the neutron scattering lengths of atoms A and B and v is the volume of the molecule. This formula yields neutron scattering length densities of -5.86 x 10^{-7}Å^{-2} and +1.04 x 10^{-6}Å^{-2} for H_2 and D_2, respectively.

Background removal

For the small angle background, a Q^{-4} power law combined with a constant and a broad Gaussian peak with FWHM between 8.5 and 11.5 Å^{-1} and centred at $Q = 0$ was found to fit the background scattering satisfactorily and a clear Gaussian peak remained after subtraction, enabling the d-spacing of the material to be measured. The broad Gaussian is probably an instrumental background feature, stemming from the fact that this instrument is not specifically optimised for small angle scattering measurements. This applies to the X-ray data too, which was collected on a fixed wavelength laboratory scale diffractometer, using capillary geometry.

6.3.2 IRIS

Beamtime on the high resolution backscattering time-of-flight spectrometer, IRIS [193], based at the ISIS pulsed neutron facility at RAL, was awarded for four days in February 2010 and five days in March 2013. The key features of this instrument are shown in Figure 6.7. The dynamic scattering function was measured using the 002 reflection of pyrolytic graphite. With this analyser and an incident neutron wavelength of 6.6 Å, IRIS has a FWHM energy resolution of 17.5 μeV, with a total energy window of ±0.5 meV [193]. The time resolution of IRIS is 10^{-10}-10^{-12}ps.

IRIS's resolution function and detector efficiencies were determined using a cylindrical canister of pure vanadium. Samples were transferred into an annular cylindrical high-pressure aluminium cell, consisting of two interlocking cylinders, with a diameter difference of 2 mm, leaving a cylindrical shell for the sample. This geometry reduces the likelihood of multiple scattering events and minimises beam attenuation. The can was sealed with an indium gasket and placed in a temperature-controlled environment equipped with a top-loading closed cycle refrigerator (TLCCR), using liquid helium. All measurement temperatures were controlled within 2 K. The cell was equipped with top and bottom heaters, as well as a temperature sensor and

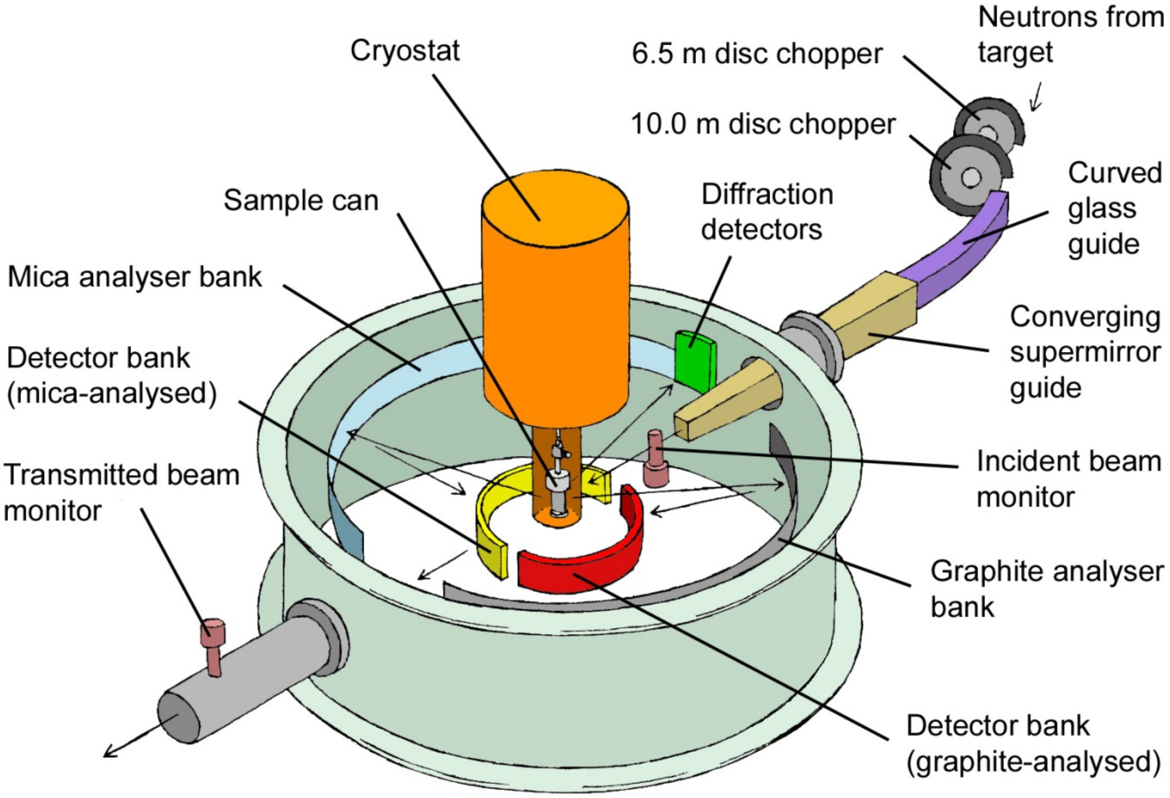

Figure 6.7: (Drawn by Arthur Lovell.) Schematic representation of the layout of the IRIS backscattering TOF spectrometer at RAL.

baratron pressure sensor. Excess gas was pumped out *in situ*, using a turbo pump, down to 2 x 10^{-6} mbar for at least an hour, to remove any water vapour which may have been absorbed during transfer from the oven to the sample can. The dry sample masses were: 6.68 g of Ca-laponite (RD), 8.20 g of Na-laponite (RD) and 6.83 g of Ca-laponite (EL). The sealed sample can was carefully tested for any leaks before loading onto the beamline.

All separate volumes forming part of the gas rig attached to the IRIS sample chamber were calibrated using a sequential volumetric technique based on Boyle's law, with Helium gas. The gas in a known volume was released into each new volume and allowed to equilibrate before recording the new pressure. The temperature of the room was measured with a mercury thermometer and all volumes were assumed to be at this temperature, since no heating or cooling systems were in operation.

The sample was cooled to around 6 K and quasi- and inelastic measurements were performed in vacuum, in order to obtain background readings. The sample was then heated to 50 K and dosed with 1 bar of H_2. This dosing temperature is below the literature standard of 77 K, but was selected so as to maximize the amount of H_2 absorbed, while still being supercritical. The latter is crucial to avoid H_2 liquefaction and capillary condensation in either the pipes or the sample. By watching the pressure readings, the speed at which the H_2 was adsorbed could be observed and a reasonable equilibration point determined. The adsorption was fairly rapid (less than 5 mins) and about 400 mbar of H_2 was absorbed before stabilising. The sample cell was sealed off and cooled to 6 K for background measurements.

Scattering data at this point did not reveal any ortho-para conversion: the elastic signal remained at a steady level for a reasonable length of time (>1 hour). This check is performed at the beginning of any neutron experiment on a sample in a hydrogen atmosphere, because if the sample surface catalyses the ortho-para transition, the elastic intensity and consequently the resolution, will be reduced. Ortho to para conversion significantly affects the interpretation of the results and would be indicated by an exponential decay in the intensity of the elastic signal. If no conversion has occurred, then the total intensity will drop in proportion to the reducing adsorbate population and the elastic intensity will drop while the inelastic intensity increases as H_2 starts diffusing.

The pressure at 6 K is 0, because all substances in the sample are subcritical and the molecules are no longer moving around, meaning that all signal intensity lies within the elastic window. Below the critical point temperature, the H_2 populations will consist of adsorbed, solid and capillary condensed H_2. Above critical, the populations should be only gaseous and adsorbed H_2, because any H_2-H_2 bonds will have been thermally broken, even for those condensed in micropores. If the interaction between the surface and H_2 is weaker than that between H_2 molecules, then all adsorbed H_2 will desorb by 33 K. Based on a volumetric calculation, using the pressure drop when hydrogen was introduced to the sample cell, the amount of adsorbed hydrogen is estimated to be ~0.54 wt% at 50 K. The H_2 gas used was ultra-high purity (99.999% pure) from Sigma-Aldrich, with 3:1 ortho:para ratio.

Quasi-elastic measurements were performed on the sample in vacuum and subsequently at 100 K, 80 K, 60 K and 40 K, under a 1 bar H_2 atmosphere. Counts for all but the last temperature of Ca-laponite-RD, exceeded 500 μAmp, running for at least 8 hours each.

IRIS's 49 functional detectors were grouped into 17 spectral groups, spanning scattering angles corresponding to a Q-range of 0.421 - 1.17 $Å^{-1}$. The QENS spectra were analysed using the onsite IRIS analysis package, MODES, v3.0 [194], accounting for multiple scattering, absorption and detailed balance for each temperature and deconvolving the data from the instrument's resolution function, obtained from the vanadium measurement. The data were corrected for self-absorption, detector efficiency and sample container (can plus sample in vacuum at 6.5 K) and normalised to the elastic window intensity at 6 K. In all cases, background readings of the clay substrate at 6 K in vacuum were subtracted from the signal measured for the sample exposed to H_2. The resulting data showed a reasonable fit to the model of an elastic line and just one quasielastic peak. The spectra and their fit components for a range of spectral groups at one temperature per sample are shown in Figures 6.8, 6.9, 6.10 for Na-laponite (RD), Ca-laponite (RD) and Ca-laponite (EL) respectively.

For most spectral groups, satisfactory fits with χ^2_{red} values in the range 0.67 - 2.05, were obtained. However, for Na-laponite (RD) and Ca-laponite (EL) at higher temperatures, the data was harder to fit, because the signal decreased as hydrogen desorbed from the laponite. This was particularly noticeable at higher values of Q. Two examples of this are given in the highest Q group in Figures 6.8 and 6.10. The fit parameters were imported into Matlab and analysed using Mfit, v4.2 [195], with custom-built functions representing the rotational and translational diffusion models considered in Sections 5.3.1 and 5.3.1 respectively.

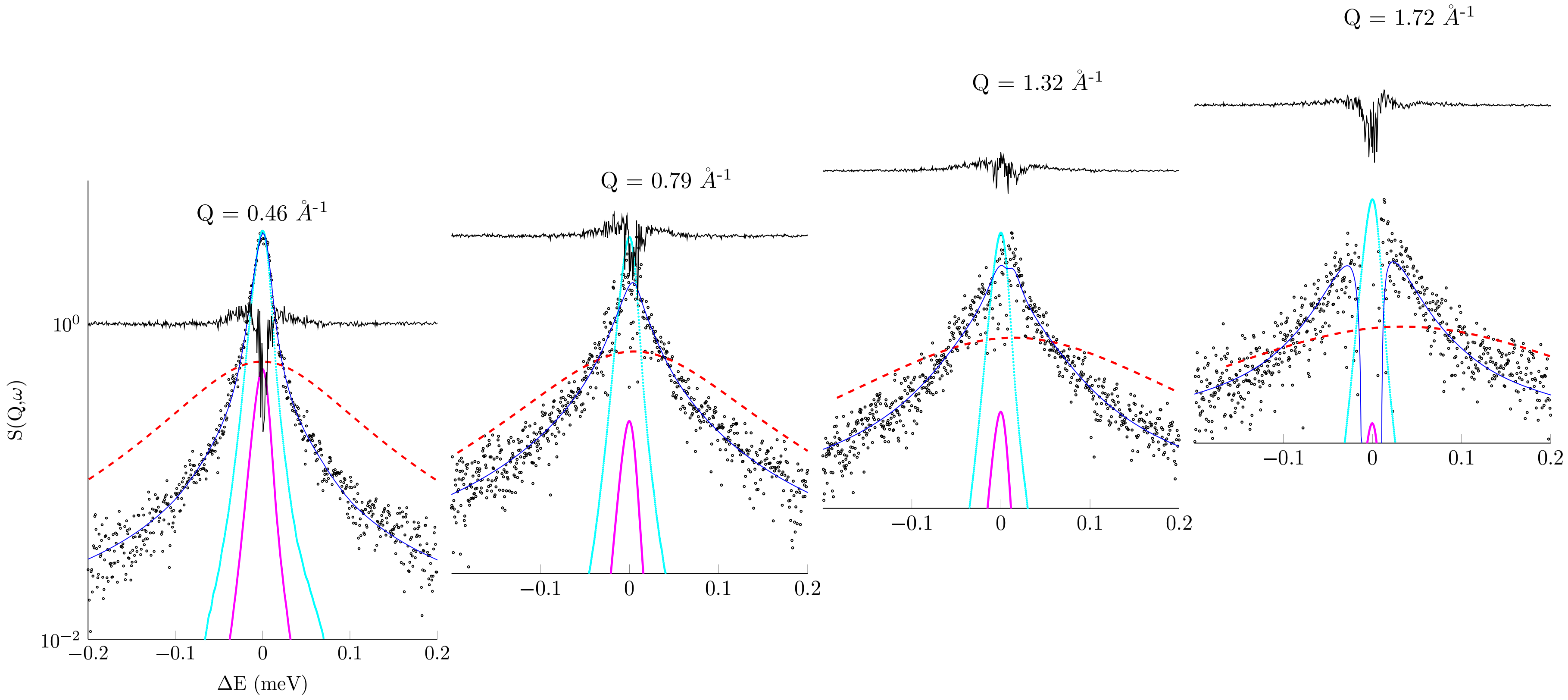

Figure 6.8: All components of QENS fits to a range of spectral groups for the data collected for Na-laponite (RD) at 40 K, showing the Q-dependent broadening of the quasielastic peak (dashed red line). For this sample, problems arose at higher Q (top right) where the signal, particularly the elastic signal, is greatly diminished. However, the width of the fitted quasielastic peak appears to be approximately correct. The measured data is represented by black dots, the fit is shown as a solid blue line and the light blue line shows the instrumental resolution. The Lorentzian components of the fit are the elastic peak (magenta line) and the single quasielastic peak. Note that the y-axis is a log scale and the components are not properly scaled. The residuals (solid black line) are shifted by 1, to avoid them obscuring the data.

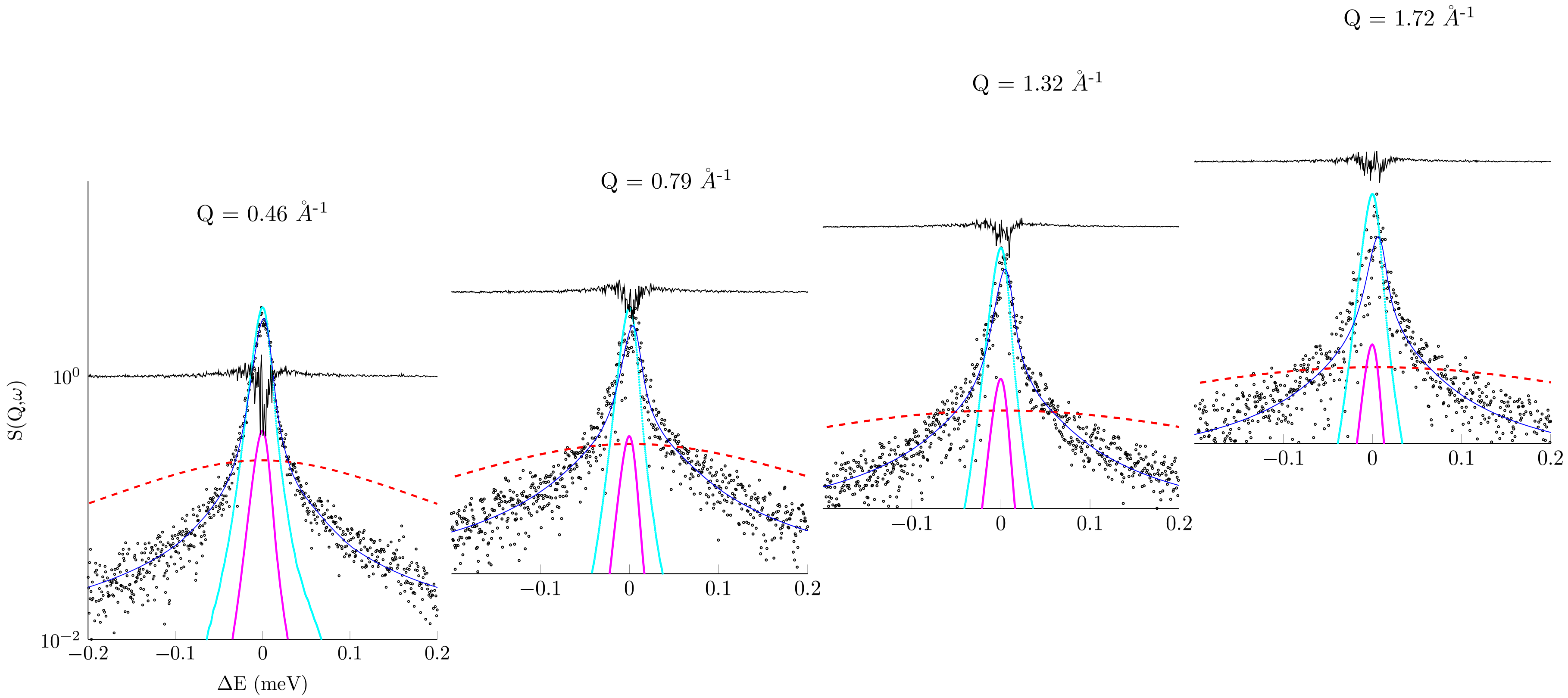

Figure 6.9: All components of QENS fits to a range of spectral groups for the data collected for Ca-laponite (RD) at 80 K, showing the Q-dependent broadening of the quasielastic peak (dashed red line). For this sample, problems arose at higher Q (top right) where the signal is diminished. The fit for the data at top right is off-centre, although the width appears to be approximately correct. The measured data is represented by black dots, the fit is shown as a solid blue line and the light blue line shows the instrumental resolution. The Lorentzian components of the fit are the elastic peak (magenta line) and the single quasielastic peak. Note that the y-axis is a log scale and the components are not properly scaled. The residuals (solid black line) are shifted by 1, to avoid them obscuring the data.

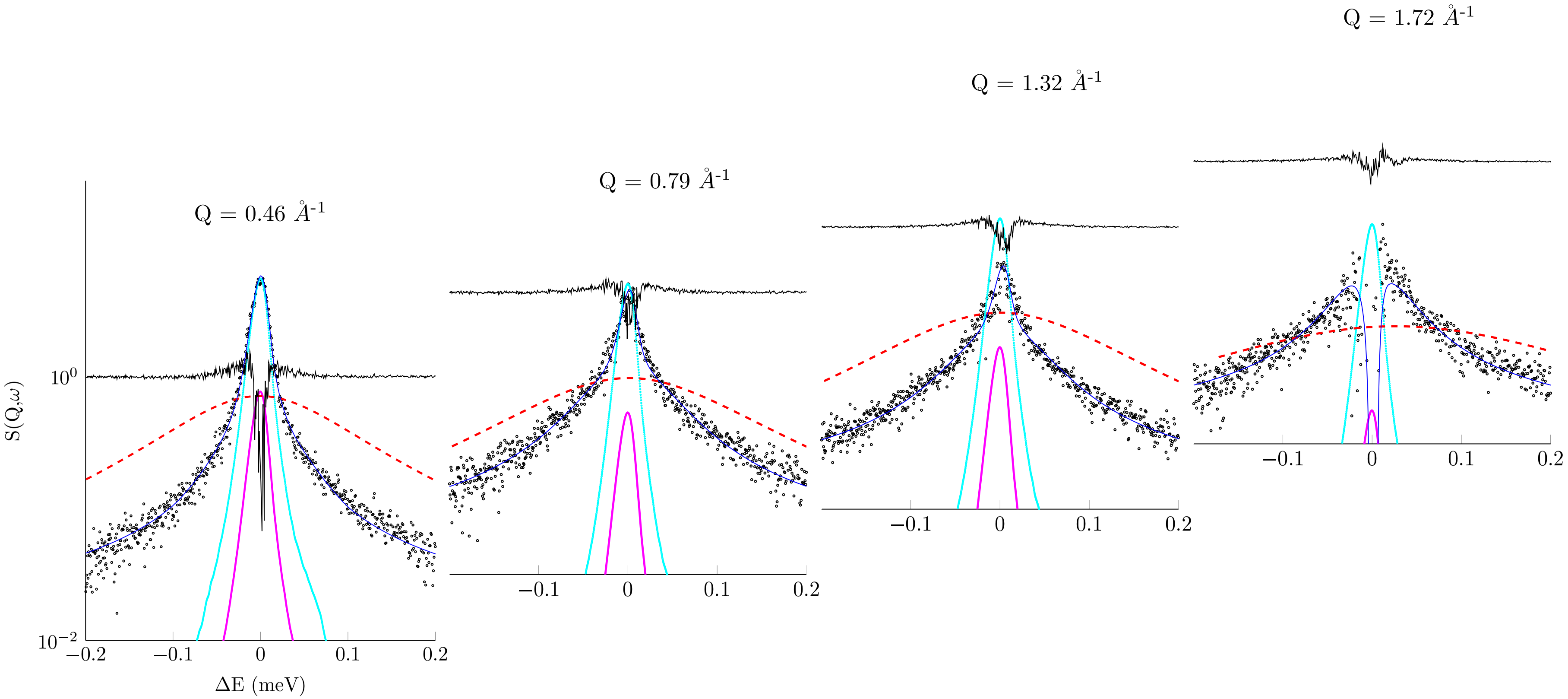

Figure 6.10: All components of QENS fits to a range of spectral groups for the data collected for Ca-laponite(EL) at 60 K, showing the Q-dependent broadening of the quasielastic peak (dashed red line). For this sample, problems arose at higher Q (top right) where the signal, particularly the elastic signal, is greatly diminished. However, the width of the fitted quasielastic peak appears to be approximately correct. The measured data is represented by black dots, the fit is shown as a solid blue line and the light blue line shows the instrumental resolution. The Lorentzian components of the fit are the elastic peak (magenta line) and the single quasielastic peak. Note that the y-axis is a log scale and the components are not properly scaled. The residuals (solid black line) are shifted by 1, to avoid them obscuring the data.

Two techniques were used to obtain the relative elastic and quasielastic intensities: elastic window integration and analysis of the fit components. Both use integration under the measured curve of counts. In elastic window integration, an energy range of 0-0.03 meV, covering 99% of the elastic window, is used to distinguish elastic from quasielastic scattering, estimated from the rest of the energy range (0.03-1.2 meV). The area under the fitted components is a more accurate way to separate elastic from quasielastic, but can only be performed on statistically sound data having long counting times.

6.3.3 IN4

Beamtime on the high resolution TOF inelastic neutron scattering (INS) spectrometer, IN4 [196], at the Institut Laue Langevin (ILL) facility in Grenoble, was awarded for three days in November 2010. The geometry of this instrument is illustrated in Figure 6.11. The resolution of this instrument varies systematically with energy, but follows a Gaussian form. Measurements were taken using a high-flux Cu_{111} monochromator and an incident wavelength of 1.968 Å, with time-focussing optimised for the 15 meV energy-transfer region. This gave a FWHM elastic ($\frac{\Delta E}{E_i}$) resolution of 1.05 meV, where E_i is the incident neutron energy, and a flux of 25% of the maximum (1.25 x 10^5 cm^{-2} s^{-1}), giving 12.6 counts per second per detector. This resolution was deemed to be sufficient for inelastic measurements, but not for resolving slower QENS motions.

IN4's resolution function and detector efficiencies were determined using a cylindrical canister of pure vanadium. IN4 uses aluminium cells to hold the sample in a solid cylindrical geometry, instead of the cylindrical shell format used for IRIS. For the Ca-laponite (RD) sample, a similar gas rig to that used on IRIS was used for gas dosing, including a capillary heater to prevent freezing in the capillary pipes. The volumes were calibrated as per the IRIS experiment and leak tests were performed to ensure that any pressure drop at supercritical temperatures can be entirely attributed to adsorption. For lower temperatures, capillary condensation may play a role and therefore the capillary pipes were heated and suitable equilibration times were allowed. A dry mass of 9.35 g of Ca-laponite (RD) was loaded and placed under a dynamic vacuum for at least an hour using a turbo pump to bring the pressure down to 2 x 10^{-6} mbar. The sample dosage was calculated to provide only one H_2 per Ca^{2+} and this was carefully controlled using pressure as an indicator of the

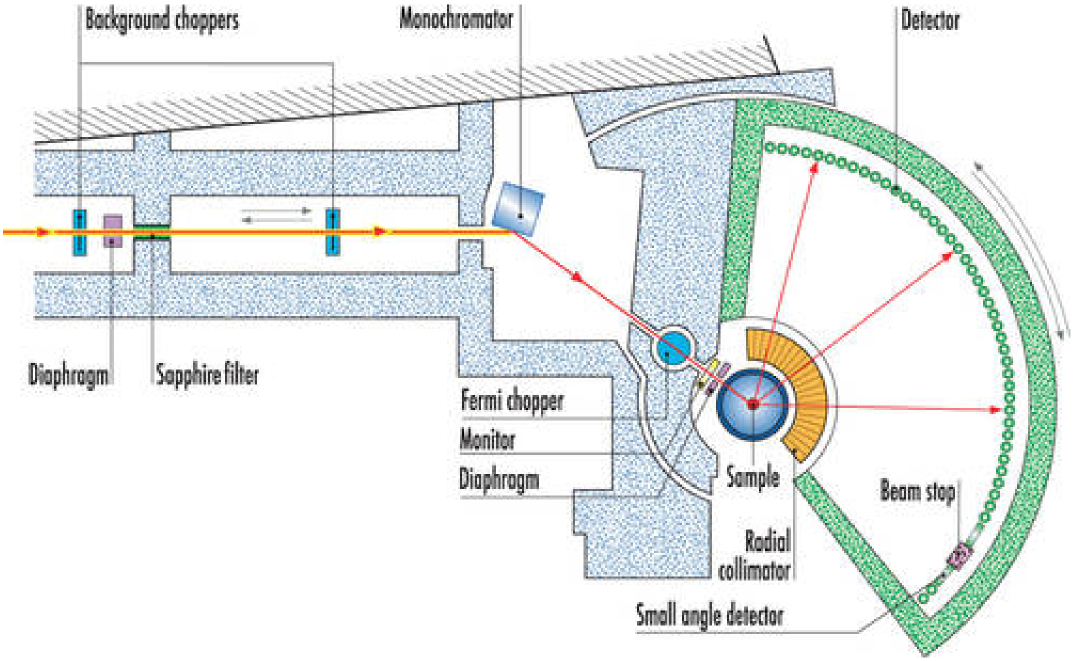

Figure 6.11: (From the ILL website.) The IN4 direct-geometry TOF spectrometer at the Institut-Laue-Langevin facility in Grenoble, France.

number of moles of H_2 and the drop in pressure to indicate how many millimoles were adsorbed to the sample. The required number of moles of H_2 gas was stored in a holding bottle, taken directly from a standard cylinder of ultra-high purity gas at a pressure of 10 bar and introduced to the sample cell at 50 K during dosing. The deuterated samples of Na-laponite (RD) and Ca-laponite (EL), 9.90 g and 8.27 g respectively, were measured at a later date, with different gas dosing equipment: H_2 dosages were very precisely controlled with the use of a Hiden Isochema HTP. Due to time constraints, only a single dose could be achieved on Na-laponite (RD), that of (4 H_2:Na^+), while Ca-laponite (EL) was subjected to a range of doses (1, 2, 3, 4 and 9 H_2:Ca^{2+}). The adsorption amounts corresponding to each measurement were calculated from the pressure differential for all samples, temperatures and loadings. However, in the absence of an accurate chemical formula for Ca-laponite (EL), the loading calculations for this sample may not be accurate. It is likely that, in order to achieve its higher surface charge, this sample has a higher density of cations, reducing the H_2:Ca^{2+} ratios.

The aim of this experiment was to investigate the quantum mechanical features of hydrogen binding in laponite. To this end, the inelastic neutron scattering spectra were measured on the samples in vacuum and also under a low- to mid-pressure H_2 atmosphere, at corresponding temperatures. For Ca-laponite (RD), five temperatures were measured: 5 K, 10 K, 25 K, 50 K and 77 K. For Na-laponite (RD) and

Ca-laponite (EL), four temperatures were measured: 6 K, 9 K, 23 K and 48 K. At each temperature, a reasonable equilibration time was allowed before more than one hour of counting at a flux of 1.25 x 10^5 cm^{-2} s^{-1} was performed, to ensure good statistics.

The incoherent scattering function, $S_{inc}(\bar{\mathbf{Q}}, \omega)$, was extracted using the ILL's Large Array Manipulation Program (LAMP) [197], [198]. The counts which formed part of the same data were added together, using only those with suitably stable temperatures. These data were normalised and a constant background removed. Corrections were made for detector efficiencies, removing any which were non-functional. For this experiment, the detectors at 30°, 66° and 117° were known to be damaged. The TOF data was suitably grouped and converted to energy transfer, before being appropriately rebinned, however LAMP does not account for detailed balance. Since the choppers filter out all harmonics for Cu_{111}, all visible features in the corrected data can be considered to be valid. Fitting routines within LAMP were used, to determine whether the peak shapes were Gaussian or Lorentzian. The LAMP data was extracted into ASCII files, imported into Matlab and analysed using Mfit v4.2 [195] to fit the minimum number of Gaussians.

For Ca-laponite (RD), an incident wavelength of 1.968 Å was used, giving a FWHM resolution of 1.05 meV. For this wavelength, the maximum energy transfer of the neutron to the sample is approximately 21 meV, resulting in neutrons with no kinetic energy, requiring infinite time to reach the detectors. This effect results in an intensity drop-off at higher energy ranges on the Stoke's side of the spectrum, which is difficult to correct for. Measurements close to this maximum are therefore less reliable and the fittings were restricted to an energy window of 5-20 meV. Below 5 meV, spectral features were largely obscured by the quasielastic broadening of the elastic line. For the Na-laponite (RD) and Ca-laponite (EL) samples, the incident wavelength was 1.773 Å, for which the FWHM resolution is 1.07 meV. The maximum energy transfer possible in this case is approximately 26 meV, allowing the fitting window to be extended slightly, to 10-23 meV. However, the interpretation of peaks appearing near the high-energy edge of this window should be treated with caution.

The results presented in Chapter 11 all lie on the neutron energy loss side (the Stoke's side) of the spectrum. On this side, the resolution width is not expected to vary much and all inelastic peaks should have a similar width. Therefore the fits were constrained to use a fixed width for all peaks, in order to limit the variability of the fits: too many unconstrained parameters increase the chances of the fit converging on false minima which are sensitive to the starting parameters. It is better, in this case, to constrain the peak widths, because the heights and centres of the peaks represent physical data relevant to the hindered rotor model, while the widths only reflect the resolution of the instrument. However, the value of the fixed width was not chosen arbitrarily: the fits were run for a range of fixed width values and the value which gave the best fit was selected. Through this method, a width of between 2.35 and 2.73 meV was found to give the best fits for the Na-laponite (RD) and Ca-laponite (EL) samples, which is about twice the width expected for IN4's resolution.

The fits for Ca-laponite (RD), however, required much narrower peaks, with widths of 1.41 meV. In addition, for higher loadings of Na-laponite (RD) and Ca-laponite (EL), the inclusion of two narrow peaks, also with FWHM of ~1.41 meV, is required to adequately describe the spectral features. This suggests that the widths of the fitted peaks may be too broad. The residuals, shown in Figure 11.1, also appear to hint at more narrow peaks being present in the data, suggesting a spectral decomposition of a larger number of hindered rotor peaks with FWHM of ~1.40 meV. This was attempted with Gaussians constrained only by width and an example is given in Figure 6.12a, showing that more than twice as many peaks are required. In this case, it is possible to include the free rotor peak, however when the peaks are constrained to form hindered rotor pairs, the fit quality deteriorates, as shown in Figure 6.12b.

In order to minimise fitting parameters, fewer, broader peaks were used and the resulting fits, presented and discussed in Chapter 11, are satisfactory and also comply with the physical model. It is possible that the additional narrow peaks are artefacts caused by the rigidity of the constraints for the quantum-paired hindered rotor peaks. For each pair of peaks, their positions relative to each other cannot easily be allowed to vary in the fitting algorithm, but in real data, some uncertainty would be expected in the splitting between these Gaussian pairs. These peaks could then be the remainders from imperfectly overlapping peaks. A third possibility is the shape of the inelastic peaks: if they should be Lorentzian, rather than Gaussian, the narrow peaks could be the unfitted Lorentzian peak tips.

Figure 6.13 shows two examples of the background readings for the three samples, also showing Gaussian peak fittings to two visible spectral features. This background was subtracted from the measurements of the clay immersed in H_2, to isolate the signal from any adsorbed H_2.

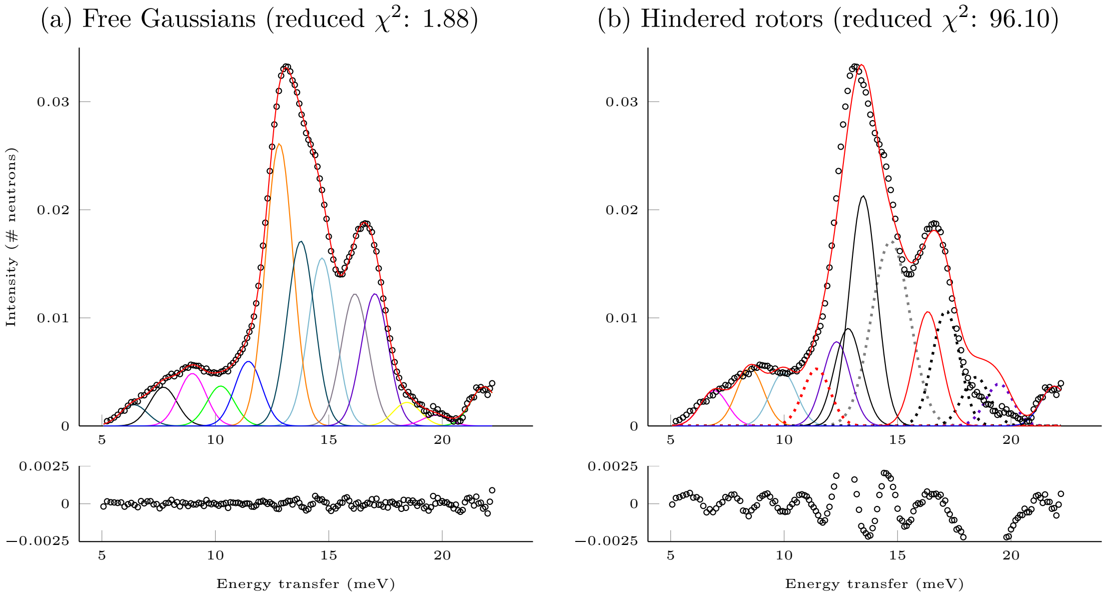
(a) Free Gaussians (reduced χ^2: 1.88)

(b) Hindered rotors (reduced χ^2: 96.10)

Figure 6.12: Attempts at fitting narrower peaks, with widths matching the expected resolution for IN4 with incident wavelength 1.773 Å, to the spectrum for Na-laponite (RD), measured at 6 K. The fit for unconstrained Gaussian peak reproduces the spectrum very closely, however these peaks cannot be easily constrained to fit the quantum model for the H_2 hindered rotor, as the fit statistics show. The hindered rotor pairs are colour-matched: the solid lines represent the degenerate m_J=±1 peaks and the dashed lines show the non-degenerate m_J=0 peaks.

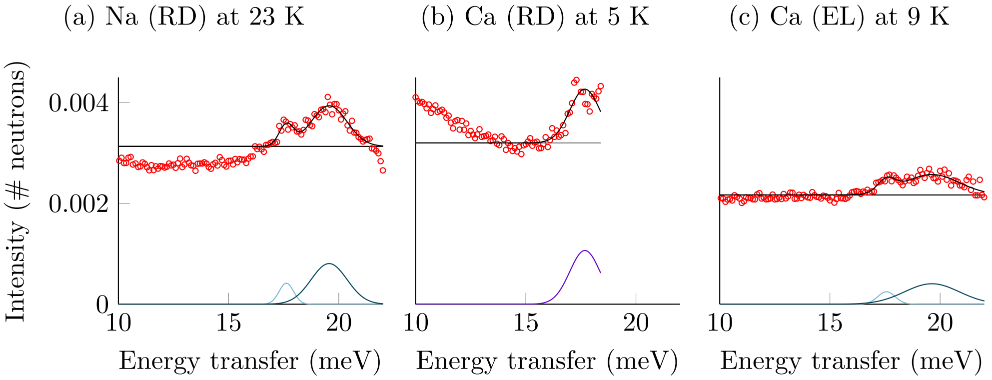
(a) Na (RD) at 23 K

(b) Ca (RD) at 5 K

(c) Ca (EL) at 9 K

Figure 6.13: Measurements of the clay substrate in vacuum, showing two peaks, fitted to Gaussian peaks. The signal from the clay itself was subtracted from subsequent measurements at matching temperatures in an H_2 atmosphere.

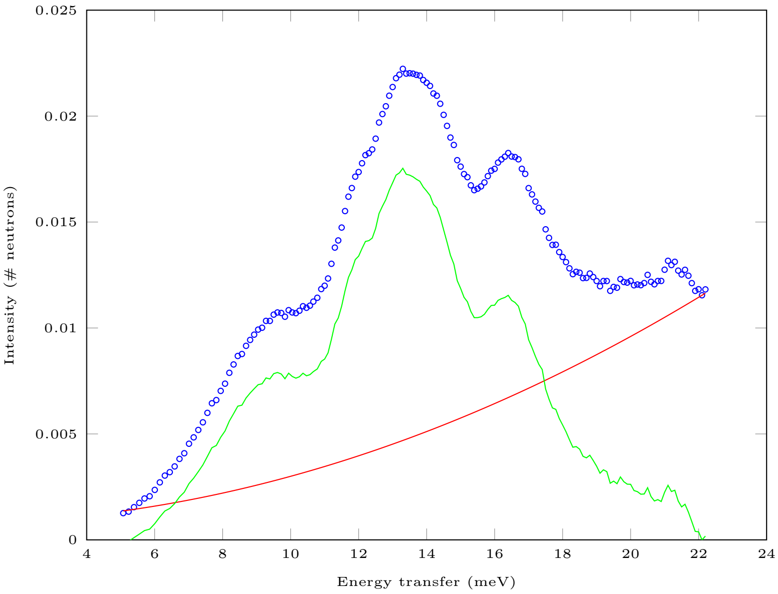

Figure 6.14: A second-order polynomial function, shown by the solid red line, was fitted to the data (blue circles) by estimation and subtracted from the data. The resulting signal is displayed in green.

After subtraction of the background, further treatment was necessary to remove a sloping background from the isolated H_2 signal. Early fits to the data, in which the widths of the fitted peaks were unconstrained, suggested the presence of a very broad peak, spanning the entire window. Since there is no physical reason why such a broad peak would be present, it was thought to suggest the presence of a sloping background, better approximated by a second-order polynomial function. This was fitted to the low and high energy extremes of the fitting region by eye, an example of which is given in Figure 6.14. The removal of a polynomial background, representing the recoil line of hydrogen, is a common procedure in studies of hydrogen [199] [45] [200] and was therefore considered to be appropriate in this case.

The Gaussian peak shape was chosen after comparisons of a fit to a series of Lorentzians with a fit to a series of Gaussians. The Gaussian fits produced a much better fit, so this shape was used for all subsequent fits. The principle behind the hindered rotor peak fits was to first attempt a fit to a set of Gaussian peaks, constrained only to be a minimum even number. A new pair of peaks was only introduced if their inclusion made a significant improvement to the fit. Once the number of hindered rotor pairs was determined by this method, comparing across samples, temperatures and loadings, the fitting model was constrained to follow the quantum mechanical expectations of a ratio of energy offset from the free rotor peak centre (14.74 meV [37]) of 1:2 and an amplitude ratio of 2:1 for the $m_J=\pm1$ to the $m_J=0$ bands. The residuals from these fits were examined, to see if any peaks had been omitted. This led to the inclusion of two single, narrow Gaussian peaks in the higher loadings of the Na-laponite (RD) and Ca-laponite (EL) samples, which greatly improved the fit. The inclusion of a single free rotor peak was attempted for all fittings, but in all measurements of Na-laponite (RD) and Ca-laponite (EL), this resulted in a much larger reduced χ^2 value. In the data from Ca-laponite (RD), a free rotor peak greatly improved the fit for all temperatures.

The starting parameters for the fits to the spectra of the sample at the lowest loading of < 1 H_2:Ca^{2+} were taken from the results of fits to the higher loading of 1 H_2:Ca^{2+}. This was necessary in this case, because the data for the lowest loading are more noisy, since the signal from fewer H_2 molecules is weaker and the fits are thus prone to converge on a variety of possible minima. All other fits had starting parameters which were selected from the best fits from a number of attempts. The validity of these fits is strongly supported by their consistency of position and shape across all temperatures and across all loadings for this sample, despite a variation in overall spectral shape. The consistency between samples also supports the results of all fits made and validates the constraints chosen. These consistencies can be seen in the discussion on the results, in Chapter 11.

7. PILLARING TEMPERATURE

7.1 Controlling water content

In order to prepare the sample in a sub-monolayer state, approximately 1 H_2O per cation, an estimate of the required drying temperature was obtained using thermogravimetric analysis (TGA). Only mild temperatures are required to remove most of the interlayer water molecules, because they are loosely bound to each other through a hydrogen bonding network and to the charged inner surfaces of the clay interlayer. The water around the cations requires more energy to remove, due to stronger bonds in the solvation shells. Figure 7.1 shows the weight loss as a percentage of the total amount loaded, as the temperature is gradually increased from ambient to 573 K, under N_2 flow at ambient pressure. Beyond 473 K, structural water is typically lost in smectites [201], so the total amount of interlayer water present in the sample at ambient conditions can be estimated from the weight lost up to this temperature - highlighted for each sample in Figure 7.1. Also shown are the temperatures associated with sufficient weight loss to leave each sample with approximately 1 $H_2O{:}Ca^{2+}$. The Ca- and Mg-laponite forms require the highest temperatures for sufficient drying, demonstrating that their higher valencies give a stronger binding energy to their solvation shells.

The TGA data provides a rough estimate of the drying temperature required per sample, but the drying temperature may vary under vacuum. Therefore the water content of Ca-laponite (RD) was measured using thermogravimetric analysis on a Hiden Isochema Intelligent Gravimetric Analyzer (IGA). Figure 7.2a shows the sequence of heating the sample from ambient to 473 K, but most of the weight loss, from a total of 191.274 mg at loading, had already occurred during the period of gradual evacuation prior to heating. Figure 7.2b shows heating of a fresh batch of the same sample to 413 K. The total amount of water in the sample at ambient

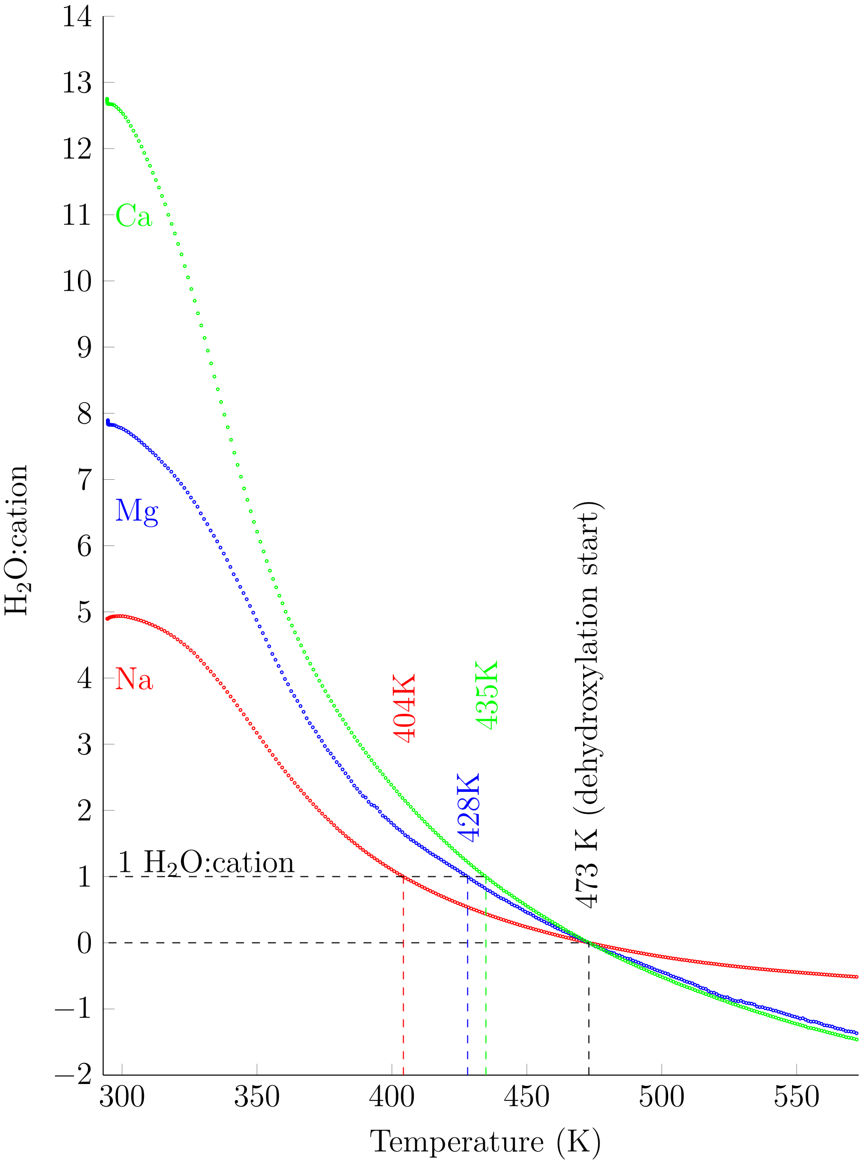

Figure 7.1: Weight loss measured for three cation-exchanged forms of laponite (RD) at ambient pressure using a Thermogravimetric Analyser. The weight loss at 473 K is assumed to represent the total proportion of interlayer water, by weight. Comparing this with the weight loss at lower temperatures gives an indication of the remaining interlayer water, from which the H_2O:Ca^{2+} ratio can be determined.

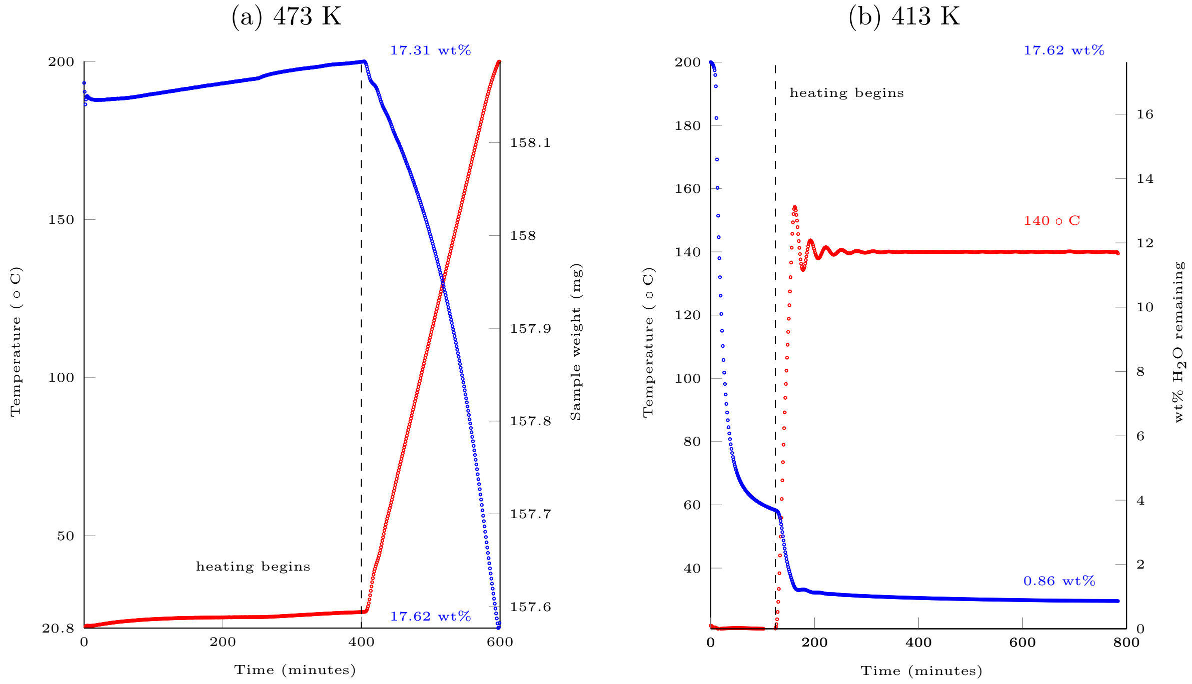
(a) 473 K

(b) 413 K

Figure 7.2: Weight loss measured under vacuum using a Hiden Isochema Intelligent Gravimetric Analyser (IGA). 7.2a shows the weight loss for heating a sample of Ca-laponite (RD) to 473 K. Note that 191.274 mg of sample was loaded and most of the weight loss occurred during the gradual evacuation, before heating (not shown here). The total weight loss calculated was 17.62 wt% H_2O. 7.2b shows the weight loss for a second sample of Ca-laponite (RD) gradually evacuated and heated to 413 K for more than ten hours. The maximum weight loss calculated in 7.2a is used to scale the right-hand vertical axis of 7.2b to the corresponding temperature on the left axis. Assuming all interlayer water is lost at 473 K, these measurements show that the remaining interlayer water content of the sample is 0.9 wt% H_2O in vacuum at 413 K.

was calculated to be 17.62 wt% H_2O and this was used to estimate the amount remaining at 413 K under vacuum: 0.9 wt% H_2O (approximately 1.05 H_2O:Ca^{2+}).

In the IRIS and IN4 neutron experiments, a certain amount of exposure to ambient air was unavoidable, since rapid *in situ* drying facilities were not available. The samples were therefore dried in a vacuum oven and transferred to the sample cell, after grinding and weighing. As mentioned in Section 6.1.4, it was observed that while weighing these samples, the weight increased by a few micrograms per second. In order to estimate the rate of reabsorption of interlayer water by the sample after drying, a sample of Ca-laponite (RD) was heated to the desired temperature in vacuum in an IGA and then re-exposed to air, while measuring the weight gain. A reabsorption rate of 0.04 mg min^{-1} was estimated. Sample exposure time was no more than 30 minutes, after which a maximum of 0.02 water molecules per Ca^{2+} may have been reabsorbed. This was therefore unlikely to have a significant effect on the results.

7.2 The effect of temperature on *d*-spacing

Taking XRD measurements of a sample of laponite while raising its temperature from ambient to around 473 K allows determination of the temperature required to achieve a particular *d*-spacing, such as that needed to allow H_2 to penetrate the clay interlayers. The Bragg peak representing the *d*-spacing of a clay falls within the same region as the scattering from the surface and this background signal, discussed in Section 5.3.3, must first be removed before the *d*-spacing can be determined. The desired *d*-spacing for laponite is approximately 12.5 Å, giving an interlayer spacing of ~3 Å after subtraction of the clay layer height, estimated from the crystallographic dimension of 9.43 Å for talc [134].

7.2.1 Background removal from XRD data

As for the neutron diffraction data obtained using NIMROD, the small-angle background scattering in the X-ray data was matched against different powers of Q, ranging from 2 to 4. While Porod scattering is not, strictly speaking, a background feature, being caused by scattering from the surface of the sample, it was removed along with the background, because it conceals the feature of interest. The combination of a constant, a decaying fourth power law for Q (amplitude ranging from 1.5 to 4) and a broad Gaussian (amplitude ranging from 3,500 to 10,000; FWHM between 10 and 12 $Å^{-1}$ and centred at $Q = 0$) was found to give the best fit. Since the laboratory XRD is not specifically optimised for small angle scattering measurements, the broad Gaussian may be an instrumental background feature. The total fit was estimated using Solver in Excel and after subtraction, a clear Gaussian peak remained from which the *d*-spacing could be extracted.

Figure 7.3 shows the typical background removal procedure for the X-ray data collected on the Na-laponite (RD) sample for four of the nine temperatures measured. Background removal reveals the (001) diffraction peak, which was fitted using a Gaussian function. The centre of this peak indicates the *d*-spacing of the clay, presented on each graph in Figure 7.3. Similarly, Figure 7.4 shows typical background fits, using the same background removal technique, for the X-ray data collected on the Ca-laponite (RD) sample for the same four temperatures.

It should be noted that this technique is prone to a number of errors. Firstly, there are many variables involved in reconstructing the background for removal and the

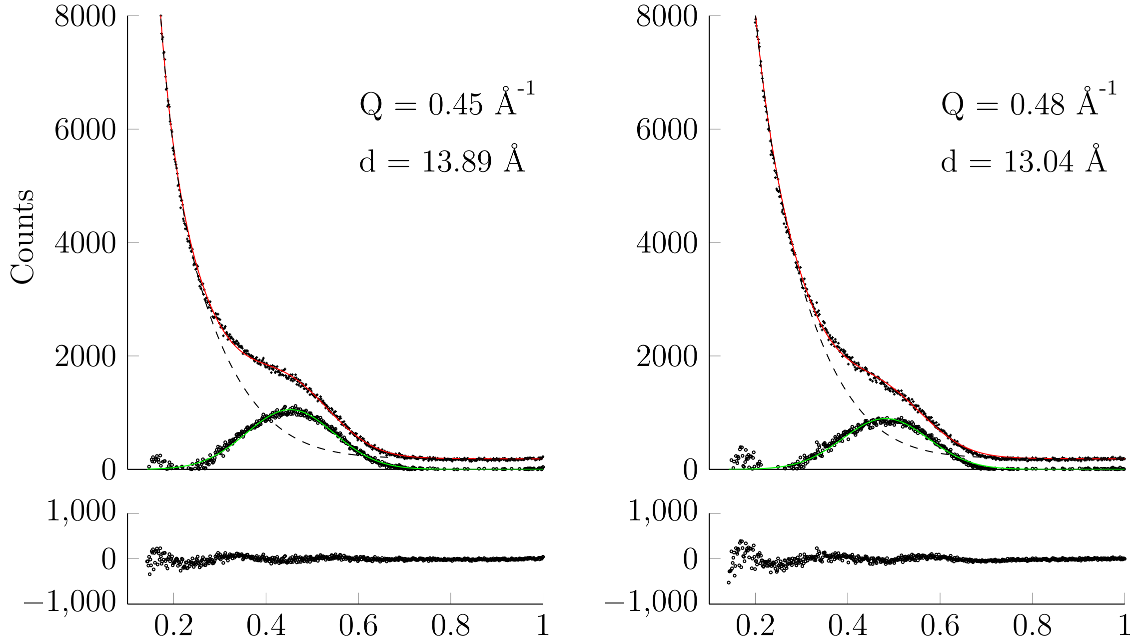

(a) 355 K

(b) 415 K

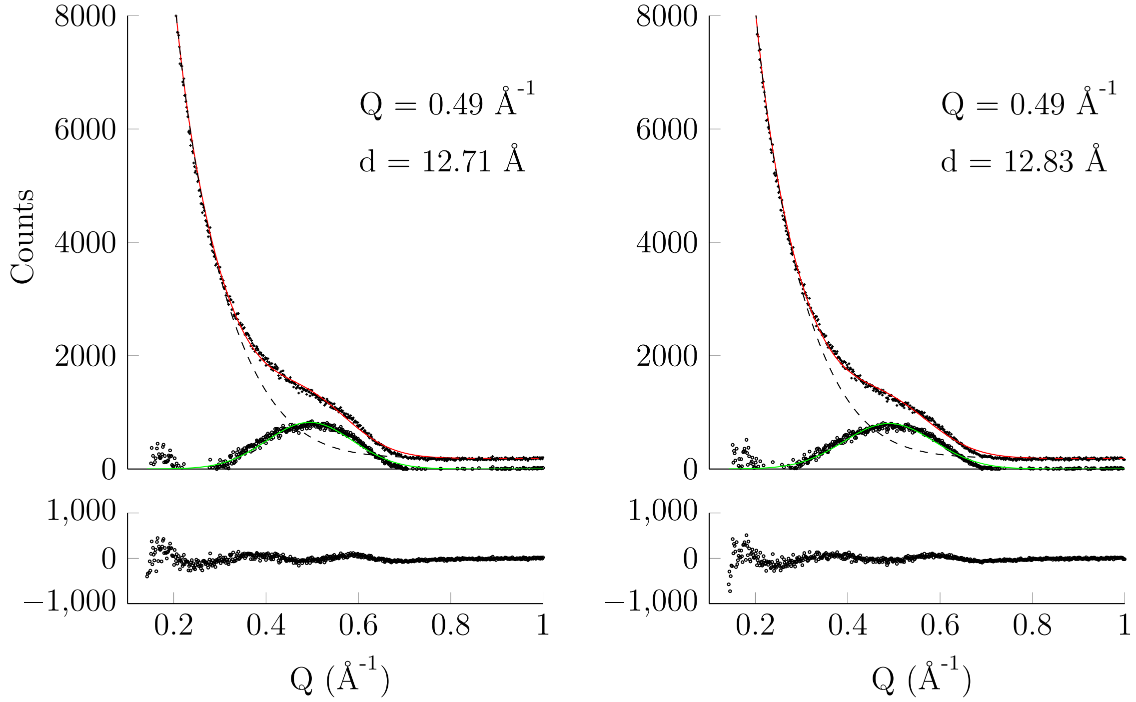

(c) 475 K

(d) 300 K

Figure 7.3: Typical XRD fits for the Na-laponite (RD) sample at four temperatures, showing the data (black dots), the total fit (solid red line) and the estimated background removed (dashed line) from the data in order to fit the Gaussian (solid green line) representing the (001) diffraction peak. The backgrounds are a combination of a decaying fourth power law for Q, with amplitude ranging from 3 to 5, a Gaussian peak centred at $Q = 0$ with amplitude ranging from 4,000 to 9,000 and a FWHM of between 13 and 14 Å^{-1} and a constant, values ranging from 176 to 179, all figures increasing with temperature. The room temperature measurement, Figure 7.3d, was taken after heating and subsequent cooling. The residuals are shown below each temperature.

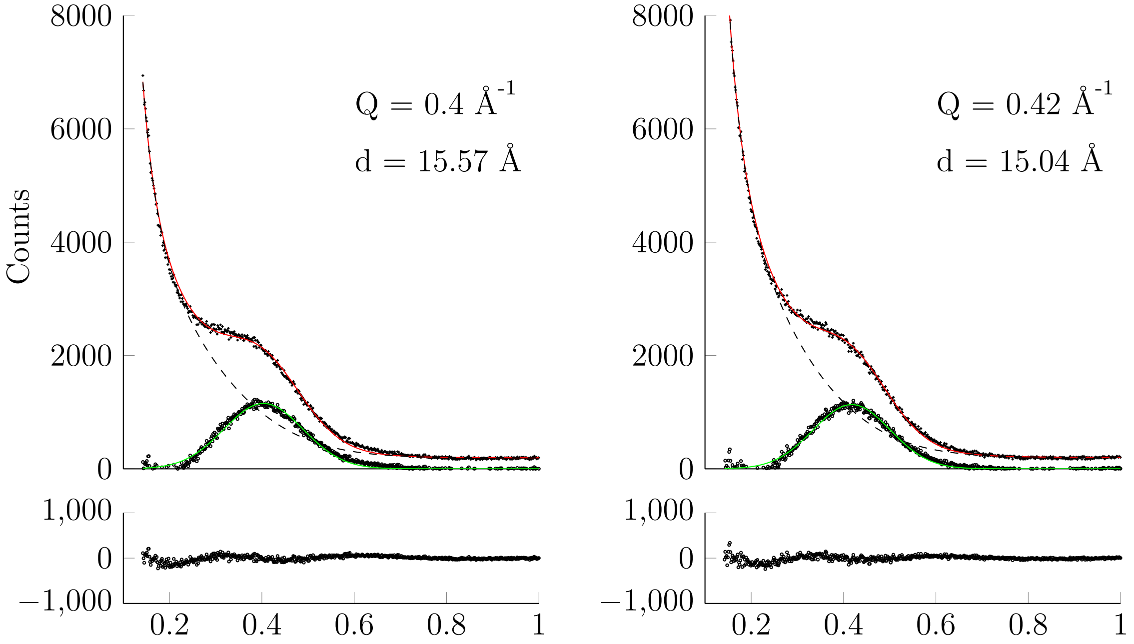

(a) 300 K

(b) 355 K

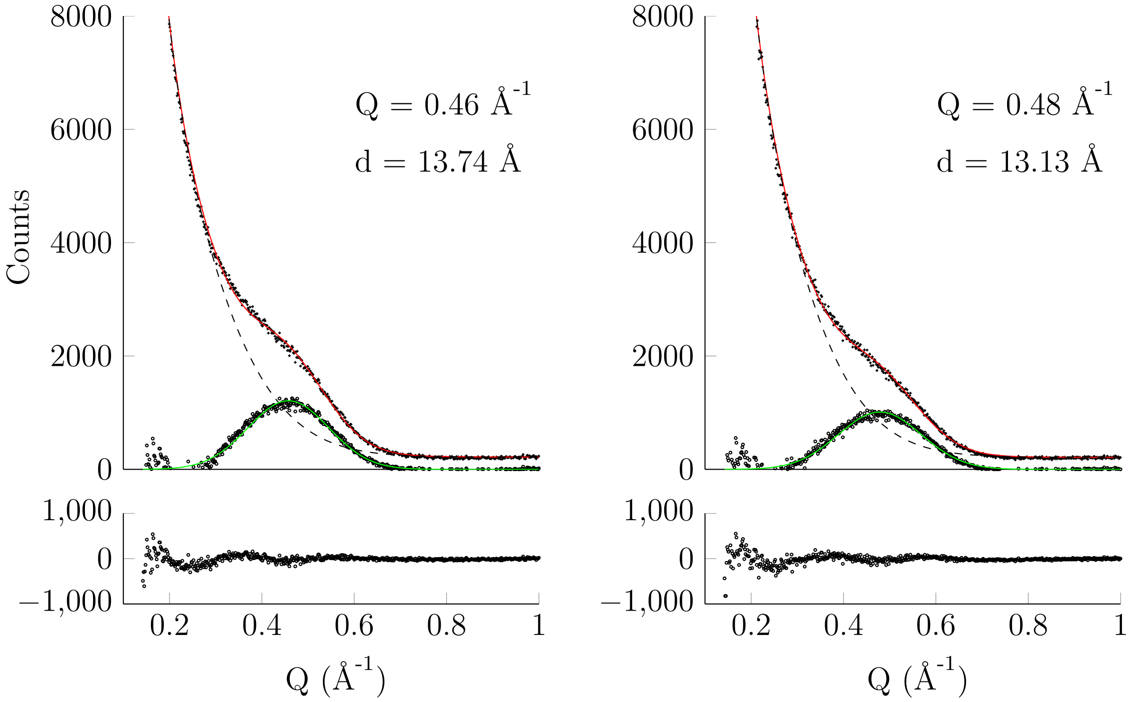

(c) 415 K

(d) 475 K

Figure 7.4: Typical XRD fits for the Ca-laponite (RD) sample at four temperatures, showing the showing the data (black dots), the total fit (solid red line) and the estimated background removed (dashed line) from the data in order to fit the Gaussian (solid green line) representing the (001) diffraction peak. The backgrounds are a combination of a decaying fourth power law for Q, with amplitude ranging from 1.5 to 4, a Gaussian peak centred at $Q = 0$ with amplitude ranging from 4,000 to 10,000 and a FWHM of between 10 and 12.6 Å^{-1} and a constant, values ranging from 194 to 205, all figures increasing with temperature. The room temperature measurement, Figure 7.4b, was taken before heating. The residuals are shown below each temperature.

combination of functions chosen to represent the background may not be valid. The full range of data could not be fitted and the fit varies slightly depending on the size of the data range selected for fitting. Secondly, the imprecision in this fit impacts the fitting of the Gaussian peak to the remainder, thus the measured value of the *d*-spacing is subject to error. However, the trend of decreasing in *d*-spacing with temperature is a well-known phenomenon of smectite clays [128] and this trend is apparent in this data set.

7.2.2 Treatment temperature selection

Figure 7.5 shows all of the Gaussian fits to the (001) peak in the diffractograms measured for Na-laponite (RD), while Figure 7.6 shows similar fits for Ca-laponite (RD). The full set of measured Q values and their associated *d*-spacings for each temperature for both samples are presented in Table 7.1. The average *d*-spacing decreases as the temperature rises, due to interlayer water evaporating from the porous clay, thereby removing pillar molecules holding the interlayers apart. In the measurements on Na-laponite (RD), the room temperature measurement was taken after subsequent cooling showing a slight increase in *d*-spacing as the clay reabsorbs water. At temperatures up to 473 K, the water loss is reversible [201], therefore if this sample were remeasured after an adequate time under ambient conditions, the *d*-spacing should recover its preheating value of approximately 14-15 Å [138].

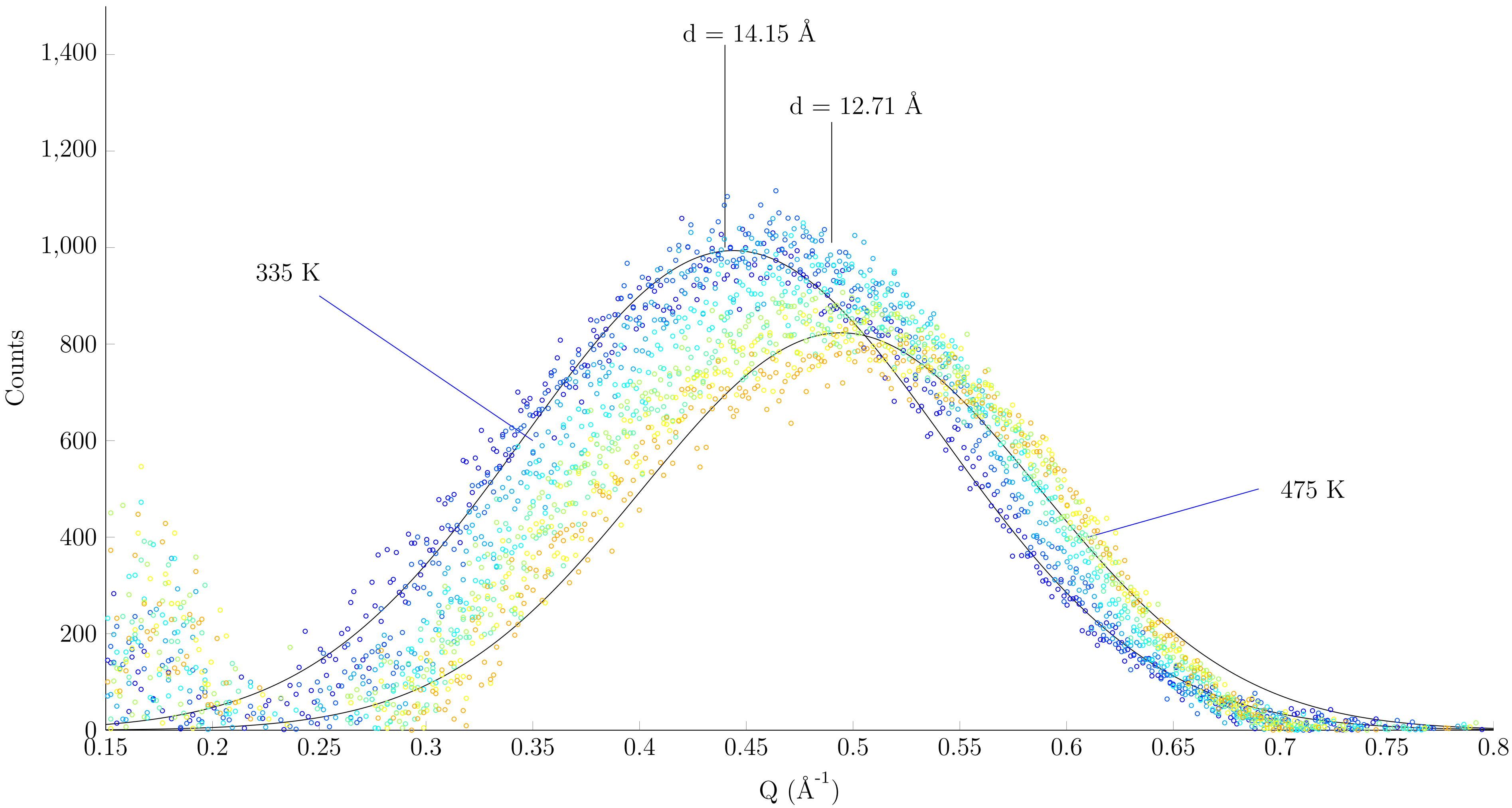

Figure 7.5: Temperature-dependency of the *d*-spacing for heated Na-laponite (RD). The background has been subtracted as described in Section 7.2.1 and the Gaussian fits to the XRD data at the highest and lowest heated temperatures (335 to 475 K) are shown as solid black lines. For this sample, the room temperature measurement was only performed after heating to 475 K and subsequent cooling and is not displayed. The results of the fits are presented in Table 7.1.

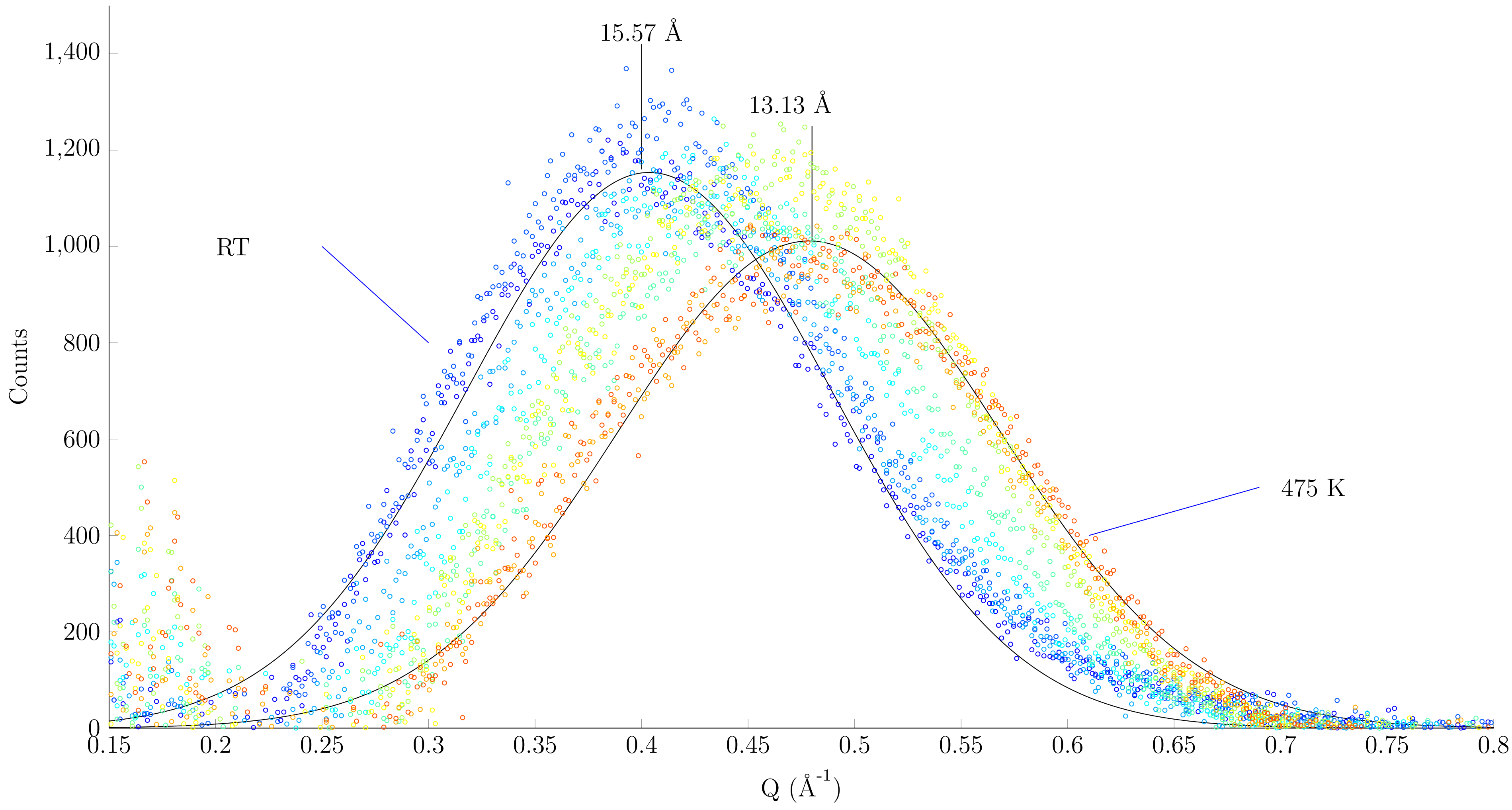

Figure 7.6: Temperature-dependency of the *d*-spacing for heated Ca-laponite (RD). The background has been subtracted as described in Section 7.2.1 and the Gaussian fits to the XRD data at the highest and lowest measured temperatures (room temperature to 475 K) are shown as solid black lines. The results of the fits are presented in Table 7.1.

Sample	**Temperature (K)**	**Q (Å^{-1})**	**D (Å)**	$\chi^2_{reduced}$
Na-laponite (RD)	335	0.444	14.155	2.86E+03
	355	0.452	13.890	3.55E+03
	375	0.464	13.543	5.90E+03
	395	0.473	13.273	7.28E+03
	415	0.482	13.036	6.99E+03
	435	0.482	13.041	8.47E+03
	455	0.489	12.841	8.74E+03
	475	0.494	12.711	9.40E+03
	RT	0.490	12.832	8.35E+03
Ca-laponite (RD)	RT	0.404	15.570	3.27E+03
	335	0.408	15.404	3.55E+03
	355	0.418	15.044	3.47E+03
	375	0.434	14.479	5.91E+03
	395	0.453	13.873	5.88E+03
	415	0.457	13.736	8.15E+03
	435	0.464	13.538	7.20E+03
	455	0.475	13.239	7.10E+03
	475	0.479	13.127	1.02E+04

Table 7.1: *d*-spacing extracted from the (001) peak in the diffractograms for Na- and Ca-laponite (RD), measured in air while raising the temperature from ambient to ~473 K. In the Na-laponite sample, the room temperature measurement was taken after subsequent cooling, where some water may have been reabsorbed. The χ^2_{red} values are very high, due to the number of fitting parameters needed to remove the low-Q background.

From these measurements, it is clear that a pretreatment temperature of slightly more than 473 K is required for the sodium form, in order to attain a *d*-spacing of ~12.5 Å, the size of laponite containing a single layer of interlayer water. Higher temperatures were not measured, because this is the onset of dehydroxylation [202], the loss of structural water from the sodium form of laponite.

For the Ca-laponite (RD) sample, Figure 7.6, the room temperature measurement was taken before heating, showing the ambient *d*-spacing of this form of laponite, containing roughly two layers of interlayer water, to be 15.57 Å. This is slightly below the 16 Å reported in the literature [203] [138] and the difference could be due to experimental error or to a difference in the relative humidity. Again, an excess of 473 K appears to be required to reduce the *d*-spacing to 12.5 Å, but higher temperatures were not measured, because dehydroxylation is expected to begin at this point. As indicated by the TGA data in Section 7.1, the temperatures required to reach the desired *d*-spacing in the calcium form are higher than those for the sodium form, reflecting the fact that water binds more strongly to the divalent Ca^{2+} than to Na^{+}. These data do not give a conclusive indication of the temperature required, because these measurements were not performed in vacuum. Therefore the dehydration temperatures of 403-433 K suggested by the TGA and IGA data were selected for drying the samples before running isotherms or neutron scattering experiments.

7.3 The effect of preheating on H_2 uptake

Samples were outgassed and subjected to a range of pretreatment conditions under vacuum. After each pretreatment procedure, low-pressure gravimetric isotherms at 77 K were collected on the same sample and compared to assess any differences in uptake. Figure 7.7 compares the adsorption parts of these isotherms for the two samples measured: Na- and Ca-laponite (RD). The sodium form appears to show some pattern, as the sample which is only outgassed, with no heating, shows a markedly lower uptake than for all other pretreatment conditions and a serial increase in uptake is observed for 413, 423, 433 and 438 K, however the isotherms for the highest temperature pretreatment, 458 K is significantly less than for 438 K and the isotherm taken after heating to 373 K, obscured by the blue diamonds representing the post-433 K isotherm, does not fit into this series as expected.

For the calcium form there is no discernible pattern, which may be due to the fact that higher temperatures are needed to remove enough interlayer water to make a difference, as suggested by the XRD with *in situ* heating results in Section 7.2.2 above. In both samples, the highest temperature pretreatment reduced the uptake, but it is not clear whether this is due to the onset of dehydroxylation with associated collapse of some of the interlayers, or due to the unreliability of these measurements. It is observed that not all of the isotherms start at the origin, making them harder to compare accurately. In some cases, this was due to the temperature being higher than the setpoint for the first one or two points, leading to an incomparable assessment of the adsorbed amount. The error bars are calculated with regard to the variation in temperature from the setpoint only. They tend to be much larger for the first few points of adsorption isotherms, because temperature equilibration takes longer under vacuum and, because it is difficult to predict the length of time required to reach temperature stability in vacuum when running automated isotherms, the temperature is likely to be much further from the setpoint at the start of the adsorption isotherm. Equilibrium times of about ten hours were used, where practicable.

The fact that not all isotherms start at the origin indicates that there is some anisotropic behaviour. Each adsorption-desorption process appears to alter the system, shifting the starting point and affecting the subsequent cycle. Various mechanisms may cause this, such as a “flushing” effect, in which some water is displaced from the interlayers with each cycle of intercalation and desorption of hydrogen. Some hydrogen molecules may become trapped within interlayers, particularly if enough water is removed to cause partial collapse of the structure. If a small fraction is very strongly bound to the surface, then the desorption temperatures may not dislodge them. For example, if the first molecules intercalating into the interlayers do cause the slight interlayer expansion suggested by the results in Section 8.1, then this suggests a strong attraction between the cations and these initial intercalants. Subsequent adsorptions may benefit from this expansion, since the interlayers will be sufficiently pillared by the earlier adsorbant population.

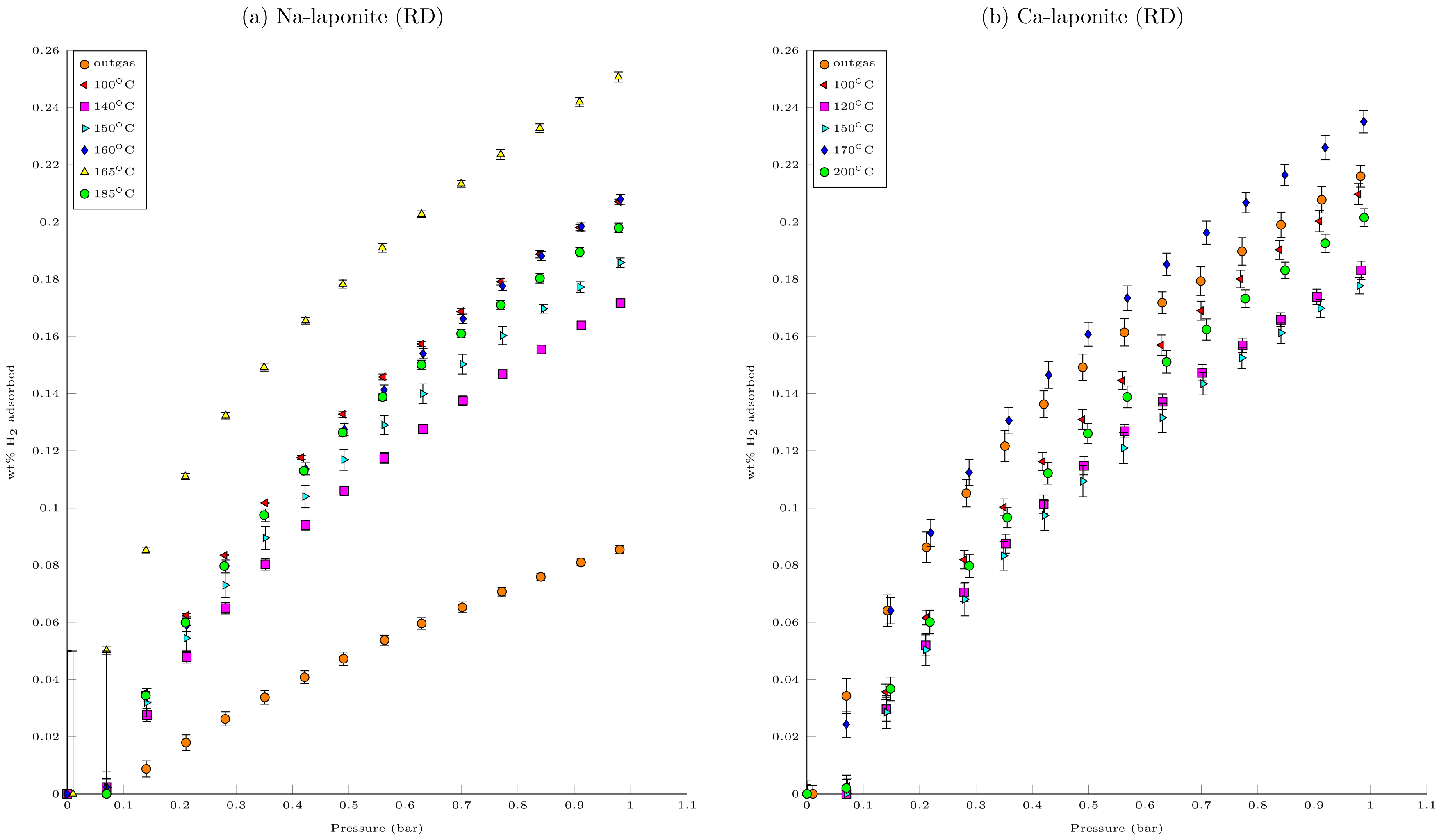
(a) Na-laponite (RD)

(b) Ca-laponite (RD)

Figure 7.7: Comparing low pressure gravimetric isotherms at 77 K for various pretreatment temperatures, for the sodium and calcium forms of laponite (RD). Note the large error bars for the low-coverage data for Na-laponite (RD), due to high temperature instability at the start of isotherms.

7.4 Chapter Summary

In this chapter, both XRD and TGA were used to determine the temperature required to dry the laponite clay sufficiently to a sub-monolayer state, through analysis of the water content and interlayer spacing, while complementary TGA techniques were used to measure the hydrogen uptake characteristics of a range of laponite clays, varying by their combined interlayer cation and grade.

From the range of room temperature up to 473 K, a temperature of 413 K emerged as the most likely treatment temperature required to reduce the laponite water content to below that for a fully saturated monolayer of water, from a comparative analysis of the results from XRD and TGA measurements. Higher temperatures were not considered, as the literature suggests the possibility of dehdroxylation beyond this, which could lead to interlayer collapse and uncertainties in any subsequent gravimetric analyses. Neither technique provides a conclusive estimate on its own, because the conditions could not be precisely controlled in all cases: for instance, the XRD measurements were performed at ambient pressure. Measurements using the IGA enabled the temperature to be estimated for the same samples under vacuum, confirming 413 K to be the best treatment temperature, as these conditions are the most relevant to all subsequent TGA measurements, as well as to the neutron measurements discussed in other chapters.

However, some contradictions arose in subsequent measurements which may indicate that the pre-treatment temperature needs to be more rigorously explored for all forms of laponite. Different interlayer cations appear to require different temperatures to achieve the same hydration state, probably due to variations in the strength of the cation's bond to water. The possibility of water readsorption by re-exposing the dried clay to ambient conditions is discussed and should be avoided for future experiments, so as to eliminate this complexity from future analysis.

For Na-laponite (RD), the treatment temperature used appears to affect the subsequent hydrogen uptake, but this effect is not apparent for the calcium form of the same laponite grade, however a clear difference in uptake exists for both samples when comparing the isotherms measured before any heating was performed on the evacuated sample to those measured shortly after at least ten hours of heating with concurrent evacuation. This confirms the need for some degree of desiccation before hydrogen can enter the clay galleries.

8. H_2 BINDING SITE STRUCTURE FROM NEUTRON DIFFRACTION

Neutron diffraction was used to confirm that H_2 intercalates into the laponite interlayers by examining the effect on the *d*-spacing and to suggest a possible structure of H_2 bound within the interlayer.

8.1 The effect of pressure on *d*-spacing

The small-angle scattering region contains the (001) basal peak, giving the *d*-spacing of the material. This was extracted from the measured differential cross-sections before inelasticity corrections were performed, because these corrections may also remove structural features. Figure 8.1 shows the results of the small angle data collected on NIMROD at two different temperatures for Ca-laponite (EL) as the H_2 pressure was increased in stages. Before any H_2 is introduced, the measured *d*-spacing of laponite in vacuum is 12.27 ± 0.06Å at 6 K and 40 K and 12.24 ± 0.05Å at 25 K. In both temperature series, it is clear that, as a general trend, the intensity of the (001) peak increases and its centre shifts to the left as H_2 pressure increases, which may be indicative of interlayer expansion. The negative scattering length of H_2 (-7.48 fm [190]) leads to a scattering density of 0.006 fm $Å^{-3}$ for the interlayer with just one intercalated H_2 per unit cell, contrasting starkly with the deuterated clay layers, having a scattering density of 0.5 fm $Å^{-3}$. Bragg reflections from structural features having similar periodicity to the introduced H_2, in this case the (001) peak, are accentuated, increasing in height as more H_2 is added. The *d*-spacings extracted from these data are considerably lower than those taken from the XRD data, because these samples were in vacuum, while the XRD measurements were performed in N_2-flow.

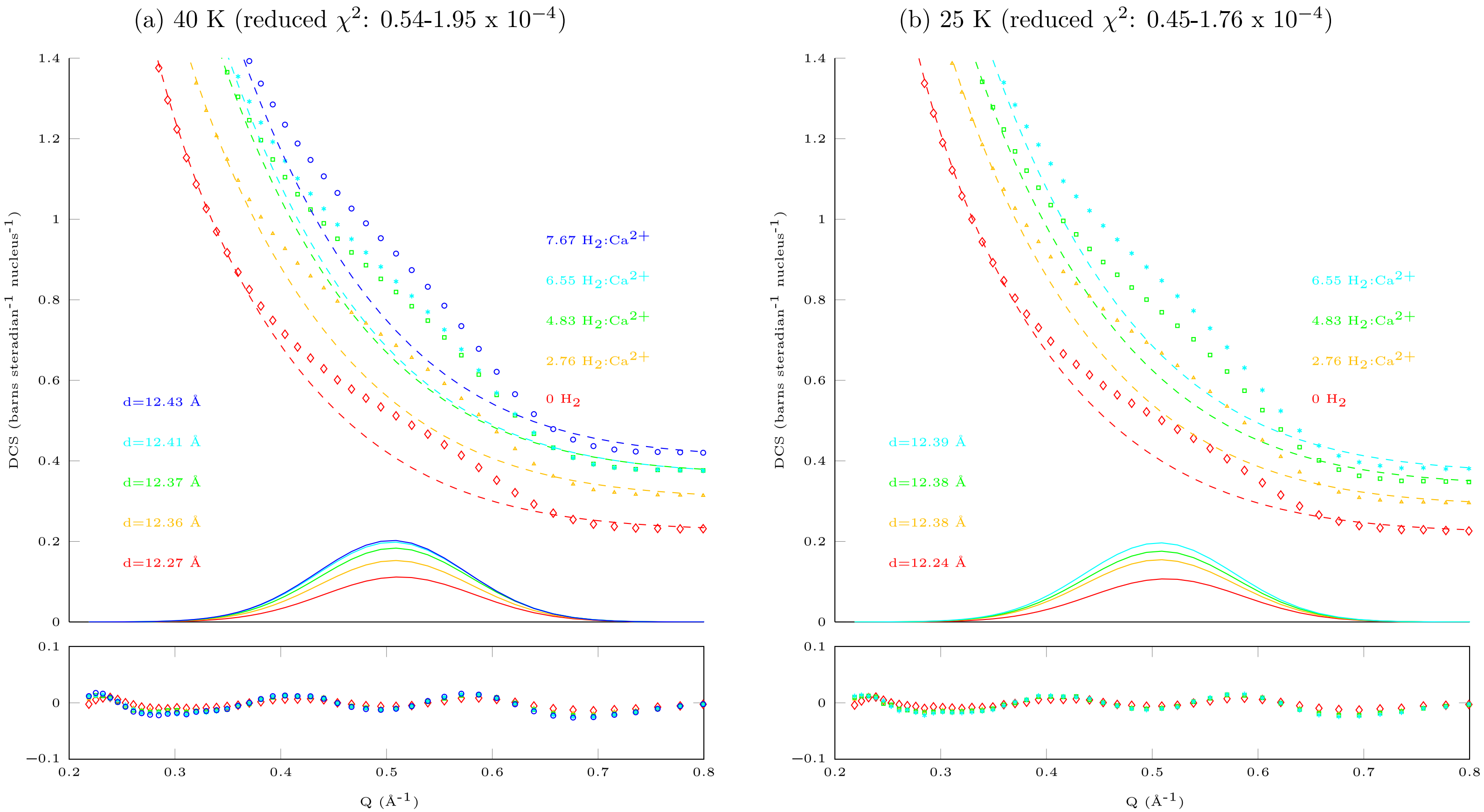
(a) 40 K (reduced χ^2: 0.54-1.95 x 10^{-4})

(b) 25 K (reduced χ^2: 0.45-1.76 x 10^{-4})

Figure 8.1: Full fits to the small angle scattering data obtained on NIMROD for Ca-laponite (EL) in vacuum (shown in red) and an H_2 atmosphere at increasing pressure, giving a range of loadings from 0 to 7.67 H_2 per Ca^{2+}, measured at two temperatures, 40 and 25 K. The measured data is represented by the open circles at the top. Colour is used to match the components for each loading. The fitting for each loading was done by first removing a background (shown as a dashed line) combining a constant, a Q^{-4} power law, representing Porod scattering from smooth surfaces [163], and a broad Gaussian (amplitudes ranging from 1.6 to 2.6, FWHM from 9.1 to 8.7 $Å^{-1}$ and centred at $Q = 0$). The remainder was fitted to a single Gaussian peak (solid lines), representing the (001) peak and the reduced χ^2 range for each temperature series is given in the captions above. The d-spacing, calculated from the centre of this Gaussian and shown on the left, increases as more H_2 is introduced. The residuals are shown on a separate axis below each plot.

The strong correlation between the (001) peak's intensity and H_2 concentration is consistent with the explanation that the H_2 molecules are intercalating into the laponite interlayers. The difference between the d-spacing in vacuum and that after the first dose of hydrogen is the largest and thereafter only small incremental changes occur. This is consistent with the expectation that layer expansion be performed by the first hydrogen molecules to intercalate into the interlayers. While each subsequent increase is of a similar order of magnitude as the experimental error margin, a definite overall trend of increasing d-spacing with H_2 pressure is apparent. If d-spacing is increased by H_2 intercalation, this suggests that the monolayer hydrated Ca-laponite (EL) d-spacing is initially not quite large enough to admit H_2 easily, and confirms that the attraction for the charged sites within the interlayer is strong enough for H_2 to push apart the interlayers. Layer expansion requires energy, affecting the adsorption enthalpy measured macroscopically through isotherms. The implication is that the measured ΔH_{ads} is lower than the true adsorption enthalpy. A larger pillaring molecule, such as a cation with a larger diameter, would avoid this complexity and allow a more accurate measure of ΔH_{ads} and may also exhibit a higher adsorption enthalpy, with no energy being expended on layer expansion.

Figure 8.2 shows the SANS spectrum and the fitting model for extracting the d-spacing and the calculated d-spacings for both H_2 adsorption and D_2 adsorption are given in Table 8.1. D_2 intercalation appears to decrease d-spacing. This is an effect of contrast-matching with the deuterated clay surface. D_2's positive coherent scattering length of 13.34 fm [190] leads to an interlayer scattering density of 0.15 fm $Å^{-3}$ for one D_2 per unit cell. As more D_2 is added, the interlayer scattering matches the scattering density of the clay layers (0.5 fm $Å^{-3}$) more closely, having the opposite effect from that caused by H_2 intercalation. Those layers which are intercalated by D_2 become less visible to the beam, leaving only those interlayers which do not yet have D_2 within them. Thus, as more D_2 is introduced, the visible (001) peak decreases in intensity and is formed from an average which includes the as yet unintercalated layers, giving the appearance of reduced d-spacing overall. The apparent d-spacing increase with increasing H_2 concentration may well be attributed to this contrast-matching as well and not to interlayer expansion, since H_2 has a strongly negative coherent scattering cross-section, providing contrast in the converse manner.

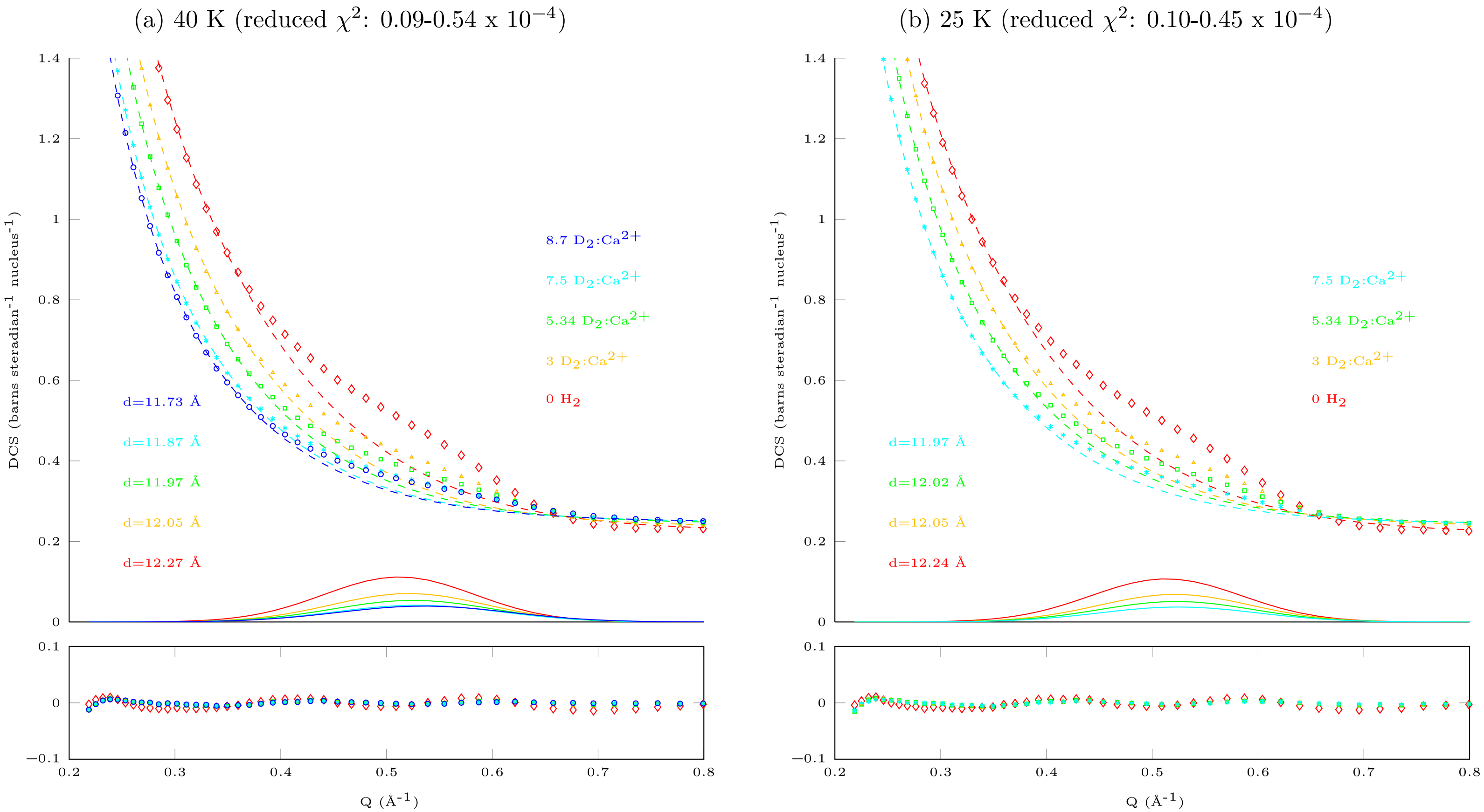
(a) 40 K (reduced χ^2: 0.09-0.54 x 10^{-4})

(b) 25 K (reduced χ^2: 0.10-0.45 x 10^{-4})

Figure 8.2: Full fits to the small angle scattering data obtained on NIMROD for Ca-laponite (EL) in vacuum (shown in red) and a D_2 atmosphere at increasing pressure, giving a range of loadings from 0 to 8.7 D_2 per Ca^{2+}, measured at two temperatures, 40 and 25 K. The measured data is represented by the open circles at the top. Colour is used to match the components for each loading. The fitting for each loading was done by first removing a background (shown as a dashed line) combining a constant, a Q^{-4} power law, representing Porod scattering from smooth surfaces [163], and a broad Gaussian (amplitudes ranging from 1.6 to 0.7, FWHM from 9.1 to 11.3 $Å^{-1}$ and centred at $Q = 0$). The remainder was fitted to a single Gaussian (solid lines), representing the (001) peak and the reduced χ^2 range for each temperature series is given in the captions above. The d-spacing, calculated from the centre of this Gaussian and shown on the left, decreases as more D_2 is introduced. The residuals are shown on a separate axis below each plot.

P (mb)	**H_2**				**D_2**			
	H_2:Ca^{2+}	**6 K**	**25 K**	**40 K**	**D_2:Ca^{2+}**	**6 K**	**25 K**	**40 K**
0	0	12.27±0.06	12.24±0.05	12.27±0.06	0	12.27±0.06	12.24±0.05	12.27±0.06
40	2.76	12.37±0.06	12.38±0.06	12.36±0.06	3	12.04±0.06	12.05±0.06	12.05±0.05
70	4.83		12.38±0.06	12.37±0.06	5.34		12.02±0.06	11.97±0.06
100	6.55		12.39±0.06	12.41±0.06	7.5		11.97±0.07	11.87±0.06
120	7.67			12.43±0.06	8.7			11.73±0.06

Table 8.1: *d*-spacing for various pressures (P in the leftmost column) and temperatures for H_2 and D_2, showing that the *d*-spacing increases slightly as the H_2 pressure is raised, but decreases as the D_2 pressure is raised. The latter is an anomaly due to contrast-matching with the clay surface, more fully explained in the text.

8.2 Q-space structure

The Q-dependencies of the differential cross-sections for Ca-laponite (EL) in H_2 and D_2 atmospheres are presented in Figures 8.3 and 8.4, respectively. This is the measured quantity from a diffraction experiment and is calculated after all the corrections discussed in Section 6.3.1 have been applied. This is the Q-space function from which the real-space $G(\bar{\mathbf{r}})$, Equation 5.35, is derived by Fourier transform [148].

The H_2 peak for 6.55 and 7.67 hydrogens per Ca^{2+} coincide, which may be due to saturation. It became increasingly difficult to match the H_2 adsorption levels to those of the D_2 as the pressure increased, confirming that the sample was close to saturation at the higher loadings. It is also possible that the concentrations for each element entered into the analysis software are inaccurate. The precise formula of Ca-laponite (EL) is protected by copyright and these levels are therefore estimates.

These functions show how the signal level changes as the gas intercalates into the clay layers. H_2 has a negative coherent scattering length and therefore as the H_2 concentration increases, the scattering signal drops further below that of the empty clay. Beyond $Q = 4$ Å^{-1}, however, the intensity goes above the empty clay background, possibly due to imperfect inelasticity corrections.

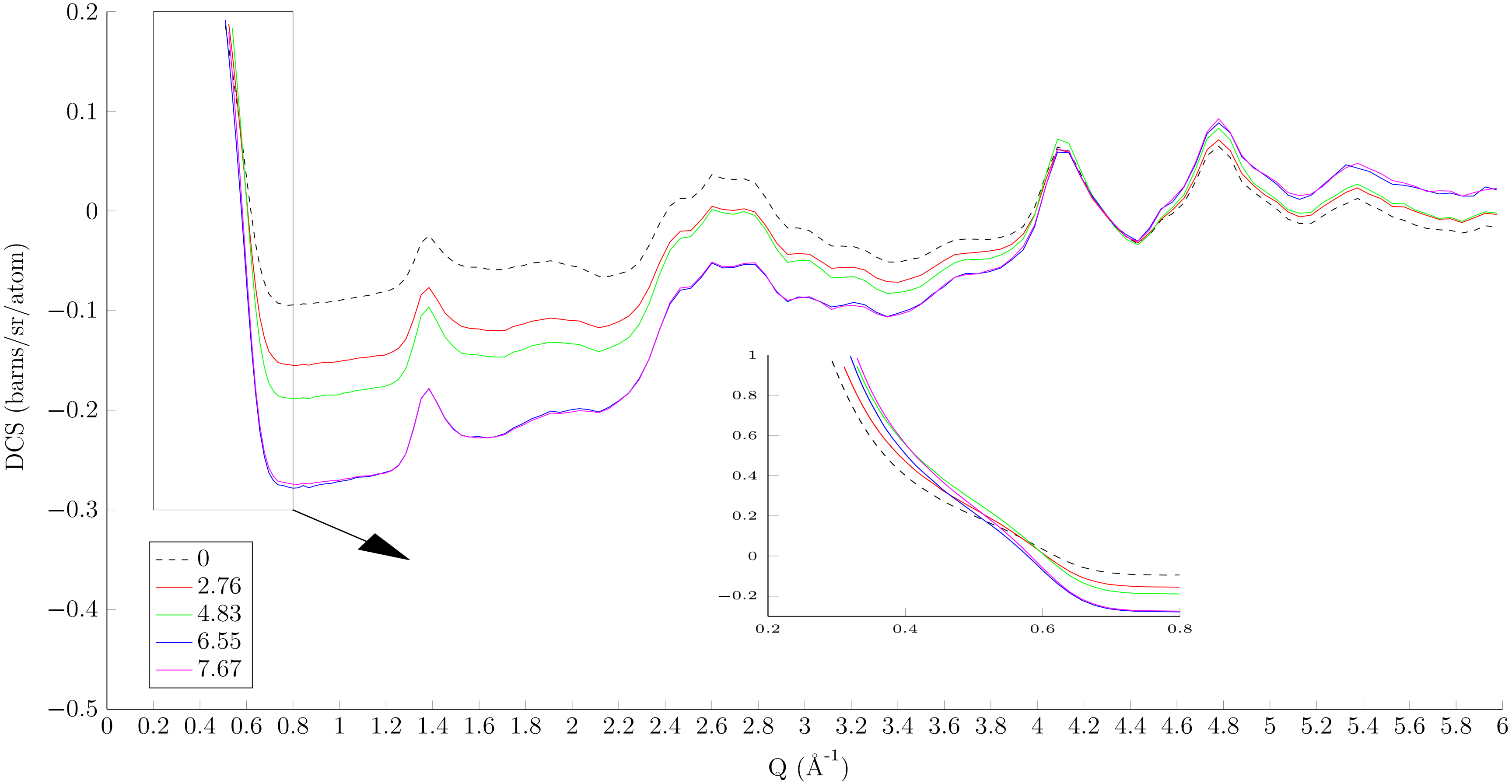

Figure 8.3: Differential cross-sections against Q, after incoherence has been removed and all other corrections, including those for inelasticity, have been made, for H_2 adsorbed on Ca-laponite (EL) at 40 K. The small angle scattering region contains the (001) peak representing the *d*-spacing of the clay and this region is magnified in the inset, where it is clear that, despite the flattening in intensity due to inelasticity corrections, the (001) peak increases as more H^2 is added. The legend on the left shows the colours corresponding to each H_2:Ca^{2+} ratio.

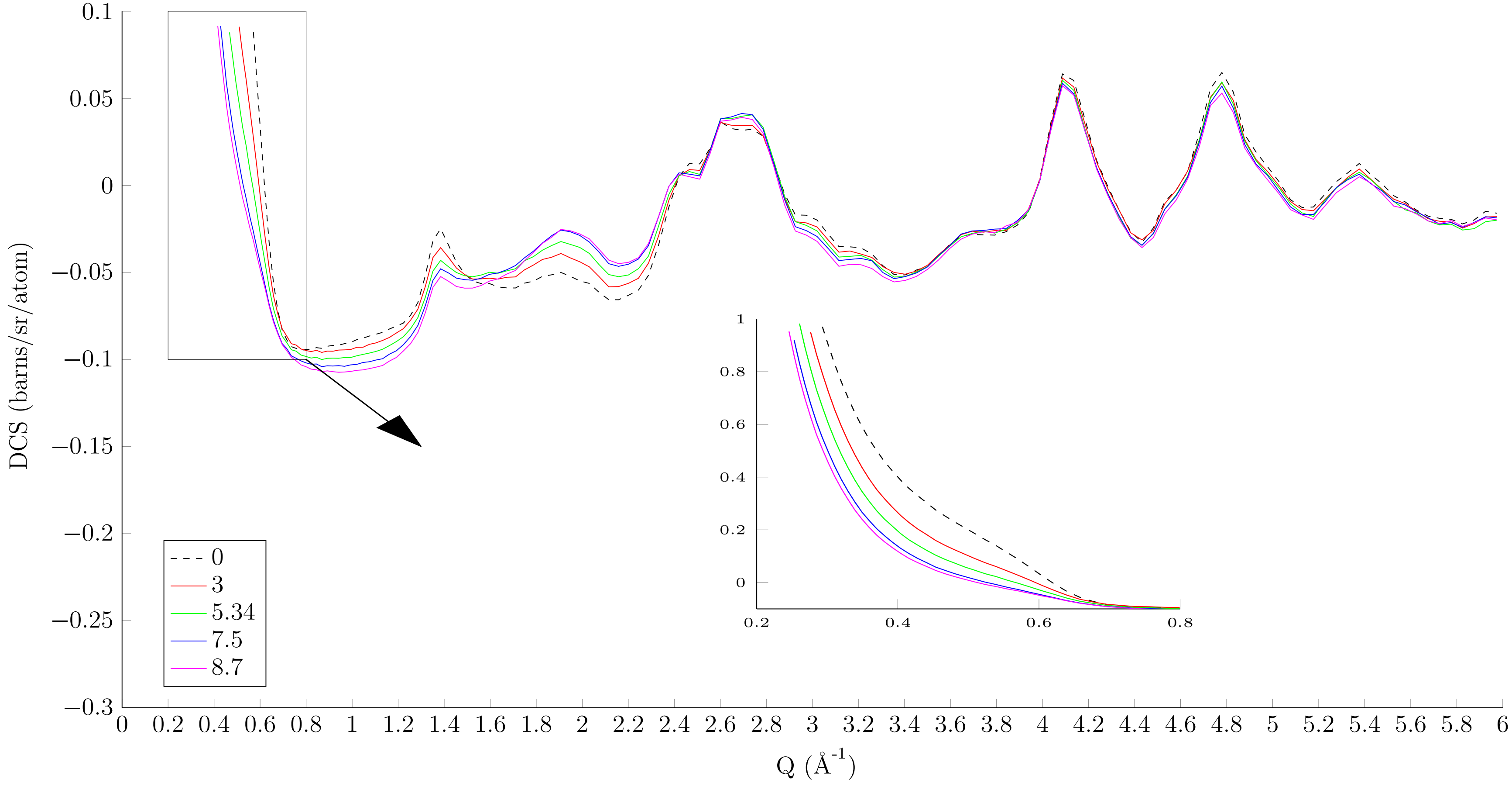

Figure 8.4: Differential cross-sections against Q, after incoherence has been removed and all other corrections, excluding those for inelasticity, have been made, for D_2 adsorbed on Ca-laponite (EL) at 40 K. The small angle scattering region contains the (001) peak representing the *d*-spacing of the clay and this region is magnified in the inset. Here it is clear that the (001) peak becomes smaller, due to the intercalated D_2 contrast matching with the clay layers. The legend on the left shows the colours corresponding to each D_2:Ca^{2+} ratio.

8.3 Structure of H_2 and D_2 in laponite interlayers

The real-space reduced PDF, $G(\bar{\mathbf{r}})$, showing pair correlations between atoms for H_2 adsorption to Ca-laponite (EL) is presented for three combinations of data in Figures 8.5, 8.8 and 8.10. The corresponding data for D_2 adsorption is shown in Figures 8.6, 8.9 and 8.11.

The oscillations observed in the low-r region are caused by truncation effects during the Fourier Transform from Q-space to real-space, thus features in the region below 0.5 Å are ignored in this analysis. Unfortunately, some of the main features of interest to this study: the H_2 and D_2 peaks, lie between 0.5 and 1 Å, close to the region affected by truncation. However, the consistency of the centre of this feature across a wide range of temperatures and loadings and the clear difference between the empty, H_2 and D_2 data, particularly the change in sign, strengthens its validity. The intensity of the low-r peaks vary due to the imperfect nature of the correction procedures.

At low temperatures, H_2 is largely in the ground state: para-H_2, having antiparallel nuclear spins. Using the ^{1}H neutron scattering lengths b_{coh} = -3.741 fm and b_{inc} = 25.28 fm [204] in Equation 3 from [199] for the intramolecular neutron cross-section:

$$v(Q, t = 0) = 2(a_{coh}^2 + a_{inc}^2) + 2(a_{coh}^2 - a_{inc}^2) exp(-2\lambda_{DW}^2 Q^2) \frac{\sin QD_e}{QD_e}, \tag{8.1}$$

results in a negative value of $v(Q, t = 0)$ for the intramolecular peak, centred at the typical interatomic bond distance of ~0.74 Å for H-H [37]. Figure 8.5 compares the empty clay with the lowest loading of H_2 at three different temperatures, clearly showing the negative peak for H_2 and also giving some idea of the temperature variation. However, the centre of this peak gives an estimate of between 0.70 and 0.72 Å for the H-H bond distance in H_2, slightly smaller than the literature value of 0.74 Å [37]. The negative H_2 peak is unexpectedly larger at 25 K, possibly due to inaccurate level estimates for this temperature. Figure 8.6 shows similar data for D_2 adsorption and here the D_2 peak for the 25 K data is lower than for the other two temperatures. This may be attributed to contrast matching.

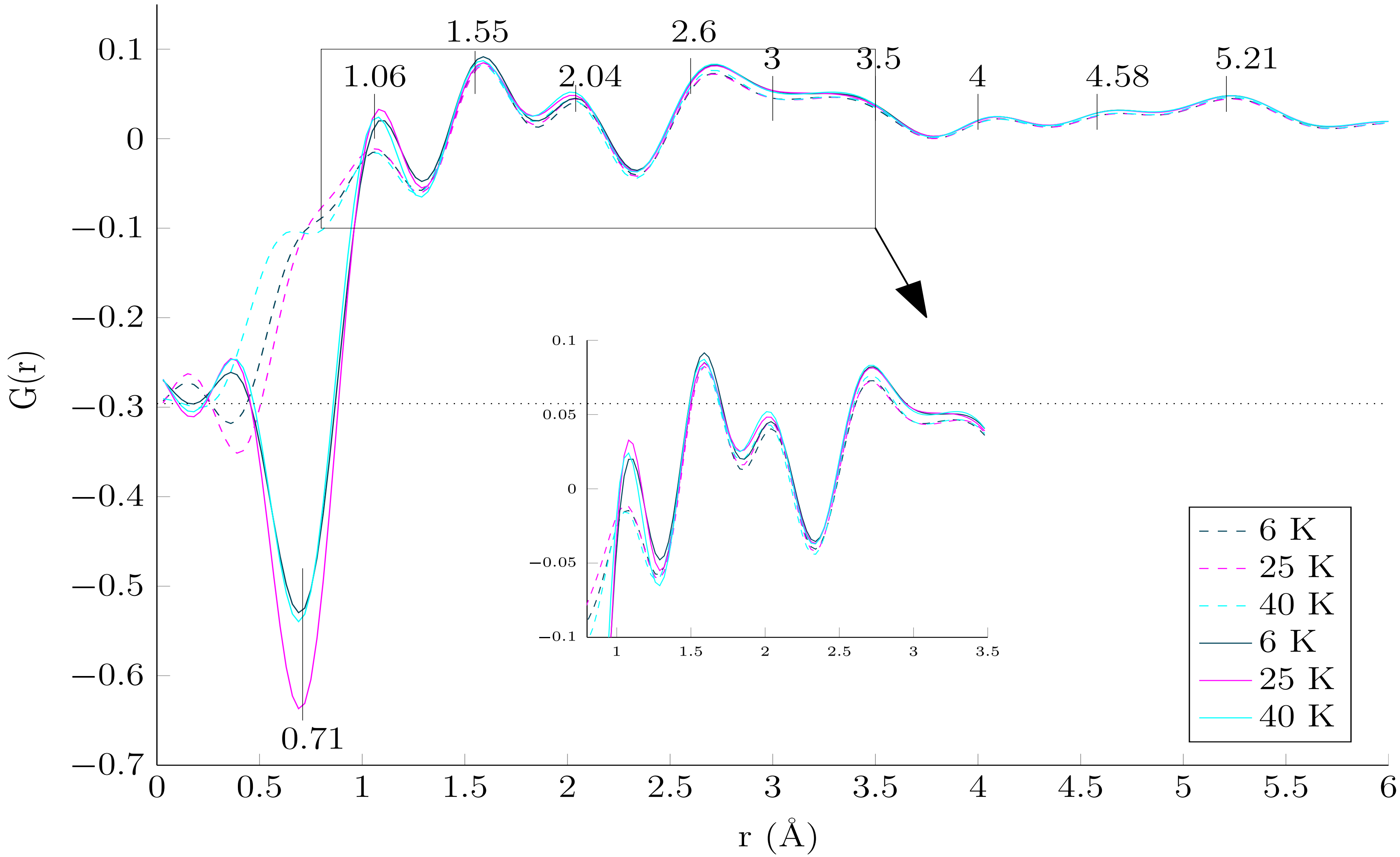

Figure 8.5: $G(r)$ compared for empty clay and clay with 2.76 H_2:Ca^{2+} adsorbed, at three temperatures. With the exception of the large peak representing the H-H bond distance in H_2, the main peaks which change are magnified in the inset. The legend on the right shows the colours representing each temperature. The dashed lines are for the clay in vacuum and the solid lines for the clay in a 40 mb H_2 atmosphere.

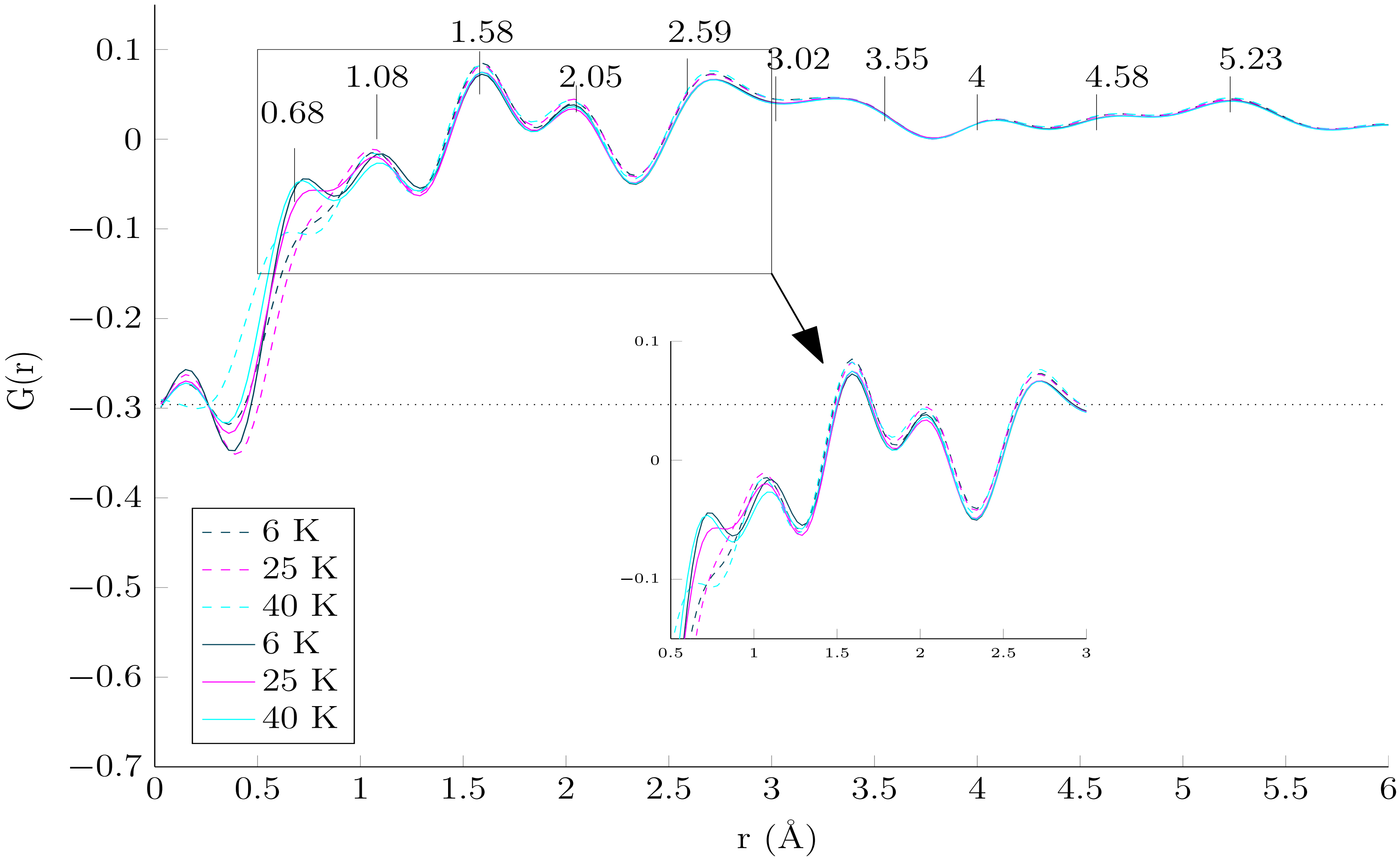

Figure 8.6: $G(r)$ compared for empty clay and clay with 3 D_2:Ca^{2+} adsorbed, at three temperatures. The main peaks which change are magnified in the inset. The legend on the left shows the colours corresponding to each temperature. The dashed lines are for the clay in vacuum and the solid lines for the clay in a 40 mb H_2 atmosphere.

The $G(r)$ at 40 K is compared across all H_2 concentrations measured at this temperature and displayed in Figure 8.8. The H_2 peak at ~0.71 Å for 6.55 and 7.67 hydrogens per Ca^{2+} coincide, which may be due to an incorrect level estimation, as mentioned previously, or it may be due to saturation.

Figure 8.7 shows a series of fitted Gaussian peaks for the $G(r)$ data for Ca-laponite (EL) at 40 K in vacuum and the lowest dosed levels for H_2 and D_2. Table 8.2 shows the fitted peak centres, indicating nearest-neighbour distances in Ca-laponite (EL), and proposes the assignment of the low-r peaks to likely chemical species, based on bond lengths found in the literature. In the $G(r)$ data shown in Figures 8.8 and 8.10, there is only one negative peak, centred at 0.72 Å, representing the H-H bond distance. The inset shows that the peaks at r ~1.08 and 2.7 Å increase as more H_2 is added. The shape of the peaks at r ~1.6 and 2.05 Å change significantly for the loading of 6.55 hydrogens per cation, but this is likely to be due to incorrect estimation of the element content for this loading, since the peaks centred at the corresponding r-value at the higher loading is similar to the two lower loadings.

Complexes involving H_2, such as the proposed Ca^{2+}-H_2, are expected to give a negative peak, however the extremely low weighting calculated for this complex shows that this peak would be very small and easily obscured by other peaks. The estimated theoretical value for Ca^{2+}-H_2 complexes in graphite is 2.4 Å [205], however there is no discernible Gaussian centred at this value. Ca-D_2O complexes are expected in all three cases (undosed, or dosed with either H_2 or D_2) and Ca-D_2 complexes are expected for Ca-laponite (EL) dosed with D_2, however the weighting for the contribution to the partial structure functions by Ca-D is not high, so this peak may also be obscured by other features. The areas under the H-H peak did not result in a coordination number of 1, indicating that this analysis needs more careful consideration.

(a) Vacuum

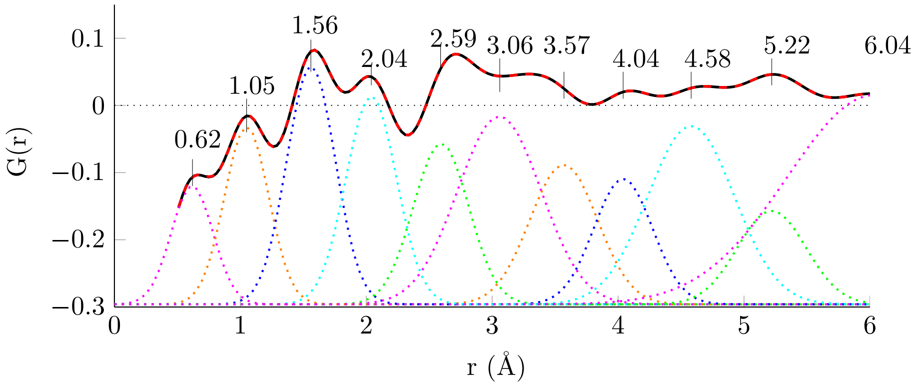

(b) 2.76 H_2:Ca^{2+}

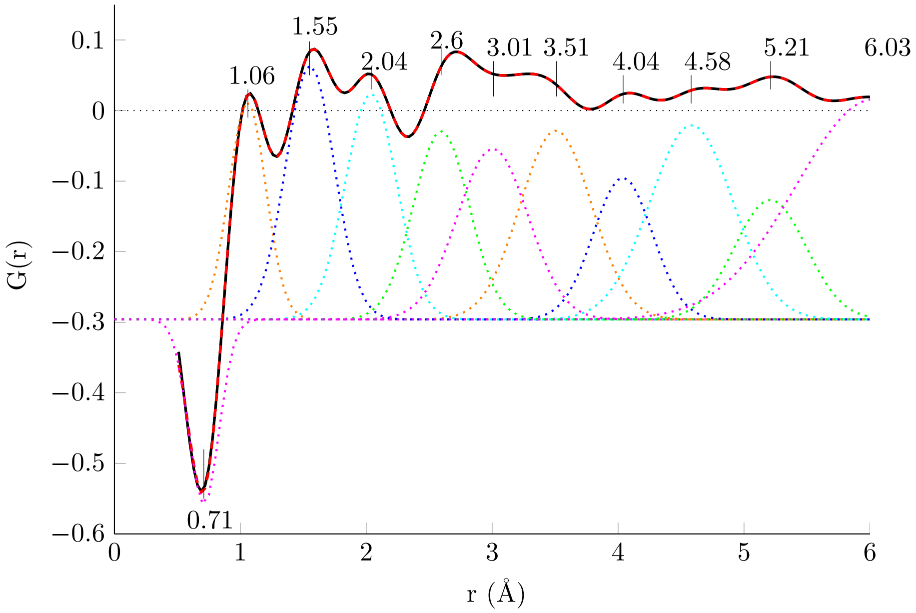

(c) 3 D_2:Ca^{2+}

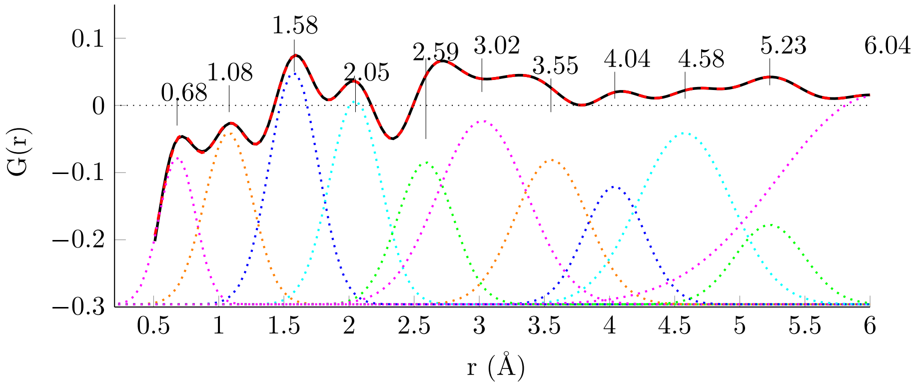

Figure 8.7: Fitted Gaussians to the $G(r)$ for Ca-Laponite (EL) at 40 K in (a) vacuum, (b) the lowest dose of H_2 and (c) the lowest dose for D_2. The region below r = 0.5 Å is excluded from the fits. The centres of these peaks are listed in Table 8.2. Typical χ^2_{red} values for these fits are on the order of 10^{-7}, due to the large number of fitting parameters.

Peak centre (Å)	**Assigned bond species**	**Bond length (Å)**	**Weighting ($\mathbf{H_2}$)**	**Weighting ($\mathbf{D_2}$)**
0.71	H-H	0.74 [37]	0.03	-
0.68	D-D	0.74 [37]	-	1.71
1.06	O-D	0.96 [62]	2.17	4.07
1.55	Si-O	1.62 [206]	2.29	2.28
2.04	Mg-O	2.05 [207]	2.04	2.03
-	Ca-H_2	2.4 [205]	-0.006	-
-	Ca-D_2/D_2O		-	0.05
2.6	O-O	2.7 [208]	9.76	9.69

Table 8.2: Assignment of likely species involved in the bonds indicated by peak centres taken from the fitted Gaussians to $G(\bar{\mathbf{r}})$ for 2.76 H_2:Ca^{2+} and 3 D_2:Ca^{2+} in Ca-laponite (EL). The bond lengths in the third column are quoted from measurements or theoretical estimates in the literature. The expected weightings for each peak is shown in the rightmost two columns, the first calculated for the sample dosed with 2.76 H_2:Ca^{2+} and the second for the same sample dosed with 3 D_2:Ca^{2+}.

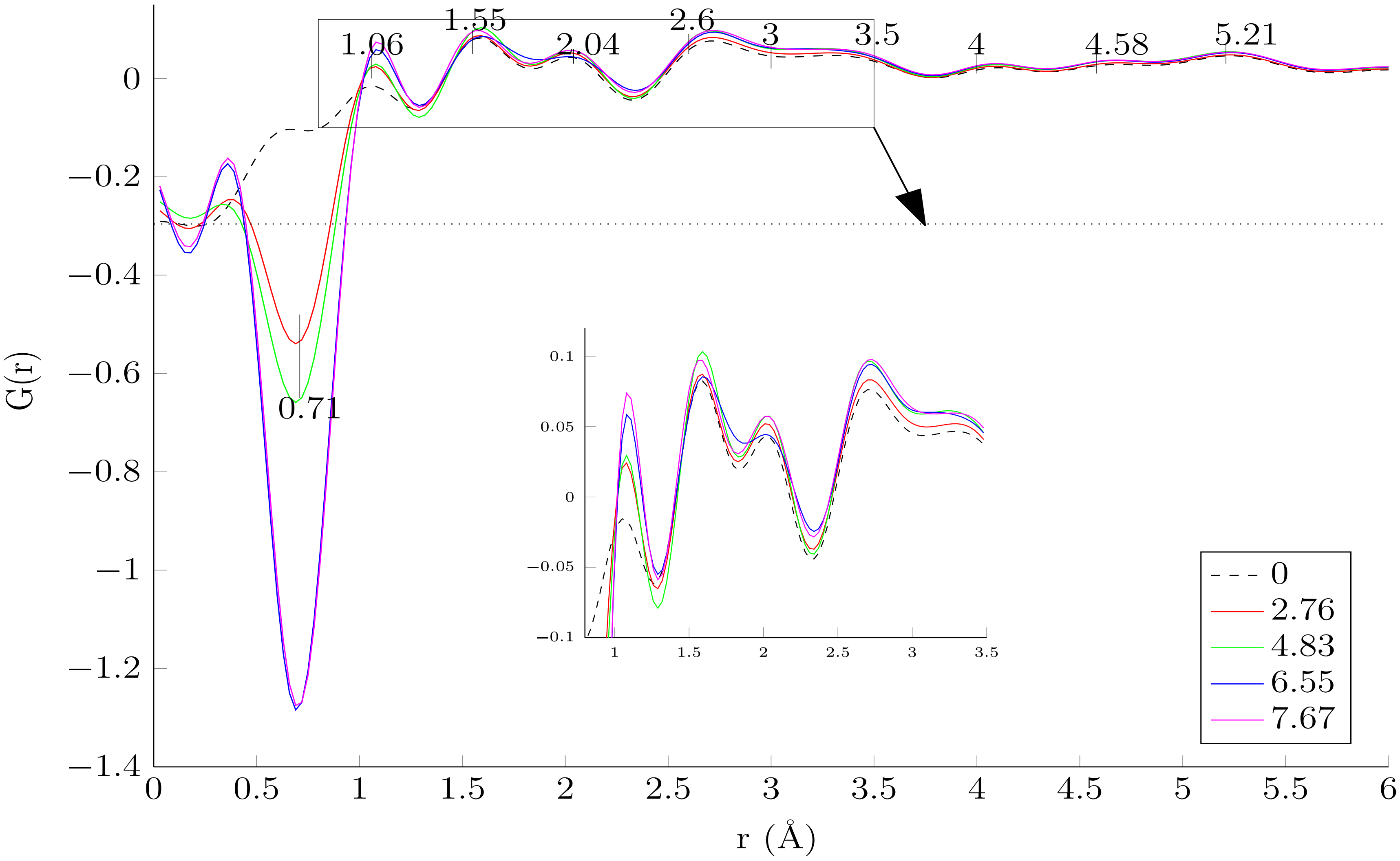

Figure 8.8: $G(r)$ compared for Ca-laponite (EL) exposed to a range of H_2 concentrations, all measured at 40 K. With the exception of the large peak representing the H-H bond distance in H_2, the main peaks which change are magnified in the inset. The legend on the right shows the colours corresponding to each H_2:Ca^{2+} ratio.

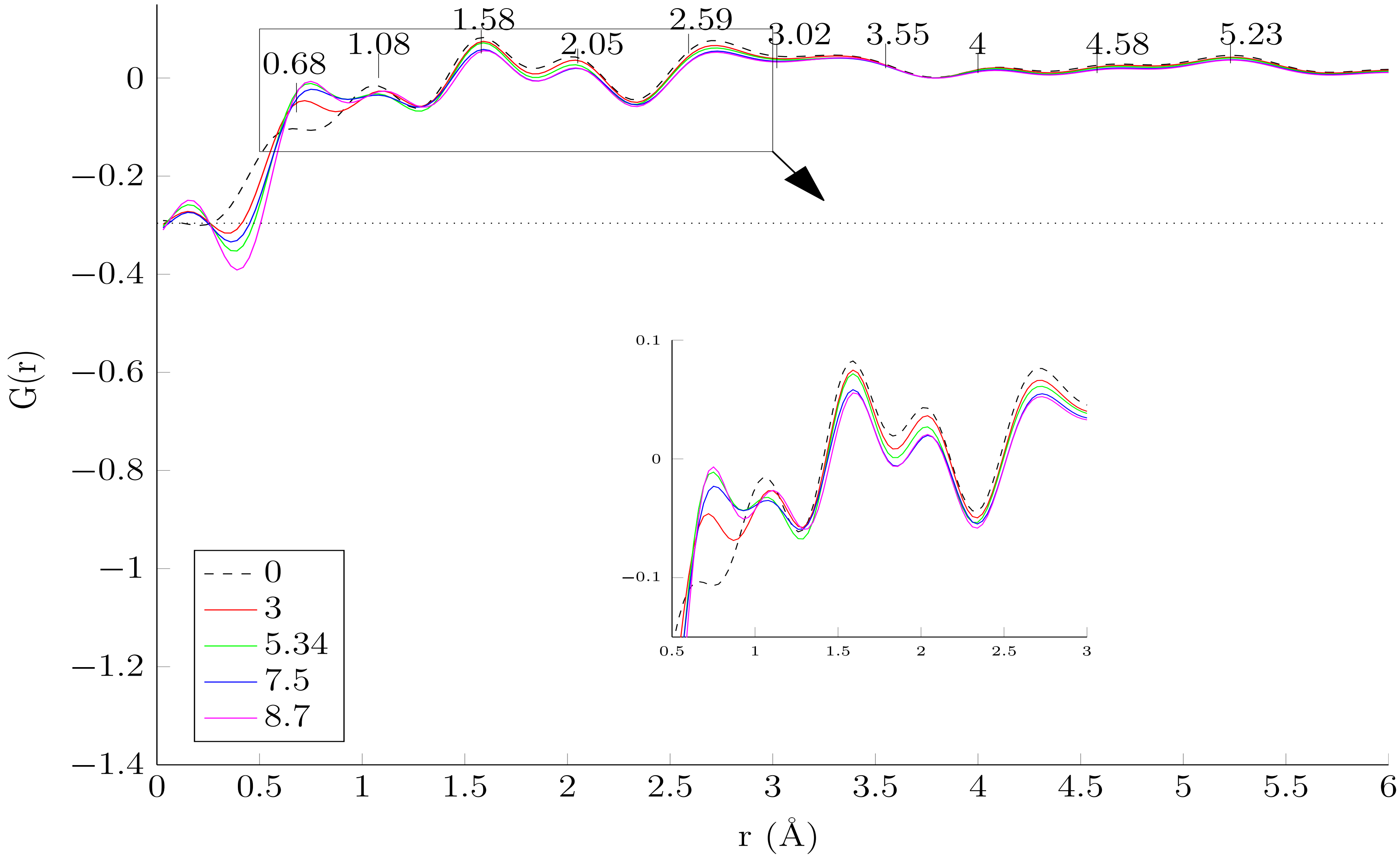

Figure 8.9: $G(r)$ compared for a range of D_2 concentrations, all measured at 40 K. The main peaks which change are magnified in the inset. The legend on the left shows the colours corresponding to each D_2:Ca^{2+} ratio.

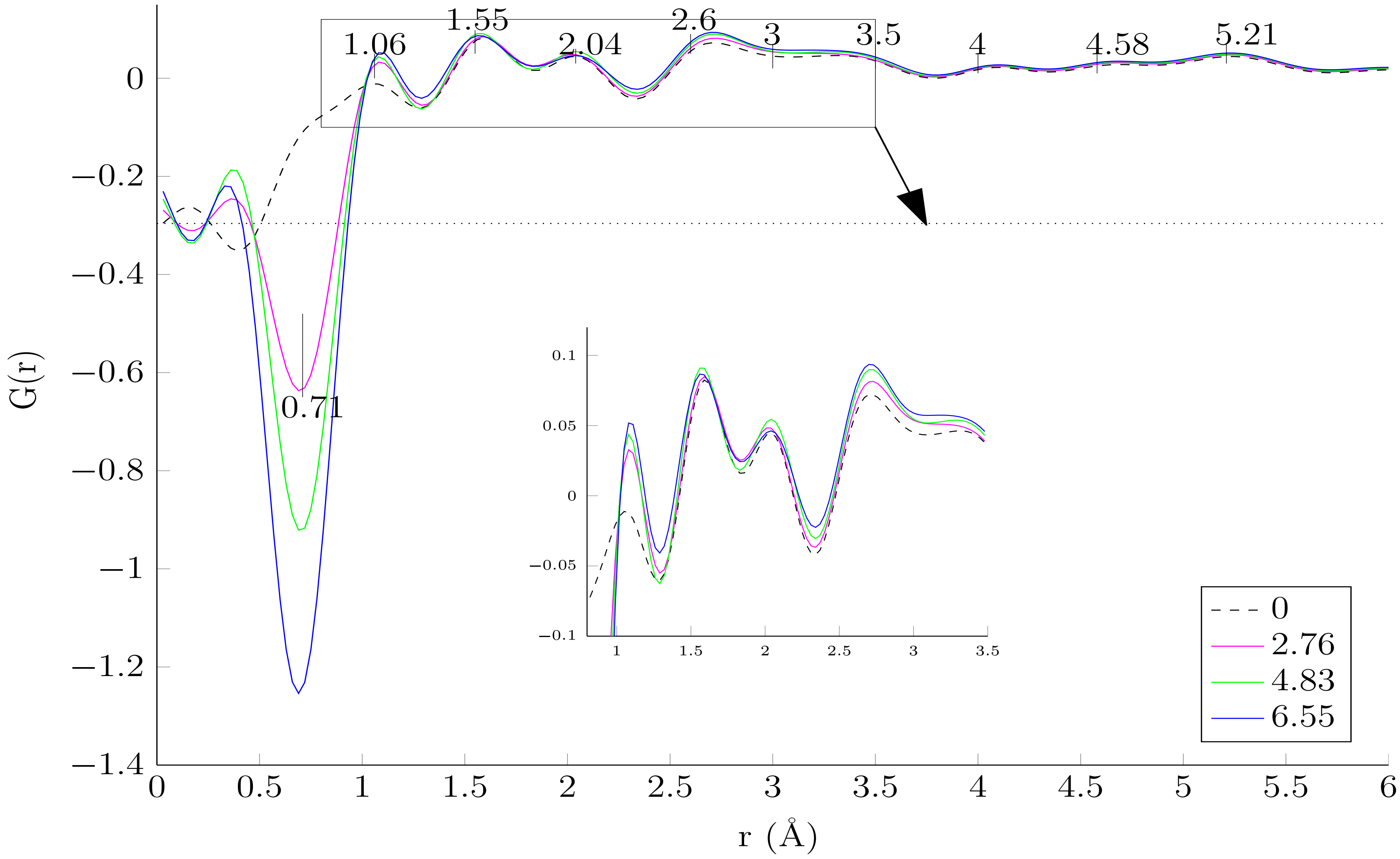

Figure 8.10: $G(r)$ compared for a range of H_2 concentrations, all measured at 25 K. With the exception of the large peak representing the H-H bond distance in H_2, the main peaks which change are magnified in the inset. The legend on the right shows the colours corresponding to each H_2:Ca^{2+} ratio.

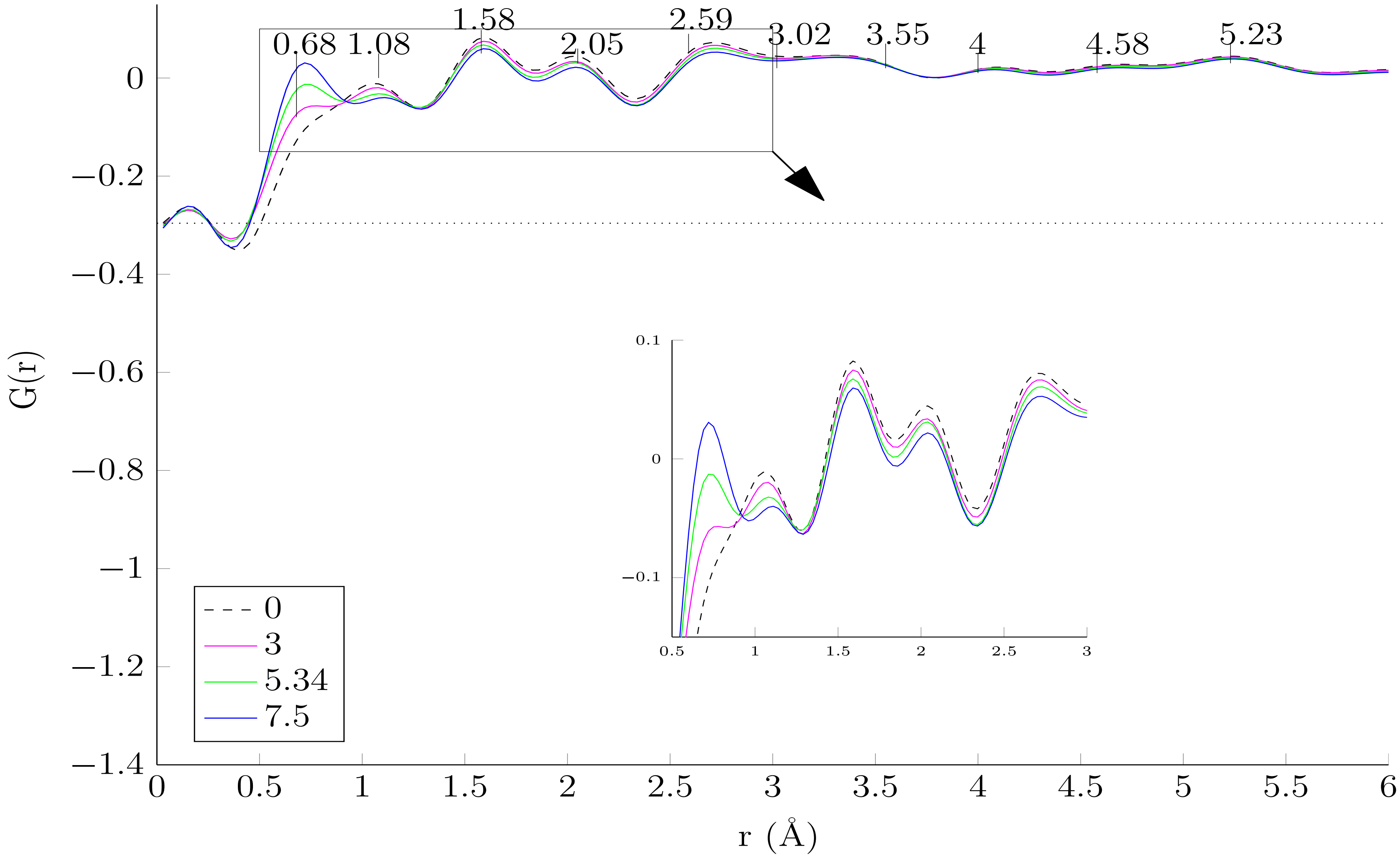

Figure 8.11: $G(r)$ compared for a range of D_2 concentrations, all measured at 25 K. The main peaks which change are magnified in the inset. The legend on the left shows the colours corresponding to each D_2:Ca^{2+} ratio.

8.4 Chapter Summary

The results in this chapter give some indication of how the structure of the interlayer changes when the dried, evacuated sample is exposed to a low-pressure H_2 or D_2 atmosphere. The *d*-spacing of the dried clay in vacuum is measured through neutron diffraction and found to be slightly less, at 12.27 Å, than the expected value of 12.5 Å for the monolayer hydrated laponite. Some interlayers may have collapsed due to the dessication and evacuation process, reducing the average *d*-spacing between the layers.

The effect both gases have on the 001 peak, being representative of the material's *d*-spacing or interlayer spacing, demonstrates that they intercalate into the smectite interlayers. This effect is most likely to be caused by a contrast matching effect, in which the difference between the scattering from the clay layers and its interlayers becomes either more or less pronounced as more H_2 or D_2, respectively, intercalates into the clay galleries. Another possibility is interlayer expansion, caused by the intercalating molecules. A distinct trend of an increase in *d*-spacing with increasing H_2 pressure and converse decrease in *d*-spacing with increasing D_2 pressure is apparent, but it is not clear whether this is due to contrast matching, interlayer expansion, or some combination of the two. The first exposure to either H_2 or D_2 results in the largest effect on the laponite *d*-spacing, with only small incremental changes resulting from subsequent increases of gas concentration. This is consistent with the first intercalating molecules having to open up the interlayers slightly, but this possibility cannot be confirmed from this data, since the error margins are of comparable values.

The reduced pair distribution function, G(r), reveals a negative peak, signature of para-hydrogen due to spin correlations leading to a negative intramolecular σ. This peak is centred at 0.72 Å, slightly smaller than the literature value of 0.74 Å [37] for the bond length between hydrogen atoms in H_2. While no clear peak can be identified to match the expected bond distance between Ca and H_2, this is unsurprising because the signal from this peak is expected to be very weak. Gaussians were readily fitted to the peaks in the G(r), however the coordination numbers revealed by their areas did not match expectations, reflecting the fact that the complexity of the system and a few experimental oversights resulted in a number of uncertainties.

The differential cross-section shows that the scattering signal increases with H_2 pressure, following an exponentially diminishing trend, indicating interlayer saturation.

The converse trend occurs with increasing D_2 pressure, but saturation appeared to be reached at a lower pressure. This difference led to difficulties in matching the H_2 and D_2 levels, required for comparative measurements. In addition, the lack of a precise formula for the EL grade of laponite used in these experiments introduced uncertainties in the analysis, limiting the conclusions that can be drawn from these data. However, this is the first attempt at using neutrons to characterise hydrogen and deuterium in clays and it is hoped that further experimental work will benefit from the lessons learned here to clarify the uncertainties through an improved experimental technique.

9. ADSORPTION ISOTHERMS

9.1 High pressure uptake

The Figures in this Section show adsorption and desorption isotherms collected up to 150 bar, using the volumetric method under a range of temperatures for the sodium, calcium and magnesium forms of laponite grades (RD) and (EL).

The error bars throughout are calculated with regard to the variation in temperature from the setpoint only and tend to be much larger for the first few points of adsorption. The Hiden Isochema equipment used to measure the isotherms does not rigorously wait for temperature stability before taking readings and it is difficult to predict how long this will take when setting up automated measurements.

The mathematical equation describing the adsorption mechanism is not yet known for H_2 on clay, hence a variety of isotherm equations were attempted and the best fits displayed in Figures 9.1 through 9.6. Also shown in each Figure is the isosteric heat of adsorption calculated from these fits to the two coldest adsorption isotherms. The full pressure range of the isotherms for all samples and temperatures are best matched to the Langmuir isotherm (Equation 6.7); the Sips (Equation 6.9) and Freundlich (Equation 6.8) models only matched a small range of pressures, below 50 bar. While the Langmuir model is not expected to be a good fit at lower pressures, because it has underlying assumptions unlikely to be valid for clay interlayers, such as homogeneity of adsorption sites, it is not surprising that it provides a reasonable fit over a wider pressure range. Only a small fraction of the available adsorption sites are expected to be strong: the vast majority will be weak interactions with the clay surface or between H_2 molecules. Thus over the full pressure range, the average behaviour of the weaker majority is observed.

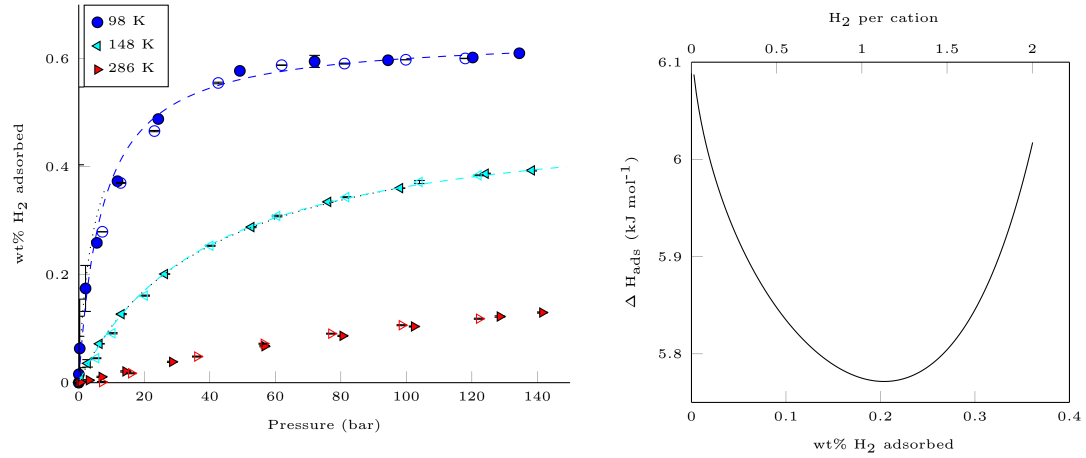

(a) Volumetric

(b) ΔH_{ads}

Figure 9.1: (a) Volumetric, high pressure isotherms measured at various temperatures for Na-laponite (RD), with the filled markers representing adsorption and the open markers in the same colour the corresponding desorption. The dashed lines in the corresponding colours show the Langmuir fits, Equation 6.7, to the two coldest adsorption isotherms, while the dotted black lines show the Tóth fits, Equation 6.10, used to calculate (b) the associated ΔH_{ads}. The fitting parameters for the Tóth fits are summarised for all measured samples in Table 9.1.

The large errors on the lower coverage points for the adsorption isotherms cast doubt on the reliability of these data. To get an accurate estimate of the isosteric heat of adsorption, a good fit, especially at low coverages, is needed to extrapolate the ΔH_{ads} values between points. Even small inaccuracies in these values can greatly distort the calculated value. The best fit for the lower pressure region (below 50 bar) is the Tóth model (Equation 6.10) and this was used to calculate ΔH_{ads} in each case.

ΔH_{ads} shows an initial decrease with coverage, which is typical in porous materials [209] [210] [57]. However, in Figures 9.1b, 9.2b, 9.3b and 9.6b, ΔH_{ads} begins to increase again, anomalously. This may be due to imperfect fitting functions, which diverge from the data as pressure increases.

In Figure 9.2, the coldest isotherm, measured at 98 K, follows an unusual pattern and is excluded from the analysis for calculating ΔH_{ads}. The inconsistency of this isotherm with those of other samples measured at the same temperature and of those taken on the same sample at different temperatures, casts doubt on its validity and it is considered to be an experimental error. The analogous isotherms for laponite samples having the same cation (e.g. Na-laponite (RD) in Figure 9.1a) or same grade (e.g. Ca-laponite (EL) in Figure 9.4a) do not have this shape. In addition, the low pressure isotherms of all three samples (Figures 9.10a, 9.10b and 9.8b) do

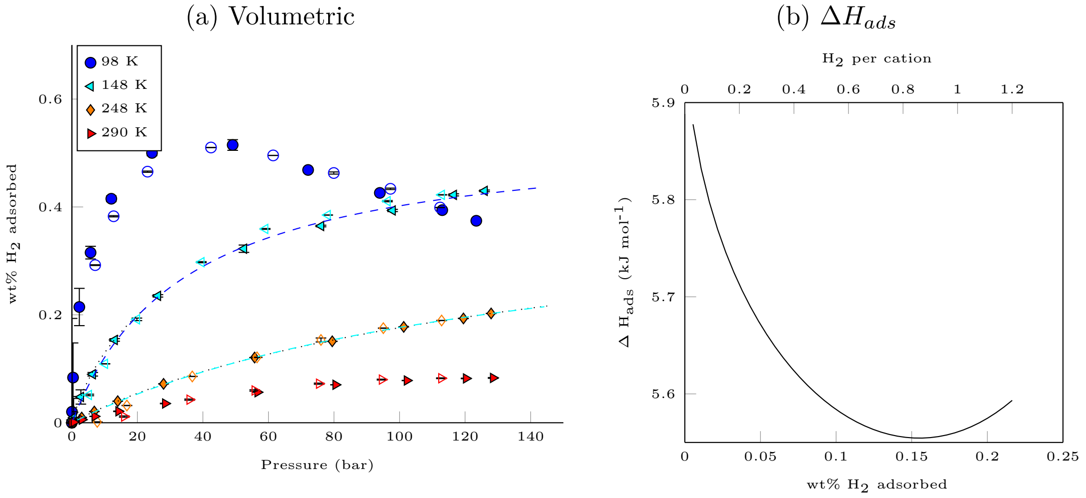

Figure 9.2: (a) Volumetric, high pressure isotherms measured at a series of temperatures for Na-laponite (EL), with the filled markers representing adsorption and the open markers in the same colour the corresponding desorption. The dashed lines in the corresponding colours show the Langmuir fits, Equation 6.7, to the 148 K and 248 K adsorption isotherms. The shape of the 98 K isotherm measured for this sample clearly diverges from the Langmuir form and was not used for fitting, for reasons explained in the text. The dotted black lines show the Tóth fits, Equation 6.10, used to calculate (b) the associated ΔH_{ads}. The fitting parameters for the Tóth fits are summarised for all measured samples in Table 9.1.

not differ markedly from each other. While the shape of this isotherm is close to the IUPAC Type 4 isotherm and could suggest that multilayer adsorption is occurring, this is considered to be unlikely, since the uptake for this sample is no higher than for the other samples. Multilayer adsorption is more commonly found in mesoporous materials, where additional layers of H_2 not in contact with any adsorbent surfaces can be accommodated. This would be a surprising result in the nanoporous interlayers of laponite at such low hydration levels and would require the *d*-spacing of this sample to expand by at least three times. It is displayed here to show some of the problems encountered during these measurements and the reason for this is unclear. It may be due to the equipment not being calibrated properly before taking these readings, however the other three temperature isotherms appear to follow a consistent pattern. This shape is visible in excess isotherms of H_2 on activated carbon, for example Bimbo *et al.* [209], being more marked in the lowest temperature isotherms.

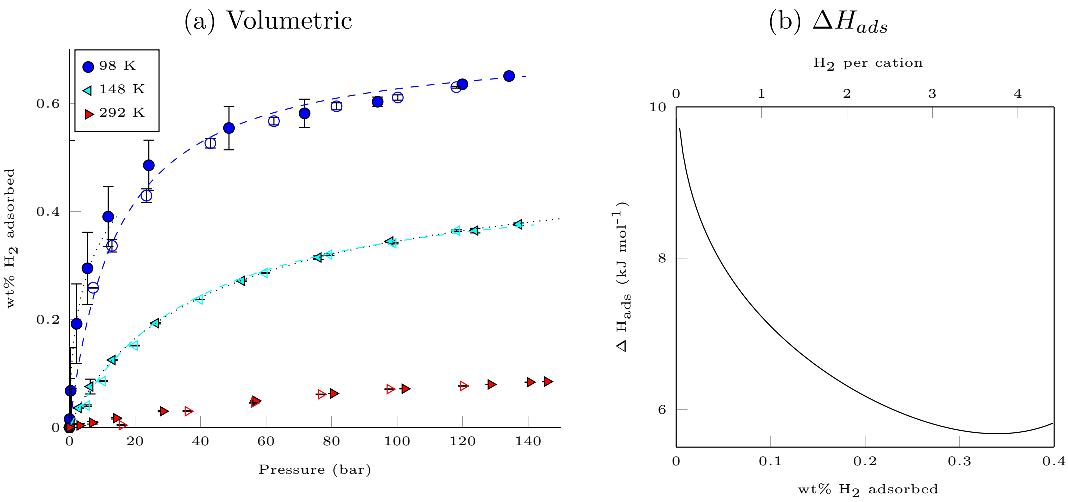

(a) Volumetric

(b) ΔH_{ads}

Figure 9.3: (a) Volumetric, high pressure isotherms measured at a range of temperatures for Ca-laponite (RD), with the filled markers representing adsorption and the open markers in the same colour the corresponding desorption. The dashed lines in the corresponding colours show the Langmuir fits, Equation 6.7, to the two coldest adsorption isotherms, while the dotted black lines show the Tóth fits, Equation 6.10, used to calculate (b) the associated ΔH_{ads}. The fitting parameters for the Tóth fits are summarised for all measured samples in Table 9.1.

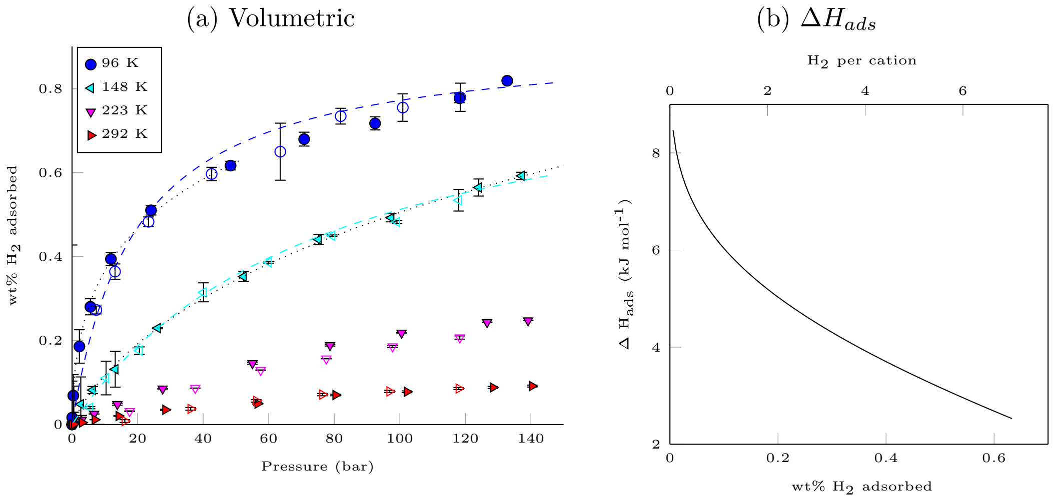

(a) Volumetric

(b) ΔH_{ads}

Figure 9.4: (a) Volumetric, high pressure isotherms measured at a series of temperatures for Ca-laponite (EL), with the filled markers representing adsorption and the open markers in the same colour the corresponding desorption. The dashed lines in the corresponding colours show the Langmuir fits, Equation 6.7, to the two coldest adsorption isotherms, while the dotted black lines show the Tóth fits , Equation 6.10, used to calculate (b) the associated ΔH_{ads}. The fitting parameters for the Tóth fits are summarised for all measured samples in Table 9.1.

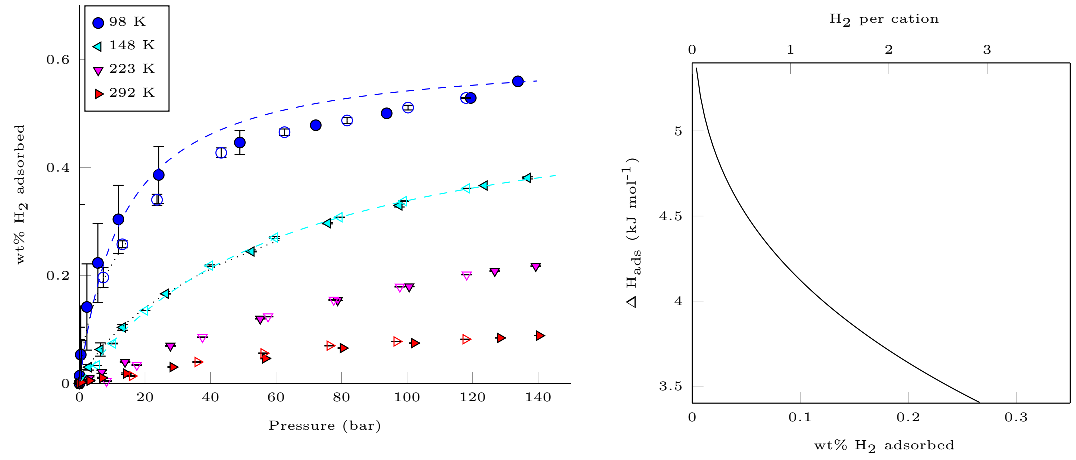

(a) Volumetric

(b) ΔH_{ads}

Figure 9.5: (a) Volumetric, high pressure isotherms measured at various temperatures for Mg-laponite (RD), with the filled markers representing adsorption and the open markers in the same colour the corresponding desorption. The dashed lines in the corresponding colours show the Langmuir fits, Equation 6.7, to the two coldest adsorption isotherms, while the dotted black lines show the Tóth, Equation 6.10, used to calculate (b) the associated ΔH_{ads}. The fitting parameters for the Tóth fits are summarised for all measured samples in Table 9.1.

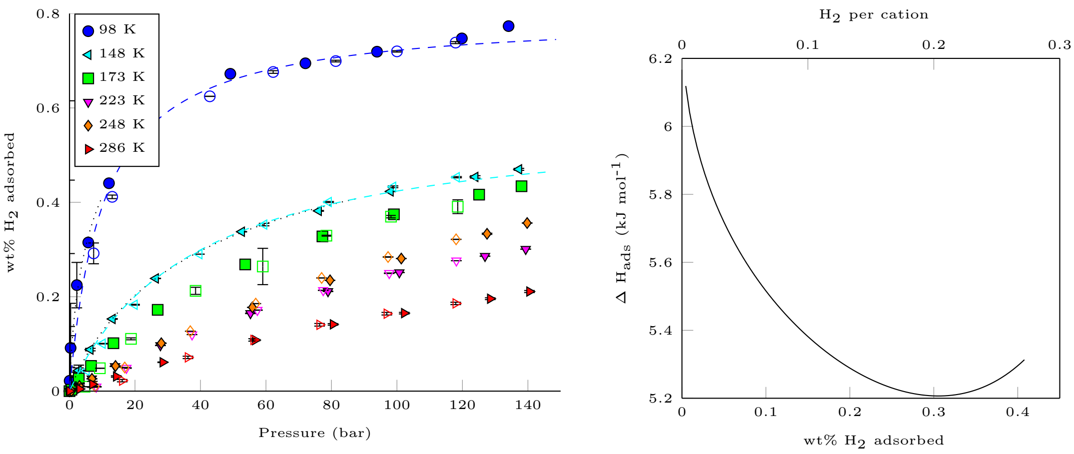

(a) Volumetric

(b) ΔH_{ads}

Figure 9.6: (a) Volumetric, high pressure isotherms measured at a range of temperatures for Mg-laponite (EL), with the filled markers representing adsorption and the open markers in the same colour the corresponding desorption. The dashed lines in the corresponding colours show the Langmuir fits, Equation 6.7, to the two coldest adsorption isotherms, while the dotted black lines show the Tóth fits, Equation 6.10, used to calculate (b) the associated ΔH_{ads}. The fitting parameters for the Tóth fits are summarised for all measured samples in Table 9.1.

Sample	**Temperature (K)**	**Saturation uptake (mole H_2)**	**Tóth constant k**	**Tóth constant m**	χ^2_{red}
Na-RD	100	1.31	0.25	0.73	577.55
Na-RD	150	1.03	0.03	0.91	7.53
Na-EL	145	0.65	0.03	0.66	1.41
Na-EL	250	0.48	0.01	0.82	32.12
Ca-RD	100	1.66	1.27	0.31	0.44
Ca-RD	150	0.77	0.03	0.78	0.54
Ca-EL	100	2.49	0.95	0.23	0.62
Ca-EL	150	2.28	0.01	0.44	0.07
Mg-RD	100	1.75	0.15	0.35	25.61
Mg-RD	150	1.38	0.02	0.51	1.02
Mg-EL	100	1.08	0.25	0.54	116.76
Mg-EL	150	0.74	0.03	0.81	10.89

Table 9.1: Summary of fitting parameters for the Tóth model, Equation 6.10, from which the ΔH_{ads} for the high pressure isotherms in Figures 9.1 through 9.6 were calculated. Some fits have unusually high χ^2_{red}, due to high variance in temperature, especially in the low coverage measurements.

9.2 Low pressure uptake

The Figures in this Section show low pressure isotherms collected up to 1 bar under a range of conditions (temperature, volumetric vs gravimetric) for twelve different forms of Laponite: three grades: (RD), (EL) and (B) for each of the four different interlayer cations: Na^+, Ca^{2+}, Mg^{2+} and Cs^+. Where more than one temperature isotherm was collected, the isosteric heat of adsorption has been calculated.

Figure 9.7 shows the low pressure gravimetric isotherms measured on only two laponite forms: Na-laponite (RD) and Mg-laponite (B). This method is extremely unreliable, with isotherms measured on the same sample and at the same temperature showing considerable variation, as is shown in Figure 9.7a. There are two observations which may shed light on the reasons for this variability. Firstly, it was extremely difficult to dry the clay and to keep it dry, even with the turbopump maintaining a high vacuum of less than 10^{-9} bar and secondly, after each isotherm's desorption had completed, the mass of the sample was always less than it had been before the same isotherm's adsorption run had begun. After heating the clay to the required pretreatment temperature, the clay was allowed to cool while under vacuum. However, the sample's mass gradually increased again over time, indicating that water vapour was being reabsorbed into the clay interlayers, despite the

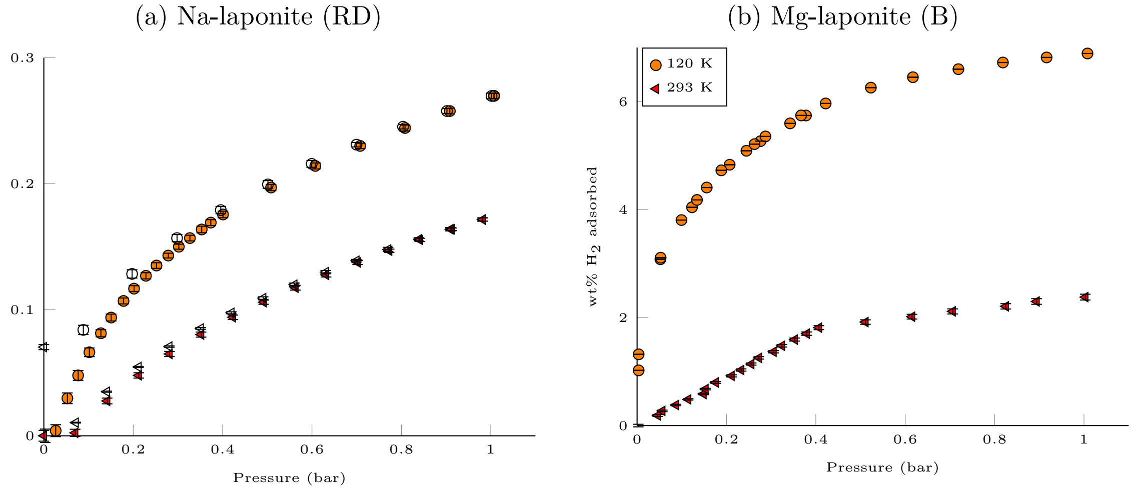

Figure 9.7: Low pressure gravimetric isotherms: a) shows isotherms taken at 77 K for two different batches of Na-laponite (RD), showing the variability in measurements and b) gives two isotherms taken at different temperatures for Mg-laponite (B). The uptake in the latter appears to be considerably higher than for the other forms of laponite, but the high degree of variability casts doubt on this estimate.

turbopump's action. It is therefore difficult to know the true water content of the clay before running isotherms and any reabsorption of water vapour would affect the mass of the sample during measurements. The post-isotherm return of the sample to a lower mass indicates that the isotherm process itself may assist with drying the clays. This is either due to the H_2 flushing the water out of the interlayers, or a freeze-drying process, due to the samples being rapidly cooled by immersion of the sample chamber in a dewar of cryogenic liquid. It is therefore recommended that alternate ways of drying the clays be considered for future isotherm measurements, for example gradual cooling using a reliable cryofurnace, as well the use of a mass spectrometer to analyse any escaping species in the outflow stream. Due to the unreliability of the current technique, the high uptake indicated by the isotherm measurement shown in Figure 9.7b must be treated with caution and confirmation is required.

Figures 9.8 through 9.13 show low pressure isotherms collected at two temperatures, 77 K (liquid N_2) and 87 K (liquid Ar), using the volumetric method. These isotherms were collected on the Quantachrome Autosorb iQ, discussed in Section 6.2.1, and are considered to be more reliable than those measured on the HTP, since immersion in a dewar of cryogenic liquid provides far more stable temperature control than that provided by the HTP's cryofurnace, however the rapid cooling issues mentioned above will still apply. The low pressure region is of particular interest for determining

Sample	1 bar, 77 K uptake (wt%)	Saturation uptake (wt%)[*]	ΔH_0 (kJ mol^{-1})[†]	ΔH_{ads} at 1H$_2$:cation (kJ mol^{-1}) [§]	ΔH_{ads} at 2H$_2$:cation (kJ mol^{-1})	Fit model
Na-RD	0.24	0.71 (0.60)	7.31	5.03 (5.77)	3.75	Tóth
Na-EL	0.32	1.25 (0.60)	7.29	6.94 (5.56)	5.40	Sips
Na-B	0.38	1.59	7.22	6.00	4.74	Sips
Ca-RD	0.23	0.45 (0.65)	7.70	5.32 (7.22)	5.22	Sips
Ca-EL	0.25	0.60 (0.80)	5.44	4.19 (6.14)	3.40	Tóth
Ca-B	0.27	0.38	8.74	6.98	5.62	Tóth
Mg-RD	0.27	0.95 (0.60)	6.21	4.94 (4.18)	4.38	Sips
Mg-EL	0.20	0.23 (0.80)	5.85	5.84 (5.55)	4.60	Sips
Mg-B	0.63	2.13	5.91	7.00	6.91	Sips
Cs-RD	0.34	1.66	6.36	5.37	4.14	Tóth
Cs-EL	0.39	1.86	5.86	5.75	5.11	Sips
Cs-B	0.41	1.52	8.07	6.17	5.04	Freundlich

[*] The number inside the brackets is the maximum uptake measured on the HTP for some samples, while the number to the left of the brackets indicates the saturation capacity extrapolated as a fitting parameter in the Sips model, Equation 6.9.

[†] Estimated from the minimum ΔH_{ads} extracted using the Clausius-Clapeyron relation (Equation 6.11) on the fits of a sixth order polynomial on two different temperature isotherms.

[§] The number to the left of the brackets is taken from the low pressure volumetric isotherms while the number inside the brackets derives from the high-pressure volumetric isotherms, for which the fits were less well matched to the low pressure region.

Table 9.2: Summary of H_2 storage capacities and binding enthalpies for a variety of laponite forms, based on the volumetric measurements presented in this Chapter. The rightmost column shows the model selected as the best match for each sample's low pressure volumetric adsorption isotherms, from which the ΔH_{ads} for 1 and 2 H_2 per cation was calculated.

the binding energy of the first few hydrogen molecules to reach the cations, which are expected to be the strongest adsorption sites.

In all cases, the Langmuir model gives the worst fit, confirming that the assumptions of this model do not apply for this material. The H_2 adsorption sites of the clay interlayer are expected to be heterogenous and the stronger interactions of the direct cation binding sites are not accounted for by the Langmuir model. Considering the region below 300 mbar, none of the models used in this study were found to give good fits and instead a sixth order polynomial function, having no physical meaning but enabling a more accurate extrapolation of the isotherm between points, was used to determine the low-coverage ΔH_{ads}. Over the full range measured, the Sips (Langmuir-Freundlich) model, Equation 6.9, was found to give better fits for about half of the samples, while the Tóth model (Equation 6.10) was the better match for the rest, with the exception of Cs-laponite (B), which appeared to follow the Freundlich model (Equation 6.8). The best full-range fitting model for each sample was used to extrapolate the data up to the higher coverages used in the neutron experiments, while the Sips model (Equation 6.9) was used for the extrapolation up to the saturation capacity, listed for each sample in Table 9.2. The justification of fitting model for extracting specific physical information and a comparison of fits to various models is given in Section 6.2.2.

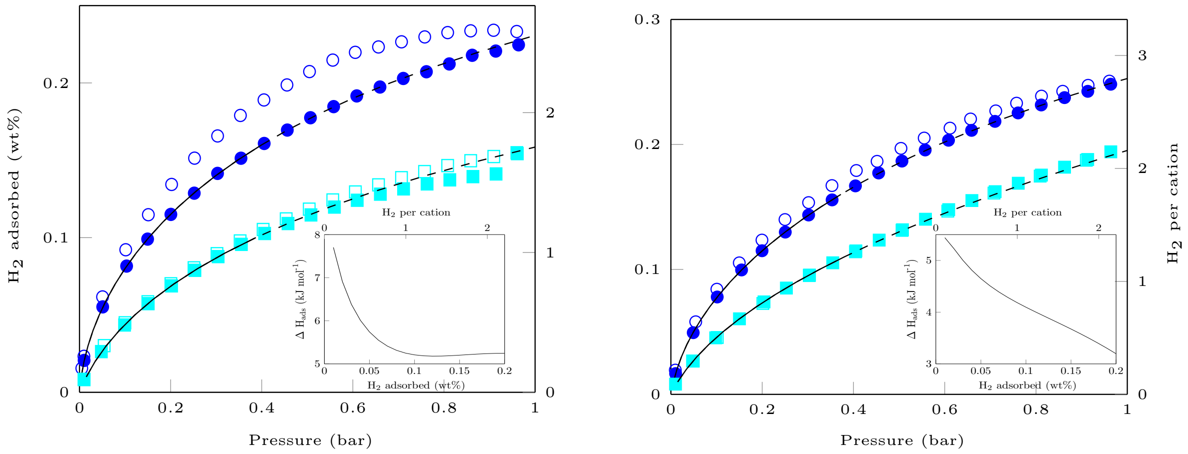
(a) Ca-laponite (RD)

(b) Ca-laponite (EL)

Figure 9.8: Volumetric, low pressure adsorption-desorption isotherms measured for two grades of Ca-laponite at two temperatures: 77 K (dark blue) and 87 K (cyan). The fits to a sixth order polynomial for a limited region only are shown by the solid lines and these are used to calculate the associated low-coverage ΔH_{ads}, shown in the insets as a function of coverage. In a), the dashed line shows the fit to the Sips (Langmuir-Freundlich) equation (Equation 6.9), whereas in b), the dashed line represents the Tóth model (Equation 6.10). Both of these fits match the data reasonably well over the full measured range, but give poor fits for the low coverage region.

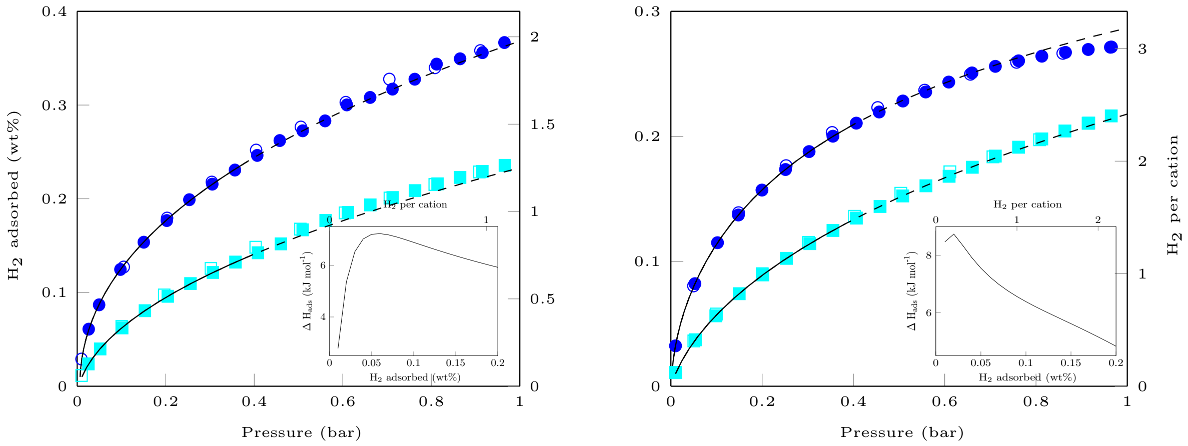
(a) Na-laponite(B)

(b) Ca-laponite(B)

Figure 9.9: Volumetric, low pressure adsorption-desorption isotherms measured for two cation forms of laponite (B) - a) Na and b) Ca - at two temperatures: 77 K (dark blue) and 87 K (cyan). The fits to a sixth order polynomial for a limited region only are shown by the solid lines and these are used to calculate the associated low-coverage ΔH_{ads}, shown in the insets as a function of coverage. In a), the dashed line shows the fit to the Sips (Langmuir-Freundlich) equation (Equation 6.9), whereas in b), the dashed line represents the Tóth model (Equation 6.10). Both of these fits match the data reasonably well over the full measured range, but give poor fits for the low coverage region.

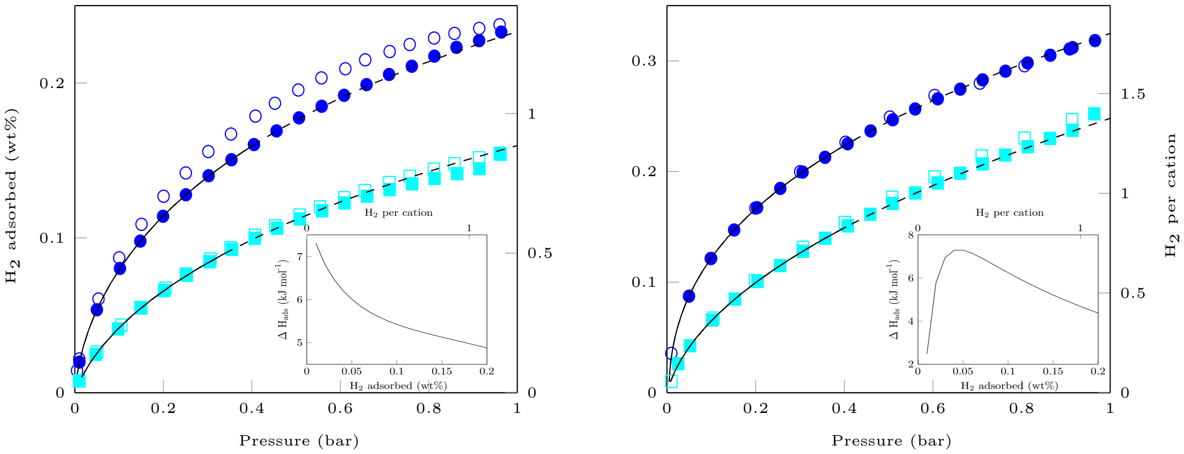

(a) Na-laponite (RD)

(b) Na-laponite (EL)

Figure 9.10: Volumetric, low pressure adsorption-desorption isotherms measured for two grades of Na-laponite - a) (RD) and b) (EL) - at two temperatures: 77 K (dark blue) and 87 K (cyan). The fits to a sixth order polynomial for a limited region only are shown by the solid lines and these are used to calculate the associated low-coverage ΔH_{ads}, shown in the insets as a function of coverage. In a), the dashed line shows the fit to the Tóth model (Equation 6.10), whereas in b), the dashed line represents the Sips (Langmuir-Freundlich) equation (Equation 6.9). Both of these fits match the data reasonably well over the full measured range, but give poor fits for the low coverage region.

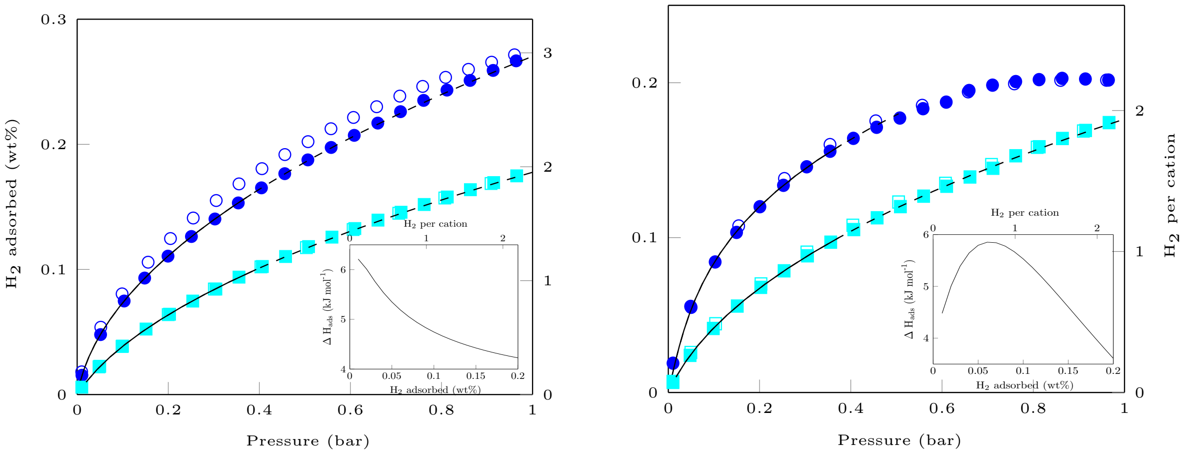

(a) Mg-laponite(RD)

(b) Mg-laponite(EL)

Figure 9.11: Volumetric, low pressure adsorption-desorption isotherms measured for two grades of Mg-laponite - a) (RD) and b) (EL) - at two temperatures: 77 K (dark blue) and 87 K (cyan). The fits to a sixth order polynomial for a limited region only are shown by the solid lines and these are used to calculate the associated low-coverage ΔH_{ads}, shown in the insets as a function of coverage. The dashed line shows the fit to the Sips (Langmuir-Freundlich) equation (Equation 6.9), matching the data reasonably well over the full measured range, but giving a poor fit for the low coverage region.

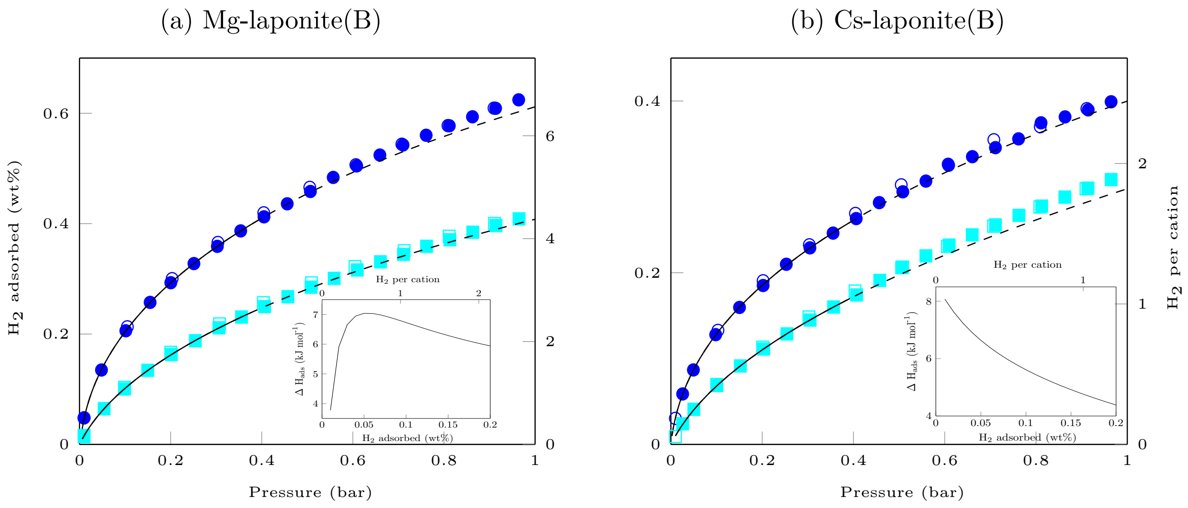
(a) Mg-laponite(B)

(b) Cs-laponite(B)

Figure 9.12: Volumetric, low pressure adsorption-desorption isotherms measured for two cation forms of laponite (B) - a) Mg and b) Cs - at two temperatures: 77 K (dark blue) and 87 K (cyan). The fits to a sixth order polynomial for a limited region only are shown by the solid lines and these are used to calculate the associated low-coverage ΔH_{ads}, shown in the insets as a function of coverage. In a), the dashed line shows the fit to the Sips (Langmuir-Freundlich) equation (Equation 6.9), whereas in b), the dashed line represents the Freundlich model (Equation 6.8). Both of these fits match the data reasonably well over the full measured range, but give poor fits for the low coverage region.

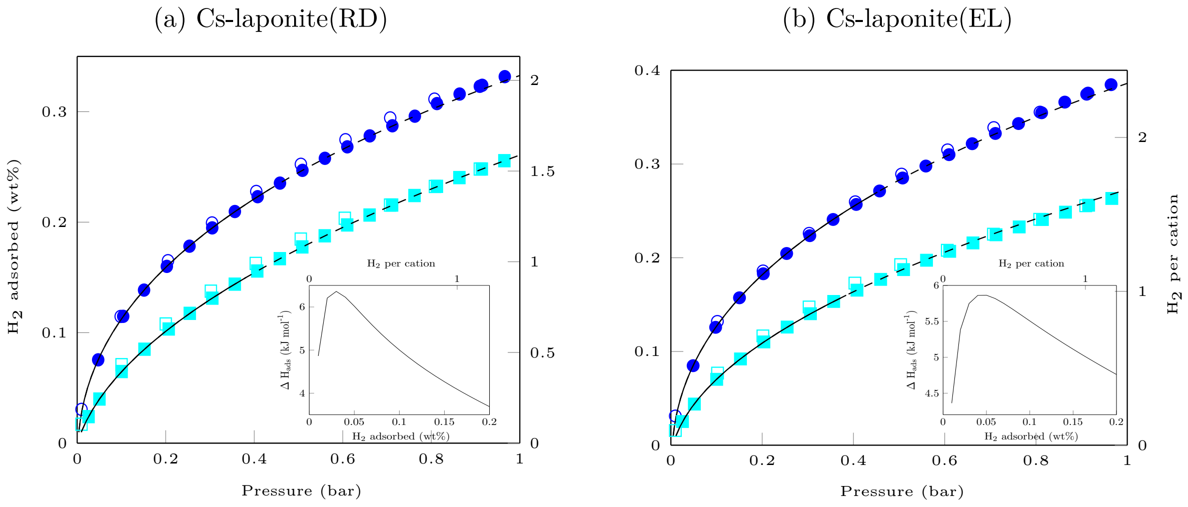
(a) Cs-laponite(RD)

(b) Cs-laponite(EL)

Figure 9.13: Volumetric, low pressure adsorption-desorption isotherms measured for two grades of Cs-laponite - a) (RD) and b) (EL) - at two temperatures: 77 K (dark blue) and 87 K (cyan). The fits to a sixth order polynomial for a limited region only are shown by the solid lines and these are used to calculate the associated low-coverage ΔH_{ads}, shown in the insets as a function of coverage. In a), the dashed line shows the fit to the Tóth model (Equation 6.10), whereas in b), the dashed line represents the Sips (Langmuir-Freundlich) equation (Equation 6.9). Both of these fits match the data reasonably well over the full measured range, but give poor fits for the low coverage region.

9.3 Hysteresis

Some slight hysteresis is apparent in the 77 K high pressure volumetric isotherms, at pressures below 60 bar. Low pressure volumetric 77 K isotherms of the sodium, calcium and magnesium forms of laponite grade (RD), Figures 9.10a, 9.8a and 9.11a respectively, show noticeable hysteresis. The hysteretic extent would need to be confirmed with repeat measurements, but they appear to follow the IUPAC type H4 pattern [89]. This is a typical pattern for Type I isotherms on materials having slit-like pores, such as activated carbons and this what is expected for clay mineral interlayers, which have essentially slit-like openings for H_2 intercalation. The changes in *d*-spacing observed in the NIMROD diffraction data for Ca-laponite (RD), shown in Figure 8.1, indicate some alteration in the pore dimensions and may explain the isothermal hysteresis.

Adsorption hysteresis is usually present in mesoporous systems, however desiccated laponite is largely nanoporous, as evident from the pore size distributions shown in Figure 9.14. Apart from the minimal hysteresis visible in the 77 K isotherm for Ca-laponite(EL) in Figure 9.8b, all other samples show no noticeable hysteresis at low pressures. In any case, the extent of the hysteresis is small in all isotherms, showing that this is a fully reversible storage mechanism for hydrogen.

9.4 Volumetric and gravimetric energy density

From the pressure-temperature data measured during the QENS experiment on Ca-laponite (RD) and considering only the volume of the interlayer region, the density of H_2 at 40 K is 67.5 kg m^{-3}, which is close to the theoretical limit of the density of liquid H_2, 70.97 kg m^{-3} [211]. This gives the adsorbate phase density under these conditions, however this density drops off rapidly with temperature, reaching only 6.29 kg m^{-3} at 100 K.

Table 9.3 compares the energy densities for the materials measured here with the literature values for a range of HSMs.

Material	ΔH_{ads} **(kJ mol^{-1}) at 1H$_2$:cation**	**Gravimetric energy density (wt% H$_2$)**	**Volumetric energy density (g H$_2$ l^{-1})**
Bulk liquid H_2 20 K, 1 bar [212]	-	-	70.97
MCM-41 (silica glass) [213]	-	0.58	-
AX-21 (activated C) [209]	5.5-6.5	5.5 (90 K, 100 bar)	20 (90 K, 100 bar)
Na-laponite (RD)	5.03	0.24	6.07
Na-laponite (EL)	6.94	0.32	8.10
Na-laponite (B)	6.00	0.38	9.61
Ca-laponite (RD)	5.32	0.23	5.82
Ca-laponite (EL)	4.19	0.25	6.32
Ca-laponite (B)	6.98	0.27	6.83
Mg-laponite (RD)	4.94	0.27	6.83
Mg-laponite (EL)	5.84	0.20	5.06
Mg-laponite (B)	7.00	0.63	15.94
Cs-laponite (RD)	5.37	0.34	8.60
Cs-laponite (EL)	5.75	0.39	9.87
Cs-laponite (B)	6.17	0.41	10.37
PFAC (activated C) [214]	14	0.2 (RT)	-
NaA zeolite	9.45 [215]	1.24 [216]	-
M'MOF 1 (Zn/Cu MOF)	12.29 [217]	1.3 (77 K, 100 bar)	-
IRMOF-20 (MOF)	-	6.7 (80 bar) [75]	34 (80 bar) [75]
MOF-177 (MOF) [218]	4.4	1.25	49 (78 bar)
MOF-324 (MOF) [218]	6.2	2.10	42 (78 bar)

Table 9.3: Volumetric vs gravimetric energy densities of a variety of physisorption materials at 77 K and 1 bar, unless otherwise stated.

9.5 Surface area and pore size distributions

Surface areas, modal pore sizes and pore volumes extracted from volumetric low pressure N_2 isotherms at 77 K using a standard DFT method on a variety of laponite forms are summarised in Table 9.4. The DFT model assumes a silica adsorbent surface and uses the NDLFT equilibrium corrections for cylindrical pores. The clay interlayer pores are expected to be slit-like, however this option for silica was not available in the software. This analysis procedure yields typical pore size distributions by volume, a few representative samples of which are displayed in Figure 9.14. These results show that clays are largely nanoporous and have high surface areas, although they only represent those pore volumes accessible to N_2. For this reason, a more analytical calculation of the surface area covered by the smaller H_2 molecule was employed, based on the crystallographic dimensions of the laponite unit cell and the adsorption amounts measured during the IRIS experiment on Ca-laponite. The *d*-spacing of laponite measured in Section 7.2 and 8.1 implies that the interlayers of partially hydrated laponite are pillared apart just enough to fit one monolayer of H_2. Since each H_2 is exposed to the surfaces of both the upper and lower interlayer, the surface area is effectively halved. These calculations estimate that H_2 covered 60% of the available surface. Since the surface area on the outer surfaces of the sparingly hydrated clay particles is significantly less than that available in the interlayers, this confirms that H_2 has intercalated into the interlayers.

Sample	**Surface area (m^2/g)**	**Pore width of mode (nm)**	**Pore volume (cc/g)**
Na-laponite (RD)	398.85±0.95	5.09±0.01	0.22±0.00
Na-laponite (EL)	474.72±0.84	1.33±0.00	0.24±0.00
Na-laponite (B)	458.19±0.45	1.56±0.00	0.20±0.00
Ca-laponite (RD)	394.66±0.61	2.58±0.00	0.21±0.00
Ca-laponite (EL)	392.17±0.61	2.58±0.00	0.22±0.00
Ca-laponite (B)	457.96±0.35	1.38±0.00	0.19±0.00
Mg-laponite (RD)	416.30±0.69	1.56±0.00	0.22±0.00
Mg-laponite (EL)	461.26±0.91	1.43±0.00	0.27±0.00
Mg-laponite (B)	895.79±1.01	1.43±0.00	0.35±0.00
Cs-laponite (RD)	479.83±0.67	1.33±0.00	0.26±0.00
Cs-laponite (EL)	513.51±0.54	1.33±0.00	0.23±0.00
Cs-laponite (B)	509.49±0.67	1.22±0.00	0.23±0.00

Table 9.4: Summary of the information extracted from a DFT model fit to the 77 K N_2 isotherms, for all samples measured.

While clay surface areas are high, they are an order of magnitude smaller than the typical 3000 m^2/g found in MOFs and super-activated carbons. This will limit the total uptake and therefore different structures of clays need to be investigated to find ways to enhance their adsorption surface areas while maintaining their chemical tunability and stability. The data in Table 9.4 shows that the surface areas of the caesium and (B)-grade forms tend to be larger, confirming the potential for this approach.

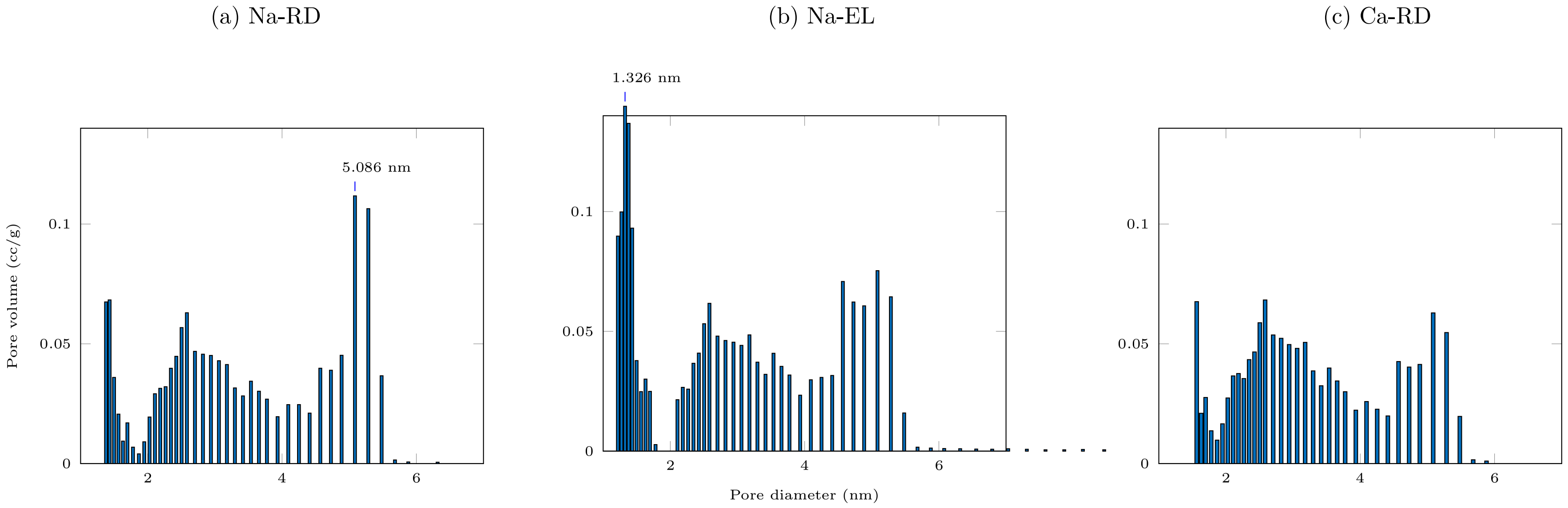
(a) Na-RD

(b) Na-EL

(c) Ca-RD

Figure 9.14: Interparticle pore size distributions by volume for a range of laponites: a) Na-laponite (RD), b) Ca-laponite (EL) and c) Cs-laponite (B), showing the modal pore widths for each. These clays are nanoporous, with an insignificant number of pores having a diameter in excess of 6 nm.

9.6 Chapter Summary

In this chapter, the results of isothermal data collected using both volumetric and gravimetric methods are presented and analysed through the use of a suite of isotherm models. For the high pressure isotherms, the best fits were obtained through the Langmuir and Tóth models. For low pressure isotherms, up to 1 bar, the Sips and Tóth models gave the best matches, but no one model provides a good fit consistently across all samples measured. In addition, few match the data over the full range of pressures measured, indicating that the assumptions of each model are not appropriate for the complexity of the adsorption sites presented by the clay interlayers. As a result, it was difficult to obtain a reliable measure of the isosteric heat of adsorption, which is especially sensitive to the fitting model. A more accurate estimate of ΔH_{ads}, particularly of H_0, was obtained by fitting a sixth order polynomial to the data for isotherms measured at two different temperatures.

For porous, physisorptive materials, ΔH_{ads} is expected to decrease with increasing coverage of the adsorption sites, as the strongest sites are filled first. This pattern was not always observed: for some measurements, ΔH_{ads} showed an increase with coverage, indicating either that the fitting models are not suitable, or that different binding mechanisms are involved in each sample, or that stronger sites are not readily accessible at first. This latter would be consistent with the findings presented in Chapter 8, in which the possibility of the interlayers being prized apart by the first intercalating molecules is suggested. A certain amount of energy, calculated from first principles calculations to be 2.88 kJ mol^{-1} per H_2 for the first 2.76 adsorbed molecules [219], would be required to expand the interlayer spacing. In this case, the first intercalating molecules will present a lower adsorption enthalpy. Some slight hysteresis is apparent in the full adsorption-desorption isotherms of the RD grades of laponite, which may be associated with interlayer expansion.

The shape of the isotherms suggests that a monolayer of hydrogen is adsorbed and the isothermal data reveal coverage of up to 60% of the available surface. Porosity measures confirm that the dried clays are nanoporous. The calculated ΔH_{ads} is in the range 4.19-7.00 kJ mol^{-1} for one hydrogen per cation, comparable to the values that can be achieved in MOFs [108] and graphite intercalates [51]. Surface area values are within the expected range for laponite clays, with the B grades having higher surface areas than the other grades. While the surface area calculated for Mg-laponite (B) is anomalously high, the uptake values for this sample are consistently also high, confirmed by two independent measurements using different techniques at 1 bar: 6.5 wt% using gravimetric isotherms at 120 K and 0.6 wt% using volumetric isotherms at 77 K, at least three times higher than for the other samples. The caesium form of laponite (B) also shows a high surface area and higher uptake than the other samples. These results, while possibly subject to experimental errors, indicate that laponite (B) has hydrogen uptake properties worthy of further investigation.

Lessons learned from the work presented in this chapter include the need for future analysis to rely more heavily on the desorption measurements of each isotherm and the need for more rigorous drying procedures. Temperature control at low vacuum is a well-known experimental problem, resulting in the low coverage points of each isotherm in the adsorption direction being less reliable. There were difficulties with controlling the water content of the clay after drying, which may have led to more than one water surrounding each cation before introduction of H_2 and a consequent underestimation of the adsorption enthalpy for a single hydrogen per cation.

10. DIFFUSION OF H_2 IN LAPONITE

QENS data for three different samples - Na-laponite (RD), Ca-laponite (RD) and Ca-laponite (EL) - were collected on IRIS and analysed using the procedures discussed in Section 6.3.2.

10.1 Samples and loadings

Na-laponite (RD)

Assuming that the clay, dried as explained in Section 6.1.2, has one remaining D_2O per interlayer cation, 8.20 g of Na-laponite (RD) represents 10.53 mmol of clay and 7.37 mmol of Na^+. At the time of dosing at 50 K, the pressure drop from 1 bar indicated that 31.31 mmol of H_2 had adsorbed to the material, giving a H_2:cation ratio of 4.25. On cooling to 40 K, slightly more was adsorbed (6.78 H_2:Na^+), dropping to 5.32 at 60 K and 4.29 at 80 K. Due to time constraints, it was not possible to measure this sample at 100 K.

Ca-laponite (RD)

A mass of 6.68 g of $(Ca^{2+})^{0.35}$ $[(Si_8\ Mg_{5.5}\ Li_{0.4})\ O_{20}\ (OH)_4]^{-0.7}.0.35D_2O.0.7H_2$ contains 8.64 mmol of clay (assuming one D_2O per cation) and 3.02 mmol of Ca^{2+}. In this experiment, the higher temperature of 100 K was measured first. The pressure differential indicated that 2.35 mmol of H_2 had adsorbed to the material, giving a H_2:cation ratio of 0.78. The sample was subsequently cooled in stages, increasing the adsorption amount to 1.97 H_2:Ca^{2+} at 80 K, 4.54 at 60 K and 8.34 at 40 K for QENS measurements.

Ca-laponite (EL)

A mass of 6.83 g Ca-laponite (EL) holds 8.76 mmol of clay (assuming one D_2O per cation and assuming that the cation density matches that of Na-laponite (RD)) and 6.13 mmol of Ca^{2+}. At the time of dosing at 50 K, 28.46 mmol of H_2 adsorbed to the material, giving a H_2:cation ratio of 4.64. On cooling to 40 K, slightly more was adsorbed (11.03 H_2:Ca^{2+}), dropping to 9.27 at 60 K, 8.08 at 80 K and 7.54 at 100 K. Due to time constraints, the 100 K was counted for half the usual time. Since at this temperature, the least amount of H_2 is retained, the resulting signal was too weak and is omitted from the fits.

10.2 Neutron scattering intensity

If all of the adsorbed H_2 lies in the beam, instead of being condensed elsewhere in the system, for instance in capillary piping, then the total intensity measured, after background removal, should correspond with the adsorption amount calculated from the pressure. Figure 10.1 compares two independent measures of the amount of H_2 present in all three samples: QENS and volumetric adsorption analysis. The adsorption amount was deduced from the difference between the dosed amount of hydrogen and the amount contained in the gas phase. This technique is valid as long as the temperature is above the critical point of H_2, thereby excluding pressure reduction by capillary condensation.

Figure 10.1 also shows the relationship of the measured elastic and quasielastic intensities with temperature, obtained from the fitted Lorentzians from all three samples. Both the intensity and adsorption data have been fitted to exponentials, which are superimposed on these plots and they correspond closely for Ca-laponite (RD), slightly less so for Na-laponite (RD), while being almost unmatched for the Ca-laponite (EL) sample. The closely matched data indicates that incoherent neutron scattering can provide an accurate measure of the amount of adsorbed H_2 in a material, however it is not clear why this does not apply to the high surface charge calcium laponite.

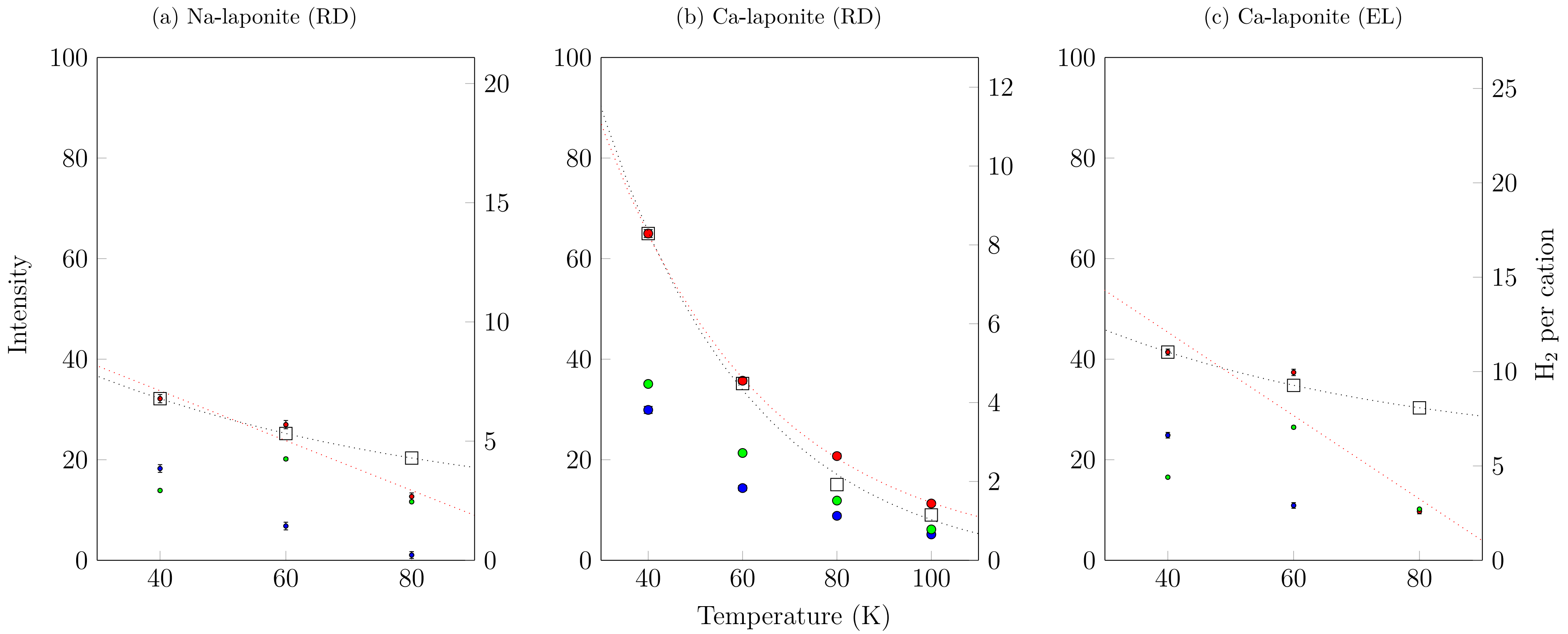
(a) Na-laponite (RD)

(b) Ca-laponite (RD)

(c) Ca-laponite (EL)

Figure 10.1: Insights from intensity and intensity ratios: the temperature-dependence of the intensity measured during QENS, showing the relative proportions attributed to elastic (blue) and quasielastic (green) scattering, as well as the total (red). The right-hand axis shows the corresponding ratio of adsorbed H_2 to Ca^{2+} cations in the clay. From simultaneous pressure measurements at each temperature and using Boyle's law, a rough estimate for this ratio can be obtained (open black squares), with a fitted exponential represented by the black dotted line. The red dotted line is a fitted exponential to the total intensity. The neutron scattering intensity and pressure are independent measures of the amount of H_2 present in the sample and these plots show how these data sets correspond. The match is best for Ca-laponite (RD), reasonable for Na-laponite (RD), but poor for Ca-laponite (EL).

The neutron data obtained for Ca-laponite (RD) indicates a stronger signal at all four temperatures, which suggests that this sample adsorbed more H_2 than the other two, however the adsorption data for Ca-laponite (EL) indicates that this sample adsorbed the most H_2. There is a large discrepancy between the adsorption data and the scattering intensity at 80 K, which seems to imply either that the H_2 was still present in the sample, but not visible in the beam, or that the adsorption data is overestimated, which could be caused by a leak. Since the system was rigorously leak-tested before placement in the beam, this seems unlikely, however a leak may have formed after the tests were performed. These discrepancies highlight the need for different data to be collected in parallel, where possible.

10.3 Jump diffusion models

Three jump diffusion models, Chudley-Elliott (C-E), Hall-Ross (H-R) and Singwi-Sjölander (S-S), discussed in Section 5.3.1, were applied to the background-subtracted results and the results of the fits for the Q^2-dependency of the FWHM over all measured temperatures for Na-laponite (RD), Ca-laponite (RD) and Ca-laponite (EL) are displayed in Figures 10.2, 10.3 and 10.4 respectively, with Tables 10.1, 10.2 and 10.3 giving the respective samples' fit parameters, calculated diffusion coefficient and statistical assessment for all three jump diffusion models. In addition, the trend expected for pure Fickian diffusion is represented by the straight red line on each graph, obtained by a linear regression fit on the two lowest Q-values. The Fickian model requires this line to pass through the origin.

T (K)	**Fit model**	L **(Å)**	τ **(ps)**	D **(Å^2 ps^{-1})**	**Red.** χ^2
80	**C-E**	3.01±0.24	2.27±0.17	0.66±0.09	2.36
	H-R	3.13±0.32	1.92±0.16	0.85±0.14	1.69
	S-S	3.35±0.43	1.60±0.15	1.17±0.24	1.16
60	**C-E**	2.91±0.26	3.89±0.37	0.36±0.06	3.21
	H-R	3.00±0.33	3.29±0.34	0.46±0.09	2.45
	S-S	3.15±0.44	2.72±0.31	0.61±0.14	1.73
40	**C-E**	2.49±0.36	5.39±0.99	0.19±0.05	1.93
	H-R	2.37±0.39	4.33±0.85	0.22±0.07	1.75
	S-S	2.37±0.49	3.47±0.77	0.27±0.10	1.50

Table 10.1: Comparison of parameters from three jump diffusion model fits to Na-laponite(RD) QENS data collected at three temperatures.

(a) 80 K

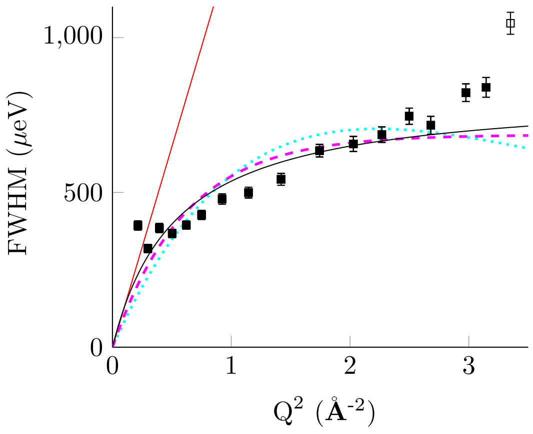

(b) 60 K

(c) 40 K

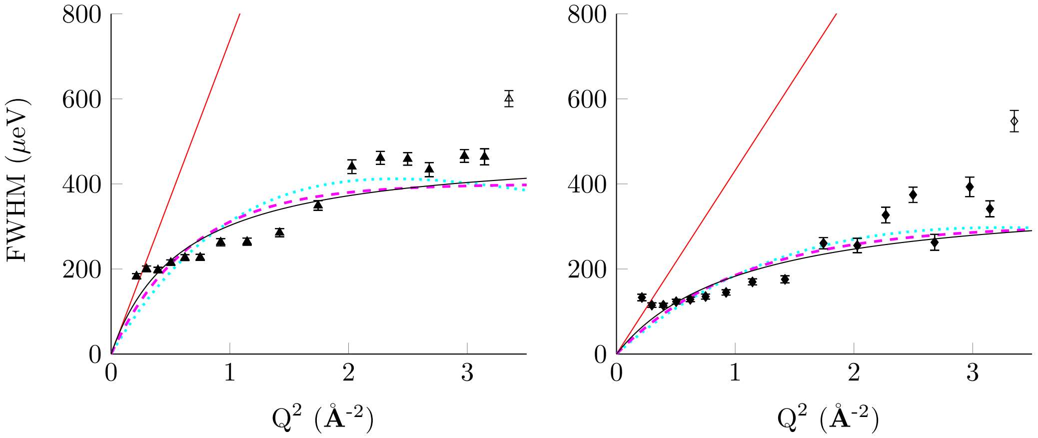

Figure 10.2: QENS FWHM data and fits for the four temperatures measured on Na-laponite (RD). Three of the models discussed in the text in Section 5.3.1 are shown for all temperatures: Singwi-Sjölander (solid black line), Chudley-Elliott (dotted cyan line) and Hall-Ross (dashed magenta line). The solid red line shows the Fickian diffusion model, obtained by a linear regression fit on the two lowest Q-values. The FWHM for spectral group 17 is shown as an open data marker, but this datum appears to be too broad for the instrument's window, as well as an outlier consistently across all temperatures and for Ca-laponite(EL) measurements too (see Figure 10.4. Consequently, this FWHM was omitted from the fits.

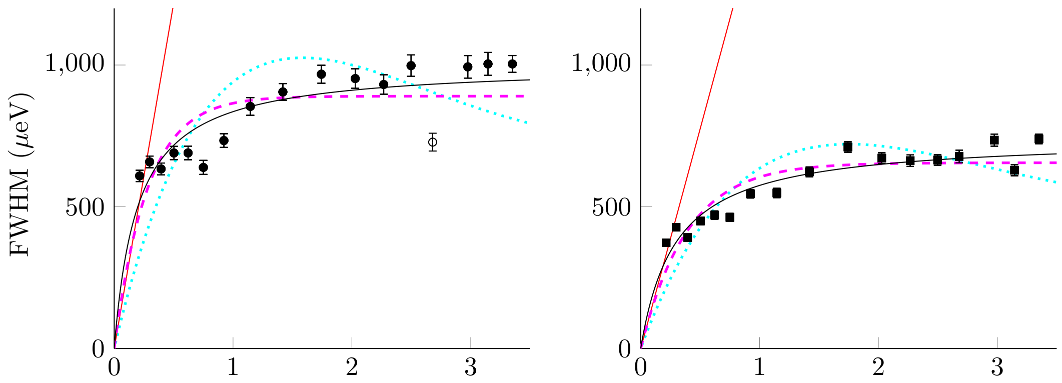
(a) 100 K

(b) 80 K

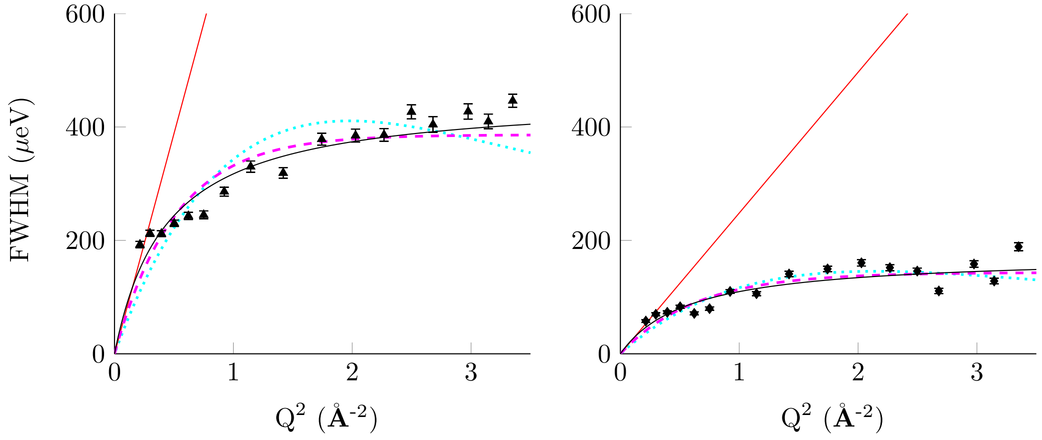
(c) 60 K

(d) 40 K

Figure 10.3: QENS FWHM data and fits for the four temperatures measured on Ca-laponite (RD). Three of the models discussed in the text in Section 5.3.1 are shown for all temperatures: Singwi-Sjölander (solid black line), Chudley-Elliott (dotted cyan line) and Hall-Ross (dashed magenta line). The solid red line shows the Fickian diffusion model, obtained by a linear regression fit on the two lowest Q-values, passing through the origin. The FWHM for spectral group 14 at 100 K is shown as an open data marker, but this datum appears to be an outlier and was omitted from the fits.

T (K)	**Fit model**	L **(Å)**	τ **(ps)**	D **(Å^2 ps^{-1})**	**Red.** χ^2
100	**C-E**	3.57±0.24	1.56±0.10	1.36±0.16	2.82
	H-R	4.63±0.42	1.48±0.07	2.42±0.33	1.12
	S-S	5.49±0.58	1.31±0.06	3.83±0.60	0.57
80	**C-E**	3.39±0.18	2.22±0.11	0.86±0.08	2.57
	H-R	3.92±0.26	2.01±0.09	1.27±0.13	1.17
	S-S	4.52±0.36	1.77±0.08	1.93±0.23	0.63
60	**C-E**	3.19±0.18	3.90±0.22	0.44±0.04	2.86
	H-R	3.43±0.24	3.41±0.19	0.57±0.07	1.60
	S-S	3.72±0.30	2.89±0.17	0.80±0.10	0.87
40	**C-E**	3.07±0.18	11.01±0.65	0.14±0.01	1.77
	H-R	3.07±0.27	9.18±0.69	0.17±0.03	1.49
	S-S	3.21±0.40	7.59±0.73	0.23±0.05	1.28

Table 10.2: Comparison of fitting parameters from various jump diffusion models applied to QENS data from H_2 diffusing in Ca-laponite(RD), collected at four temperatures.

T (K)	**Fit model**	L **(Å)**	τ **(ps)**	D **(Å^2 ps^{-1})**	**Red.** χ^2
80	**C-E**	3.36±0.25	2.29±0.15	0.82±0.10	2.88
	H-R	4.04±0.40	2.07±0.13	1.31±0.20	1.56
	S-S	4.64±0.59	1.80±0.12	1.99±0.38	0.90
60	**C-E**	3.26±0.21	3.56±0.22	0.50±0.06	3.91
	H-R	3.61±0.28	3.14±0.19	0.69±0.09	2.06
	S-S	3.91±0.35	2.65±0.16	0.96±0.13	1.06
40	**C-E**	2.84±0.30	5.40±0.64	0.25±0.05	3.21
	H-R	2.88±0.37	4.54±0.58	0.30±0.07	2.62
	S-S	3.05±0.51	3.78±0.55	0.41±0.12	1.98

Table 10.3: Comparison of parameters from three jump diffusion model fits to Ca-laponite(EL) QENS data collected at three temperatures.

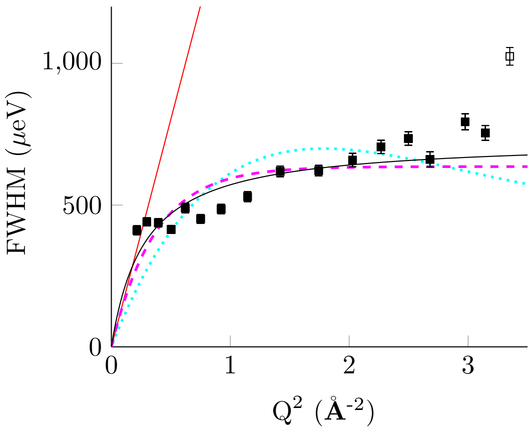
(a) 80 K

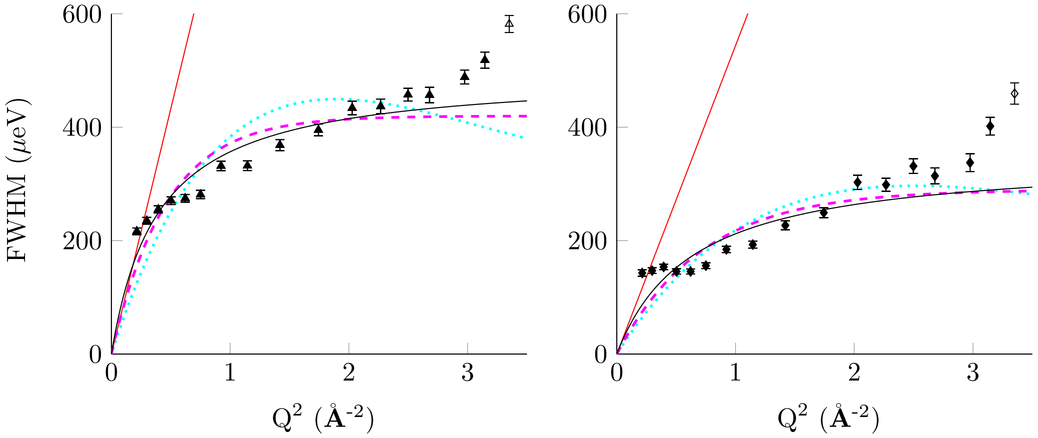
(b) 60 K
(c) 40 K

Figure 10.4: QENS FWHM data and fits for the four temperatures measured on Ca-laponite (EL). Three of the models discussed in the text in Section 5.3.1 are shown for all temperatures: Singwi-Sjölander (solid black line), Chudley-Elliott (dotted cyan line) and Hall-Ross (dashed magenta line). The solid red line shows the Fickian diffusion model, obtained by a linear least-squares regression fit on the two lowest Q-values, passing through the origin. The FWHM for spectral group 17 is shown as an open data marker, but this datum appears to be too broad for the instrument's window, as well as an outlier consistently across all temperatures and for Na-laponite (RD) measurements too (see Figure 10.2). Consequently, this FWHM was omitted from the fits.

All jump diffusion models applied to the data gave a much better fit than the Fickian model, so the motion is likely to be constrained by the clay surface in some way. The C-E model gives a comparatively poor fit and the best least-squares nonlinear regression fit is given by the S-S model in almost all cases, although the statistical assessment for the H-R model is similar. The C-E model, assuming a single jump length, can therefore be ruled out and it is clear that a distribution of hopping distances are available to the hydrogen molecules. This seems appropriate, given the complexity of the clay interlayer surface and the fact that the interlayer cations are not known to be ordered in any way, being randomly spaced over the hexagonal surfaces of the tetrahedral sheets [220].

The H-R and S-S models give very similar average jump lengths, with the H-R model predicting longer residence times, leading to slower diffusion coefficients in all cases. The difference between the H-R and S-S models is slightly more pronounced in the calcium form compared with the sodium form and are generally greater at higher temperatures. The S-S model consistently predicts longer average jump lengths and shorter average residence times for all four temperatures. The latter parameter results in the S-S model's faster diffusion coefficients.

10.4 Temperature trends in diffusion

Selecting the S-S model as the most appropriate, comparisons can be made between samples and temperatures. Figure 10.5 summarises the Q^2-dependencies of the FWHM of the QENS components of the spectra for Na-laponite (RD), Ca-laponite (RD) and Ca-laponite (EL). The fit parameters and diffusion coefficients for the Singwi-Sjölander model, as well as two independently determined estimates [221] [212] for the diffusion coefficient for bulk liquid H_2, are summarised in Table 10.4, the S-S diffusion coefficients being repeated so as to enable easy comparison.

D **(Å^2 ps^{-1})**	**100 K**	**80 K**	**60 K**	**40 K**
$D_{Na-laponite(RD)}$	-	1.17±0.24	0.61±0.14	0.27±0.10
$D_{Ca-laponite(RD)}$	3.83±0.60	1.93±0.23	0.80±0.10	0.23±0.05
$D_{Ca-laponite(EL)}$	-	1.99±0.38	0.96±0.13	0.41±0.12
D_{bulk} [221]	6.29	5.61	4.62	3.14
D_{bulk} [212]	5.48±0.84	4.90±0.84	4.07±0.83	2.80±0.82

Table 10.4: Temperature dependency of diffusion coefficients, in (Å^2 ps^{-1}), of H_2 in all laponite samples measured by QENS. Estimated diffusion coefficients for bulk liquid H_2 from two independent studies are also shown, for comparison.

Sample	**Red.** χ^2	**Intrinsic diffusivity (Å^2 ps^{-1})**	E_a **(kJ mol^{-1})**	E_a **(K)**
Bulk [212]	-	8.58±0.98	0.37±0.01	45±2
Bulk [221]	-	10.00	0.38	46
MCM-48 (silica glass) [223]	-	40.31	0.56±0.02	67±3
Activated C [224]	-	2.10±0.30	0.64±0.07	77±9
Na-laponite (RD)	0.30	4.98±0.52	1.00±0.26	120±32
Carbon black, XC-72 [225]	-	19.00±2.00	1.03±0.07	112±5
Ca-laponite (EL)	27.26	8.92±0.78	1.06±0.36	128±43
Exohedral SWCNT [226]	-	51.50±7.40	1.12±0.04	135±5
HD on Grafoil [222]	-	64.30±7.60	1.26±0.17	152±20
Ca-laponite (RD)	0.80	20.92±0.68	1.56±0.23	188±28
PFAC (activated C) [214]	-	14.06±2.24	1.62±0.01	195±2
NaA zeolite [227]	-	6.10	1.90	240
M'MOF 1 (Zn/Cu MOF) [228]	-	-	13.35±0.59	1606±71
MIL-53 (Cr) (MOF) [229]	-	-	1.6	190

Table 10.5: Results of an Arrhenius analysis on the diffusion coefficients, calculated from QENS measurements, showing the activation energies indicated by the linear regression fits of $-ln(D)$ vs $\frac{1000}{T}$.

The observed departure from Fickian diffusion suggests that H_2 interacts with the clay and this is further confirmed by the diffusion coefficients calculated from the S-S fit parameters which are, at all measured temperatures, lower than the corresponding value for bulk liquid H_2.

The temperature dependence of the measured diffusion coefficient is shown in Figure 10.6, with a comparison to the published values for bulk [212] and a few representative H_2-adsorbing materials. A classical Arrhenius model for diffusion constrained by an energy barrier (Equation 6.6) was used to extract the activation energies (E_a). The results are presented in Table 10.5, again comparing them with the values for bulk liquid H_2 and some representative H_2-adsorbing materials. The activation energies for all laponite samples exceed those found in bulk liquid hydrogen and also, in the case of Ca-laponite (RD), exceed that of H_2 diffusing in the activated carbon, XC-72. The activation energy for Ca-laponite (RD) lies between Grafoil [222] and PFAC, an activated carbon derived from polyfurfuryl alcohol [214]. Exfoliated graphite has only weak interactions with H_2, its layered structure providing little molecular confinement, while PFAC has pores smaller than 7 Å and may incorporate functional groups in its pores which provide stronger binding sites. If these functional groups can be identified, then it may be possible to incorporate them into the laponite interlayers to strengthen the adsorption interaction.

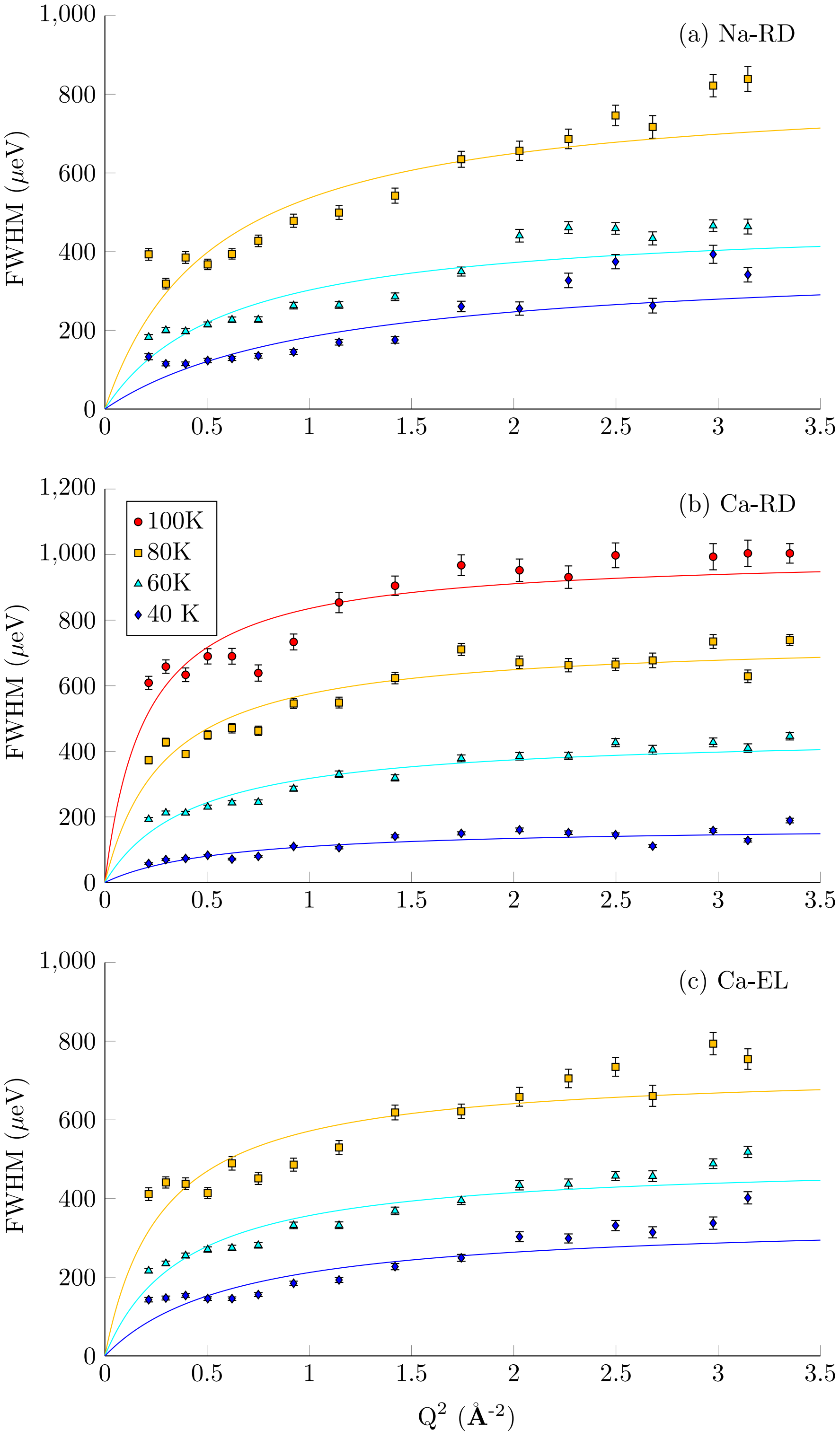

Figure 10.5: Q^2-dependence of the broadening of the quasielastic components measured at a range of temperatures per sample, showing fits to the Singwi-Sjölander jump diffusion model (solid lines). The blue diamonds represent measurements taken at 40 K, cyan triangles represent 60 K, orange squares for 80 K and red circles for measurements at 100 K.

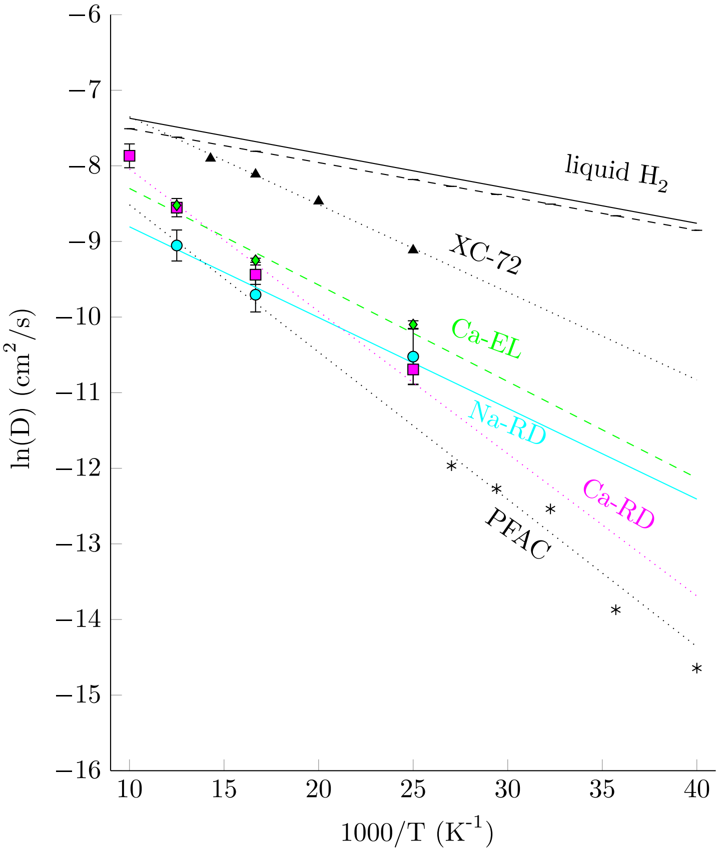

Figure 10.6: Temperature dependence of the diffusion coefficient, measured by QENS, for H_2 in Na-laponite (RD) (cyan circles), Ca-laponite (RD) (magenta squares) and Ca-laponite (EL) (green diamonds), showing Arrhenius analysis for each set of data. The diffusion coefficients for bulk liquid H_2 extrapolated to the same temperatures are represented by the top two lines: a solid black line [221] and a dashed black line [212]. Also shown are the data from two studies of hydrogen-adsorbing materials: an activated carbon, PFAC [214], shown as black asterisks, and a carbon black, XC-72 [225], shown as black triangles. Both sets of data are joined by a dotted black line representing their regression analyses.

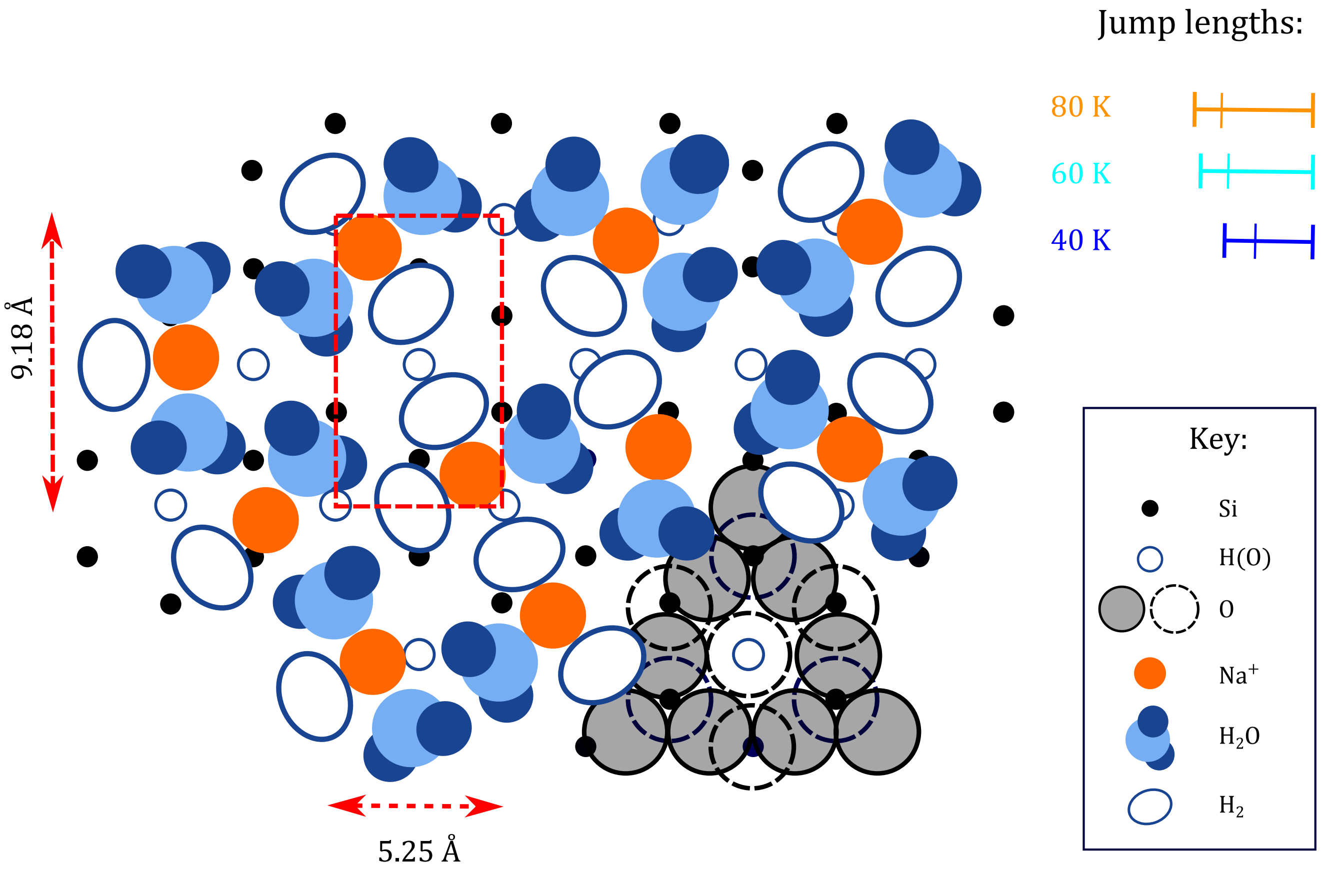

Figure 10.7: Proposed geometric arrangement of the interlayer region (top view) for Na-laponite (RD), with all components drawn to scale. The water molecules are tilted, because in the clay interlayer, the hydrogen atoms would lie in a plane orthogonal to the page, as is seen in the side view illustration in Figure 4.2. The full hexagonal structure of the inner interlayer surface, deriving from the Si-O tetrahedra, is shown for only one hexagon at the bottom right. The remaining hexagons are simplified to show only their Si framework and OH centres. The laponite unit cell is represented by the red dashed-line rectangle and its dimensions [184] are given by the arrows below and to the left. Interlayer Na^+ (orange circles), shown as evenly but randomly distributed at approximately 0.7 per unit cell, forms complexes with H_2O (blue) and H_2 (white ovals outlined with blue). In order to illustrate the theoretical possibilities, some complexes have three waters and one H_2, others have two waters and two hydrogen molecules and a few have three H_2. The measured jump lengths from the fitted QENS data at all four temperatures is shown to scale on the right, with the double line representing the uncertainty in each measurement.

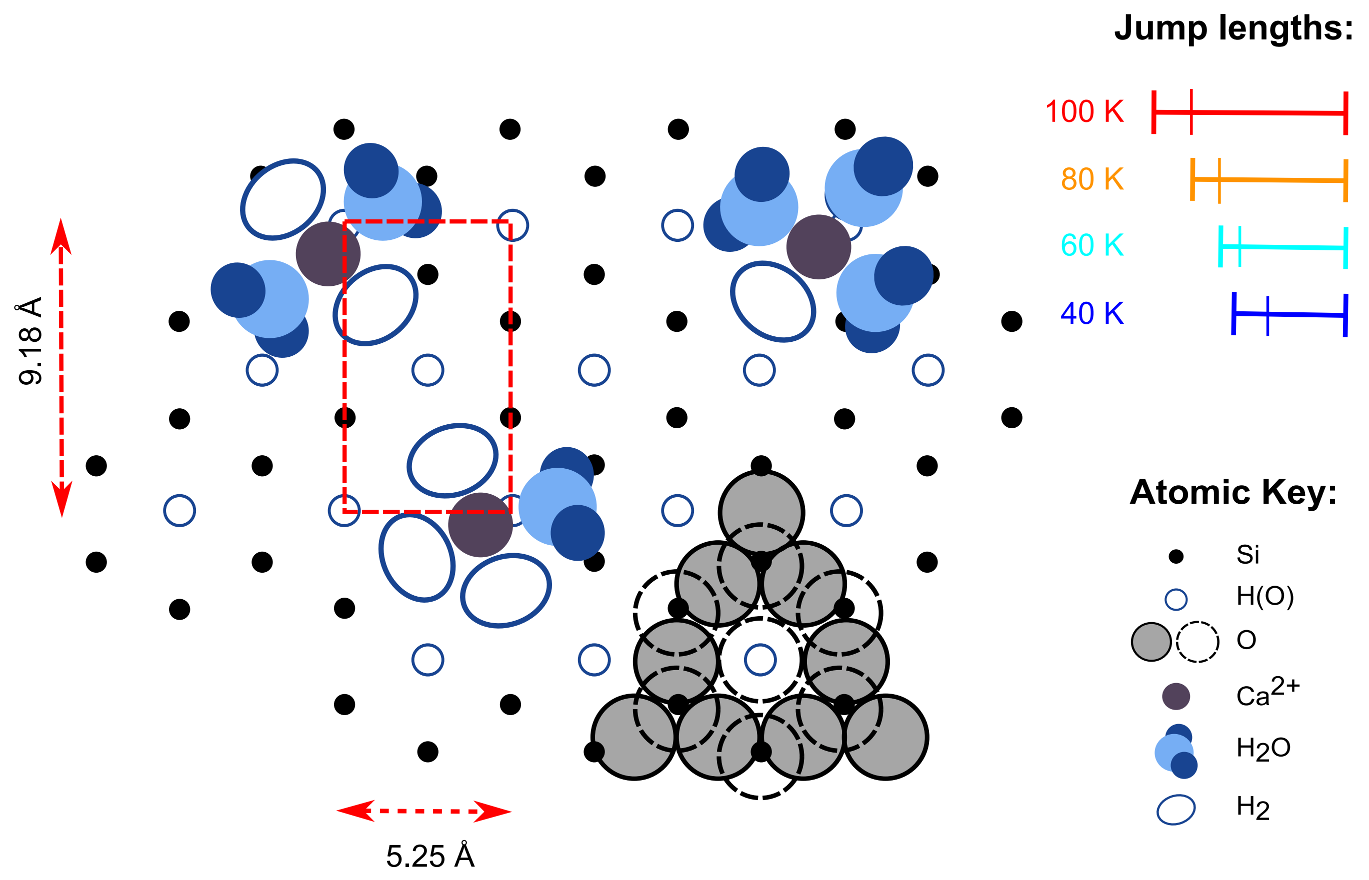

Figure 10.8: Proposed geometric arrangement of the interlayer region (top view) for Ca-laponite (RD), with all components drawn to scale. The water molecules are tilted, because in the clay interlayer, the hydrogen atoms would lie in a plane orthogonal to the page, as is seen in the side view illustration in Figure 4.2. The full hexagonal structure of the inner interlayer surface, deriving from the Si-O tetrahedra, is shown for only one hexagon at the bottom right. The remaining hexagons are simplified to show only their Si framework and OH centres. The laponite unit cell is represented by the red dashed-line rectangle and its dimensions [184] are given by the arrows below and to the left. Interlayer Ca^{2+} (purple circles), shown as evenly but randomly distributed at approximately 0.35 per unit cell, forms complexes with H_2O (blue) and H_2 (white ovals outlined with blue). In order to illustrate the theoretical possibilities, one complex is shown with two waters and two hydrogen molecules, another with three H_2 and the third with three waters and one H_2. The measured jump lengths from the fitted QENS data at all four temperatures is shown to scale on the right, with the double line representing the uncertainty in each measurement, the range taken over both calcium-exchanged laponites: (RD) and (EL).

10.5 Structure from QENS

The geometric implications of the data obtained from the jump diffusion fit are summarized in Figure 10.7 for the sodium form and Figure 10.8 for the calcium form. The distribution of the cations presented in this diagram has been estimated from the crystallographic structure: each unit cell contains 0.7 Na^+ or 0.35 Ca^{2+} and there is no evidence of ordering of the hydration complexes in laponite [220].

At 80 and 60 K, the jump length is long enough for hops between both cation complexes and hexagon centres. At 40 K, the jump lengths are shorter, possibly requiring an intermediate hop to a hexagon centre when moving between cation complexes.

In the calcium form, at all temperatures measured, the estimated jump length is sufficient for the H_2 to jump between adjacent hexagons. At 100 K, the measured jump length is long enough for H_2 to jump between cation complexes in a single hop, but lower temperatures may require intermediate hops.

10.6 Restricted motion

The plots in Figure 10.9 show the Q-dependence of the EISF for two different temperatures. The background has been removed, to eliminate any Bragg peaks and the EISF at $Q = 0$ is assumed to be 100%. These data clearly show the elastic component which persists in the Ca-laponite (RD) up to 100 K and is also present in the Na-laponite (RD) and Ca-laponite (EL) measurements, but is largely lost at temperatures above 60 K and at high Q for these latter two samples.

A reasonable fit (χ^2_{red}= 4.37) to the 40 K data for Ca-laponite (RD) (solid blue line in Figure 10.9 (b)) can be obtained by combining the powder-averaged models for localised two- [155] and three-site [156] rotational diffusion, discussed in Section 5.3.1. The radius of gyration estimated by the low temperature fits is consistently ~2.2-2.8 Å, suggesting that this may be between sites around the cation, however caution must be applied to the interpretation of these data. This suggests two populations of confined H_2, but the close similarity of the data at all measured temperatures appears to contradict this, since the population having a lower binding energy would be expected to disappear at higher temperatures, considerably altering

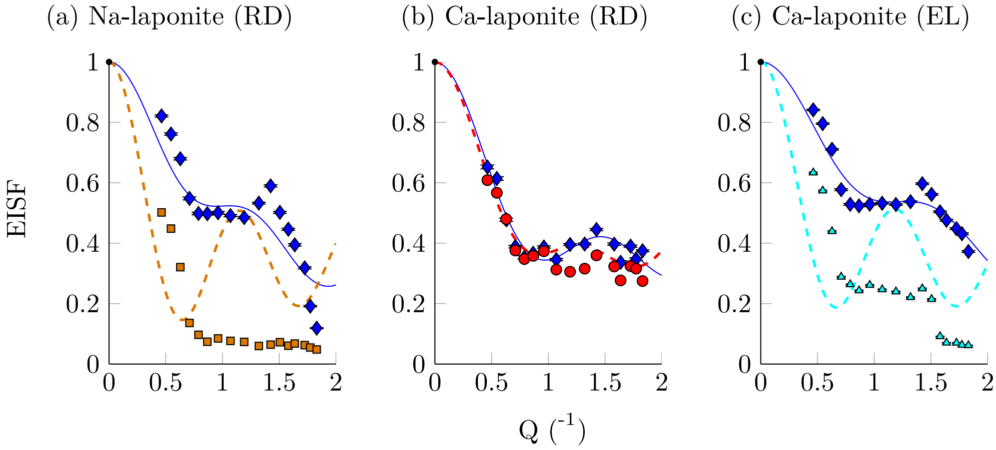

Figure 10.9: The Q-dependence of the EISF at two temperatures per sample. The blue diamonds represent measurements taken at 40 K, cyan triangles represent 60 K, orange squares for 80 K and red circles for measurements at 100 K, with fits (solid lines for the lower temperature; dashed lines for the higher temperature) to a combination of the 2-site and 3-site models explained in Section 5.3.1. The low-Q point at unity is a requirement of the fit. The fits seem reasonable for the low temperature data, but are untenable at higher temperatures. For Ca-laponite (EL) at 80 K, the elastic component disappears for Q > 1 Å^{-1}, thus only the 40 K and 60 K data are shown for this sample.

the form of the fit. In addition, for higher temperatures, such as the Ca-laponite (RD) 100 K data (dashed red line in Figure 10.9b), the fits were not sufficiently robust and had poor statistics.

The only clear conclusion which can be drawn from these data is regarding the presence of a strong elastic component at higher temperatures. Bulk liquid H_2 QENS, obtained on IRIS in 2007 [93], shows little or no elastic scattering, whereas a 1 bar H_2 atmosphere in deuterated Ca-laponite (RD) at all four supercritical temperatures has a clear elastic component, indicating a significant immobile H_2 population on the timescales of this instrument. Similarly, Na-laponite (RD) and Ca-laponite (EL) have immobile H_2 populations, but these are released at lower temperatures.

10.7 Effect of cation and surface charge on diffusion mechanism

It is difficult to tease out cation effects from surface charge effects, because in some respects, Na-laponite (RD) more closely matches Ca-laponite (EL) than Ca-laponite (RD), while in others, Ca-laponite (RD) and Ca-laponite (EL) match each other more closely. Both Na-laponite (RD) and Ca-laponite (EL) samples appear to lose their immobile H_2 populations before reaching 100 K, while Ca-laponite (RD) retains a significant elastic signal up to this temperature. This implies that Na-laponite (RD) and Ca-laponite (EL) have lower average binding energies for hydrogen than Ca-laponite (RD). Similarly, the activation energies are highest (188 K) in Ca-laponite (RD). The jump diffusion parameters are roughly similar for all three samples. The EISF data for Na-laponite (RD) and Ca-laponite (EL) match each other more closely than do either for Ca-laponite (RD), but none reach zero, indicating the presence of an immobile H_2 population in all three up to 60 K.

The amount of Ca-laponite (RD) loaded matches that for Ca-laponite (EL) (6.68 and 6.83 g, respectively), but the signal from the H_2 adsorbed to calcium-exchanged laponite is stronger at higher temperatures for the RD grade, suggesting that the H_2 desorbs from Ca-laponite (EL) at lower temperatures. The EL grade has a higher surface charge due to a larger density of interlayer cations and this may increase the energy barrier for H_2 to intercalate into the interlayers, since they are held together more closely by the stronger electrostatic forces.

The intrinsic diffusivity of the samples varies from 4.98 ± 0.52 in Na-laponite (RD) and 8.92 ± 0.78 in Ca-laponite (EL) to 20.92 ± 0.68 in Ca-laponite (RD), nearly four times as much. Thus the form having the lowest cation density, and therefore fewer hinderances to H_2 diffusivity, allows the greatest mobility of H_2 of the three. Looking at the lower temperature data for these samples, both the jump lengths between sites and the residence times at each site are greatest in Ca-laponite (RD) and smallest in Na-laponite (RD), however the error margins are large and only general trends can be taken from this data. The cations in Ca-laponite (RD) are further apart, thus the observation that the hopping distances are also longer in this sample lends weight to the model of H_2 binding to the cation-water complexes. Longer residence times may suggest stronger binding sites and this is expected for the divalent cation forms, both of which show longer residence times at 80 K and 40 K.

10.8 Insights from QENS

The quasielastic neutron spectrum of Ca-laponite (RD) reveals two populations of H_2: one which is immobile up to 100 K and the other diffusing in accordance with a jump diffusion model. In all samples and temperatures measured, the jump diffusion models provide a better fit than Fick's law, confirming that there is some degree of surface interaction. The Chudley-Elliott model gives a poor match to the data in all cases, suggesting that a single jump length cannot be assumed and that some form of distribution of the jump lengths is present, consistent with the complexity of the surface presented by the clay interlayer. While it is difficult to rule out the H-R model, since the χ^2_{red} values are very similar, the improved statistics for the S-S fit across all temperatures and all samples suggests that the exponential distribution proposed by the S-S model describes the jumping mechanism of H_2 in laponite more accurately than the Gaussian distribution of the H-R model. Small jumps occur frequently, while large jumps are rare. The physical interpretation for this model is that the diffusing molecules alternate between oscillatory motion involving small jumps and directed motion requiring larger jumps [161]. One possible interpretation in the context of H_2 diffusion in laponite is that the H_2 molecules oscillate between the closely-spaced binding sites around a single cation-water complex, making larger, less frequent translational hops between complexes.

The neutron scattering intensity generally correlates well with the uptake values calculated from the concurrent pressure and temperature measurements. At 100 K, the diffusion rate, calculated from the fitting parameters (jump length and residence time), is only slightly less than the rate in bulk liquid hydrogen. At 40 K, the diffusion rate is an order of magnitude slower than that for bulk, while the temperature and pressure data reveal an uptake of 0.76 wt% at 40 K. Considering only the volume of the interlayer, this constitutes a hydrogen density of 67.5 kg m^{-3}, close to the density of 70.97 kg m^{-3} for bulk liquid hydrogen [212]. The temperature dependency of the diffusion rate is close to that of a nanoporous activated carbon, PFAC.

Analysis of the EISF reveals a radius of gyration of 2.2-2.8 Å, consistent with rotation around the cations, however further analysis shows contradictory results. The Q^2-dependency suggests that more than one rotational motion is present, while the FWHM Q^2-dependency indicated only two populations: one immobile and the other diffusing by translational motion, thus no rotational motions. In addition, the Q^2-dependency of the EISF does not change between 40 and 100 K, which is unexpected.

Comparing the results for the different samples shows that the hydrogen uptake characteristics for Na-laponite (RD) and Ca-laponite (EL), both having a higher cation density, match each other more closely than either match with Ca-laponite

(RD). The higher cation density may make intercalation through these samples slower, due to an increased number of interactions. There may be more interactions between the hydrogen molecules surrounding each cation, giving rise to more repulsive interactions and a reduced adsorption enthalpy, resulting in a lower desorption temperature and activation energy.

11. CONFIRMATION OF H_2 BINDING FROM INS

This Chapter presents and compares results from INS experiments on three forms of sparsely hydrated laponite: Na-laponite (RD), Ca-laponite (RD) and Ca-laponite (EL). The free rotor peak, centred at 14.74 meV [37], for the neutron-facilitated para- to ortho-H_2 transition of unbound H_2 falls within the inelastic window. Any deviation of this peak indicates interaction between molecular hydrogen and an adsorption site or between adjacent H_2 molecules, providing information on the strength of H_2 adsorption sites and the symmetry of the local environment. Given the complexity of the systems studied here, the spectra presented in this Chapter are surprisingly simple, being relatively easy to fit and showing a remarkable degree of consistency across samples and temperatures.

11.1 Binding sites for Na-laponite (RD)

9.90 g of Na-laponite (RD), representing 12.74 mmol of this clay and containing 8.91 mmol interlayer Na^+, was measured at a single loading of 3 H_2:Na^+ and the spectra and fits, along with the residuals, are shown in Figure 11.1. Four binding sites for H_2 are clearly visible and the consistency of fits across all temperatures strengthens their validity. It is unclear why the inclusion of two narrow peaks at higher loadings is necessary, but some possibilities have already been discussed in Section 6.3.3, as part of the data treatment.

The fitted peak parameters and the splitting between hindered rotor pairs are presented in Table 11.1, showing the high degree of consistency of the peak positions across all temperatures. The validity of site 1 will need to be confirmed by examining the inelastic neutron spectrum at energy transfers between 20 and 30 meV, to locate the non-degenerate peak which is the hindered rotor pair for the degenerate peak visible in these spectra. The absence of a free rotor peak at 14.74 meV indicates that all H_2 present in the beam is hindered in some way by adsorption to the laponite and that there are no H_2 interacting only with each other, as they would do in the solid.

When the sample is heated up to the highest temperature reading, 48 K, the pressure increase indicates that approximately one-eighth of the hydrogen desorbs. The fit for the 48 K spectrum shows a marked difference in the position of the peaks compared with the spectra for the lower temperatures, reflecting the fact that the reduction in H_2 density has altered the adsorption environment. The intensity of the largest central peaks, representing the weakest adsorption site (referred as site 4 in Figure 11.1 and Table 11.1) remains roughly constant over the lower three temperatures, but drops significantly at 48 K, while the intensities of the peaks for site 3 do the opposite, indicating that now a larger proportion of the total is adsorbed to the latter, stronger adsorption site. This pattern is typical of adsorption, since weaker sites are expected to desorb before stronger sites through thermal activation. The intensity of the strongest site, site 1, remains largely constant over all temperatures, as does the intensity for the pair of peaks for site 2. These two sites do not appear to have been thermally activated at these temperatures. The splittings between all paired peaks has reduced, indicating that the sites remaining have lower barriers to rotation, on average. This may be due to fewer H_2-H_2 interactions. The narrow peak centred at ~13 meV is reduced, indicating that this feature is linked to a higher H_2 density.

The relative positions of the paired peaks reflects the symmetry of the adsorption site. For sites 1, 2 and 4, the $m_J = 0$ peak has shifted to a higher energy. This is typical of a 2D planar rotor, with hindering in a single dimension, increasing the energy barrier to rotation in this dimension. This is the pattern expected for cation adsorption and there are three sites which display this pattern, which may indicate that there are three different adsorption sites around the cation, varying in strength. The Na^+-D_2O-H_2 complex could provide a variety of binding sites, due to multiple configurations allowing both D_2O-H_2 and H_2-H_2 interactions to occur and some cations may have no D_2O, depending on how well the sample was dried. Site 3 has the pattern of a 1D-rotor, since the $m_J = \pm 1$ peak has shifted to the higher energy, indicating that there are rotational hinderances in two dimensions. This pattern could be expected for adsorption between the surfaces of the laponite interlayer, or for adsorption to a cation which has more than one H_2 surrounding it. The

(a) 6 K (reduced χ^2: 14.43) (b) 9 K (reduced χ^2: 9.78)

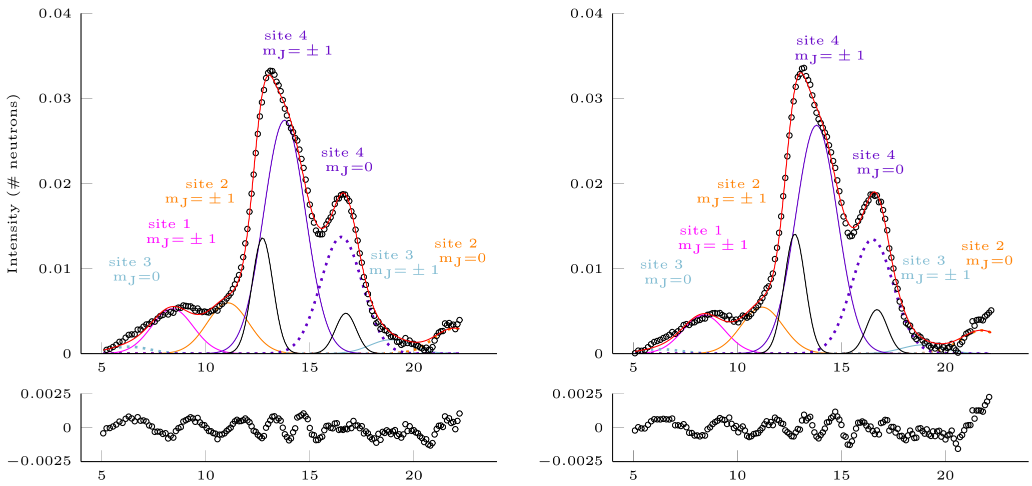

(c) 23 K (reduced χ^2: 9.78) (d) 48 K (reduced χ^2: 5.7)

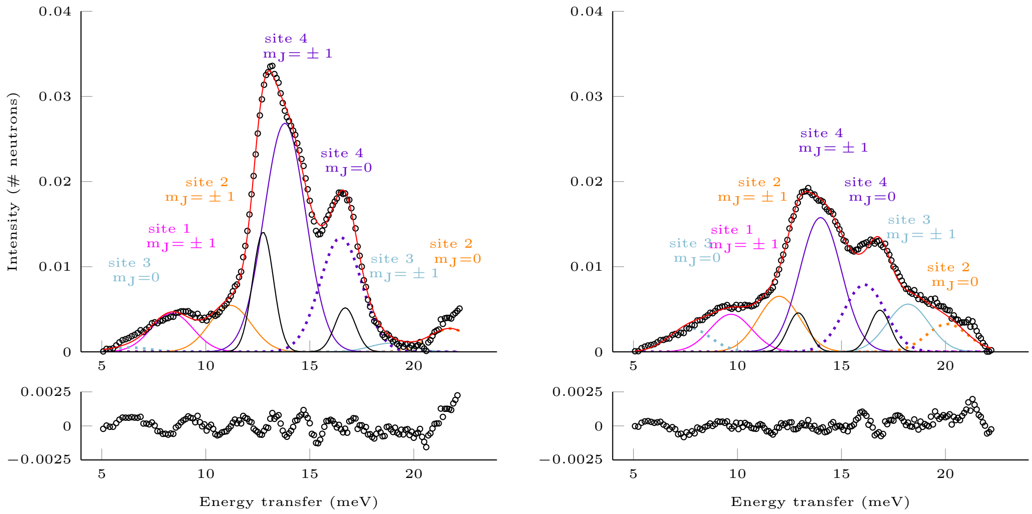

Figure 11.1: INS data and fits for Na-laponite (RD) in a 12 bar H_2 atmosphere (3 H_2:Na^+), showing the consistency of fitted peak positions over four temperatures, ranging from 6-48 K. A polynomial background was removed before fitting a set of paired Gaussian peaks, following the constraints of the quantum model for the H_2 hindered rotor and with the width fixed at 2.35 meV (selected by choosing the best fit from a series of fits run at different fixed values). The black circles are the measured data points, the superimposed solid red line is the full fit and the pairs of Gaussian peaks are colour-matched. The doubly-degenerate peak of each pair is shown by a solid line and its corresponding non-degenerate peak as a dotted line in the same colour. Corresponding with the numbering of sites presented in Table 11.1, site 1 is shown in magenta, site 2 in orange, site 3 in light blue and site 4 in dark blue. Some peaks appear to be unpaired (magenta and orange for lower temperatures), presumably because their corresponding peaks lie outside the measured energy transfer window. The free rotor peak, centred at 14.74 meV, is absent in each case. Note that the scale on the residuals is slightly different from the main plots.

T	Splitting (meV)	Amp. (x10^{-}3)	Centre (meV)	Amp. (x10^{-}3)	Centre (meV)
Site 1		$m_J = 0$		$m_J = \pm 1$	
6 K	*18.92±0.05*	*2.64±0.14*	*27.31±0.05*	5.27±0.14	8.39±0.05
9 K	*18.96±0.05*	*2.27±0.14*	*27.34±0.05*	4.54±0.14	8.38±0.05
23 K	*18.96±0.05*	*2.27±0.14*	*27.34±0.05*	4.54±0.14	8.38±0.05
48 K	*15.04±0.05*	*2.21±0.14*	*24.73±0.05*	4.42±0.14	9.69±0.05
Site 2		$m_J = 0$		$m_J = \pm 1$	
6 K	10.90±0.05	2.98±0.13	21.97±0.05	5.97±0.13	11.07±0.05
9 K	10.56±0.05	2.73±0.14	21.74±0.05	5.47±0.14	11.18±0.05
23 K	10.56±0.05	2.73±0.14	21.74±0.05	5.47±0.14	11.18±0.05
48 K	8.08±0.04	3.27±0.20	20.09±0.04	6.53±0.20	12.01±0.04
Site 3		$m_J = 0$		$m_J = \pm 1$	
6 K	12.60±0.12	0.82±0.17	6.30±0.12	1.63±0.17	18.90±0.12
9 K	12.62±0.20	0.51±0.17	6.29±0.20	1.02±0.17	18.91±0.20
23 K	12.63±0.20	0.51±0.17	6.28±0.20	1.02±0.17	18.91±0.20
48 K	10.51±0.03	2.80±0.18	7.69±0.03	5.61±0.18	18.20±0.03
Site 4		$m_J = 0$		$m_J = \pm 1$	
6 K	2.73±0.01	13.72±0.31	16.52±0.01	27.45±0.31	13.79±0.01
9 K	2.69±0.01	13.43±0.33	16.49±0.01	26.85±0.33	13.80±0.01
23 K	2.69±0.01	13.43±0.33	16.49±0.01	26.85±0.33	13.80±0.01
48 K	2.12±0.02	7.89±0.29	16.11±0.02	15.78±0.29	13.99±0.02

Table 11.1: Comparison of hindered rotor peak parameters from the fits to the INS spectra for Na-laponite(RD) in a 12 bar H_2 atmosphere (3 H_2:Na^+), at four different temperatures. A fixed width of 2.35 meV was used in these fits. The amplitude and centre of each peak is given, as well as the separation between their centres. The numbering of the sites matches those in Figure 11.1. The text in italics is data requiring confirmation, owing to the non-degenerate peak of the pair being outside the measured energy window.

potential for such a complex is as yet unknown, but may provide this symmetry, with interactions with the other bound H_2 molecules causing the additional rotational hinderance. Thus the adsorption sites in Na-laponite (RD) vary not only in strength, but also in structure. The strengths of the barrier potential for each site and their symmetries are summarised for this and the two other samples in Table 11.5.

11.2 Binding sites for Ca-laponite (RD)

For this sample, 9.35 g was loaded onto the beam, representing 12.16 mmol clay and 4.26 mmol of interlayer Ca^{2+}, and subjected to a single loading of 1 H_2:Ca^{2+}. This was measured at four temperatures and the spectra and their decomposition for the energy transfer window of 10 - 20 meV are presented in Figure 11.2, with the fit results summarised in Table 11.2. The INS signal is very clear and fittings could be performed with just four, unconstrained Gaussian peaks closely fitting the expected quantum model for two hindered rotor adsorption sites: each pair of peaks having

T	Splitting (meV)	Amp. (x10^{-}3)	Centre (meV)	Width (meV)	Amp. (x10^{-}3)	Centre (meV)	Width (meV)
Site 1		$m_J = 0$			$m_J = \pm1$		
5 K	3.95±0.03	6.18±0.33	17.34±0.03	1.07±0.04	15.75±0.12	13.40	1.34±0.01
10 K	3.87±0.04	9.32±0.21	17.28±0.04	1.51±0.08	19.32±0.31	13.41±0.02	1.43±0.03
25 K	3.85±0.05	7.61±0.17	17.30±0.04	1.58±0.09	15.23±0.23	13.45±0.02	1.52±0.03
50 K	3.90±0.17	1.29±0.08	17.27±0.10	1.60±0.26	2.37±0.70	13.38±0.14	1.22±0.14
Site 5		$m_J = 0$			$m_J = \pm1$		
5 K	1.82±0.10	4.17±0.00	14.65±0.04	1.41	2.98±0.34	16.47±0.09	1.41
10 K	1.26±0.17	5.61±0.00	14.65±0.10	1.41	4.31±0.33	15.91±0.13	1.41
25 K	1.06±0.31	3.05±0.00	14.78±0.20	1.41	2.53±0.36	15.84±0.24	1.41
50 K	1.47±0.69	1.20±0.00	14.20±0.41	1.41	0.37±0.12	15.67±0.56	1.41

Table 11.2: Comparison of fit parameters for four Gaussian peaks, resulting from the fits to the INS spectra over four different temperatures for Ca-laponite(RD) in a 2 bar H_2 atmosphere, giving a loading of $1H_2$:Ca^{2+}. The amplitude and centre of each peak is given, as well as the separation between the paired hindered rotor peak centres. With the exception of the widths of the peaks for site 5, the fits were unconstrained, allowing all other parameters to vary. Uncertainties have been included only where they exceed 0.01 meV.

the expected amplitude ratios and shifts from the free rotor centre. The stronger site closely matches the weakest site, site 4 of Na-laponite (RD), whereas the weaker site, numbered here as site 5, has no analogue in either of the other two samples. When a Gaussian representing this site was included in the fits, the intensity of this peak was always very close to zero or negative, implying that it is not required to improve the fit.

The symmetry of the single adsorption site in Ca-laponite (RD) is typical of a 2D planar rotor, having an energy barrier to rotation in a single dimension. The sample has a low loading of 1 H_2 per Ca^{2+} and the cations in this sample are more spread out, with three unit cells sharing a single cation. Thus the signal from this sample is very clear, showing a single adsorption site having an INS pattern typical of cation adsorption. There are no H_2-H_2 interactions, since each cation is bound to at most one H_2 molecule and sufficiently far from neighbouring cations for the Ca^{2+}-D_2O-H_2 complexes to interact. However, it is also possible that the stronger sites seen in the other two samples would be present in this sample, too, if it had not been exposed to air on transfer from the vacuum oven to the sample can for IN4, allowing it to reabsorb water which may have adsorbed to the stronger sites. The transferral process was more rigorously controlled in the other two samples. This possibility can only be excluded by repeating the experiment with this sample, using the more rigorous transferral process. The strengths of the barrier potential for each site and their symmetries are summarised for all three samples in Table 11.5 and discussed further in Section 11.4.

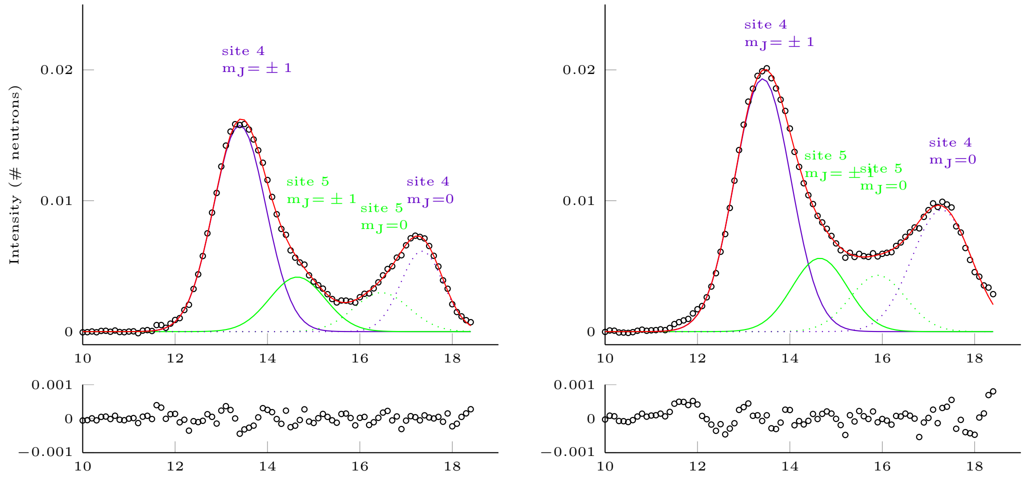

(a) 5 K (reduced χ^2: 0.82)

(b) 10 K (reduced χ^2: 2.32)

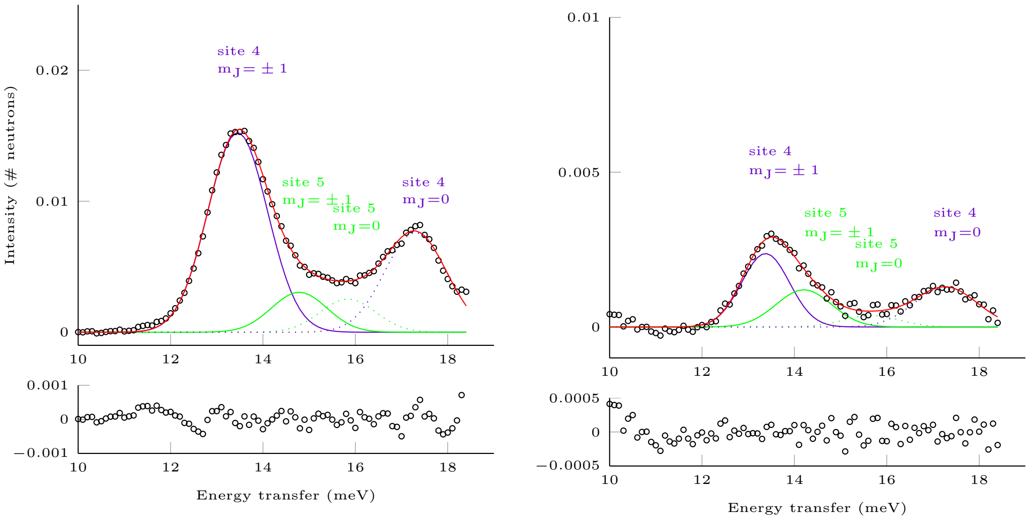

(c) 25 K (reduced χ^2: 1.86)

(d) 50 K (reduced χ^2: 1.01)

Figure 11.2: INS data and fits for Ca-laponite (RD) in a 2 bar H_2 atmosphere (1 H_2:Ca^{2+}), showing the consistency of fitted peak positions over four temperatures, ranging from 5-50 K. The background (clay measured in vacuum) was removed before fitting two pairs of unconstrained Gaussian peaks. The dimensions and energy shifts of the pairs of peaks match the hindered rotor model. The black circles are the measured data points and the superimposed solid red line is the full fit. The singly-degenerate peaks of the hindered rotor pairs are shown by a dotted line and its corresponding doubly-degenerate peak as a solid line in dark blue for site 4, colour-matched with its corresponding site in Na-laponite (RD) (see Figure 11.1) and in green for site 5, which has no analogue in the other two samples. No other inelastic peaks were visible in the range 0 - 20 meV. Note that the scale on the residuals is slightly different from the main plots and that the scale for 48 K is almost double that of the other three temperatures.

11.3 Binding sites for Ca-laponite (EL)

A sample of 8.2704 g of this clay, representing 10.76 mmol Ca-laponite (EL) and containing 3.77 mmol of interlayer Ca^{2+}, was subjected to a range of loadings and each at the same four temperatures as for the other two samples, allowing comparisons of low to high H_2 density conditions. The lowest loading, holding less than 1 H_2:Ca^{2+}, is shown in Figure 11.4, showing that all four binding sites, closely matching those found in Na-laponite (RD), are already present. The spectra and fits for two higher loadings are shown in Figures 11.4 and 11.6, for 1 and 9 H_2:Ca^{2+}, respectively, in which the consistency of the fits across all four temperatures can be seen. Note that these loadings are calculated based on the only compositional formula available for Ca-laponite (EL). Since this sample has a higher surface charge density, the number of cations per unit cell should be higher, reducing the loading ratios, but the exact figures could not be calculated without knowing the precise composition. A ratio of 9 H_2's per Ca^{2+} seems unlikely and is more likely to be closer to 5 H_2:Ca^{2+}, taking saturation into account. Figure 11.5 shows the consistency of the fits across four different loadings at 6 K. The fit parameters for the highest loading are given in Table 11.3. Lower loadings have very similar parameters and are omitted here for brevity.

Generally, a trend is expected in which the stronger sites fill up first and the weakest last, however it seems all sites fill up almost simultaneously in this sample. The same four sites found in Na-laponite (RD) are present in this sample and even at a loading where some cations have no H_2 to interact with and none have more than one. It seems unlikely that all four sites can be attributed to cation adsorption, although this structure may reflect the random distribution of Ca^{2+}-D_2O complexes in submonolayer hydrated laponite: some cations will have no D_2O and some will have one. Some cations may form denser pockets. The overall density of cations in this high surface charge sample is greater than that for Ca-laponite (RD), resulting in a more complex adsorption landscape as a consequence of overlapping potentials, such as H_2-H_2 interactions or H_2-D_2O interactions. However, as mentioned in Section 11.2 above, this complexity may simply be visible in this sample because its exposure to water vapour in the air was less than a minute, compared with 5-10 minutes for Ca-laponite (RD).

Looking at the differences across all four temperatures, the spectrum and fits are almost identical between 6 and 23 K, but for 48 K, the relative intensities of the

(a) 6 K (reduced χ^2: 1.21) (b) 9 K (reduced χ^2: 1.14)

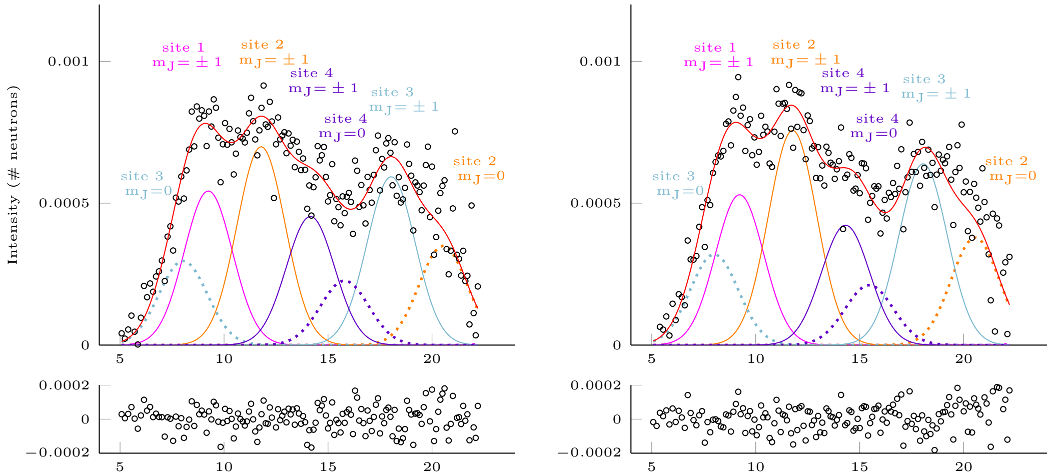

(c) 23 K (reduced χ^2: 1.08) (d) 48 K (reduced χ^2: 1.49)

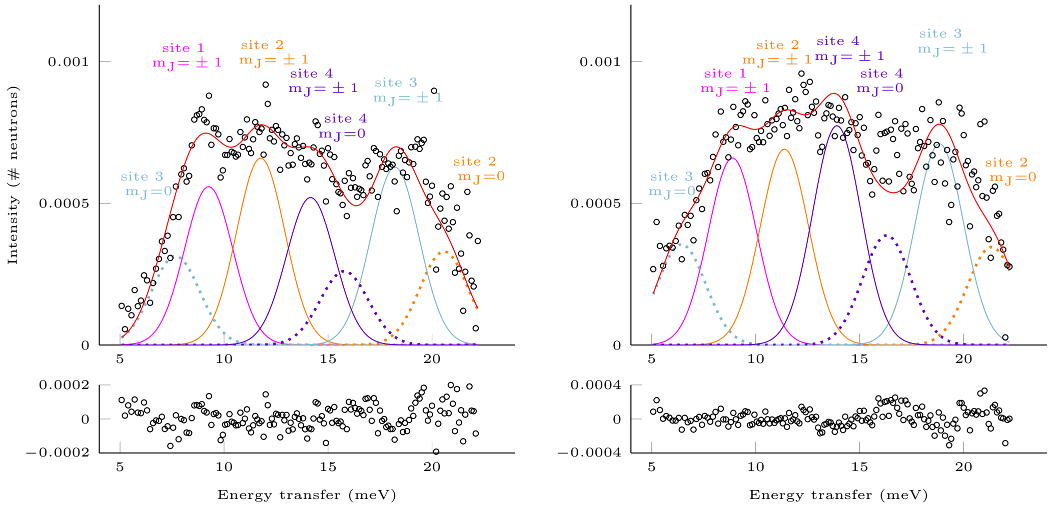

Figure 11.3: INS spectra and fits for Ca-laponite (EL) in a 0.5 bar H_2 atmosphere (<1 H_2:Ca^{2+}), showing the consistency of fitted peak positions across four temperatures, ranging from 6-48 K. A polynomial background was removed before fitting a set of paired Gaussian peaks, following the constraints of the quantum model for the H_2 hindered rotor. The start parameters for these fits were derived from the results at higher loadings, because the data is less clear and a reasonable fit could probably be obtained from a variety of Gaussian sets. The black circles are the measured data points, the superimposed solid red line is the full fit and the pairs of Gaussian peaks are colour-matched. The doubly-degenerate peak of each pair is shown by a solid line and its corresponding non-degenerate peak as a dotted line in the same colour. Corresponding with the numbering of sites presented in Table 11.3, site 1 is shown in magenta, site 2 in orange, site 3 in light blue and site 4 in dark blue. The magenta peak appears to be unpaired, presumably because the corresponding non-degenerate peak lies outside the measured energy transfer window. The free rotor peak, centred at 14.74 meV [37], is absent in each case. Note that the scale on the residuals for 48 K is reduced compared to the other three temperatures, indicating slightly larger residuals than for the lower temperatures.

peaks alter slightly, with site 4 becoming slightly more prominent. This is unexpected, since this site is the weakest and should therefore lose intensity at higher temperatures, relative to the stronger sites. The peaks for sites 1-3 are largely unaffected by temperature, even after the desorption of approximately 1.1% of the H_2 at 48 K. Thus, at a low loading in which few H_2-H_2 or H_2-D_2O interactions are possible, the adsorption sites are reasonably stable up to 48 K.

A similar temperature trend can be seen for the data at a loading of 1 H_2:Ca^{2+} as for the $<$ 1 H_2:Ca^{2+} data: the peaks for site 4 become more prominent at 48 K, while the peaks for sites 1, 2 and 3 lose intensity at the higher temperature, after partial desorption of 1.4% of the H_2. Again, the pattern is not as expected, with the stronger sites desorbing before the weaker site. It seems that site 4 is only accessible at higher loadings, but once adsorption to this site has occurred, it is less likely to be thermally activated. This would suggest that the strength of the barrier to rotation is not necessarily indicative of the activation energy of the site [37].

Across all loadings at 23 K and below, the peaks for site 4 are about the same size or smaller than those for sites 1 and 2. As more H_2 is added, these peaks become more prominent. By comparison, the intensity of the peaks for the other sites grow only slightly with each additional dose of H_2, appearing to saturate at 3 H_2:Ca^{2+}. This pattern fits the expected trend of stronger sites filling up first, leaving only weaker sites for the latecomers to bind to.

At the highest loading of this sample, the same two narrow peaks that are present in the Na-laponite (RD) spectrum appear, possibly for the same reasons. The cation density of Ca-laponite (EL) is likely to be similar, so these peaks may be due to overlapping potentials. Their absence at lower loadings makes it less likely that they are artefacts from choosing the wrong peak shape or from the fitting constraints necessary to ensure quantum pairing. This may indicate that the data should be refitted to a larger set of narrower peaks, which may clarify the temperature and loading trends, showing more clearly which sites saturate first. This was attempted and the reasons for not re-analysing the data in this way is discussed in Section 6.3.3.

Table 11.4 shows how the splittings and peak positions vary as the density of adsorbed H_2 increases in this sample, for the 6 K data only. The values are largely consistent, although there seems to be a slight increase in the splitting between the degenerate and non-degenerate peaks of each pair up to 4 H_2:Ca^{2+} and then this

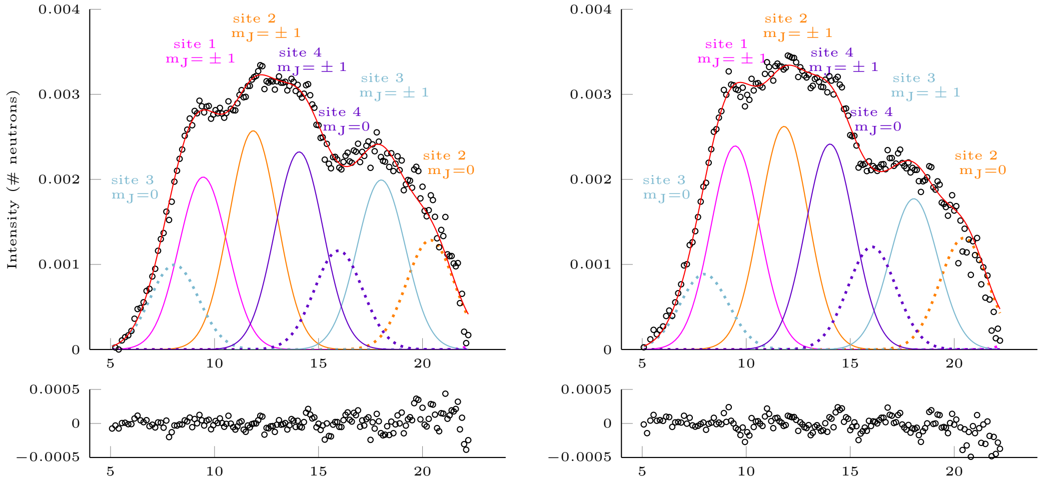

(a) 6 K (reduced χ^2: 1.60)

(b) 9 K (reduced χ^2: 1.73)

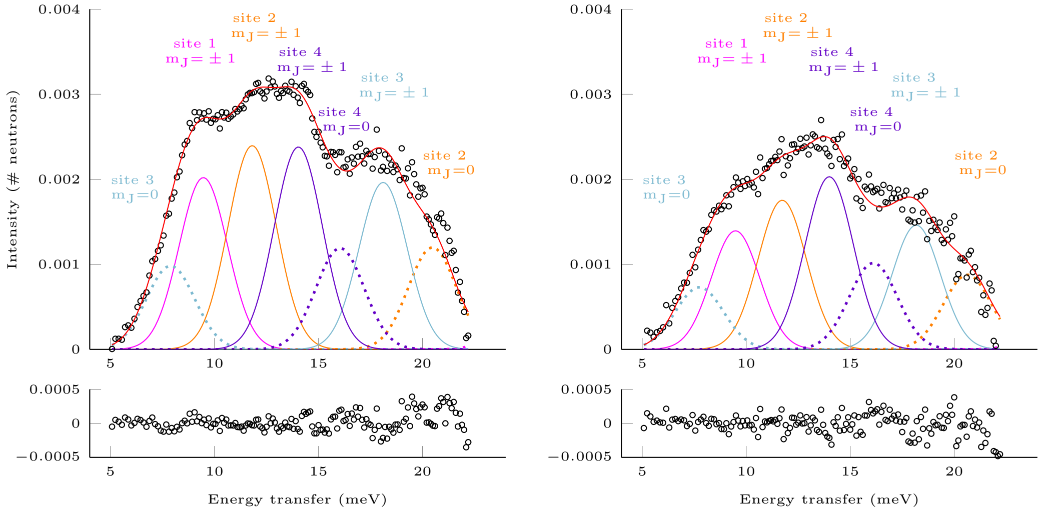

(c) 23 K (reduced χ^2: 1.45)

(d) 48 K (reduced χ^2: 1.47)

Figure 11.4: INS spectra and fits for Ca-laponite (EL) in a 2 bar H_2 atmosphere (1 H_2:Ca^{2+}), showing the consistency of fitted peak positions across four temperatures, ranging from 6-48 K. A polynomial background was removed before fitting a set of paired Gaussian peaks, following the constraints of the quantum model for the H_2 hindered rotor. The black circles are the measured data points, the superimposed solid red line is the full fit and the pairs of Gaussian peaks are colour-matched. The doubly-degenerate peak of each pair is shown by a solid line and its corresponding non-degenerate peak as a dotted line in the same colour. Corresponding with the numbering of sites presented in Table 11.3, site 1 is shown in magenta, site 2 in orange, site 3 in light blue and site 4 in dark blue. The magenta peak appears to be unpaired, presumably because the corresponding non-degenerate peak lies outside the measured energy transfer window. The free rotor peak, centred at 14.74 meV [37], is absent in each case.

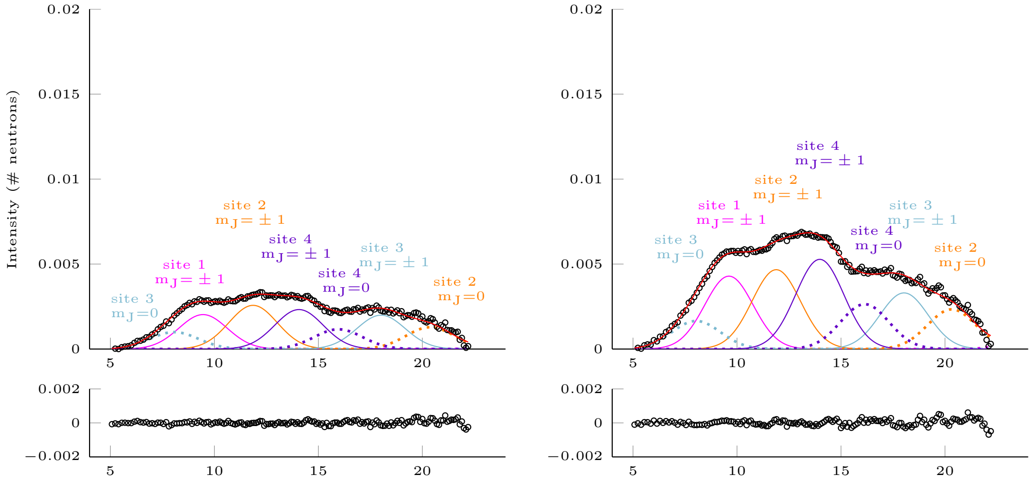
(a) 1 H_2:Ca^{2+} (reduced χ^2: 1.6)

(b) 2 H_2:Ca^{2+} (reduced χ^2: 2.3)

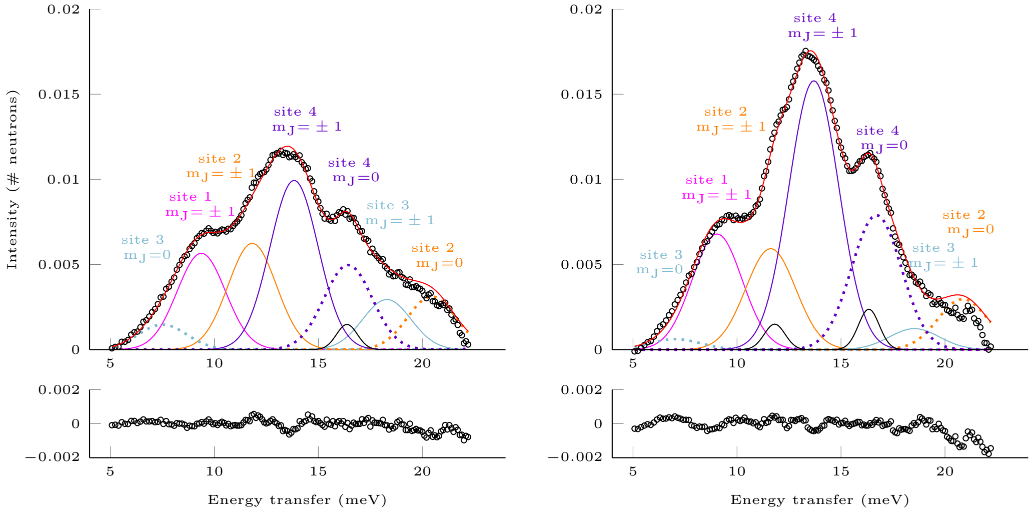
(c) 3 H_2:Ca^{2+} (reduced χ^2: 4.9)

(d) 4 H_2:Ca^{2+} (reduced χ^2: 9.3)

Figure 11.5: INS spectra and fits for Ca-laponite (EL) at 6 K, showing the consistency of fitted peak positions across four loadings ranging from 1-4 H_2:Ca^{2+}. A polynomial background was removed before fitting a set of paired Gaussian peaks, following the constraints of the quantum model for the H_2 hindered rotor. The black circles are the measured data points, the superimposed solid red line is the full fit and the pairs of Gaussian peaks are colour-matched. The non-degenerate peak of each pair is shown by a dotted line and its corresponding doubly-degenerate peak as a solid line in the same colour. The magenta peak centred at ~9 meV appears to be unpaired, presumably because its corresponding non-degenerate peak lies outside the measured energy transfer window. The free rotor peak, centred at 14.74 meV [37], is absent in each case.

(a) 6 K (reduced χ^2: 29.4) (b) 9 K (reduced χ^2: 27.8)

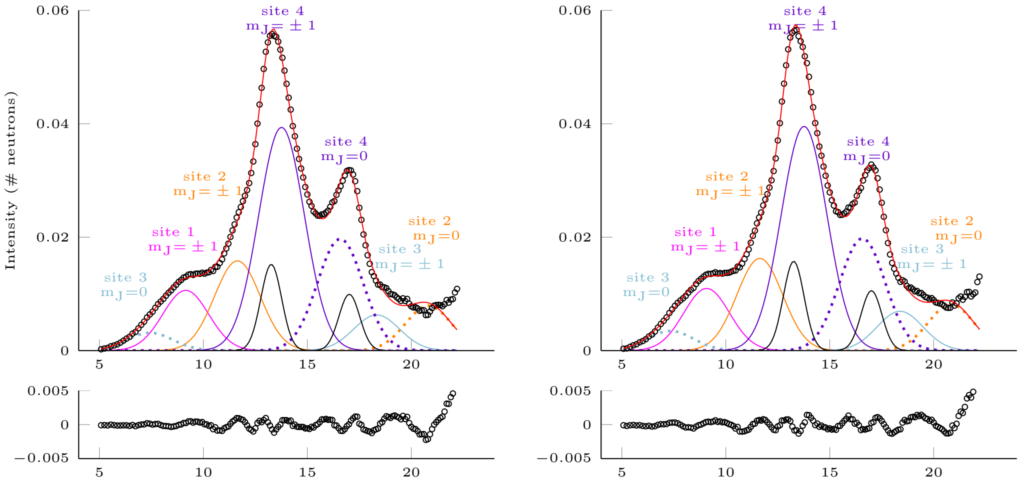

(c) 23 K (reduced χ^2: 19.3) (d) 48 K (reduced χ^2: 13.9)

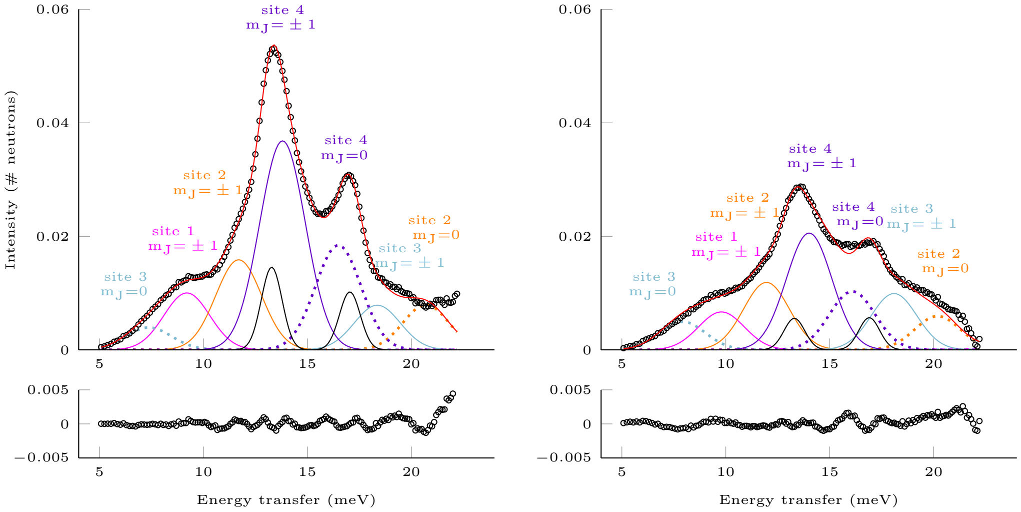

Figure 11.6: INS spectra and fits for Ca-laponite (EL) in an 18 bar H_2 atmosphere (9 H_2:Ca^{2+}), showing the consistency of fitted peak positions across four temperatures, ranging from 6-48 K, as well as the evolution of the peak shapes with a much higher loading. A polynomial background was removed before fitting a set of paired Gaussian peaks, following the constraints of the quantum model for the H_2 hindered rotor. The black circles are the measured data points, the superimposed solid red line is the full fit and the pairs of Gaussian peaks are colour-matched. The non-degenerate peak of each pair is shown by a dotted line and its corresponding doubly-degenerate peak as a solid line in the same colour. The magenta peak centred at ~9 meV is unpaired, presumably because its corresponding peak lies outside the measured energy transfer window. Two narrower peaks of FWHM 0.5 meV were needed to achieve a reasonable fit. Omitting these peaks did not reproduce all the spectral features and inclusion of a free rotor peak made the fit worse in all cases. At lower loadings, the peak parameters are very similar. The two narrow peaks only appear at loadings exceeding 2 H_2:Ca^{2+}.

T	Splitting (meV)	Amp. (x10^{-}3)	Centre (meV)	Amp. (x10^{-}3)	Centre (meV)
Site 1		$m_J = 0$		$m_J = \pm1$	
6 K	*16.65±0.03*	*5.31±0.27*	*25.80±0.03*	10.63±0.27	9.15±0.03
9 K	*16.87±0.04*	*5.48±0.29*	*25.94±0.04*	10.96±0.29	9.08±0.04
23 K	*16.49±0.03*	*5.01±0.23*	*25.70±0.03*	10.03±0.23	9.20±0.03
48 K	*14.74±0.05*	*3.34±0.27*	*24.52±0.05*	6.68±0.27	9.79±0.05
Site 2		$m_J = 0$		$m_J = \pm1$	
6 K	9.19±0.03	7.92±0.28	20.83±0.03	15.83±0.28	11.64±0.03
9 K	9.20±0.03	8.13±0.32	20.83±0.03	16.26±0.32	11.63±0.03
23 K	9.01±0.02	7.93±0.27	20.70±0.02	15.87±0.27	11.70±0.02
48 K	8.23±0.03	5.94±0.32	20.19±0.03	11.88±0.32	11.96±0.03
Site 3		$m_J = 0$		$m_J = \pm1$	
6 K	10.90±0.04	3.14±0.34	7.43±0.04	6.29±0.34	18.33±0.04
9 K	11.04±0.04	3.47±0.38	7.34±0.04	6.94±0.38	18.38±0.04
23 K	10.99±0.03	3.93±0.30	7.37±0.03	7.87±0.30	18.36±0.03
48 K	10.18±0.03	4.96±0.32	7.92±0.03	9.92±0.32	18.09±0.03
Site 4		$m_J = 0$		$m_J = \pm1$	
6 K	2.82±0.01	19.69±0.64	16.58±0.01	39.37±0.64	13.76±0.01
9 K	2.80±0.01	19.77±0.73	16.57±0.01	39.54±0.73	13.77±0.01
23 K	2.68±0.01	18.41±0.60	16.49±0.01	36.82±0.60	13.81±0.01
48 K	2.08±0.03	10.29±0.61	16.08±0.03	20.58±0.61	14.01±0.03

Table 11.3: Comparison of hindered rotor peak parameters from the fits to the INS spectra for Ca-laponite(EL) in an 18 bar H_2 atmosphere (9 H_2:Ca^{2+}), showing the variation with temperature. The amplitude and centre of each peak is given, as well as the separation between the paired hindered rotor peak centres. The widths for all paired peaks were fixed at 2.59 meV. The text in italics is data requiring confirmation, owing to the non-degenerate peak of the pair being outside the measured energy window.

Loading (H_2:Ca^{2+})	**Splitting (meV)**	**Width (meV)**	**Amp. (x10^{-}3)**	**Centre (meV)**	**Amp. (x10^{-}3)**	**Centre (meV)**
Site 1		$m_J = 0$		$m_J = \pm1$		
0.25	*16.37±0.07*	2.73	*0.27±0.03*	*25.61±0.07*	0.54±0.03	9.24±0.07
1	*15.73±0.03*	2.73	*1.01±0.04*	*25.19±0.03*	2.03±0.04	9.46±0.03
2	*15.26±0.02*	2.73	*2.15±0.06*	*24.88±0.02*	4.29±0.06	9.61±0.02
3	*15.98±0.02*	2.73	*2.83±0.09*	*25.35±0.02*	5.66±0.09	9.37±0.02
4	*16.96±0.03*	2.83	*3.40±0.13*	*26.01±0.03*	6.79±0.13	9.05±0.03
9	*16.65±0.03*	2.59	*5.31±0.27*	*25.80±0.03*	10.63±0.27	9.15±0.03
Site 2		$m_J = 0$		$m_J = \pm1$		
0.25	8.75±0.06	2.73	0.35±0.03	20.53±0.06	0.70±0.03	11.78±0.06
1	8.52±0.02	2.73	1.29±0.04	20.38±0.02	2.57±0.04	11.86±0.02
2	8.44±0.02	2.73	2.34±0.06	20.33±0.02	4.67±0.06	11.89±0.02
3	8.63±0.02	2.73	3.12±0.09	20.45±0.02	6.24±0.09	11.82±0.02
4	9.24±0.04	2.83	2.96±0.14	20.86±0.04	5.93±0.14	11.62±0.04
9	9.19±0.03	2.59	7.92±0.28	20.83±0.03	15.83±0.28	11.64±0.03
Site 3		$m_J = 0$		$m_J = \pm1$		
0.25	10.00±0.05	2.73	0.30±0.02	8.03±0.05	0.59±0.02	18.03±0.05
1	9.95±0.02	2.73	1.00±0.03	8.07±0.02	1.99±0.03	18.02±0.02
2	9.99±0.02	2.73	1.65±0.05	8.04±0.02	3.30±0.05	18.03±0.02
3	10.78±0.03	2.73	1.47±0.08	7.51±0.03	2.94±0.08	18.29±0.03
4	11.49±0.11	2.83	0.62±0.13	7.04±0.11	1.23±0.13	18.53±0.11
9	10.90±0.04	2.59	3.14±0.34	7.43±0.04	6.29±0.34	18.33±0.04
Site 4		$m_J = 0$		$m_J = \pm1$		
0.25	1.64±0.08	2.73	0.23±0.03	15.79±0.08	0.45±0.03	14.15±0.08
1	1.89±0.02	2.73	1.16±0.04	15.96±0.02	2.32±0.04	14.07±0.02
2	2.16±0.01	2.73	2.64±0.06	16.14±0.01	5.28±0.06	13.98±0.01
3	2.60±0.01	2.73	4.97±0.11	16.43±0.01	9.94±0.11	13.83±0.01
4	3.01±0.01	2.83	7.89±0.16	16.71±0.01	15.79±0.16	13.70±0.01
9	2.82±0.01	2.59	19.69±0.64	16.58±0.01	39.37±0.64	13.76±0.01

Table 11.4: Trends with increasing H_2 density for sites observed in the INS spectra for Ca-laponite (EL), taken from the measurements at 6 K. For each loading, the widths were fixed values for all peaks. The text in italics is data requiring confirmation, owing to the non-degenerate peak of the pair being outside the measured energy window.

drops slightly at the higher loading, possibly indicating the advent of unfavourable interactions as the adsorption layer saturates.

The relative positions of the paired peaks for each site are the same as for the other two samples. The strengths of the barrier potential for each site and their symmetries are summarised for all three samples in Table 11.5 and discussed further in the next Section. Looking at the temperature trends at this highest loading, the structure has changed significantly at 48 K, corresponding with a 52% loss of adsorbed H_2. This time, the intensities of the stronger sites are almost unaffected, while the peaks of the weakest site have lost approximately half of their intensity, suggesting that the H_2 molecules bound to this site desorbed first. This desorption loss brings the H_2:Ca^{2+} ratio down to a similar level as for the measurements taken in an 8 bar atmosphere, which is calculated to give 4 H_2:Ca^{2+}. The structure of

Sample	**Site**	**Splitting (meV)**	**Barrier height (kJ mol^{-1})**	**Symmetry**
Na-laponite (RD)	site 1	*18.92±0.05*	*4.8*	2D rotor
Na-laponite (RD)	site 2	10.90±0.05	2.7	2D rotor
Na-laponite (RD)	site 3	12.60±0.12	1.9	1D rotor
Na-laponite (RD)	site 4	2.73±0.01	0.7	2D rotor
Ca-laponite (RD)	site 4	3.95±0.03	1.0	2D rotor
Ca-laponite (RD)	site 5	1.82±0.10	0.4	2D rotor
Ca-laponite (EL)	site 1	*16.65±0.03*	*4.0*	2D rotor
Ca-laponite (EL)	site 2	9.19±0.03	2.3	2D rotor
Ca-laponite (EL)	site 3	10.90±0.04	2.7	1D rotor
Ca-laponite (EL)	site 4	2.82±0.01	0.7	2D rotor

Table 11.5: Barrier strengths and symmetries for all sites, taken from the measurements at 6 K and the highest loading for each sample. The text in italics is data requiring confirmation, owing to the non-degenerate peak of the pair being outside the measured energy window.

these two spectra are compared in Figures 11.7a and 11.7b, showing that there are some differences depending on whether H_2 is adsorbing to or desorbing from the material. The peaks for sites 2 and 3 are more prominent in the desorption direction, relative to the other peaks. It is possible that these sites only become accessible at higher pressures. This is supported by the evidence for *d*-spacing enlargement with pressure, discussed in Chapter 8. However, comparing the spectrum for 3 H_2:Ca^{2+} at a low temperature with the high temperature, post-desorption spectrum for 4 H_2:Ca^{2+} shows very similar peak structure. The effect, if it is real, may only manifest at sufficiently high pressures.

11.4 Sample comparison

The sites found in the sodium-exchanged laponite are consistently stronger than the corresponding sites found in Ca-laponite (EL), but site 4, which is common to all three samples, is strongest in Ca-laponite (RD). The similarity of the site complexity and structure between Na-laponite (RD) and Ca-laponite (EL), both samples being distinct from the lower density Ca-laponite (RD), suggests that cation density plays a stronger role than the cation species. More densely clustered adsorption sites provide a more complex adsorption landscape through overlapping potentials.

The strongest site is the most likely candidate for cation adsorption, however the estimated barrier potentials for each site, presented in Table 11.5, are all less than 5 kJ mol^{-1}. This may indicate that there is no direct cation-H_2 interaction present,

(a) 4 H_2:Ca^{2+} at 23 K

(b) 9 H_2:Ca^{2+} at 48 K

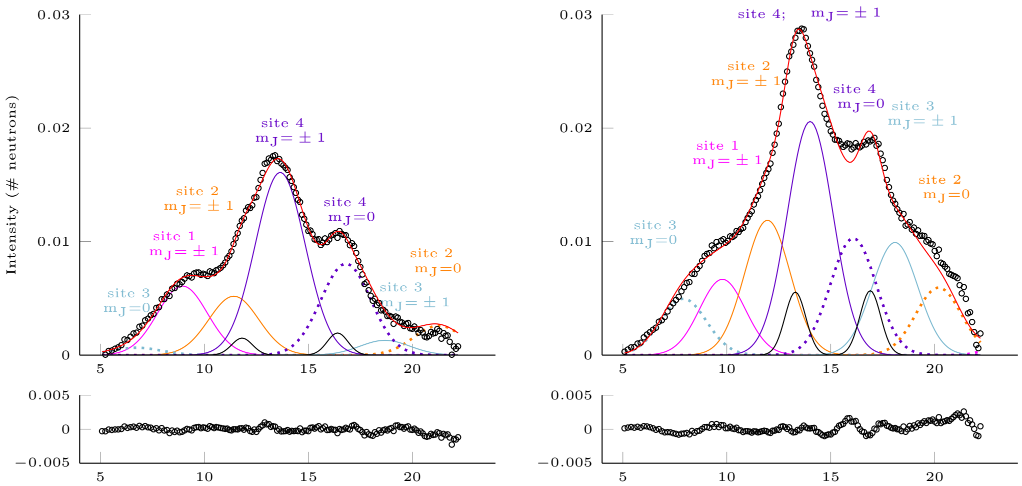

(c) 3 H_2:Ca^{2+} at 6 K

(d) 4 H_2:Ca^{2+} at 48 K

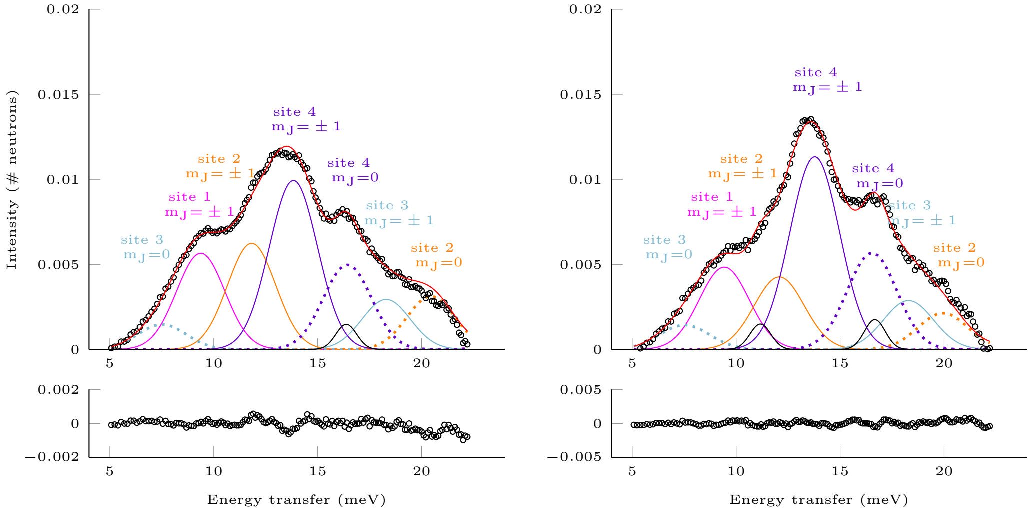

Figure 11.7: Comparison of the site structure for Ca-laponite (EL) for roughly equivalent H_2 adsorption amounts in two directions: a) shows the structure of a lower loading after adsorption and b) shows the structure after the adsorbed H_2 at a higher loading has undergone approximately 52% thermal desorption. Sites 2 (orange) and 3 (light blue) are relatively more prominent and the splitting for site 1 (magenta) has reduced. c) shows the fits for a lower loading at 6 K and d) shows the post-desorption spectrum and fits from a higher loading. In this case, the spectra are very similar, with a slight reduction in site 2 (orange).

possibly due to the presence of the water molecules. However, barrier potentials give only an approximate indication of the binding energy involved: a low rotational barrier may have a higher binding energy.

It is difficult to quantify the water content of all three samples, but since Ca-laponite (RD) had longer exposure to air during transfer from vacuum oven to sample can, the simplicity of the spectra for this sample may be partly owing to fewer adsorption sites, the cation binding sites being saturated by a more complete monolayer of water. Measurements on the IGA of dried clay re-exposed to laboratory air indicated a water reabsorption rate of 1.16 mg/min, assuming that the gravimetric increase can be attributed to water vapour alone. The air exposure of the sample at the ILL chemical laboratory was no more than 30 minutes, indicating that up to 0.37 wt% of water was reabsorbed by the sample during this time. This is the equivalent of 0.45 waters per Ca^{2+}: sufficient for about half of the cations to gain a second water. A more rigorous drying procedure at a higher temperature, without re-exposure to air, will expose more adsorption sites.

In Ca-laponite (EL), the filling order appears to begin with site 3, saturating at between 1 and 2 H_2:Ca^{2+}, followed by site 2 and site 1, both saturating at around 3 H_2:Ca^{2+} and finally 4, which continues to grow up to the highest loading measured. The first hydrogen molecules to enter the interlayers usually bind to the strongest binding site, thus site 3, which shows the biggest barrier potential, is likely to be the strongest site and may be the exposed cation binding site. Sites 2 and 1 may be binding sites near the cation-water-H_2 complex. Site 4 fills up last and also presents the smallest rotational hindrance, so this represents the weakest site, probably furthest from the cations. Site 4 also has the largest capacity and is therefore the most common binding site. Since the average adsorption enthalpy, measured from isotherms in Chapter 9 is low, the majority of the sites are expected to be weak, thus site 4 is probably a weak binding to the slightly negatively charged interlayer surface. On desorption, as the temperature is raised, the sites empty in the reverse order, with the height of the peaks of site 4 almost halving between 23 and 48 K, while the peaks of sites 2 and 1 decrease in height only slightly and those for site 3 are largely unaffected up to 48 K. Site 3 is the only site to show the quantum mechanical symmetry of a 1D hindered rotor, i.e. being hindered in two dimensions. This site therefore shows a higher degree of confinement than the other three.

11.5 Insights from INS

The INS spectra of three forms of laponite: the sodium form of laponite (RD) and the calcium forms of laponite (RD) and (EL), are examined in this chapter. The Gaussian fits applied to the spectra are validated by their consistency across a range of samples, temperatures and H_2 contents, as well as their close match to the predictions of the quantum mechanical “hindered rotor” model for adsorbed hydrogen. The spectra for Na-laponite (RD) and Ca-laponite (EL) have closely matched, complex features, whereas the spectrum for Ca-laponite (RD) has a much simpler structure. This observation is consistent with the findings from the QENS measurements, in which the H_2 uptake and diffusion characteristics of Ca-laponite (RD) are distinctly different from those of both Na-laponite (RD) and Ca-laponite (EL), these more closely matching each other.

The Ca-laponite (RD) spectrum reveals only two weak binding sites, while the peaks in the spectra of Na-laponite (RD) and Ca-laponite (EL) are attributable to at least four binding sites. This increased complexity may be due to the higher cation density found in both Na-laponite (RD) and Ca-laponite (EL), leading to interactions between neighbouring cation complexes. However, Ca-laponite (RD) was exposed to air for longer after drying than the other two samples, which may have resulted in some binding sites in the interlayers being blocked by water. In this case, fewer sites would be accessible to H_2, resulting in a simpler H_2 rotation spectrum.

In all measurements, no free rotor peak was discernible, implying that all of the adsorbed H_2 is bound to the surface in some way. All of the observed adsorption sites have weak binding energies, below 5 kJ mol^{-1}. This implies that H_2 is not directly bound to a naked cation, but instead to a complex formed of the cation with some surrounding D_2O or H_2O molecules. If air exposure of the samples did lead to significant water reabsorption, then higher binding energies may be achieved through better desiccation techniques.

Comparing the measurements on each sample as the H_2:cation ratios are altered reveals that, in general, the strongest sites saturate first as the pressure increases and are the last to empty as the temperature rises. All of the adsorption sites in the spectra for Na-laponite (RD) and Ca-laponite (EL) are visible at the lowest loadings, implying that the clay structure enables rapid, even uptake. The overall lack of hysteresis in most of the isotherms confirms this, however some anomalies do exist. For instance, for Ca-laponite (EL), when the temperature is raised to 48 K, desorbing some of the H_2, the adsorption sites appear to weaken. The opposite is expected, since the more weakly bound H_2 should desorb first, leaving stronger sites, on average, behind.

In some cases, it was possible to compare the post-adsorption (pressure increase) and post-desorption (temperature increase) spectra for Ca-laponite (EL) where the resulting H_2:Ca^{2+} ratios roughly matched. For low H_2 contents, these spectra were very similar, but they had noticeable differences at higher loadings, implying that pressure may lead to structural changes. This may be linked to the observation in Chapter 8 of it being harder to attain the same levels of D_2, loaded after desorption and evacuation following the adsorption of H_2 to saturation.

Four of the identified adsorption sites show 2D planar symmetry, suggestive of binding either to the clay surface or to the cation. The site showing the strongest rotational barrier has the symmetry expected for a 1D rotor, indicating a high degree of confinement for this site, which may be expected for H_2 confined between the interlayer surfaces, or bound to a number of molecules in a coordinated cation complex.

Difficulties encountered in the analysis of these data included the lack of a precise formula for Ca-laponite (EL) and the wrong choice of fitting width. The formula for Ca-laponite (RD) was used in the calculations instead, which may mean that the cation ratios for this sample are inaccurate. For complete accuracy, the spectra of peaks of Na-laponite (RD) and Ca-laponite (EL) should be refitted to a larger set of narrower peaks, with their widths matching those found for Ca-laponite (RD). This was omitted from this study, as it was felt that it would not add anything significant to the understanding of this system, other than clarifying the number of sites and their quantum mechanical symmetries. The complexity of these systems is high and could be reduced by using more rigorous drying procedures, such as drying and loading the sample inside a glove box, to eliminate the uncertainty in the water content. In addition, some insights may be gained by modelling the system using molecular dynamics simulations. These were not included in this study, as it was felt to be beyond the scope of an experimental thesis.

12. CONCLUSIONS

H_2 is an ideal energy carrier to replace petroleum, addressing the impact of CO_2 emissions on the Earth's biosphere. However, H_2 storage is hampered by its low volumetric energy density. The solution to this is key to the implementation of a hydrogen economy [68], in which H_2 is generated and stored on site at central locations or in a distributed energy network at homes and businesses, allowing intermittent renewable energy technologies to be integrated into the grid. H_2 gas can be pressurised and stored up to 80 MPa in modern cylinders, while liquid H_2 requires cryogenic temperatures (~21 K), both approaches consuming a third of the stored energy. Solid state storage offers two promising alternatives: chemisorption, in which H_2 dissociates and is chemically incorporated into a substrate, and physisorption, involving the interaction between H_2 molecules and several surface atoms in a solid matrix. Chemisorption materials typically require temperatures $>$ 500 K, to re-emit gaseous H_2, while significant physisorption only occurs at temperatures $<$ 100 K. Physisorption promises a fully reversible storage mechanism, allowing rapid access to H_2 without damaging the store and requiring only small pressure/temperature changes. Porous materials are good candidates, having high surface areas for binding large quantities of H_2. The key challenge for physisorption materials is to optimise binding energy between H_2 and the material's surface, allowing near-ambient storage.

The emphasis for much research into H_2 storage has been placed on the limiting requirements for land-based vehicles, the key requirement being that the materials have low weight. The US DoE targets focus on high gravimetric density of 6.5 wt% H_2 at room temperature. However, for the shift to a hydrogen economy, large-scale storage of energy in stationary containers is equally, if not more, important. A heavy fuel store could be an advantage for shipping, since it will also incorporate ballast. Thus a shift of emphasis to the volumetric energy density of HSMs, rather than gravimetric, would open up new research possibilities in materials, such as clay minerals, hitherto overlooked because of their intrinsic weight.

To my knowledge, this Ph.D. thesis constitutes the first ever demonstration of H_2 storage in the diverse family of swelling clay minerals, thereby introducing clays as an entirely new class of HSM. Compared with other physisorption materials under consideration, clays have greater density, which is a disadvantage for automotive applications, but no handicap for static storage. They have chemically tunable, nanoporous networks allowing fully reversible H_2 storage, as well as abundance and low cost: both key factors for viable large-scale storage. Clays are extremely cheap to synthesise from widely-available chemicals, readily produced at the large scale and may therefore be a key enabling technology to realise a hydrogen economy. In addition, clays are stable, non-toxic materials requiring simple chemical treatments producing few chemical byproducts. Unlike the highly crystalline cages of zeolites, the dimensions of clay interlayer pores can be reduced so as to confine H_2 molecules, strengthening the H_2-surface bond by exposing each molecule to a greater potential through an enhanced interaction with the surface.

In addition to energy storage, research into the dynamics of H_2 confined in clay interlayers is both scientifically novel and interesting for other applications. The smectite-H_2 system presents intriguing quantum mechanics, providing a tunable, two-dimensional model system for studying the fundamental properties of confined H_2. One application of this is the measurement of the diffusion rate of H_2 in clays, an important factor in predicting long-term viability of containing nuclear waste in clay barriers. Another application is H_2 purification through reformation of natural gas (splitting methane into H_2 and CO_2), since the dimensions of clay interlayers can be controlled, admitting molecules of a particular size only.

Thermal and structural studies of the clay substrate, using TGA as well as X-ray and neutron diffraction, indicate that evacuation and heating to a temperature of 413 K sufficiently dehydrates the clay, leaving an average of one water molecule per cation and a d-spacing of 12.27 Å. Since the effective thickness of the laponite layer is approximately that of talc (9.43 Å), this leaves a spacing of 2.85 Å between the interlayer atoms, closely matching the kinetic diameter of H_2. Further neutron diffraction studies of H_2 physisorbed to laponite confirmed that the (001) peak height, relating to the clay's d-spacing, correlated with H_2 or D_2 concentration, confirming that H_2 intercalates into the laponite interlayers. From XRD and isotherms, it is clear that the hydration level of the clay plays a role in the uptake, since samples that were subjected to only a short evacuation process with no heating show a much reduced uptake. These results suggest that the abundant, non-toxic water molecule can act as a pillar holding the interlayers apart, however computer simulations have shown that 2.9 kJ mol^{-1} per H_2 is required by the first hydrogen molecules to enter the interlayer [219], expanding the interlayer space slightly. Further research is needed to investigate the effects of using larger pillar molecules, such as Cs^+ or an organic cation.

The low temperature dynamics of H_2 measured by quasielastic neutron spectroscopy studies reveals two populations of H_2 in Ca-laponite (RD): one which is immobile up to 100 K, probably localised to the partially hydrated Ca^{2+} and the other diffusing in a manner closely matching that predicted by the Singwi-Sjölander jump diffusion model, yielding a jump length of 3.21±0.40 Å at 40 K for H_2. While no single data set presented in this work conclusively shows localisation around the cations, all the data considered together strongly suggests this. Confirmation of such could be obtained by NMR or Raman spectroscopy, both of which were beyond the scope of this PhD. Adsorption calculations yield an adsorbate phase density of H_2 in the interlayers at 40 K of 67.08 kg m^{-3}: close to the boiling point density, 70.97 kg m^{-3}, of pure liquid H_2 at 1 bar and 23 K. For this to occur at a temperature above the triple point of 33 K implies a two-dimensional liquid-like structure, with H_2 molecules bound to adsorption sites separated by distances similar to the nearest-neighbour distance of condensed H_2. In solid H_2, this distance is 3.79 Å [37], slightly more than the 3.2±0.4 Å jump lengths estimated by the fit of the Singwi-Sjölander model to the QENS data at 40 K. Thus the emerging adsorption structure forms a coherent model, backed by data from a variety of measurements. In addition, the achievement of a confined two-dimensional film of H_2 having a liquid-like density at a temperature twice the boiling point (23 K) of H_2, is of great scientific interest, raising the prospect for studying superfluidics of confined gases. As water in the clay interlayer is observed to have a lower freezing point [230], so the supercooling of liquid hydrogen below the predicted Bose-Einstein condensation temperature at 1 K [231] may be experimentally achievable.

An estimate for the diffusion rate of H_2 in Ca-laponite (RD) at a range of temperatures was obtained from the Q-dependent broadening of quasielastic features, yielding 1.93±0.23 Å^2 ps^{-1} at 80 K. Similarly, diffusion rates for higher cation density forms of laponite at three of the same temperatures were measured, yielding 1.17±0.24 Å^2 ps^{-1} at 80 K for Na-laponite (RD) and 1.99±0.38 Å^2 ps^{-1} at 80 K for Ca-laponite (EL). Comparing these figures with the extrapolated rate for bulk liquid hydrogen of 4.90±0.84 Å^2 ps^{-1} at this temperature, shows a 60% reduction in the diffusion rate in the calcium forms and a 76% reduction in the sodium form. At 40 K, the rate is reduced by an order of magnitude, confirming that H_2 mobility is slowed down by interactions with the substrate. An Arrhenius analysis of the temperature dependency of these diffusion rates gave a measure of the activation energies involved: 188±28 K for Ca-laponite (RD), 128±43 K for Ca-laponite (EL) and 120±32 K for Na-laponite (RD). These activation energies and diffusion coefficients compare favourably with activated carbons.

Adsorption isotherms and additional volumetric data gathered during neutron scattering experiments indicate that partially hydrated laponites rapidly physisorb up to 0.6 wt% H_2 at 77 K and 80 bar for Na-laponite (RD), and Ca-laponite (RD), up to 0.7 wt% H_2 at 77 K and 80 bar for Ca-laponite (EL) and Mg-laponite (EL) and up to 0.6 wt% H_2 at 77 K and only 1 bar for Mg-laponite (B). At room temperature, the saturation uptake is slightly below 0.1 wt%, but only at pressures exceeding 100 bar. These gravimetric storage densities are much lower than for MOFs and activated carbons, partly due to the much lower surface areas for clays and partly due to the higher weight of the clay layer. Considering the storage density as a function of volume and using the known solid density of laponite (2.53 g/cc), the caesium laponites can hold up to 22.8 g H_2 per litre at 77 K and 80 bar, which is below the standard density for physisorbed H_2 under these conditions of 30 g H_2 per litre [68], but slightly above that for AX-21 of 20 g H_2 per litre at 90 K and 100 bar [209] and below that for IRMOF-20 of 34 g H_2 per litre at 77 K and 60 bar [75]. Adsorption-desorption isotherms for laponites show virtually no hysteresis, indicating that the physisorption mechanism is reversible, however cyclical measurements over long periods are needed to confirm that this reversibility does not degrade with repeated saturation and evacuation.

The maximum uptake is lower than that for many activated carbons, but the potential for improving the adsorption enthalpy may be higher. The binding enthalpy for the activated carbon AX-21 is 5.5-6.5 kJ mol^{-1} [209], but the calcium, magnesium and caesium forms of the fluorinated (B) grade laponite having slightly higher binding enthalpies of 6.98, 7 and 6.17 kJ mol^{-1} respectively, showing that experimenting with the chemical composition is a promising strategy. INS results for Ca-laponite (RD) clearly show that H_2 is physisorbed to a binding site, presenting spectral features closely fitting the quantum mechanical model. Further research is needed to analyse the binding strength of this site. Neutrons are a highly sensitive probe of the H_2 local environment and the INS spectra for laponite reveal the quantum mechanical features of H_2's rotation spectrum, giving a clear, strong signal. For Ca-laponite (RD), where the cation density is reasonably low at approximately one third per formula unit, four peaks representing two sites and almost exactly matching the proportions and energy shifts expected for the hindered rotor model for a single adsorption site are clearly visible. The more complex spectra for Na-laponite (RD) and Ca-laponite (EL) show three more adsorption sites, reflecting the higher cation densities in these materials. The consistency of the fits across temperatures, H_2 concentrations and samples strengthens their validity and shows that the signal from these systems show clear structure from which its constituent peaks can be readily deconvolved, a difficult task when many peaks overlap into a single broad feature, as is common in other materials. These spectra demonstrate that clays are a good model system for studying the low temperature uptake and dynamics of H_2.

A range of binding sites is desirable for a practical hydrogen store, because it allows gradual release of the H_2 as pressure and/or temperature is altered. The complexity of the spectra for the samples having higher cation density, Na-laponite (RD) and Ca-laponite (EL), reflect the diversity of interlayer structure and imply a range of binding mechanisms. The adsorption site in these materials presenting the greatest rotational barrier has a hindering potential of about 5 kJ mol^{-1}.

Future strategies for improving the hydrogen storage properties of clays must include the identification of suitable clays from the diverse compositions in the 2:1 classes, including smectites, vermiculites, micas, chlorites and inverted ribbons, as well as the diverse class of charged layered double hydroxides (LDH), having a similar structure to smectites, with reciprocal charge - i.e. the layers are slightly positive, attracting anions into the interlayers. They may therefore allow investigation of the interaction between H_2 and a range of anions in LDH interlayers. Anions tend to be larger than cations and thus have reduced polarising power, but since experimental data on fundamental interactions between H_2 and anions is lacking, this would be of general scientific interest.

The optimum size of interlayer for maximising H_2 uptake and/or H_2 binding energy through molecular confinement effects needs to be determined and an investigation of the effects of exchanging the interlayer cation, considering not only inorganic cations such as K^+ and Rb^+, but the wide range of larger, organic cations is needed. Larger cations will expand the interlayers more, reducing the need for the first hydrogen molecules to expend energy on expansion, however they may have reduced polarising abilities. The use of larger cations may permit the use of pillaring molecules other than water, reducing competition for adsorption at charged sites and increasing interlayer capacity by exposing both interlayer surfaces for adsorption. The improvements in capacity and binding energy seen in the (B) grade forms show promise for this route. Other considerations are techniques which remove more solvent from the cation centres, reducing their coordinative saturation and making them more accessible for H_2 adsorption. These include freeze-drying and the selection of a sample-specific optimum temperature for drying. The trend in gravimetric isotherms for Na-laponite (RD) shows that an improvement of 0.2 wt% H_2 uptake is achievable by drying the clay before introducing H_2. The volumetric densities may be improved by compressing the clays, reducing the interparticle volumes. The effect of the surface charge on uptake needs to be investigated. Higher surface charges usually lead to smaller, more rigid interlayer spacing, but may provide stronger binding sites. The ideal clay would be sufficiently pillared to allow two intercalant layers of H_2 and have a high density of exposed metal sites for adsorption.

At this early stage, it is not clear what the role of clays will be in the realm of hydrogen storage, since the possibilities in this diverse class are unexplored. The results presented in this thesis show that while clays exhibit a low capacity, this is still a promising start for an entirely new class and it is hoped that improvements mirroring the scale of recent advances in carbon materials can be expected. Clays offer other advantages, such as low synthesis and manufacture costs, stability and low toxicity. Figure 12.1 places clays on a map comparing the gravimetric and volumetric storage capacities for a variety of materials and proposes their possible future position, by analogy with carbon materials. At the very least, clays can contribute to the understanding of the fundamental interactions of H_2 with a variety of chemical species and porous structures.

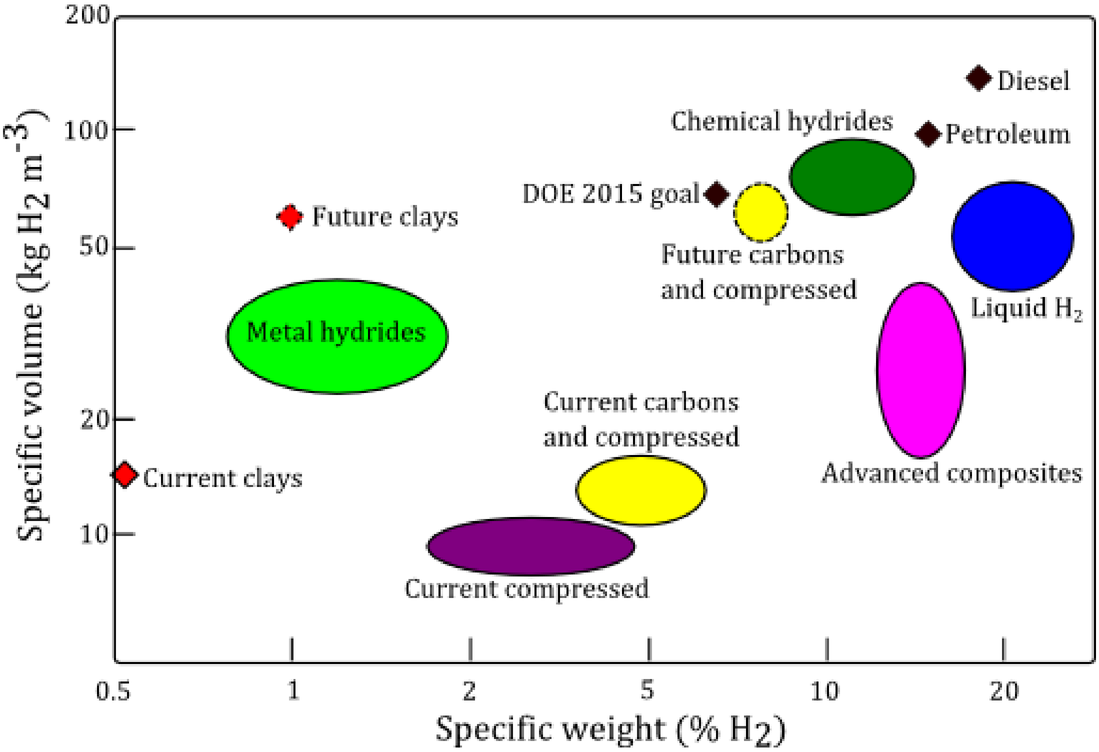

Figure 12.1: (Adapted from [232].) Current and proposed future research status of H_2 storage materials, comparing their gravimetric and volumetric storage capacities. Clay minerals - a new class of materials - adsorb H_2 by physisorption, as do carbons. By analogy with the improvements to H_2 uptake achieved in carbon materials, the red crosses indicate the initial and expected future position for clay minerals. While the gravimetric density of H_2 in clays will always be low, due to the high intrinsic weight of clays (900 g mol^{-1} for sodium laponite), for some applications, such as shipping and stationary storage at a power station or in homes, this is not a handicap, while the extremely low cost and wide abundance of clays is a great advantage.

References

References

[1] E. W. Wolff and I. Fung, “Climate change: evidence & causes.,” tech. rep., The Royal Society and US National Academy of Sciences, 2014.

[2] T. F. Stocker, D. Qin, G.-K. Plattner, M. M. B. Tignor, S. K. Allen, J. Boschung, A. Nauels, Y. Xia, V. Bex, and P. M. Midgley, “Climate Change 2013: The physical science basis.,” tech. rep., Intergovernmental Panel on Climate Change, 2013.

[3] “Climate change act 2008,” 2008.

[4] D. Abbott, “Keeping the energy debate clean: How do we supply the world’s energy needs?,” *Proc. IEEE*, vol. 98, pp. 42–66, Jan. 2010.

[5] U. Bossel, “Does a Hydrogen Economy Make Sense?,” *Proc. IEEE*, vol. 94, pp. 1826–1837, Oct. 2006.

[6] B. Kongtragool and S. Wongwises, “A review of solar-powered Stirling engines and low temperature differential Stirling engines.,” *Renew. Sustain. Energy Rev.*, vol. 7, pp. 131–154, Apr. 2003.

[7] C. W. Forsberg, P. F. Peterson, and H. Zhao, “High-Temperature Liquid-Fluoride-Salt Closed-Brayton-Cycle Solar Power Towers.,” *J. Sol. Energy Eng.*, vol. 129, no. 2, p. 141, 2007.

[8] A. Züttel, A. Borgschulte, and L. Schlapbach, *Hydrogen as a future energy carrier.* Weinheim: Wiley-VCH, 2008.

[9] T. Pregger, D. Graf, W. Krewitt, C. Sattler, M. Roeb, and S. Möller, “Prospects of solar thermal hydrogen production processes.,” *Int. J. Hydrogen Energy*, vol. 34, pp. 4256–4267, May 2009.

[10] J. K. Kaldellis and D. Zafirakis, “The wind energy (r)evolution: A short review of a long history.,” *Renew. Energy*, vol. 36, pp. 1887–1901, July 2011.

[11] M. E. Meral and F. Dinçer, “A review of the factors affecting operation and efficiency of photovoltaic based electricity generation systems.,” *Renew. Sustain. Energy Rev.*, vol. 15, pp. 2176–84, June 2011.

[12] M. Amoretti, “Towards a peer-to-peer hydrogen economy framework.,” *Int. J. Hydrogen Energy*, vol. 36, pp. 6376–6386, June 2011.

[13] C. Doll and M. Wietschel, “Externalities of the transport sector and the role of hydrogen in a sustainable transport vision.,” *Energy Policy*, vol. 36, pp. 4069–4078, Nov. 2008.

[14] H. Gehrke, K. Ruthardt, J. Mathiak, and C. Roosen, “Hydrogen: A small molecule with large impact.,” *Oil Gas-Eur. Mag.*, vol. 37, no. 1, pp. 29–33, 2011.

[15] M. S. Dresselhaus and I. L. Thomas, “Alternative energy technologies.,” *Nature*, vol. 414, pp. 332–7, Nov. 2001.

[16] N. Vargaftik, *Tables on the Thermophysical Properties of Liquids and Gases.* New York: John Wiley & Sons, 1975.

[17] Z. Mileeva, D. K. Ross, D. Wilkinson, S. M. King, T. A. Ryan, and H. Sharrock, “The use of small angle neutron scattering with contrast matching and variable adsorbate partial pressures in the study of porosity in activated carbons.,” *Carbon N. Y.*, vol. 50, pp. 5062–5075, Nov. 2012.

[18] L. Schlapbach and A. Züttel, “Hydrogen-storage materials for mobile applications.,” *Nature*, vol. 414, no. November, pp. 353–8, 2001.

[19] K. Friedrich and F. Buchi, *Fuel cells using hydrogen.*, ch. 8, pp. 335–363. Weinheim: Wiley, 2008.

[20] K. Sasaki, J. X. Wang, M. Balasubramanian, J. McBreen, F. Uribe, and R. R. Adzic, “Ultra-low platinum content fuel cell anode electrocatalyst with a long-term performance stability.,” *Electrochim. Acta*, vol. 49, pp. 3873–3877, Sept. 2004.

[21] S. Guo, S. Zhang, L. Wu, and S. Sun, "Co/CoO nanoparticles assembled on graphene for electrochemical reduction of oxygen.," *Angew. Chem. Int. Ed. Engl.*, vol. 51, pp. 11770–3, Nov. 2012.

[22] A. Godula-Jopek, W. Jehle, and J. Wellnitz, *Hydrogen Storage Technologies.* Weinheim: Wiley, 2012.

[23] DoE, "H2usa programme.," May 2013.

[24] C. Chen, Y. Kang, Z. Huo, Z. Zhu, W. Huang, H. L. Xin, J. D. Snyder, D. Li, J. A. Herron, M. Mavrikakis, M. Chi, K. L. More, Y. Li, N. M. Markovic, G. A. Somorjai, P. Yang, and V. R. Stamenkovic, "Highly crystalline multimetallic nanoframes with three-dimensional electrocatalytic surfaces.," *Science*, 2014.

[25] R. Edwards, J.-C. Griesemann, J.-F. Larivé, and V. Mahieu, "Well-to-wheels analysis of future automotive fuels and powertrains in the european context.," tech. rep., Joint Research Centre, 2004.

[26] M. Andreani, I. Daniel, and M. Poillet-Villard, "Aluminum speeds up the hydrothermal alteration of olivine.," *Am. Mineral.*, vol. 98, pp. 1738–44, 2013.

[27] D. Graham-Rowe, "Do the locomotion.," *Nature*, vol. 454, no. 7208, p. 1036, 2008.

[28] S. Satyapal, J. Petrovic, C. Read, G. Thomas, and G. Ordaz, "The U.S. Department of Energy's National Hydrogen Storage Project: Progress towards meeting hydrogen-powered vehicle requirements.," *Catal. Today*, vol. 120, pp. 246–256, Feb. 2007.

[29] R. J. Keaton, J. M. Blacquiere, and R. T. Baker, "Base metal catalyzed dehydrogenation of ammonia-borane for chemical hydrogen storage.," *J. Am. Chem. Soc.*, vol. 129, pp. 1844–5, Feb. 2007.

[30] H. Furukawa, N. Ko, Y. B. Go, N. Aratani, S. B. Choi, E. Choi, A. O. Yazaydin, R. Q. Snurr, M. O'Keeffe, J. Kim, and O. M. Yaghi, "Ultrahigh porosity in metal-organic frameworks.," *Science (80-.).*, vol. 329, pp. 424–8, July 2010.

[31] J. L. Mendoza-Cortes, W. A. I. Goddard, H. Furukawa, and O. M. Yaghi, “A covalent organic framework that exceeds the DOE 2015 volumetric target for H2 uptake at 298 K.,” *J. Phys. Chem. Lett.*, vol. 3, pp. 2671–5, 2012.

[32] A. Gil, R. Trujillano, M. A. Vicente, and S. A. Korili, “Hydrogen adsorption by microporous materials based on alumina-pillared clays.,” *Int. J. Hydrogen Energy*, vol. 34, pp. 8611–5, Oct. 2009.

[33] D. W. Oscarson and S. C. H. Cheung, “Evaluation of phyllosilicates as a buffer component in the disposal of nuclear fuel waste.,” Tech. Rep. December, Atomic Energy of Canada Ltd, Pinawa, 1983.

[34] F. T. Madsen, “Clay mineralogical investigations related to nuclear waste disposal.,” *Clay Miner.*, vol. 33, pp. 109–29, Mar. 1998.

[35] S. Kosiewicz, “Gas generation from the alpha radiolysis of bitumen.,” *Nucl. Chem. Waste Manag.*, vol. 1, no. 2, pp. 139–41, 1980.

[36] A. Husain and J. P. Krasznai, “Compaction of radioactive incinerator ash: gas generation effects.,” *Waste Manag.*, vol. 14, no. 6, pp. 521–30, 1994.

[37] I. F. Silvera, “The solid molecular hydrogens in the condensed phase: Fundamentals and static properties.,” *Rev. Mod. Phys.*, vol. 52, no. 2, pp. 393–452, 1980.

[38] J. G. Vitillo, A. Damin, A. Zecchina, and G. Ricchiardi, “Theoretical characterization of dihydrogen adducts with alkaline cations.,” *J. Chem. Phys.*, vol. 122, p. 114311, Mar. 2005.

[39] A. D. McLean, “Molecular properties which depend on the square of the electronic coordinates; H2 and NNO.,” *J. Chem. Phys.*, vol. 45, no. 10, pp. 3676–81, 1966.

[40] W. Kolos and L. Wolniewicz, “Polarizability of the Hydrogen Molecule.,” *J. Chem. Phys.*, vol. 46, no. 4, p. 1426, 1967.

[41] R. C. Lochan and M. Head-Gordon, “Computational studies of molecular hydrogen binding affinities: the role of dispersion forces, electrostatics, and orbital interactions.,” *Phys. Chem. Chem. Phys.*, vol. 8, pp. 1357–70, Mar. 2006.

[42] T. Weber, A. O. Czasch, O. Jagutzki, A. K. Müller, V. Mergel, A. Kheifets, E. Rotenberg, G. Meigs, M. H. Prior, S. Daveau, A. Landers, C. L. Cocke, T. Osipov, R. Díez Muiño, H. Schmidt-Böcking, and R. Dörner, “Complete photo-fragmentation of the deuterium molecule.,” *Nature*, vol. 431, pp. 437–40, Sept. 2004.

[43] J. Van Kranendonk, *Solid hydrogen.* New York: Plenum Press, 1983.

[44] A. J. Horsewill, K. S. Panesar, S. Rols, M. R. Johnson, Y. Murata, K. Komatsu, S. Mamone, A. Danquigny, F. Cuda, S. Maltsev, M. C. Grossel, M. Carravetta, and M. H. Levitt, “Quantum translator-rotator: inelastic neutron scattering of dihydrogen molecules trapped inside anisotropic fullerene cages.,” *Phys. Rev. Lett.*, vol. 102, p. 013001, 2009.

[45] A. J. Ramirez-Cuesta and P. C. H. Mitchell, “Hydrogen adsorption in a copper ZSM5 zeolite - An inelastic neutron scattering study.,” *Catal. Today*, vol. 120, pp. 368–373, Feb. 2007.

[46] D. White and E. N. Lassettre, “Theory of ortho-para hydrogen separation by adsorption at low temperatures, isotope separation.,” *J. Chem. Phys.*, vol. 32, no. 1, pp. 72–84, 1960.

[47] I. F. Silvera and M. Nielsen, “INS and separation coefficient of absorbed H - molecular alignment and energy levels.,” *Phys. Rev. Lett.*, vol. 37, no. 19, pp. 1275–8, 1976.

[48] L. Pauling, “The rotational motion of molecules in crystals.,” *Phys. Rev.*, vol. 36, pp. 430–43, 1930.

[49] W. J. Stead, P. Meehan, and J. W. White, “Librations of hydrogen in stage II caesium graphite, C24Cs.,” *J. Chem. Soc. Faraday Trans. 2*, vol. 84, no. 10, pp. 1655–88, 1988.

[50] A. P. Smith, R. Benedek, F. R. Trouw, M. Minkoff, and L. H. Yang, “Quasi-two-dimensional quantum states of H2 in stage-2 Rb-intercalated graphite.,” *Phys. Rev. B. Condens. Matter*, vol. 53, pp. 10187–10199, Apr. 1996.

[51] A. Lovell, F. Fernandez-Alonso, N. T. Skipper, K. Refson, S. M. Bennington, and S. F. Parker, “Quantum Delocalization of Molecular Hydrogen in Alkali-Graphite Intercalates.,” *Phys. Rev. Lett.*, vol. 101, pp. 126101.2–126101.5, Sept. 2008.

[52] J. Eckert and G. J. Kubas, “Barrier to rotation of the dihydrogen ligand in metal complexes.,” *J. Phys. Chem.*, vol. 97, pp. 2378–2384, Mar. 1993.

[53] G. J. Kubas, “Fundamentals of H2 binding and reactivity on transition metals underlying hydrogenase function and H2 production and storage.,” *Chem. Rev.*, vol. 107, pp. 4152–205, Oct. 2007.

[54] S. K. Bhatia and A. L. Myers, “Optimum conditions for adsorptive storage.,” *Langmuir*, vol. 22, pp. 1688–700, Feb. 2006.

[55] X. Solans-Monfort, M. Sodupe, C. M. Zicovich-Wilson, E. Gribov, G. Spoto, C. Busco, and P. Ugliengo, “Can Cu+-exchanged zeolites store molecular hydrogen ? An ab-initio periodic study compared with low-temperature FTIR.,” *J. Phys. Chem. B*, vol. 108, pp. 8278–86, 2004.

[56] A. J. Ramirez-Cuesta, P. C. H. Mitchell, D. K. Ross, P. A. Georgiev, P. A. Anderson, H. W. Langmi, and D. Book, “Dihydrogen in zeolite CaX - An inelastic neutron scattering study.,” *J. Alloys Compd.*, vol. 446-447, pp. 393–396, Oct. 2007.

[57] M. DincÄƒ, A. Dailly, Y. Liu, C. M. Brown, D. A. Neumann, and J. R. Long, “Hydrogen storage in a microporous metal-organic framework with exposed Mn2+ coordination sites.,” *J. Am. Chem. Soc.*, vol. 128, pp. 16876–83, Dec. 2006.

[58] X. Periole, D. Allouche, J.-P. Daudey, and Y.-H. Sanejouand, “Simple two-body cation-water interaction potentials derived from ab initio calculations. Comparison to results obtained with an empirical approach.,” *J. Phys. Chem. B*, vol. 101, pp. 5018–25, June 1997.

[59] R. Harrison, *Book of data: Chemistry, Physical Sciences, Physics.* London: Nuffield Advanced Science, Longman, 1980.

[60] M. Barbatti, G. Jalbert, and M. A. C. Nascimento, "Clustering of hydrogen molecules around a molecular cation: The Li3+(H2)n clusters (n= 1 - 6).," *J. Phys. Chem. A*, vol. 106, pp. 551–555, 2002.

[61] H. Ohtaki and T. Radnai, "Structure and dynamics of hydrated ions.," *Chem. Rev.*, vol. 93, pp. 1157–1204, 1993.

[62] D. Lide and H. Frederikse, *CRC Handbook of Chemistry and Physics.* Florida: CRC Press, 1994.

[63] A. C. Dillon, E. Whitney, C. Engtrakul, C. J. Curtis, K. J. O'Neill, P. A. Parilla, L. J. Simpson, M. J. Heben, Y. Zhao, Y.-H. Kim, and S. B. Zhang, "Novel organometallic fullerene complexes for vehicular hydrogen storage.," *Phys. Status Solidi*, vol. 244, pp. 4319–22, Nov. 2007.

[64] C. R. Wood, N. T. Skipper, and M. J. Gillan, "Ca-intercalated graphite as a hydrogen storage material: Stability against decomposition into CaH2 and graphite.," *J. Solid State Chem.*, vol. 184, pp. 1561–5, June 2011.

[65] M. DincÄƒ and J. R. Long, "Strong H(2) binding and selective gas adsorption within the microporous coordination solid Mg(3)(O(2)C-C(10)H(6)-CO(2))(3).," *J. Am. Chem. Soc.*, vol. 127, pp. 9376–7, July 2005.

[66] M. Gardiner, J. Cunningham, and R. Moore, "Compressed hydrogen storage for fuel cell vehicles," in *Future Transportation Technology Conference*, SAE Technical Paper Series SP-1635, (Costa Mesa, California), 2001.

[67] A. Züttel, "Materials for hydrogen storage.," *Mater. Today*, vol. 6, pp. 24–33, Sept. 2003.

[68] A. Züttel, A. Remhof, A. Borgschulte, and O. Friedrichs, "Hydrogen: the future energy carrier.," *Philos. Trans. A. Math. Phys. Eng. Sci.*, vol. 368, pp. 3329–42, July 2010.

[69] W. Lubitz and W. Tumas, “Hydrogen: an overview.,” *Chem. Rev.*, vol. 107, pp. 3900–3, Oct. 2007.

[70] P. Jena, “Materials for Hydrogen Storage: Past, Present, and Future.,” *J. Phys. Chem. Lett.*, vol. 2, pp. 206–211, Feb. 2011.

[71] D. Ruthven, *Principles of adsorption and adsorption processes.* New York: John Wiley & Sons, 1984.

[72] “Doe hydrogen program 2006 annual program report.,” tech. rep., US Department of Energy (DoE), 2006.

[73] B. Panella, M. Hirscher, and S. Roth, “Hydrogen adsorption in different carbon nanostructures.,” *Carbon N. Y.*, vol. 43, pp. 2209–2214, Aug. 2005.

[74] J. M. Blackman, J. W. Patrick, A. Arenillas, W. Shi, and C. E. Snape, “Activation of carbon nanofibres for hydrogen storage.,” *Carbon N. Y.*, vol. 44, pp. 1376–1385, July 2006.

[75] A. G. Wong-Foy, A. J. Matzger, and O. M. Yaghi, “Exceptional H2 saturation uptake in microporous metal-organic frameworks.,” *J. Am. Chem. Soc.*, vol. 128, pp. 3494–5, Mar. 2006.

[76] “Doe office of energy efficiency and renewable energy hydrogen, fuel cells & infrastructure technologies program multi-year research, development and demonstration plan.,” tech. rep., US Department of Energy (DoE), 2009.

[77] S. Gregg and K. Sing, *Adsorption, Surface Area and Porosity.* London: Academic Press, 2nd ed., 1982.

[78] Q. Wang and J. K. Johnson, “Molecular simulation of hydrogen adsorption in single-walled carbon nanotubes and idealized carbon slit pores.,” *J. Chem. Phys.*, vol. 110, no. 1, p. 577, 1999.

[79] A. Kleinhammes, R. J. Anderson, Q. Chen, Y. Jeong, T. C. M. Chung, and Y. Wu, “Enhanced Binding Energy and Slow Kinetics of H2 in Boron-Substituted Graphitic Carbon,” *J. Phys. Chem. C*, vol. 114, pp. 13705–13708, Aug. 2010.

[80] E. Akiba, *Metal Hydrides.*, ch. 19, pp. 395–413. Weinheim: Wiley, 2010.

[81] J. J. Vajo, F. Mertens, C. C. Ahn, R. C. Bowman, and B. Fultz, “Altering Hydrogen Storage Properties by Hydride Destabilization through Alloy Formation: LiH and MgH2 Destabilized with Si.,” *J. Phys. Chem. B*, vol. 108, pp. 13977–13983, Sept. 2004.

[82] K. L. Lim, H. Kazemian, Z. Yaakob, and W. R. W. Daud, “Solid-state materials and methods for hydrogen storage: A critical review.,” *Chem. Eng. Technol.*, vol. 33, pp. 213–26, Feb. 2010.

[83] E. Fakiolu, “A review of hydrogen storage systems based on boron and its compounds.,” *Int. J. Hydrogen Energy*, vol. 29, pp. 1371–1376, Oct. 2004.

[84] D. Teichmann, W. Arlt, P. Wasserscheid, and R. Freymann, “A future energy supply based on Liquid Organic Hydrogen Carriers (LOHC).,” *Energy Environ. Sci.*, vol. 4, no. 8, p. 2767, 2011.

[85] L. M. Kustov, A. L. Tarasov, J. Sung, and D. Y. Godovsky, “Hydrogen storage materials.,” *Mendeleev Commun.*, vol. 24, pp. 1–8, Jan. 2014.

[86] H. G. Schimmel, G. Nijkamp, G. J. Kearley, A. Rivera, K. P. De Jong, and F. M. Mulder, “Hydrogen adsorption in carbon nanostructures compared.,” *Mater. Sci. Eng. B*, vol. 108, pp. 124–129, Apr. 2004.

[87] A. Kidnay and M. Hiza, “High pressure adsorption isotherms of neon, hydrogen and helium at 76 k.,” *Adv. Cryog. Eng.*, vol. 12, no. 1, pp. 730–6, 1967.

[88] J. Pang, J. E. Hampsey, Z. Wu, Q. Hu, and Y. Lu, “Hydrogen adsorption in mesoporous carbons.,” *Appl. Phys. Lett.*, vol. 85, no. 21, pp. 4887–4889, 2004.

[89] F. Rouquerol, J. Rouquerol, and K. Sing, *Adsorption by powders and porous solids - Principles, methodology and applications.* London: Academic Press, 2nd ed., 1999.

[90] R. Chahine and T. K. Bose, "Low-pressure adsorption storage of hydrogen.," *Int. J. Hydrogen Energy*, vol. 19, no. 2, pp. 161–4, 1994.

[91] G. Zheng, "New structure of carbon nanofibers after high-temperature heat-treatment," *Carbon N. Y.*, vol. 41, no. 4, pp. 853–856, 2003.

[92] E. Senoz and R. P. Wool, "Hydrogen storage on pyrolyzed chicken feather fibers," *Int. J. Hydrogen Energy*, vol. 36, pp. 7122–7127, June 2011.

[93] F. Fernandez-Alonso, F. J. Bermejo, C. Cabrillo, R. O. Loutfy, V. Leon, and M.-L. Saboungi, "Nature of the Bound States of Molecular Hydrogen in Carbon Nanohorns.," *Phys. Rev. Lett.*, vol. 98, pp. 2–5, May 2007.

[94] A. Chambers, C. Park, R. T. K. Baker, and N. M. Rodriguez, "Hydrogen storage in graphite nanofibers.," *J. Phys. Chem. B*, vol. 102, pp. 4253–4256, Feb. 1998.

[95] A. C. Dillon, K. M. Jones, T. A. Bekkedahl, C. H. Kiang, D. S. Bethune, and M. J. Heben, "Storage of hydrogen in single-walled carbon nanotubes.," *Nature*, vol. 386, pp. 377–379, 1997.

[96] A. C. Dillon and M. J. Heben, "Hydrogen storage using carbon adsorbents: past, present and future.," *Appl. Phys. A Mater. Sci. Process.*, vol. 72, pp. 133–142, Feb. 2001.

[97] P. Bénard and R. Chahine, "Storage of hydrogen by physisorption on carbon and nanostructured materials.," *Scr. Mater.*, vol. 56, pp. 803–808, May 2007.

[98] M. S. Dresselhaus and G. Dresselhaus, "Intercalation compounds of graphite.," *Adv. Phys.*, vol. 51, pp. 1–186, Jan. 2002.

[99] A. Lovell, N. T. Skipper, S. M. Bennington, and R. I. Smith, "A high-resolution neutron scattering study of the hydrogen-driven metal-insulator phase transition in KC8Hx.," *J. Alloys Compd.*, vol. 446-447, pp. 397–401, Oct. 2007.

[100] J. Purewal, J. Keith, C. Ahn, B. Fultz, C. Brown, and M. Tyagi, "Adsorption and melting of hydrogen in potassium-intercalated graphite," *Phys. Rev. B*, vol. 79, pp. 1–7, Feb. 2009.

[101] J. Purewal, J. B. Keith, C. C. Ahn, C. M. Brown, M. Tyagi, and B. Fultz, "Hydrogen diffusion in potassium intercalated graphite studied by quasielastic neutron scattering," *J. Chem. Phys.*, vol. 137, no. 22, p. 224704, 2012.

[102] R. Barrer, *Zeolites and Clay Minerals as Sorbents and Molecular Sieves.* London: Academic Press, 1978.

[103] H. W. Langmi, A. Walton, M. M. Al-Mamouri, S. R. Johnson, D. Book, J. D. Speight, P. P. Edwards, I. Gameson, P. A. Anderson, and I. R. Harris, "Hydrogen adsorption in zeolites A, X, Y and RHO.," *J. Alloys Compd.*, vol. 356-357, pp. 710–5, Aug. 2003.

[104] H. W. Langmi, D. Book, A. Walton, S. R. Johnson, M. M. Al-Mamouri, J. D. Speight, P. P. Edwards, I. R. Harris, and P. A. Anderson, "Hydrogen storage in ion-exchanged zeolites.," *J. Alloys Compd.*, vol. 404-406, pp. 637–42, Dec. 2005.

[105] G. T. Palomino, M. R. L. Carayol, and C. O. Arean, "Hydrogen adsorption on magnesium-exchanged zeolites.," *J. Mater. Chem.*, vol. 16, pp. 2884–5, 2006.

[106] Y. H. Hu and L. Zhang, "Hydrogen storage in metal-organic frameworks.," *Adv. Mater.*, vol. 22, pp. E117–30, May 2010.

[107] G. Férey, C. Mellot-Draznieks, C. Serre, F. Millange, J. Dutour, S. Surblé, and I. Margiolaki, "A chromium terephthalate-based solid with unusually large pore volumes and surface area.," *Science (80-.).*, vol. 309, pp. 2040–2, Sept. 2005.

[108] J. L. C. Rowsell and O. M. Yaghi, "Strategies for hydrogen storage in metal-organic frameworks.," *Angew. Chem. Int. Ed. Engl.*, vol. 44, pp. 4670–9, July 2005.

[109] L. Pan, M. B. Sander, X. Huang, J. Li, M. Smith, E. Bittner, B. Bockrath, and J. K. Johnson, "Microporous metal organic materials: promising candidates as sorbents for hydrogen storage.," *J. Am. Chem. Soc.*, vol. 126, pp. 1308–9, Feb. 2004.

[110] W. Zhou, H. Wu, M. R. Hartman, and T. Yildirim, "Hydrogen and Methane Adsorption in Metal-Organic Frameworks: A High-Pressure Volumetric Study.," *J. Phys. Chem. C*, vol. 111, pp. 16131–16137, Nov. 2007.

[111] M. DincÄƒ and J. R. Long, "High-enthalpy hydrogen adsorption in cation-exchanged variants of the microporous metal-organic framework Mn3[(Mn4Cl)3(BTT)8(CH3OH)10]2.," *J. Am. Chem. Soc.*, vol. 129, pp. 11172–6, Sept. 2007.

[112] A. K. Singh, A. Sadrzadeh, and B. I. Yakobson, "Metallacarboranes: toward promising hydrogen storage metal organic frameworks.," *J. Am. Chem. Soc.*, vol. 132, pp. 14126–9, Oct. 2010.

[113] P. Wang, S. Orimo, T. Matsushima, H. Fujii, and G. Majer, "Hydrogen in mechanically prepared nanostructured h-BN: a critical comparison with that in nanostructured graphite.," *Appl. Phys. Lett.*, vol. 80, no. 2, p. 318, 2002.

[114] G. G. Wicks, L. K. Heung, and R. F. Schumacher, "Microspheres and microworlds.," *Am. Ceram. Soc. Bull.*, vol. 87, no. 6, pp. 23–8, 2008.

[115] D. B. Rapp and J. E. Shelby, "Photo-induced hydrogen outgassing of glass.," *J. Non. Cryst. Solids*, vol. 349, pp. 254–259, Dec. 2004.

[116] W. L. Mao and H.-K. Mao, "Hydrogen storage in molecular compounds.," *Proc. Natl. Acad. Sci. U. S. A.*, vol. 101, pp. 708–10, Jan. 2004.

[117] C. Aguzzi, P. Cerezo, C. Viseras, and C. Caramella, "Use of clays as drug delivery systems: Possibilities and limitations," *Appl. Clay Sci.*, vol. 36, pp. 22–36, Apr. 2007.

[118] W. P. Gates, A. Bouazza, and G. J. Churchman, "Bentonite Clay Keeps Pollutants at Bay," *Elements*, vol. 5, pp. 105–110, May 2009.

[119] J. T. Kloprogge, "Synthesis of smectites and porous pillared clay catalysts: a review.," *J. Porous Mater.*, vol. 41, pp. 5–41, 1998.

[120] J. M. Diamond, "Dirty eating for healthy living," *Nature*, vol. 400, no. July, pp. 120–1, 1999.

[121] S. Solin, "Clays and clay intercalation compounds: Properties and physical phenomena.," *Annu. Rev. Mater. Sci.*, vol. 27, no. 4, pp. 89–115, 1997.

[122] S. Olejnik, G. C. Stirling, and J. W. White, "Neutron scattering studies of hydrated layer silicates.," *Spec. Discuss. Faraday Soc.*, vol. 58, pp. 194–201, 1970.

[123] D. J. Cebula, R. K. Thomas, and J. W. White, "Neutron diffraction from clay-water systems," *Clays Clay Miner.*, vol. 27, no. 1, pp. 39–52, 1979.

[124] D. E. Woessner and B. S. J. Snowden, "A Study of the Orientation of Adsorbed Water Molecules on Montmorillonite Clays by Pulsed NMR.," *J. Colloid Interface Sci.*, vol. 30, no. 1, pp. 54–68, 1969.

[125] G. J., *NMR spectroscopy of molecules and ions at clay surfaces.*, ch. 19, pp. 216–246. Amsterdam, The Netherlands: Elsevier, 2004.

[126] G. Brindley and G. Pedro, "Meeting of the nomenclature committee of a.i.p.e.a.," *A.I.P.E.A. Newsletter*, vol. 12, pp. 5–6, 1976.

[127] W. Deer, R. Howie, and J. Zussman, *An introduction to the rock-forming minerals.* New York: Wiley-Interscience, 2nd ed., 1992.

[128] G. Sposito and R. Prost, "Structure of water adsorbed in smectites.," *Chem. Rev.*, vol. 82, pp. 553–73, Jan. 1982.

[129] I. Shainberg and W. Kemper, "Hydration status of adsorbed cations.," *Soil Sci. Soc. Am. J.*, vol. 30, pp. 707–13, 1966.

[130] G. Brindley and G. Brown, *Crystal Structures of Clay Minerals and their X-ray Identification.* London: The Mineralogical Society, 1984.

[131] R. W. Mooney, A. G. Keenan, and L. A. Wood, "Adsorption of water vapor by montmorillonite. II. Effect of exchangeable ions and lattice swelling as measured by X-Ray diffraction.," *J. Am. Chem. Soc.*, vol. 74, pp. 1371–51, 1952.

[132] J. Swenson, R. Bergman, and W. S. Howells, "Quasielastic neutron scattering of two-dimensional water in a vermiculite clay.," *J. Chem. Phys.*, vol. 113, no. 7, p. 2873, 2000.

[133] A. V. De Siqueira, C. Lobban, N. T. Skipper, G. D. Williams, A. K. Soper, R. Done, J. W. Dreyer, R. J. Humphreys, and J. A. R. Bones, "The structure of pore fluids in swelling clays at elevated pressures and temperatures.," *J. Phys. Condens. Matter*, vol. 11, pp. 9179–88, 1999.

[134] A. Newman, *Chemistry of clays and clay minerals.* New York: Wiley-Interscience, 1987.

[135] R. Additives, "Laponite.," 2010. Product Brochure.

[136] E. Balnois, S. Durand-Vidal, and P. Levitz, "Probing the morphology of Laponite clay colloids by Atomic Force Microscopy.," *Langmuir*, vol. 19, pp. 6633–6637, 2003.

[137] N. Skipper and R. De Carvalho, "Atomistic computer simulation of the clay-fluid interface in colloidal laponite," *J. Chem. Phys.*, vol. 114, no. 8, pp. 3727–33, 2001.

[138] S. Borsacchi, M. Geppi, L. Ricci, G. Ruggeri, and C. A. Veracini, "Interactions at the surface of organophilic-modified laponites: a multinuclear solid-state NMR study.," *Langmuir*, vol. 23, pp. 537–44, Mar. 2007.

[139] N. T. Skipper, A. K. Soper, and J. D. C. McConnell, "The structure of interlayer water in vermiculite.," *J. Chem. Phys.*, vol. 94, no. 8, pp. 5751–60, 1991.

[140] G. Brown, "Crystal structures of clay minerals and related phyllosilicates.," *Philos. Trans. R. Soc. A Math. Phys. Eng. Sci.*, vol. 311, pp. 221–240, 1984.

[141] M. Vlot, J. Huinink, and J. van der Eerden, “Free energy calculations on systems of rigid molecules: An application to the tip4p model of h2o.,” *J. Chem. Phys.*, vol. 110, pp. 55–61, 1999.

[142] G. Squires, *Introduction to the theory of thermal neutron scattering.* Cambridge: Cambridge University Press, 2012.

[143] S. Marshall, W.; Lovesey, *Theory of Thermal Neutron Scattering.* Oxford: Oxford Press, 1971.

[144] L. Van Hove, “Correlations in space and time and Born approximation scattering in systems of interacting particles.,” *Phys. Rev.*, vol. 95, no. 1, pp. 249–62, 1954.

[145] E. Merzbacher, *Quantum mechanics.* New York: John Wiley & Sons, 1998.

[146] A. Furrer, J. Mesot, and T. Strässler, *Neutron scattering in condensed matter physics.* Singapore: World Scientific, 2009.

[147] K. Lefmann, “Basics of neutron scattering.,” September 2013.

[148] A. K. Soper, “Gudrunn and gudrunx: programs for correcting raw neutron and x-ray diffraction data to differential scattering cross section.,” Tech. Rep. RAL-TR-2011-013, Rutherford Appleton Laboratories: Oxon, U.K., 2011.

[149] H. E. Fischer, A. C. Barnes, and P. S. Salmon, “Neutron and x-ray diffraction studies of liquids and glasses,” *Reports Prog. Phys.*, vol. 69, pp. 233–299, Jan. 2006.

[150] H. N. Bordallo, L. P. Aldridge, G. J. Churchman, W. P. Gates, M. T. F. Telling, K. Kiefer, P. Fouquet, T. Seydel, and S. A. Kimber, “Quasi-Elastic Neutron Scattering Studies on Clay Interlayer-Space Highlighting the Effect of the Cation in Confined Water Dynamics.,” *J. Phys. Chem. C*, vol. 112, pp. 13982–91, Sept. 2008.

[151] J. J. Tuck, P. L. Hall, M. H. B. Hayes, D. K. Ross, and C. Poinsignon, “Quasi-elastic neutron-scattering studies of the dynamics of intercalated molecules in charge-deficient layer silicates.,” *J. Chem. Soc. Faraday Trans. 1*, vol. 80, pp. 309–24, 1984.

[152] N. Malikova, A. Cadène, V. Marry, E. Dubois, and P. Turq, “Diffusion of water in clays on the microscopic scale: modeling and experiment.,” *J. Phys. Chem. B*, vol. 110, pp. 3206–14, Feb. 2006.

[153] E. Pefoute, E. Kemner, J. C. Soetens, M. Russina, and A. Desmedt, “Diffusive Motions of Molecular Hydrogen Confined in THF Clathrate Hydrate.,” *J. Phys. Chem. C*, vol. 116, pp. 16823–9, Aug. 2012.

[154] E. Cohen de Lara and R. Kahn, “Diffusivity of hydrogen and methane molecules in A zeolites : Neutron scattering measurements and comparison.,” *Zeolites*, vol. 12, no. March, pp. 256–60, 1992.

[155] R. Hempelmann, *Quasielastic neutron scattering and solid state diffusion.* Clarendon: Oxford Press, 2000.

[156] J. W. Clark, P. G. Hall, A. J. Pidduck, and C. J. Wright, “Molecular diffusion in monolayer films of water adsorbed on a silica surface.,” *J. Chem. Soc. Faraday Trans. 1*, vol. 81, no. 9, pp. 2067–82, 1985.

[157] A. Fick, “On liquid diffusion,” *Phil. Mag.*, vol. 10, p. 30, 1855.

[158] P. L. Hall and D. K. Ross, “Incoherent neutron scattering functions for random jump diffusion in bounded and infinite media.,” *Mol. Phys.*, vol. 43, no. 3, pp. 673–682, 1981.

[159] D. Frenkel and B. Smit, *Understanding molecular simulation: from algorithms to applications.* London: Academic Press, 2nd ed., 2002.

[160] C. T. Chudley and R. J. Elliott, “Neutron scattering from a liquid on a jump diffusion model.,” *Proc. Phys. Soc.*, vol. 77, pp. 353–361, 1961.

[161] K. S. Singwi and A. SjoÌˆlander, “Diffusive motions in water and cold neutron scattering.,” *Phys. Rev.*, vol. 119, no. 3, pp. 863–71, 1960.

[162] D. J. Cebula, R. K. Thomas, and J. W. White, “Diffusion of water in Li-montmorillonite studied by QENS.,” *Clays Clay Miner.*, vol. 29, no. 4, pp. 241–8, 1981.

[163] R.-J. Roe, *Methods of X-ray and neutron scattering in polymer science.* Oxford: Oxford University Press, 2000.

[164] M. Al-Mukhtar, Y. Qi, J.-F. Alcover, J. Conard, and F. Bergaya, "Hydromechanical effects: (II) on the water-Na-smectite system.," *Clay Miner.*, vol. 35, pp. 537–44, 2000.

[165] S. Aceman, N. Lahav, and S. Yariv, "XRD study of the dehydration and rehydration behaviour of Al-pillared smectites differing in source of charge.," *J. Therm. Anal.*, vol. 50, pp. 241–256, 1997.

[166] S. Lantenois, "Hydrothermal synthesis and characterization of dioctahedral smectites: A montmorillonites series.," *Appl. Clay Sci.*, vol. 38, pp. 165–178, Feb. 2008.

[167] F. R. Trouw and D. L. Price, "Chemical applications of neutron scattering.," *Annu. Rev. Phys. Chem.*, vol. 50, pp. 571–601, 1999.

[168] T. Blach and E. Gray, "Sieverts apparatus and methodology for accurate determination of hydrogen uptake by light-atom hosts.," *J. Alloys Compd.*, vol. 446-447, pp. 692–697, Oct. 2007.

[169] W. P. Gates, H. N. Bordallo, L. P. Aldridge, T. Seydel, H. Jacobsen, V. Marry, and G. J. Churchman, "Neutron Time-of-Flight Quantification of Water Desorption Isotherms of Montmorillonite.," *J. Phys. Chem. C*, vol. 116, pp. 5558–5570, Mar. 2012.

[170] D. P. Broom, "The accuracy of hydrogen sorption measurements on potential storage materials.," *Int. J. Hydrogen Energy*, vol. 32, pp. 4871– 4888, 2007.

[171] S. Brunauer, P. H. Emmett, and E. Teller, "Adsorption of gases in multimolecular layers.," *J. Am. Chem. Soc.*, vol. 60, no. 2, pp. 309–19, 1938.

[172] M. S. Graboski and T. E. Daubert, "A Modified Soave Equation of State for Phase Equilibrium Calculations. 1. Hydrocarbon Systems.," *Ind. Eng. Chem. Process Des. Dev.*, vol. 17, pp. 443–448, Oct. 1978.

[173] C. Zhang, X. Lu, and A. Gu, "How to accurately determine the uptake of hydrogen in carbonaceous materials.," *Int. J. Hydrogen Energy*, vol. 29, pp. 1271–6, 2004.

[174] E. W. Lemmon, M. L. Huber, and M. O. McLinden, "NIST Reference Fluid Thermodynamic and Transport Properties - REFPROP.," tech. rep., 2007.

[175] A. Bondi, "Van der Waals volumes and radii.," *J. Phys. Chem.*, vol. 68, no. 3, pp. 441–51, 1964.

[176] A. V. Neimark and P. I. Ravikovitch, "Calibration of Pore Volume in Adsorption Experiments and Theoretical Models.," *Langmuir*, vol. 13, pp. 5148–5160, Sept. 1997.

[177] A. L. Myers and P. A. Monson, "Adsorption in Porous Materials at High Pressure: Theory and Experiment.," *Langmuir*, vol. 18, pp. 10261–73, Dec. 2002.

[178] I. Langmuir, "The constitution and fundamental properties of solids and liquids. Part I. Solids.," *J. Am. Chem. Soc.*, vol. 38, no. 11, pp. 2221–95, 1916.

[179] A. W. C. Van den Berg, S. T. Bromley, J. C. Wojdel, and J. C. Jansen, "Molecular hydrogen confined within nanoporous framework materials: Comparison of density functional and classical force-field descriptions.," *Phys. Rev. B*, vol. 72, pp. 155428(1–7), Oct. 2005.

[180] M. J. Sanchez-Martin, M. S. Rodriguez-Cruz, M. S. Andrades, and M. Sanchez-Camazano, "Efficiency of different clay minerals modified with a cationic surfactant in the adsorption of pesticides: Influence of clay type and pesticide hydrophobicity.," *Appl. Clay Sci.*, vol. 31, pp. 216–228, Mar. 2006.

[181] R. Sips, "On the structure of a catalyst surface.," *J. Chem. Phys.*, vol. 16, no. 5, pp. 490–5, 1948.

[182] S. Ma, J. Eckert, P. M. Forster, J. W. Yoon, Y. K. Hwang, J.-S. Chang, C. D. Collier, J. B. Parise, and H.-C. Zhou, "Further investigation of the effect of framework catenation on hydrogen uptake in metal-organic frameworks.," *J. Am. Chem. Soc.*, vol. 130, pp. 15896–902, Nov. 2008.

[183] H. Furukawa, M. A. Miller, and O. M. Yaghi, "Independent verification of the saturation hydrogen uptake in MOF-177 and establishment of a benchmark for hydrogen adsorption in metal-organic frameworks.," *J. Mater. Chem.*, vol. 17, no. 30, p. 3197, 2007.

[184] R. J. F. L. De Carvalho and N. T. Skipper, "Atomistic computer simulation of the clay-fluid interface in colloidal laponite.," *J. Chem. Phys.*, vol. 114, no. 8, p. 3727, 2001.

[185] A. L. Myers, "Thermodynamics of Adsorption.," in *Chem. Thermodyn. Ind.* (T. Letcher, ed.), ch. 21, pp. 243–53, The Royal Society of Chemistry, 2004.

[186] S. Tedds, A. Walton, D. P. Broom, and D. Book, "Characterisation of porous hydrogen storage materials: carbons, zeolites, MOFs and PIMs.," *Faraday Discuss.*, vol. 151, p. 75, 2011.

[187] "Determination of the specific surface area of powders - part i: Bet method of gas adsorption for solids (including porous materials).," Tech. Rep. BS 4359-1 : 1996 (ISO 9277: 1995), British Standards Institution, 1996.

[188] M. Dogan, A. U. Dogan, F. I. Yesilyurt, D. Alaygut, I. Buckner, and D. E. Wurster, "Baseline studies of The Clay Minerals Society special clays: specific surface area by the Brunauer Emmett Teller (BET) method.," *Clays Clay Miner.*, vol. 55, pp. 534–541, Oct. 2007.

[189] D. T. Bowron, A. K. Soper, K. Jones, S. Ansell, S. Birch, J. Norris, L. Perrott, D. Riedel, N. J. Rhodes, S. R. Wakefield, A. Botti, M. A. Ricci, F. Grazzi, and M. Zoppi, "NIMROD: The Near and InterMediate Range Order Diffractometer of the ISIS second target station.," *Rev. Sci. Instrum.*, vol. 81, p. 033905, Mar. 2010.

[190] V. Sears, “Neutron scattering lengths and cross sections.,” *Neutron News*, vol. 3, no. 3, pp. 26–37, 1992.

[191] A. De Stefanis, A. A. G. Tomlinson, T. A. Steriotis, K. L. Stefanopoulos, and U. Keiderling, “Nanostructural characterisation of catalysts by SANS.,” *Phys. B Condens. Matter*, vol. 350, pp. E521–E524, July 2004.

[192] D. H. Powell, H. E. Fischer, and N. T. Skipper, “The Structure of Interlayer Water in Liâˆ’Montmorillonite Studied by Neutron Diffraction with Isotopic Substitution,” *J. Phys. Chem. B*, vol. 102, pp. 10899–10905, Dec. 1998.

[193] C. J. Carlile and M. A. Adams, “The design of the IRIS inelastic neutron spectrometer and improvements to its analysers.,” *Phys. B Condens. Matter*, vol. 182, pp. 431–40, 1992.

[194] W. Howells, V. García Sakai, F. Demmel, M. Telling, and F. Fernandez-Alonso, *MODEs (1998-2006) A graphic user interface for IRIS data analysis.*, February 2010.

[195] E. Farhi and D. McMorrow, *Mfit.*, February 1999.

[196] H. Mutka, “Coupled time and space focusing for time-of-flight inelastic scattering.,” *Nucl. Instruments Methods A*, vol. 338, pp. 144–150, Jan. 1994.

[197] ILL, *LAMP, the Large Array Manipulation Program.*

[198] D. Richard, M. Ferrand, and G. J. Kearley, “Analysis and visualisation of neutron-scattering data.,” *J. Neutron Res.*, vol. 4, pp. 33–39, Dec. 1996.

[199] M. Zoppi, M. Celli, and A. K. Soper, “Neutron diffraction determination of the thermodynamic derivatives of the microscopic structure of liquid parahydrogen.,” *Phys. Rev. B*, vol. 58, pp. 11905–10, Nov. 1998.

[200] J. Eckert, J. M. Nicol, J. Howard, and F. R. Trouw, “Adsorption of Hydrogen in Ca-Exchanged Na-A Zeolites Probed by Inelastic Neutron Scattering Spectroscopy.,” *J. Phys. Chem.*, vol. 100, pp. 10646–10651, Jan. 1996.

[201] P. Bala, B. K. Samantaray, and S. K. Srivastava, “Dehydration transformation in Ca-montmorillonite.,” *Bull. Mater. Sci.*, vol. 23, pp. 61–7, Feb. 2000.

[202] J. M. Green, K. J. D. Mackenzie, and J. H. Sharp, “Thermal Reactions of Synthetic Hectorite.,” *Clays Clay Miner.*, vol. 18, pp. 339–46, 1970.

[203] E. Paterson and D. R. Clark, “Pressure-induced cation exchange in bentonite/laponite mixtures.,” *Clay Miner.*, vol. 26, pp. 371–5, 1991.

[204] S. Mughabghab, M. Divadeenam, and N. Holden, *Neutron Cross Sections.* New York: Academic Press, 1981.

[205] G. Srinivas, A. Lovell, C. A. Howard, N. T. Skipper, M. Ellerby, and S. M. Bennington, “Structure and phase stability of hydrogenated first-stage alkali- and alkaline-earth metal-graphite intercalation compounds.,” *Synth. Met.*, vol. 160, pp. 1631–1635, Aug. 2010.

[206] P. J. Chupas, X. Qiu, J. C. Hanson, P. L. Lee, C. P. Grey, and S. J. L. Billinge, “Rapid-acquisition pair distribution function (RA-PDF) analysis.,” *J. Appl. Crystallogr.*, vol. 36, pp. 1342–7, Nov. 2003.

[207] D. Li, M. Peng, and T. Murata, “Coordination and local structure of magnesium in silicate minerals and glasses: Mg K-edge XANES study.,” *Can. Mineral.*, vol. 37, pp. 199–206, 1999.

[208] N. T. Skipper, A. K. Soper, and M. V. Smalley, “Neutron Diffraction Study of Calcium Vermiculite: Hydration of Calcium Ions in a Confined Environment.,” *J. Phys. Chem.*, vol. 98, no. 3, pp. 942–5, 1994.

[209] N. Bimbo, J. E. Sharpe, V. P. Ting, A. Noguera-Díaz, and T. J. Mays, “Isosteric enthalpies for hydrogen adsorbed on nanoporous materials at high pressures.,” *Adsorption*, vol. 19, Oct. 2013.

[210] P. A. Georgiev, A. Albinati, and J. Eckert, “Room temperature isosteric heat of dihydrogen adsorption on Cu(I) cations in zeolite ZSM-5,” *Chem. Phys. Lett.*, vol. 449, pp. 182–185, Nov. 2007.

[211] A. Holleman and E. Wiberg, *Inorganic Chemistry.* London: Academic Press, 2001.

[212] D. E. O’Reilly and E. M. Peterson, “Self-diffusion of liquid hydrogen and deuterium.,” *J. Chem. Phys.*, vol. 66, no. 3, pp. 934–7, 1977.

[213] M. G. Nijkamp, J. E. M. J. Raaymakers, A. J. Van Dillen, and K. P. De Jong, “Hydrogen storage using physisorption - materials demands.,” *Appl. Phys. A*, vol. 72, pp. 619–23, 2001.

[214] C. I. Contescu, D. Saha, N. C. Gallego, E. Mamontov, A. I. Kolesnikov, and V. V. Bhat, “Restricted dynamics of molecular hydrogen confined in activated carbon nanopores.,” *Carbon N. Y.*, vol. 50, pp. 1071–82, Mar. 2012.

[215] L. A. Vashchenko, V. V. Katal’nikova, V. V. Ershov, and V. V. Serpinskii, “Adsorption of hydrogen on zeolite NaA at low temperatures.,” *Bull. Acad. Sci. USSR Div. Chem. Sci.*, vol. 39, pp. 1950–1952, Sept. 1990.

[216] F. Stephanie-Victoire, A.-M. Goulay, and E. Cohen de Lara, “Adsorption and Coadsorption of Molecular Hydrogen Isotopes in Zeolites. 1. Isotherms of H2, HD, and D2 in NaA by Thermomicrogravimetry.,” *Langmuir*, vol. 14, pp. 7255–9, 1998.

[217] D. Zhao, D. Yuan, and H.-C. Zhou, “The current status of hydrogen storage in metal-organic frameworks.,” *Energy Environ. Sci.*, vol. 1, no. 2, p. 222, 2008.

[218] D. J. Tranchemontagne, K. S. Park, H. Furukawa, J. Eckert, C. B. Knobler, and O. M. Yaghi, “Hydrogen storage in new metal-organic frameworks.,” *J. Phys. Chem. C*, vol. 116, pp. 13143–51, Feb. 2012.

[219] J. S. Edge, N. T. Skipper, F. Fernandez-Alonso, A. Lovell, G. Srinivas, S. M. Bennington, V. Garcia Sakai, and T. G. A. Youngs, “Structure and Dynamics of Molecular Hydrogen in the Interlayer Pores of a Swelling 2:1 Clay by Neutron Scattering.,” *J. Phys. Chem. C*, vol. 118, pp. 25740–7, Nov. 2014.

[220] A. Delville, “Structure of liquids at a solid interface: an application to the swelling of clay by water.,” *Langmuir*, vol. 8, pp. 1796–805, July 1992.

[221] W. P. A. Hass, G. Seidel, and N. J. Poulis, “Nuclear spin relaxation and molecular diffusion in liquid H.,” *Physica*, vol. 26, pp. 834–52, 1960.

[222] M. Bienfait, P. Zeppenfeld, R. C. J. Ramos, J. M. Gay, O. E. Vilches, and G. Coddens, “Isotopic ordering in adsorbed hydrogen monolayers.,” *Phys. Rev. B*, vol. 60, pp. 11773–82, Oct. 1999.

[223] Y. J. Glanville, J. V. Pearce, P. E. Sokol, B. Newalker, and S. Komarneni, “Study of H2 confined in the highly ordered pores of MCM-48.,” *Chem. Phys.*, vol. 292, pp. 289–93, 2003.

[224] Y. Yang, C. M. Brown, C. Zhao, A. L. Chaffee, B. Nick, D. Zhao, P. A. Webley, J. Schalch, J. M. Simmons, Y. Liu, J.-H. Her, C. E. Buckley, and D. A. Sheppard, “Micro-channel development and hydrogen adsorption properties in templated microporous carbons containing platinum nanoparticles.,” *Carbon N. Y.*, vol. 49, pp. 1305–1317, Apr. 2011.

[225] O.-E. Haas, J. M. Simon, S. Kjelstrup, A. L. Ramstad, and P. Fouquet, “Quasi-elastic neutron scattering investigation of the hydrogen surface self-diffusion on polymer electrolyte membrane fuel cell catalyst support.,” *J. Phys. Chem. C*, vol. 112, pp. 3121–5, 2008.

[226] D. G. Narehood, J. V. Pearce, P. C. Eklund, P. E. Sokol, R. E. Lechner, J. Pieper, J. R. D. Copley, and J. C. Cook, “Diffusion of H2 adsorbed on single-walled carbon nanotubes.,” *Phys. Rev. B*, vol. 67, pp. 1–5, May 2003.

[227] R. Kahn, E. Cohen de Lara, and E. Viennet, "Diffusivity of the hydrogen molecule sorbed in NaA zeolite by a neutron scattering experiment.," *J. Chem. Phys.*, vol. 91, no. 8, p. 5097, 1989.

[228] B. Chen, X. Zhao, A. Putkham, K. Hong, E. B. Lobkovsky, E. J. Hurtado, A. J. Fletcher, and K. M. Thomas, "Surface interactions and quantum kinetic molecular sieving for H2 and D2 adsorption on a mixed metal-organic framework material.," *J. Am. Chem. Soc.*, vol. 130, pp. 6411–23, May 2008.

[229] F. Salles, H. Jobic, G. Maurin, M. Koza, P. Llewellyn, T. Devic, C. Serre, and G. Ferey, "Experimental Evidence Supported by Simulations of a Very High H2 Diffusion in Metal Organic Framework Materials.," *Phys. Rev. Lett.*, vol. 100, p. 245901, June 2008.

[230] R. Bergman and J. Swenson, "Dynamics of supercooled water in confined geometry," *Nature*, vol. 403, pp. 283–6, Jan. 2000.

[231] O. N. Osychenko, R. Rota, and J. Boronat, "Superfluidity of metastable glassy bulk para-hydrogen at low temperature," *Phys. Rev. B*, vol. 85, p. 224513, June 2012.

[232] M. Conte, P. Prosini, and S. Passerini, "Overview of energy/hydrogen storage: state-of-the-art of the technologies and prospects for nanomaterials.," *Mater. Sci. Eng. B*, vol. 108, pp. 2–8, Apr. 2004.

List of Figures

1.1 (Adapted from [8].) Schematic view of an acidic proton exchange membrane (PEM) fuel cell, showing input fuels and waste products, as well as the chemical reactions at each electrode. 13

2.1 The INS rotational spectrum of solid p-H_2, showing the strong, free rotor transition peak at 14.74 meV (from [45]). 23

2.2 Schematic representation of H_2 physisorption, showing the angles represented in the potential equation: $V(\theta, \phi) = \phi \cos^2 \theta$ (Equation 2.3). 24

2.3 (Adapted from [52].) 2D hindered rotor for H_2 in the cylindrically symmetric potential, $V(\theta) = V_0(1 - \cos 2\theta)$. 25

2.4 (Adapted from [49].) Splitting pattern for the 2D hindered rotor rotational energy levels of H_2, showing how the height of the rotational barrier can be determined from the degree of splitting between ground and first excited state energies. 25

2.5 The phase diagram of H_2, showing transition points (simplified from [67]). 29

2.6 (Adapted from [70].) Schematic illustration of the three regions of H_2 binding to the surface of a solid state material (represented simply by the horizontal lines). a) Shows the typical configuration and distances involved in physisorption, while b) shows that for chemisorption. The region inbetween these two extemes is illustrated in c), where the H-H bond elongates and approaches the surface more closely. 33

3.1 Zeolite framework structures: (a) A, (b) X and Y, (c) Rho (from [103]). The H_2 molecule is shown to scale for comparison. 42

3.2 Examples of basic crystalline units for MOF frameworks: (A) MOF-5, (B) MOF-177 (from [108]). Black spheres represent carbon, red spheres oxygen. Hydrogen atoms have been omitted. Yellow spheres represent the largest sphere fitting into the cages without touching the van der Waals' volumes of the framework atoms. Blue polyhedra represent coordinating metal ions. The H_2 molecule is shown to scale for comparison. 44

4.1 The layered structure of clay minerals. (a) A single $SiO_4{}^{4-}$ tetrahedron, (b) A single $AlO_8{}^{5-}$ octahedron, (c) Octahedral sheet of linked AlO_8, (d) Tetrahedral sheet of linked SiO_4, (e) A tetrahedral sheet links to an octahedral sheet to form a 1:1 layer. Colours: blue circles are Si atoms; red circles are Al atoms; dark purple circles are O atoms; green circles are H atoms. 48

4.2 Schematic view of the interlayer structure, showing the suitability of the dimensions for (a) an ideal clay, showing the exposed cations (atomic or polyatomic) and minimum interlayer spacing required for H_2 adsorption and (b) a one-layer hydrate Ca-smectite. 55

5.1 The momentum relation for a scattering experiment, in which the incident beam having wavevector $\bar{\mathbf{k}}_\mathbf{i}$ interacts with atoms in the sample and is reradiated with wavevector $\bar{\mathbf{k}}_\mathbf{s}$. In this case, the scattering is inelastic, having $|k_s| < |k_i|$. The momentum transfer, Q, can be inferred from the scattering angle, 2θ by: $|Q| = \frac{4\pi \sin\theta}{\lambda}$. The detectors scan through all 2θ, so as to capture the scattered signal for a range of Q's. 59

5.2 The geometry of a scattering experiment in polar coordinates, showing a monochromatic incident beam (in blue), characterised by its wavevector $\bar{\mathbf{k}}_\mathbf{i}$ being scattered by the sample into a solid angle, $d\Omega$ (shown in red), in the direction defined by the angles θ and ϕ. In this example, the scattering particle has gained energy ($|\bar{\mathbf{k}}_\mathbf{s}| > |\bar{\mathbf{k}}_\mathbf{i}|$). 59

5.3 An incident plane wave is scattered elastically by a single fixed nucleus, with identical incident and scattered wavelengths. The wave is scattered isotropically from the point-like nucleus as an s-wave and reaches a detector placed far from the nucleus ($|\bar{\mathbf{r}} - \bar{\mathbf{r}}_j| >> b_j$). Positions of the nucleus and detector are defined by vectors from some chosen origin. 63

5.4 (Adapted from [148].) A typical atomic PDF for a model liquid (solid line), such as Ni. The schematic on the left shows how the two-dimensional radial distribution function progresses outwards from a reference atom (red), through the first (green), second (blue) and third (orange) coordination shells of a disordered material. In the graph on the right, the solid line shows the $g(r)$ for liquid Ni, while the dashed line shows the $g(r)$ for crystalline Ni, having much sharper peaks. The integral under the curve between successive troughs, represented by shaded areas, gives the coordination number for each shell. 71

5.5 Direct geometry TOF measurements, showing the pulsed nature of the beam and how this is controlled at each stage of the instrument, from the selection of a specific wavevector from the incoming beam by choppers or filters, to the detection of scattered neutrons dispersed by the sample. The scattering triangle, relating $\bar{\mathbf{k}}_i$ (fixed), $\bar{\mathbf{k}}_s$ and $\bar{\mathbf{Q}}$, is shown on the right. 76

5.6 Indirect geometry TOF measurements, showing how the beam pulses are controlled at each stage of the instrument, from the initial filtering of the incoming beam by choppers, to the selection of a specific wavevector from neutrons scattered by the sample. The relation between the $\bar{\mathbf{k}}_s$ (fixed), $\bar{\mathbf{k}}_i$ and $\bar{\mathbf{Q}}$,is shown on the right. 76

5.7 Schematic representation of an incoherent neutron scattering spectrum, displaying a single quasielastic component (magenta), centred at zero, broadening the base of the elastic line (blue), having amplitude A_1 and full width half-maximum (FWHM) Γ_1. Some peaks from the inelastic window are also shown here in green, but these may be difficult to distinguish from the quasielastic components. . . . 78

5.8 (from [158]) The left hand figure shows the jump length distributions used in the jump diffusion models proposed by (a) Singwi-Sjölander (exponential) [161] and (b) Hall-Ross (Gaussian) [158]. The right hand figure shows the broadening behaviour resulting from these distributions, with (c) showing the broadening due to Fick's law. 84

5.9 Quantum rotational transitions between the ground ($J = 0$) and first excited ($J = 1$) states for a) unhindered H_2, b) H_2 bound in such a way that one dimension is hindered and c) H_2 hindered in two dimensions. The degeneracy of the m_J states is lifted when H_2 is in the presence of a potential, so that the hindered dimension(s) have a higher energy level. 86

5.10 (Modified from [45].) The relationship between quantum mechanical energy levels and the rotational barrier field strength, showing how the degeneracy may be lifted when H_2 is exposed to an asymmetrical potential. 86

6.1 Thermogravimetric curves obtained for untreated laponite. Green shows the mass loss with temperature; blue shows the differential scanning calorimetry for this relation. The arrow indicates the mass loss attributable to interlayer water evaporation (96.7%) for 413 K. . 89
6.2 Typical Langmuir isotherms, showing how the characteristic shape of the curve is affected by the value of the Langmuir constant, b. 97
6.3 Comparing a variety of fit models for the low pressure region of adsorption isotherms for three representative samples of laponite. The measured data points for 77 and 87 K are shown as open circles and open squares, respectively, while the lines represent the fits. The solid magenta line gives the Freundlich fit (Equation 6.8); the solid blue shows the Sips (Langmuir-Freundlich) (Equation 6.9); the solid green line shows the Tóth model (Equation 6.10) and the dotted black line is the virial expansion model (Equation 6.12), this last being the best fit across all samples and temperatures. 100
6.4 Extraction of the isosteric heat of adsorption, ΔH_{ads}, for a particular coverage requires two isotherms at different temperatures, $T_1 > T_2$. For physisorption systems, the pressure required to achieve the same coverage at a higher temperature will be lower. 102
6.5 (From the ISIS website.) A schematic of the NIMROD diffractometer on target station 2 at the ISIS facility of RAL, showing the choppers and the detector array, covering a scattering angle range of 0.5-40°. . 106
6.6 Small angle scattering data from NIMROD measurements of Ca-laponite (EL), showing that, for the same pressures of H_2/D_2, the d-spacing remains constant over three temperatures. The red, representing the sample at 6 K, is obscured by the 40 K data, confirming that the small angle-data is not subject to either thermal or instrumental fluctuations and therefore changes here can be fully ascribed to the H_2/D_2 adsorption amount. 108
6.7 (Drawn by Arthur Lovell.) Schematic representation of the layout of the IRIS back-scattering TOF spectrometer at RAL. 110

6.8 All components of QENS fits to a range of spectral groups for the data collected for Na-laponite (RD) at 40 K, showing the Q-dependent broadening of the quasielastic peak (dashed red line). For this sample, problems arose at higher Q (top right) where the signal, particularly the elastic signal, is greatly diminished. However, the width of the fitted quasielastic peak appears to be approximately correct. The measured data is represented by black dots, the fit is shown as a solid blue line and the light blue line shows the instrumental resolution. The Lorentzian components of the fit are the elastic peak (magenta line) and the single quasielastic peak. Note that the y-axis is a log scale and the components are not properly scaled. The residuals (solid black line) are shifted by 1, to avoid them obscuring the data. 113

6.9 All components of QENS fits to a range of spectral groups for the data collected for Ca-laponite (RD) at 80 K, showing the Q-dependent broadening of the quasielastic peak (dashed red line). For this sample, problems arose at higher Q (top right) where the signal is diminished. The fit for the data at top right is off-centre, although the width appears to be approximately correct. The measured data is represented by black dots, the fit is shown as a solid blue line and the light blue line shows the instrumental resolution. The Lorentzian components of the fit are the elastic peak (magenta line) and the single quasielastic peak. Note that the y-axis is a log scale and the components are not properly scaled. The residuals (solid black line) are shifted by 1, to avoid them obscuring the data. 114

6.10 All components of QENS fits to a range of spectral groups for the data collected for Ca-laponite(EL) at 60 K, showing the Q-dependent broadening of the quasielastic peak (dashed red line). For this sample, problems arose at higher Q (top right) where the signal, particularly the elastic signal, is greatly diminished. However, the width of the fitted quasielastic peak appears to be approximately correct. The measured data is represented by black dots, the fit is shown as a solid blue line and the light blue line shows the instrumental resolution. The Lorentzian components of the fit are the elastic peak (magenta line) and the single quasielastic peak. Note that the y-axis is a log scale and the components are not properly scaled. The residuals (solid black line) are shifted by 1, to avoid them obscuring the data. 115

6.11 (From the ILL website.) The IN4 direct-geometry TOF spectrometer at the Institut-Laue-Langevin facility in Grenoble, France. 117

6.12 Attempts at fitting narrower peaks, with widths matching the expected resolution for IN4 with incident wavelength 1.773 Å, to the spectrum for Na-laponite (RD), measured at 6 K. The fit for unconstrained Gaussian peak reproduces the spectrum very closely, however these peaks cannot be easily constrained to fit the quantum model for the H_2 hindered rotor, as the fit statistics show. The hindered rotor pairs are colour-matched: the solid lines represent the degenerate $m_J=\pm1$ peaks and the dashed lines show the non-degenerate $m_J=0$ peaks. 120

6.13 Measurements of the clay substrate in vacuum, showing two peaks, fitted to Gaussian peaks. The signal from the clay itself was subtracted from subsequent measurements at matching temperatures in an H_2 atmosphere. 120

6.14 A second-order polynomial function, shown by the solid red line, was fitted to the data (blue circles) by estimation and subtracted from the data. The resulting signal is displayed in green. 121

7.1 Weight loss measured for three cation-exchanged forms of laponite (RD) at ambient pressure using a Thermogravimetric Analyser. The weight loss at 473 K is assumed to represent the total proportion of interlayer water, by weight. Comparing this with the weight loss at lower temperatures gives an indication of the remaining interlayer water, from which the H_2O:Ca^{2+} ratio can be determined. 124

7.2 Weight loss measured under vacuum using a Hiden Isochema Intelligent Gravimetric Analyser (IGA). 7.2a shows the weight loss for heating a sample of Ca-laponite (RD) to 473 K. Note that 191.274 mg of sample was loaded and most of the weight loss occurred during the gradual evacuation, before heating (not shown here). The total weight loss calculated was 17.62 wt% H_2O. 7.2b shows the weight loss for a second sample of Ca-laponite (RD) gradually evacuated and heated to 413 K for more than ten hours. The maximum weight loss calculated in 7.2a is used to scale the right-hand vertical axis of 7.2b to the corresponding temperature on the left axis. Assuming all interlayer water is lost at 473 K, these measurements show that the remaining interlayer water content of the sample is 0.9 wt% H_2O in vacuum at 413 K. 125

7.3 Typical XRD fits for the Na-laponite (RD) sample at four temperatures, showing the data (black dots), the total fit (solid red line) and the estimated background removed (dashed line) from the data in order to fit the Gaussian (solid green line) representing the (001) diffraction peak. The backgrounds are a combination of a decaying fourth power law for Q, with amplitude ranging from 3 to 5, a Gaussian peak centred at $Q = 0$ with amplitude ranging from 4,000 to 9,000 and a FWHM of between 13 and 14 Å^{-1} and a constant, values ranging from 176 to 179, all figures increasing with temperature. The room temperature measurement, Figure 7.3d, was taken after heating and subsequent cooling. The residuals are shown below each temperature. 127

7.4 Typical XRD fits for the Ca-laponite (RD) sample at four temperatures, showing the showing the data (black dots), the total fit (solid red line) and the estimated background removed (dashed line) from the data in order to fit the Gaussian (solid green line) representing the (001) diffraction peak. The backgrounds are a combination of a decaying fourth power law for Q, with amplitude ranging from 1.5 to 4, a Gaussian peak centred at $Q = 0$ with amplitude ranging from 4,000 to 10,000 and a FWHM of between 10 and 12.6 Å^{-1} and a constant, values ranging from 194 to 205, all figures increasing with temperature. The room temperature measurement, Figure 7.4b, was taken before heating. The residuals are shown below each temperature. . . 128

7.5 Temperature-dependency of the *d*-spacing for heated Na-laponite (RD). The background has been subtracted as described in Section 7.2.1 and the Gaussian fits to the XRD data at the highest and lowest heated temperatures (335 to 475 K) are shown as solid black lines. For this sample, the room temperature measurement was only performed after heating to 475 K and subsequent cooling and is not displayed. The results of the fits are presented in Table 7.1. 130

7.6 Temperature-dependency of the *d*-spacing for heated Ca-laponite (RD). The background has been subtracted as described in Section 7.2.1 and the Gaussian fits to the XRD data at the highest and lowest measured temperatures (room temperature to 475 K) are shown as solid black lines. The results of the fits are presented in Table 7.1. 131

7.7 Comparing low pressure gravimetric isotherms at 77 K for various pretreatment temperatures, for the sodium and calcium forms of laponite (RD). Note the large error bars for the low-coverage data for Na-laponite (RD), due to high temperature instability at the start of isotherms. 135

8.1 Full fits to the small angle scattering data obtained on NIMROD for Ca-laponite (EL) in vacuum (shown in red) and an H_2 atmosphere at increasing pressure, giving a range of loadings from 0 to 7.67 H_2 per Ca^{2+}, measured at two temperatures, 40 and 25 K. The measured data is represented by the open circles at the top. Colour is used to match the components for each loading. The fitting for each loading was done by first removing a background (shown as a dashed line) combining a constant, a Q^{-4} power law, representing Porod scattering from smooth surfaces [163], and a broad Gaussian (amplitudes ranging from 1.6 to 2.6, FWHM from 9.1 to 8.7 Å^{-1} and centred at $Q = 0$). The remainder was fitted to a single Gaussian peak (solid lines), representing the (001) peak and the reduced χ^2 range for each temperature series is given in the captions above. The *d*-spacing, calculated from the centre of this Gaussian and shown on the left, increases as more H_2 is introduced. The residuals are shown on a separate axis below each plot. 138

8.2 Full fits to the small angle scattering data obtained on NIMROD for Ca-laponite (EL) in vacuum (shown in red) and a D_2 atmosphere at increasing pressure, giving a range of loadings from 0 to 8.7 D_2 per Ca^{2+}, measured at two temperatures, 40 and 25 K. The measured data is represented by the open circles at the top. Colour is used to match the components for each loading. The fitting for each loading was done by first removing a background (shown as a dashed line) combining a constant, a Q^{-4} power law, representing Porod scattering from smooth surfaces [163], and a broad Gaussian (amplitudes ranging from 1.6 to 0.7, FWHM from 9.1 to 11.3 $Å^{-1}$ and centred at $Q = 0$). The remainder was fitted to a single Gaussian (solid lines), representing the (001) peak and the reduced χ^2 range for each temperature series is given in the captions above. The *d*-spacing, calculated from the centre of this Gaussian and shown on the left, decreases as more D_2 is introduced. The residuals are shown on a separate axis below each plot. 140

8.3 Differential cross-sections against Q, after incoherence has been removed and all other corrections, including those for inelasticity, have been made, for H_2 adsorbed on Ca-laponite (EL) at 40 K. The small angle scattering region contains the (001) peak representing the *d*-spacing of the clay and this region is magnified in the inset, where it is clear that, despite the flattening in intensity due to inelasticity corrections, the (001) peak increases as more H^2 is added. The legend on the left shows the colours corresponding to each H_2:Ca^{2+} ratio. . . 142

8.4 Differential cross-sections against Q, after incoherence has been removed and all other corrections, excluding those for inelasticity, have been made, for D_2 adsorbed on Ca-laponite (EL) at 40 K. The small angle scattering region contains the (001) peak representing the *d*-spacing of the clay and this region is magnified in the inset. Here it is clear that the (001) peak becomes smaller, due to the intercalated D_2 contrast matching with the clay layers. The legend on the left shows the colours corresponding to each D_2:Ca^{2+} ratio. 143

8.5 $G(r)$ compared for empty clay and clay with 2.76 H_2:Ca^{2+} adsorbed, at three temperatures. With the exception of the large peak representing the H-H bond distance in H_2, the main peaks which change are magnified in the inset. The legend on the right shows the colours representing each temperature. The dashed lines are for the clay in vacuum and the solid lines for the clay in a 40 mb H_2 atmosphere. . 145

8.6 $G(r)$ compared for empty clay and clay with 3 D_2:Ca^{2+} adsorbed, at three temperatures. The main peaks which change are magnified in the inset. The legend on the left shows the colours corresponding to each temperature. The dashed lines are for the clay in vacuum and the solid lines for the clay in a 40 mb H_2 atmosphere. 146

8.7 Fitted Gaussians to the $G(r)$ for Ca-Laponite (EL) at 40 K in (a) vacuum, (b) the lowest dose of H_2 and (c) the lowest dose for D_2. The region below r = 0.5 Å is excluded from the fits. The centres of these peaks are listed in Table 8.2. Typical χ^2_{red} values for these fits are on the order of 10^{-7}, due to the large number of fitting parameters. 148

8.8 $G(r)$ compared for Ca-laponite (EL) exposed to a range of H_2 concentrations, all measured at 40 K. With the exception of the large peak representing the H-H bond distance in H_2, the main peaks which change are magnified in the inset. The legend on the right shows the colours corresponding to each H_2:Ca^{2+} ratio. 150

8.9 $G(r)$ compared for a range of D_2 concentrations, all measured at 40 K. The main peaks which change are magnified in the inset. The legend on the left shows the colours corresponding to each D_2:Ca^{2+} ratio. 151

8.10 $G(r)$ compared for a range of H_2 concentrations, all measured at 25 K. With the exception of the large peak representing the H-H bond distance in H_2, the main peaks which change are magnified in the inset. The legend on the right shows the colours corresponding to each H_2:Ca^{2+} ratio. 152

8.11 $G(r)$ compared for a range of D_2 concentrations, all measured at 25 K. The main peaks which change are magnified in the inset. The legend on the left shows the colours corresponding to each D_2:Ca^{2+} ratio. 153

9.1 (a) Volumetric, high pressure isotherms measured at various temperatures for Na-laponite (RD), with the filled markers representing adsorption and the open markers in the same colour the corresponding desorption. The dashed lines in the corresponding colours show the Langmuir fits, Equation 6.7, to the two coldest adsorption isotherms, while the dotted black lines show the Tóth fits, Equation 6.10, used to calculate (b) the associated ΔH_{ads}. The fitting parameters for the Tóth fits are summarised for all measured samples in Table 9.1. . . . 157

9.2 (a) Volumetric, high pressure isotherms measured at a series of temperatures for Na-laponite (EL), with the filled markers representing adsorption and the open markers in the same colour the corresponding desorption. The dashed lines in the corresponding colours show the Langmuir fits, Equation 6.7, to the 148 K and 248 K adsorption isotherms. The shape of the 98 K isotherm measured for this sample clearly diverges from the Langmuir form and was not used for fitting, for reasons explained in the text. The dotted black lines show the Tóth fits, Equation 6.10, used to calculate (b) the associated ΔH_{ads}. The fitting parameters for the Tóth fits are summarised for all measured samples in Table 9.1. 158

9.3 (a) Volumetric, high pressure isotherms measured at a range of temperatures for Ca-laponite (RD), with the filled markers representing adsorption and the open markers in the same colour the corresponding desorption. The dashed lines in the corresponding colours show the Langmuir fits, Equation 6.7, to the two coldest adsorption isotherms, while the dotted black lines show the Tóth fits, Equation 6.10, used to calculate (b) the associated ΔH_{ads}. The fitting parameters for the Tóth fits are summarised for all measured samples in Table 9.1. . . . 159

9.4 (a) Volumetric, high pressure isotherms measured at a series of temperatures for Ca-laponite (EL), with the filled markers representing adsorption and the open markers in the same colour the corresponding desorption. The dashed lines in the corresponding colours show the Langmuir fits, Equation 6.7, to the two coldest adsorption isotherms, while the dotted black lines show the Tóth fits , Equation 6.10, used to calculate (b) the associated ΔH_{ads}. The fitting parameters for the Tóth fits are summarised for all measured samples in Table 9.1. . . . 159

9.5 (a) Volumetric, high pressure isotherms measured at various temperatures for Mg-laponite (RD), with the filled markers representing adsorption and the open markers in the same colour the corresponding desorption. The dashed lines in the corresponding colours show the Langmuir fits, Equation 6.7, to the two coldest adsorption isotherms, while the dotted black lines show the Tóth, Equation 6.10, used to calculate (b) the associated ΔH_{ads}. The fitting parameters for the Tóth fits are summarised for all measured samples in Table 9.1. 160

9.6 (a) Volumetric, high pressure isotherms measured at a range of temperatures for Mg-laponite (EL), with the filled markers representing adsorption and the open markers in the same colour the corresponding desorption. The dashed lines in the corresponding colours show the Langmuir fits, Equation 6.7, to the two coldest adsorption isotherms, while the dotted black lines show the Tóth fits, Equation 6.10, used to calculate (b) the associated ΔH_{ads}. The fitting parameters for the Tóth fits are summarised for all measured samples in Table 9.1. . . . 160

9.7 Low pressure gravimetric isotherms: a) shows isotherms taken at 77 K for two different batches of Na-laponite (RD), showing the variability in measurements and b) gives two isotherms taken at different temperatures for Mg-laponite (B). The uptake in the latter appears to be considerably higher than for the other forms of laponite, but the high degree of variability casts doubt on this estimate. 162

9.8 Volumetric, low pressure adsorption-desorption isotherms measured for two grades of Ca-laponite at two temperatures: 77 K (dark blue) and 87 K (cyan). The fits to a sixth order polynomial for a limited region only are shown by the solid lines and these are used to calculate the associated low-coverage ΔH_{ads}, shown in the insets as a function of coverage. In a), the dashed line shows the fit to the Sips (Langmuir-Freundlich) equation (Equation 6.9), whereas in b), the dashed line represents the Tóth model (Equation 6.10). Both of these fits match the data reasonably well over the full measured range, but give poor fits for the low coverage region. 164

9.9 Volumetric, low pressure adsorption-desorption isotherms measured for two cation forms of laponite (B) - a) Na and b) Ca - at two temperatures: 77 K (dark blue) and 87 K (cyan). The fits to a sixth order polynomial for a limited region only are shown by the solid lines and these are used to calculate the associated low-coverage ΔH_{ads}, shown in the insets as a function of coverage. In a), the dashed line shows the fit to the Sips (Langmuir-Freundlich) equation (Equation 6.9), whereas in b), the dashed line represents the Tóth model (Equation 6.10). Both of these fits match the data reasonably well over the full measured range, but give poor fits for the low coverage region. . . . 164

9.10 Volumetric, low pressure adsorption-desorption isotherms measured for two grades of Na-laponite - a) (RD) and b) (EL) - at two temperatures: 77 K (dark blue) and 87 K (cyan). The fits to a sixth order polynomial for a limited region only are shown by the solid lines and these are used to calculate the associated low-coverage ΔH_{ads}, shown in the insets as a function of coverage. In a), the dashed line shows the fit to the Tóth model (Equation 6.10), whereas in b), the dashed line represents the Sips (Langmuir-Freundlich) equation (Equation 6.9). Both of these fits match the data reasonably well over the full measured range, but give poor fits for the low coverage region. . . . 165

9.11 Volumetric, low pressure adsorption-desorption isotherms measured for two grades of Mg-laponite - a) (RD) and b) (EL) - at two temperatures: 77 K (dark blue) and 87 K (cyan). The fits to a sixth order polynomial for a limited region only are shown by the solid lines and these are used to calculate the associated low-coverage ΔH_{ads}, shown in the insets as a function of coverage. The dashed line shows the fit to the Sips (Langmuir-Freundlich) equation (Equation 6.9), matching the data reasonably well over the full measured range, but giving a poor fit for the low coverage region. 165

9.12 Volumetric, low pressure adsorption-desorption isotherms measured for two cation forms of laponite (B) - a) Mg and b) Cs - at two temperatures: 77 K (dark blue) and 87 K (cyan). The fits to a sixth order polynomial for a limited region only are shown by the solid lines and these are used to calculate the associated low-coverage ΔH_{ads}, shown in the insets as a function of coverage. In a), the dashed line shows the fit to the Sips (Langmuir-Freundlich) equation (Equation 6.9), whereas in b), the dashed line represents the Freundlich model (Equation 6.8). Both of these fits match the data reasonably well over the full measured range, but give poor fits for the low coverage region. 166

9.13 Volumetric, low pressure adsorption-desorption isotherms measured for two grades of Cs-laponite - a) (RD) and b) (EL) - at two temperatures: 77 K (dark blue) and 87 K (cyan). The fits to a sixth order polynomial for a limited region only are shown by the solid lines and these are used to calculate the associated low-coverage ΔH_{ads}, shown in the insets as a function of coverage. In a), the dashed line shows the fit to the Tóth model (Equation 6.10), whereas in b), the dashed line represents the Sips (Langmuir-Freundlich) equation (Equation 6.9). Both of these fits match the data reasonably well over the full measured range, but give poor fits for the low coverage region. . . . 166

9.14 Interparticle pore size distributions by volume for a range of laponites: a) Na-laponite (RD), b) Ca-laponite (EL) and c) Cs-laponite (B), showing the modal pore widths for each. These clays are nanoporous, with an insignificant number of pores having a diameter in excess of 6 nm. 170

10.1 Insights from intensity and intensity ratios: the temperature-dependence of the intensity measured during QENS, showing the relative proportions attributed to elastic (blue) and quasielastic (green) scattering, as well as the total (red). The right-hand axis shows the corresponding ratio of adsorbed H_2 to Ca^{2+} cations in the clay. From simultaneous pressure measurements at each temperature and using Boyle's law, a rough estimate for this ratio can be obtained (open black squares), with a fitted exponential represented by the black dotted line. The red dotted line is a fitted exponential to the total intensity. The neutron scattering intensity and pressure are independent measures of the amount of H_2 present in the sample and these plots show how these data sets correspond. The match is best for Ca-laponite (RD), reasonable for Na-laponite (RD), but poor for Ca-laponite (EL). . . . 175

10.2 QENS FWHM data and fits for the four temperatures measured on Na-laponite (RD). Three of the models discussed in the text in Section 5.3.1 are shown for all temperatures: Singwi-Sjölander (solid black line), Chudley-Elliott (dotted cyan line) and Hall-Ross (dashed magenta line). The solid red line shows the Fickian diffusion model, obtained by a linear regression fit on the two lowest Q-values. The FWHM for spectral group 17 is shown as an open data marker, but this datum appears to be too broad for the instrument's window, as well as an outlier consistently across all temperatures and for Ca-laponite(EL) measurements too (see Figure 10.4. Consequently, this FWHM was omitted from the fits. 177

10.3 QENS FWHM data and fits for the four temperatures measured on Ca-laponite (RD). Three of the models discussed in the text in Section 5.3.1 are shown for all temperatures: Singwi-Sjölander (solid black line), Chudley-Elliott (dotted cyan line) and Hall-Ross (dashed magenta line). The solid red line shows the Fickian diffusion model, obtained by a linear regression fit on the two lowest Q-values, passing through the origin. The FWHM for spectral group 14 at 100 K is shown as an open data marker, but this datum appears to be an outlier and was omitted from the fits. 178

10.4 QENS FWHM data and fits for the four temperatures measured on Ca-laponite (EL). Three of the models discussed in the text in Section 5.3.1 are shown for all temperatures: Singwi-Sjölander (solid black line), Chudley-Elliott (dotted cyan line) and Hall-Ross (dashed magenta line). The solid red line shows the Fickian diffusion model, obtained by a linear least-squares regression fit on the two lowest Q-values, passing through the origin. The FWHM for spectral group 17 is shown as an open data marker, but this datum appears to be too broad for the instrument's window, as well as an outlier consistently across all temperatures and for Na-laponite (RD) measurements too (see Figure 10.2). Consequently, this FWHM was omitted from the fits. 180

10.5 Q^2-dependence of the broadening of the quasielastic components measured at a range of temperatures per sample, showing fits to the Singwi-Sjölander jump diffusion model (solid lines). The blue diamonds represent measurements taken at 40 K, cyan triangles represent 60 K, orange squares for 80 K and red circles for measurements at 100 K. 183

10.6 Temperature dependence of the diffusion coefficient, measured by QENS, for H_2 in Na-laponite (RD) (cyan circles), Ca-laponite (RD) (magenta squares) and Ca-laponite (EL) (green diamonds), showing Arrhenius analysis for each set of data. The diffusion coefficients for bulk liquid H_2 extrapolated to the same temperatures are represented by the top two lines: a solid black line [221] and a dashed black line [212]. Also shown are the data from two studies of hydrogen-adsorbing materials: an activated carbon, PFAC [214], shown as black asterisks, and a carbon black, XC-72 [225], shown as black triangles. Both sets of data are joined by a dotted black line representing their regression analyses. 184

10.7 Proposed geometric arrangement of the interlayer region (top view) for Na-laponite (RD), with all components drawn to scale. The water molecules are tilted, because in the clay interlayer, the hydrogen atoms would lie in a plane orthogonal to the page, as is seen in the side view illustration in Figure 4.2. The full hexagonal structure of the inner interlayer surface, deriving from the Si-O tetrahedra, is shown for only one hexagon at the bottom right. The remaining hexagons are simplified to show only their Si framework and OH centres. The laponite unit cell is represented by the red dashed-line rectangle and its dimensions [184] are given by the arrows below and to the left. Interlayer Na^+ (orange circles), shown as evenly but randomly distributed at approximately 0.7 per unit cell, forms complexes with H_2O (blue) and H_2 (white ovals outlined with blue). In order to illustrate the theoretical possibilities, some complexes have three waters and one H_2, others have two waters and two hydrogen molecules and a few have three H_2. The measured jump lengths from the fitted QENS data at all four temperatures is shown to scale on the right, with the double line representing the uncertainty in each measurement. 185

10.8 Proposed geometric arrangement of the interlayer region (top view) for Ca-laponite (RD), with all components drawn to scale. The water molecules are tilted, because in the clay interlayer, the hydrogen atoms would lie in a plane orthogonal to the page, as is seen in the side view illustration in Figure 4.2. The full hexagonal structure of the inner interlayer surface, deriving from the Si-O tetrahedra, is shown for only one hexagon at the bottom right. The remaining hexagons are simplified to show only their Si framework and OH centres. The laponite unit cell is represented by the red dashed-line rectangle and its dimensions [184] are given by the arrows below and to the left. Interlayer Ca^{2+} (purple circles), shown as evenly but randomly distributed at approximately 0.35 per unit cell, forms complexes with H_2O (blue) and H_2 (white ovals outlined with blue). In order to illustrate the theoretical possibilities, one complex is shown with two waters and two hydrogen molecules, another with three H_2 and the third with three waters and one H_2. The measured jump lengths from the fitted QENS data at all four temperatures is shown to scale on the right, with the double line representing the uncertainty in each measurement, the range taken over both calcium-exchanged laponites: (RD) and (EL). 186

10.9 The Q-dependence of the EISF at two temperatures per sample. The blue diamonds represent measurements taken at 40 K, cyan triangles represent 60 K, orange squares for 80 K and red circles for measurements at 100 K, with fits (solid lines for the lower temperature; dashed lines for the higher temperature) to a combination of the 2-site and 3-site models explained in Section 5.3.1. The low-Q point at unity is a requirement of the fit. The fits seem reasonable for the low temperature data, but are untenable at higher temperatures. For Ca-laponite (EL) at 80 K, the elastic component disappears for $Q > 1$ Å^{-1}, thus only the 40 K and 60 K data are shown for this sample. . 188

11.1 INS data and fits for Na-laponite (RD) in a 12 bar H_2 atmosphere (3 H_2:Na^+), showing the consistency of fitted peak positions over four temperatures, ranging from 6-48 K. A polynomial background was removed before fitting a set of paired Gaussian peaks, following the constraints of the quantum model for the H_2 hindered rotor and with the width fixed at 2.35 meV (selected by choosing the best fit from a series of fits run at different fixed values). The black circles are the measured data points, the superimposed solid red line is the full fit and the pairs of Gaussian peaks are colour-matched. The doubly-degenerate peak of each pair is shown by a solid line and its corresponding non-degenerate peak as a dotted line in the same colour. Corresponding with the numbering of sites presented in Table 11.1, site 1 is shown in magenta, site 2 in orange, site 3 in light blue and site 4 in dark blue. Some peaks appear to be unpaired (magenta and orange for lower temperatures), presumably because their corresponding peaks lie outside the measured energy transfer window. The free rotor peak, centred at 14.74 meV, is absent in each case. Note that the scale on the residuals is slightly different from the main plots. 194

11.2 INS data and fits for Ca-laponite (RD) in a 2 bar H_2 atmosphere (1 H_2:Ca^{2+}), showing the consistency of fitted peak positions over four temperatures, ranging from 5-50 K. The background (clay measured in vacuum) was removed before fitting two pairs of unconstrained Gaussian peaks. The dimensions and energy shifts of the pairs of peaks match the hindered rotor model. The black circles are the measured data points and the superimposed solid red line is the full fit. The singly-degenerate peaks of the hindered rotor pairs are shown by a dotted line and its corresponding doubly-degenerate peak as a solid line in dark blue for site 4, colour-matched with its corresponding site in Na-laponite (RD) (see Figure 11.1) and in green for site 5, which has no analogue in the other two samples. No other inelastic peaks were visible in the range 0 - 20 meV. Note that the scale on the residuals is slightly different from the main plots and that the scale for 48 K is almost double that of the other three temperatures. 197

11.3 INS spectra and fits for Ca-laponite (EL) in a 0.5 bar H_2 atmosphere (<1 H_2:Ca^{2+}), showing the consistency of fitted peak positions across four temperatures, ranging from 6-48 K. A polynomial background was removed before fitting a set of paired Gaussian peaks, following the constraints of the quantum model for the H_2 hindered rotor. The start parameters for these fits were derived from the results at higher loadings, because the data is less clear and a reasonable fit could probably be obtained from a variety of Gaussian sets. The black circles are the measured data points, the superimposed solid red line is the full fit and the pairs of Gaussian peaks are colour-matched. The doubly-degenerate peak of each pair is shown by a solid line and its corresponding non-degenerate peak as a dotted line in the same colour. Corresponding with the numbering of sites presented in Table 11.3, site 1 is shown in magenta, site 2 in orange, site 3 in light blue and site 4 in dark blue. The magenta peak appears to be unpaired, presumably because the corresponding non-degenerate peak lies outside the measured energy transfer window. The free rotor peak, centred at 14.74 meV [37], is absent in each case. Note that the scale on the residuals for 48 K is reduced compared to the other three temperatures, indicating slightly larger residuals than for the lower temperatures. 199

11.4 INS spectra and fits for Ca-laponite (EL) in a 2 bar H_2 atmosphere (1 H_2:Ca^{2+}), showing the consistency of fitted peak positions across four temperatures, ranging from 6-48 K. A polynomial background was removed before fitting a set of paired Gaussian peaks, following the constraints of the quantum model for the H_2 hindered rotor. The black circles are the measured data points, the superimposed solid red line is the full fit and the pairs of Gaussian peaks are colour-matched. The doubly-degenerate peak of each pair is shown by a solid line and its corresponding non-degenerate peak as a dotted line in the same colour. Corresponding with the numbering of sites presented in Table 11.3, site 1 is shown in magenta, site 2 in orange, site 3 in light blue and site 4 in dark blue. The magenta peak appears to be unpaired, presumably because the corresponding non-degenerate peak lies outside the measured energy transfer window. The free rotor peak, centred at 14.74 meV [37], is absent in each case. 201

11.5 INS spectra and fits for Ca-laponite (EL) at 6 K, showing the consistency of fitted peak positions across four loadings ranging from 1-4 H_2:Ca^{2+}. A polynomial background was removed before fitting a set of paired Gaussian peaks, following the constraints of the quantum model for the H_2 hindered rotor. The black circles are the measured data points, the superimposed solid red line is the full fit and the pairs of Gaussian peaks are colour-matched. The non-degenerate peak of each pair is shown by a dotted line and its corresponding doubly-degenerate peak as a solid line in the same colour. The magenta peak centred at ~9 meV appears to be unpaired, presumably because its corresponding non-degenerate peak lies outside the measured energy transfer window. The free rotor peak, centred at 14.74 meV [37], is absent in each case. 202

11.6 INS spectra and fits for Ca-laponite (EL) in an 18 bar H_2 atmosphere (9 H_2:Ca^{2+}), showing the consistency of fitted peak positions across four temperatures, ranging from 6-48 K, as well as the evolution of the peak shapes with a much higher loading. A polynomial background was removed before fitting a set of paired Gaussian peaks, following the constraints of the quantum model for the H_2 hindered rotor. The black circles are the measured data points, the superimposed solid red line is the full fit and the pairs of Gaussian peaks are colour-matched. The non-degenerate peak of each pair is shown by a dotted line and its corresponding doubly-degenerate peak as a solid line in the same colour. The magenta peak centred at ~9 meV is unpaired, presumably because its corresponding peak lies outside the measured energy transfer window. Two narrower peaks of FWHM 0.5 meV were needed to achieve a reasonable fit. Omitting these peaks did not reproduce all the spectral features and inclusion of a free rotor peak made the fit worse in all cases. At lower loadings, the peak parameters are very similar. The two narrow peaks only appear at loadings exceeding 2 H_2:Ca^{2+}. 203

11.7 Comparison of the site structure for Ca-laponite (EL) for roughly equivalent H_2 adsorption amounts in two directions: a) shows the structure of a lower loading after adsorption and b) shows the structure after the adsorbed H_2 at a higher loading has undergone approximately 52% thermal desorption. Sites 2 (orange) and 3 (light blue) are relatively more prominent and the splitting for site 1 (magenta) has reduced. c) shows the fits for a lower loading at 6 K and d) shows the post-desorption spectrum and fits from a higher loading. In this case, the spectra are very similar, with a slight reduction in site 2 (orange). 207

12.1 (Adapted from [232].) Current and proposed future research status of H_2 storage materials, comparing their gravimetric and volumetric storage capacities. Clay minerals - a new class of materials - adsorb H_2 by physisorption, as do carbons. By analogy with the improvements to H_2 uptake achieved in carbon materials, the red crosses indicate the initial and expected future position for clay minerals. While the gravimetric density of H_2 in clays will always be low, due to the high intrinsic weight of clays (900 g mol^{-1} for sodium laponite), for some applications, such as shipping and stationary storage at a power station or in homes, this is not a handicap, while the extremely low cost and wide abundance of clays is a great advantage. 217

List of Tables

1.1 Comparison of relevant safety properties for hydrogen, methane and petroleum [18]. 12
1.2 DoE technical targets for onboard hydrogen storage [22]. 16

2.1 Calculated binding strengths between hydrogen molecules and bare Na^+ and Mg^{2+} cations, showing the variation of energies and bond distances expected for the first three H_2's in a hypothetical solvation shell (from [41]). 28

4.1 Comparison of prices of HSMs available from Sigma-Aldrich, ignoring all considerations of storage temperature. Prices were obtained from the Sigma-Aldrich online catalogue on 22/04/2014. Unfortunately, no price could be found for AX-21, which achieves 5 wt% H_2 - a typical activated carbon is presented instead. 56

5.1 Comparison between X-rays and thermal neutrons. 62
5.2 Neutron cross-sections for some elements and isotopes relevant to this study [146]. 64

7.1 *d*-spacing extracted from the (001) peak in the diffractograms for Na- and Ca-laponite (RD), measured in air while raising the temperature from ambient to ~473 K. In the Na-laponite sample, the room temperature measurement was taken after subsequent cooling, where some water may have been reabsorbed. The χ^2_{red} values are very high, due to the number of fitting parameters needed to remove the low-Q background. 132

8.1 *d*-spacing for various pressures (P in the leftmost column) and temperatures for H_2 and D_2, showing that the *d*-spacing increases slightly as the H_2 pressure is raised, but decreases as the D_2 pressure is raised. The latter is an anomaly due to contrast-matching with the clay surface, more fully explained in the text. 141
8.2 Assignment of likely species involved in the bonds indicated by peak centres taken from the fitted Gaussians to $G(\bar{\mathbf{r}})$ for 2.76 H_2:Ca^{2+} and 3 D_2:Ca^{2+} in Ca-laponite (EL). The bond lengths in the third column are quoted from measurements or theoretical estimates in the literature. The expected weightings for each peak is shown in the rightmost two columns, the first calculated for the sample dosed with 2.76 H_2:Ca^{2+} and the second for the same sample dosed with 3 D_2:Ca^{2+}. 149

9.1 Summary of fitting parameters for the Tóth model, Equation 6.10, from which the ΔH_{ads} for the high pressure isotherms in Figures 9.1 through 9.6 were calculated. Some fits have unusually high χ^2_{red}, due to high variance in temperature, especially in the low coverage measurements. 161
9.2 Summary of H_2 storage capacities and binding enthalpies for a variety of laponite forms, based on the volumetric measurements presented in this Chapter. The rightmost column shows the model selected as the best match for each sample's low pressure volumetric adsorption isotherms, from which the ΔH_{ads} for 1 and 2 H_2 per cation was calculated. 163
9.3 Volumetric vs gravimetric energy densities of a variety of physisorption materials at 77 K and 1 bar, unless otherwise stated. 168
9.4 Summary of the information extracted from a DFT model fit to the 77 K N_2 isotherms, for all samples measured. 169

10.1 Comparison of parameters from three jump diffusion model fits to Na-laponite(RD) QENS data collected at three temperatures. 176
10.2 Comparison of fitting parameters from various jump diffusion models applied to QENS data from H_2 diffusing in Ca-laponite(RD), collected at four temperatures. 179
10.3 Comparison of parameters from three jump diffusion model fits to Ca-laponite(EL) QENS data collected at three temperatures. 179

10.4 Temperature dependency of diffusion coefficients, in (Å^2 ps^{-1}), of H_2 in all laponite samples measured by QENS. Estimated diffusion coefficients for bulk liquid H_2 from two independent studies are also shown, for comparison. 181

10.5 Results of an Arrhenius analysis on the diffusion coefficients, calculated from QENS measurements, showing the activation energies indicated by the linear regression fits of $-ln(D)$ vs $\frac{1000}{T}$. 182

11.1 Comparison of hindered rotor peak parameters from the fits to the INS spectra for Na-laponite(RD) in a 12 bar H_2 atmosphere (3 H_2:Na^+), at four different temperatures. A fixed width of 2.35 meV was used in these fits. The amplitude and centre of each peak is given, as well as the separation between their centres. The numbering of the sites matches those in Figure 11.1. The text in italics is data requiring confirmation, owing to the non-degenerate peak of the pair being outside the measured energy window. 195

11.2 Comparison of fit parameters for four Gaussian peaks, resulting from the fits to the INS spectra over four different temperatures for Ca-laponite(RD) in a 2 bar H_2 atmosphere, giving a loading of 1H_2:Ca^{2+}. The amplitude and centre of each peak is given, as well as the separation between the paired hindered rotor peak centres. With the exception of the widths of the peaks for site 5, the fits were unconstrained, allowing all other parameters to vary. Uncertainties have been included only where they exceed 0.01 meV. 196

11.3 Comparison of hindered rotor peak parameters from the fits to the INS spectra for Ca-laponite(EL) in an 18 bar H_2 atmosphere (9 H_2:Ca^{2+}), showing the variation with temperature. The amplitude and centre of each peak is given, as well as the separation between the paired hindered rotor peak centres. The widths for all paired peaks were fixed at 2.59 meV. The text in italics is data requiring confirmation, owing to the non-degenerate peak of the pair being outside the measured energy window. 204

11.4 Trends with increasing H_2 density for sites observed in the INS spectra for Ca-laponite (EL), taken from the measurements at 6 K. For each loading, the widths were fixed values for all peaks. The text in italics is data requiring confirmation, owing to the non-degenerate peak of the pair being outside the measured energy window. 205

11.5 Barrier strengths and symmetries for all sites, taken from the measurements at 6 K and the highest loading for each sample. The text in italics is data requiring confirmation, owing to the non-degenerate peak of the pair being outside the measured energy window. 206